Analysis of Heat Loss during Flame Wall Interaction of Premixed Propagative Flames and Diffusive Spray Flames

Abhijit Padhiary

THESE

Pour l'obtention du Grade de
DOCTEUR DE L'ECOLE NATIONALE SUPERIEURE DE MECANIQUE ET D'AEROTECHNIQUE
(Diplôme National – Arrêté du 25 mai 2016)

Ecole Doctorale : Sciences et Ingénierie en Matériaux, Mécanique, Energétique

Secteur de Recherche : Fluides, Thermique et Combustion

Présentée par : Abhijit Padhiary

****

Analysis of heat loss during flame wall interaction of premixed propagative flames and diffusive spray flames

****

Directeur de thèse : Julien Sotton
Co-encadrant : Marc Bellenoue et Guillaume Pilla

****

Soutenue le 20 May 2022

devant la Commission d'Examen

****

JURY

Rapporteurs :
Cédric Galizzi , Professeur, INSA Lyon / CETHIL
Brian Peterson, Associate Professor, University of Edimburgh/ IMT

Membres du jury :
Christine Rousselle, Professeur Polytech'Orléans / PRISME
Guillaume Pilla, Ingénieur de recherche, ONERA
Marc Bellenoue, Professeur ISAE-ENSMA /PPRIME
Julien Sotton, Professeur ISAE-ENSMA /PPRIME

Membre invité:
Adele Poubeau, Ingénieur de recherche, IFP Énergies nouvelles

Acknowledgments

The journey to the completion of this Ph.D. is a life-changing experience that would not have been possible for me without the guidance and support that I had. Thank you, Prof. Andreas Dreizler for the amazing lectures that inspired me to pursue research in optical diagnostics.

First and foremost, I would like to thank my advisors Dr. Guillaume Pilla, Dr. Julien Sotton, and Dr. Marc Bellenoue. Guillaume was always available for discussion, continuously pushing me towards the right approach to carry out research. Julien and Marc are exceptional in providing me with a rigorous method to evaluate scientific questions and answer them. I am grateful to Guillaume, Julien, and Marc for the time they invested in helping me to plan experiments, participating actively in scientific discussions, monitoring the progress of my thesis, encouraging me, and making sure that I have the resources that I needed to complete this thesis.

I thank all engineers (Dr. Michele Bardi, Dr. Loui M Malbec, Dr. Phillip Schiffman, Dr. Matheiu Cordier, and many others), Ph.D. students (Dr. Julien Moussou, Dr. Fabien Tagliante, Dr. Louise Ganeau, Kamal Shway, Mohammad Chemak Amine, Andreas Kopf, Mouad Daoudi, Ivano Cornacchi) and technicians of IFPEN (special mention Jerome Cherel and Clement Bramoulle) especially the optical diagnostics group that has contributed immensely during my experiments carried out in this thesis.

Thank you, my father, mother, my brother Asit, and my wife Rucha who have been the bed rock that supported me through the tough evaluations of life making me capable to sustain this Ph.D.

I acknowledge the support from IFPEN and ENSMA for funding, experiment facility, and other resources necessary to carry out my Ph.D.

TABLE OF CONTENTS

Nomenclature

A	area of engine cylinder
a,b	power-law coefficients
ASOI	after start of injection
BL, thermal BL	momentum boundary layer, thermal boundary layer
c	concentration of tracer used in LIF
C	degree peak locking
CAD	crank angle degree
CI	compression ignition
c_P, c_{P1}	specific heat capacity, specific heat capacity in fresh gas
CVC	constant volume chamber
d_P	diameter of PIV particle
ECN	engine combustion network
EGR	exhaust gas recirculation
FFT	fast Fourier transform
FWI	flame-wall interaction
g	gravity
h	convection heat transfer coefficient
HOQ	head on quenching
I	LIF signal intensity
ID	ignition delay
IMEP	indicated mean effective pressure
k	thermal conductivity
K_a	Karlovitz number
Kx,Ky	kurtosis in x and y component
L	estimated largest length scale for engine applications
LHV	lower heating value of the fuel
LIF	laser induced fluorescence
LoL	lift-off-length
L_t	turbulent integral length scale used in literature
$L_{u,t}$	turbulent integral length scale estimated in this thesis
$\dot{m}$	mass flow rate of fuel during engine operation
n	number density of fluorescent atom
PC	prechamber
Pe	Peclet number
P	pressure in combustion chamber
P_{int}	pressure during interaction
PIV	particle image velocimetry
Pr	Prandtle number
PSD	power spectrum density
q	turbulence intensity
Q	heat flux
Q_Σ	flame power
Q_H	heat of reaction

Q_{HF}	high frequency heat flux fluctuations
Q_{HR}	average heating rate
Q_{integ}	integrated heat loss
Q_P, Q_W	peak of heat flux
Q_π	non dimensional heat flux in engines
r	radial distance from the center of spray/jet
RCM	rapid compression machine
RFW	relative flame wrinkling
ROI	region of interest
RPM	engine speed, rotations per minute
$R_{u,t}$	correlation coefficient
SI	spark ignited
S_L	laminar flame speed
S_T	turbulent flame speed
St	Stokes number
SWQ	side wall quenching
Sx,Sy	skewness in x and y component
t	time after spark for propagative FWI/time after start of injection for spray
T	wall surface temperature after spark
T_W	wall surface temperature after start of injection
T_1	fresh gas temperature
t_1,t_2,t_3,t_4	different instant of FWI given in Figure 23
T_2	burnt gas temperature
Tmax	adiabatic gas temperature
T_∞	free stream temperature
T_{amb}	hot gas temperature before spray
TC	thermocouple
T_g	hot gas temperature near the wall
T_m	mean gas temperature in the engine chamber
t_p	characteristic time of drag on particle
t_t	largest time scale estimated from literature
t_Δ	smallest time scale estimated from literature
U	velocity vector
u'	fluctuation in velocity vector
U^+	normalized velocity vector
$\overline{U}$	average velocity vector
u'_{cycle}	cycle-to-cycle fluctuation in velocity
u'_{HF}	high frequency velocity
U_{LF}	low frequency velocity
$u'_{reynolds}$	fluctuations determined using Reynold's decomposition
u'_{RMS}	root mean square of turbulent fluctuations
X_D	distance between spark plug and wall-TC assembly
X_x, X_y	displacement in pixels in x component and y component
y	distance from the wall
y^+	normalized distance from the wall
Y_D	distance between the injector tip and wall-TC assembly
Y^1_F	fuel mass fraction in fresh gas
δ_F	laminar flame thickness

δ_q	quenching distance
ΔT	temperature difference near the wall
Δt, Δt_r, Δt_f	duration for rise and fall in heat flux trace, rise time, fall time
Δt_q	duration of FWI used in literature
Δy	gradient on distance from wall
η_k	Kolmogorov scale
k_1	thermal conductivity of fresh gas
ρ, $\rho 1$	density, density of fresh gas
ρ_P	density of PIV particle
τ_c	chemical time scale
τ_k	time scale of Kolmogorov scale
μ	viscosity
Δ	smallest turbulence scale estimated from the literature

List of Figures

Introduction

The internal combustion engine was man's workhorse in the last century. Even with the advent of new energy technologies, internal combustion (IC) engines will remain relevant for decades to come [1]. Though IC engines provide the power on which humanity develops, they also degrade the environment by emitting carbon dioxide and other pollutants. CO_2 is a major greenhouse gas that acts to warm the atmosphere of the earth, a phenomenon called global warming. The evolution of CO_2 emissions over the years (1990-2019) by different sectors is presented in Figure 1. The transportation sector, which includes IC engines, contributes about 24% every year. The fraction of CO_2 emissions from subsectors in the transportation sector is presented in Figure 2. In this figure, we can see that 87% of the total emissions are from passenger road vehicles, passenger freight vehicles, rail, and shipping sectors which predominantly use IC engines. It is important for the sustainability of our planet that we strive toward sustainable development and utilization of energy. One of the immediate goals is to reduce the CO_2 emitted by engines. This could be achieved by increasing the efficiency of engines. Global fuel economy targets set by the International Energy Agency aim for the improvement of the IC engine's fuel economy by 3.7% over the current rate of improvement. IC engine efficiency can be improved by decreasing the losses they incur. One of the important components of losses is the heat loss caused by the hot gases encountered during combustion inside the engine. These losses can reach over 30% of the total fuel energy used in the engine. This thesis will probe into heat loss through experimental work characterizing the thermal exchanges during representative IC engine combustion.

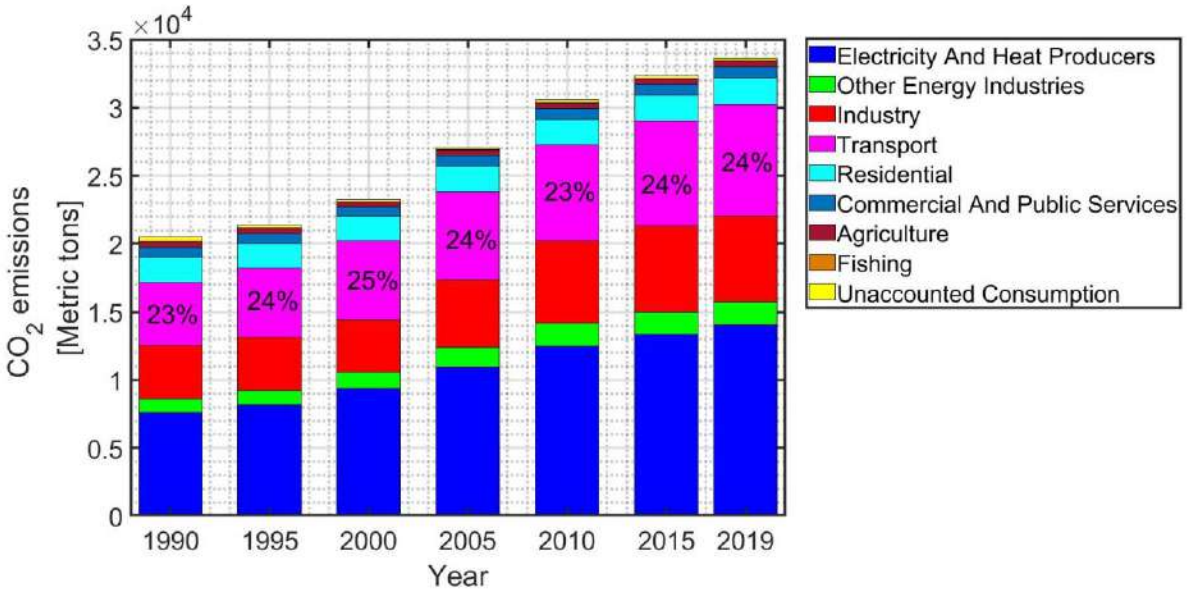

Figure 1: CO_2 emissions by the transportation sector. Data collected from the reference [2]

Figure 2: Distribution of CO_2 emissions (in %) in different subsectors of the transport sector in 2018. Data collected from the reference [3]

The reduction of heat losses in IC engines is possible by understanding the heat loss mechanism in different modes of combustion and identifying important parameters that can control the heat losses. Accurate heat loss prediction can help to optimize the engine, and its performance to increase its efficiency. Further, such predictions will help towards future engines development using sustainable fuels like hydrogen, ammonia, synthetic fuels, etc. Towards this goal, many studies are carried out in the literature, which will be discussed throughout the thesis. There are still many open issues that are discussed in this thesis. High instantaneous heat flux of the order of MW/m^2 is observed during flame-wall interaction (FWI). This thesis plans to study FWI found in two common modes of the combustion engine, i.e., propagative, and diffusive combustion, typically found in spark-ignition (SI) engines and diesel

engines, respectively. During any engine operation, various controlling parameters are coupled, hence a constant volume chamber (CVC) is used where these parameters can be decoupled using a fixed boundary condition during experiments. In this thesis, the premixed FWI is studied in a CVC using thin junction thermocouple (TC) to measure surface temperature to deduce the instantaneous heat flux during FWI. Using a variation of the distance between the spark plug and the thermocouples we will find the effect of pressure during interaction ($\boldsymbol{P_{int}}$) on the peak of heat flux ($\boldsymbol{Q_P}$) in laminar conditions. Simultaneous PIV measurements are planned to be carried out to determine the turbulence intensity before FWI. Using different fan operating strategies inside the CVC we plan to obtain both laminar and turbulent flames. Using these measurements, we will find the effect of turbulence intensity on the heat flux during FWI. Variations in the gas composition will be carried out to understand the effect of dilution through 5% and 10% extra CO_2 and N_2 (by mole fraction). Further variation of flame power, the position of measurement, and fuel type are planned to be carried out to understand their effect on $\boldsymbol{Q_P}$. Diffusive combustion will also be studied in the CVC with surface temperature measurements and chemiluminescence visualization. The heat flux in both a reactive spray FWI and a non-reactive spray-wall interaction will be studied to separate the contribution of reaction and spray dynamics on the heat flux. These measurements are planned to be carried out at 3 different locations of TC measurement enabling us to understand the heat flux at different locations during a spray FWI. Further two different ambient temperatures are planned to be used to understand their effect on the heat flux during spray FWI. Premixed propagative FWI is carried out in a port-fuel SI engine using both conventional SI and prechamber (PC) ignition systems to compare the heat flux. Parametric variations like tumble variation, location of thermocouple, ignition timing variation, and IMEP variation are also conducted to understand their effect on the heat flux FWI in an engine.

This thesis is organized into five main chapters. Chapter 1 presents a literature review that elaborates on the important open issues in FWI. Chapter 2 presents the methods employed to study FWI

through experiments, numerical calculations, and post-processing methods used in this thesis is discussed. The results of the different experiments carried out in this thesis for premixed FWI in CVC and their analysis are presented in Chapter 3. Chapter 4 presents the different experiments carried out in this thesis for diffusive FWI due to spray wall interaction in CVC. Chapter 5 presents the experiments and analysis of premixed FWI in an engine. Finally, a conclusion is presented to summarize the outcome of this thesis and provide perspectives for future work.

Chapter 1: Bibliography

In this chapter, we present the analysis of the literature to identify important questions that can assist us in better understanding wall heat losses in IC engines. First, we present IC engines and their different losses leading to identifying the best strategies to enhance IC engine's efficiency. The magnitude of heat losses and the measurement techniques are then analyzed to identify the best approach for experimental characterization. Next, the topic of flame-wall interaction is discussed in detail to identify important parameters whose effects need to be understood to resolve the associated heat loss.

1.1. COMBUSTION IN ENGINES

In this section, the general working of engines is discussed which leads to identifying important losses mechanisms. Further, the fundamentals of different combustion modes are highlighted pointing out the important parameters for each mode of combustion.

1.1.1. GENERAL WORKING OF AN ENGINE

An IC engine works by combusting fuel to convert the chemical energy into mechanical work through heat release into the combustion chamber. In this thesis, we will study spark ignition (SI) and compression ignition (CI) engines. The working of the engine occurs generally in four strokes. In some cases, these four strokes are combined into two strokes [4]. Figure 3 shows a schematic of the working process of both SI and CI engines. The first stroke, called the intake stroke, is responsible to suck the air-fuel mixture or fresh gas inside the engine combustion chamber, using the downward motion of the piston after the intake valve opening. The second stroke (compression stroke) compresses the mixture to a high temperature at which combustion can occur and sustain itself. In SI engine, the fuel is added through fuel-air mixture during the intake stroke, or through direct injection after the intake stroke. In a CI engine fuel is introduced

by direct injection. After the compression stroke, the chemical energy of the fuel is released into the system as heat. Typically, in a SI engine, a spark is used to ignite the fuel-air mixture while in CI, the fuel-air mixture auto-ignites. Combustion generates high temperature and pressure which work against the piston leading to the third stroke called the expansion stroke. After the expansion, the burned gases cool to lower pressure, and the piston forces them out through the opened exhaust valve. This cycle of four strokes then repeats itself producing work in the engine. Modifications to this general working are achieved in the two-stroke engine, however, the concept remains the same [4].

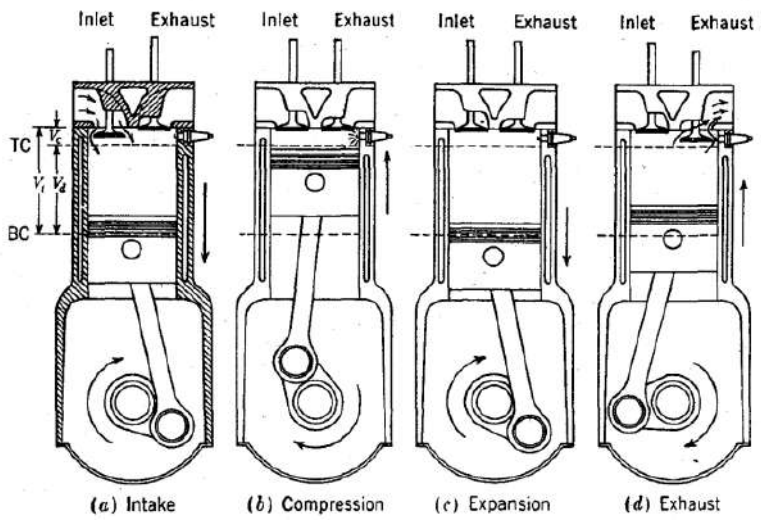

Figure 3: Working of a 4 stroke engine [4]

This four-stroke cycle can be described using an ideal thermodynamic cycle called the Otto cycle. It is presented in Figure 4. Step 1-2 represents the compression stroke, 2-3 represents the combustion inside the engine to release the chemical energy of fuel as heat, 3-4 represents the expansion stroke, 4-5 represents the exhaust stroke and 6-1 represents the intake stroke. The area inside the curves represents the total work done by the engine cycle. This description is ideal. In reality, only a part of the total work is utilized by the engine cycle due to inefficiencies and losses. The next section will discuss these losses in engines.

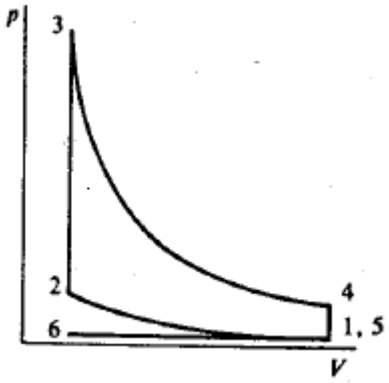

Figure 4: Ideal Otto cycle [4]

1.1.2. LOSSES IN ENGINES

A real combustion cycle differs from the ideal cycle due to the different losses in engines [4]. An overview of these losses in a spark-ignition engine can be found in the literature [5]. The major losses responsible for engine inefficiency can be summarized as follows [4, 6]:

1. Combustion Losses
2. Mechanical losses
3. Exhaust losses
4. Heat loss to the walls

It can be subjective to categorize the energy used by vehicle systems like the electrical control systems, pumping losses, injection pumps, auxiliary units, etc. as losses. However, for simplistic presentation, these losses are included in vehicle demand as effective work output [7].

The first category of losses, combustion losses, can be divided into two components: un-burnt fuels, and non-instantaneous combustion. Combustion in engines is incomplete when the time available for complete combustion (typically the expansion stroke duration) is not sufficient. Hence, a small portion of the fuel is passed into the exhaust as un-burnt fuel. Figure 5 shows the effect of combustion losses in an

ideal Otto cycle. These losses, represent about 1-5% in four-stroke spark-ignition engines and above 10% in two-stroke engines [4, 5, 8]. Strategies like lean combustion, or turbulence enhancement are effective to reduce these losses below 1%, and hence the combustion losses are considered negligible [4, 5]. Un-burnt fuel can also result from combustion quenching at the combustion chamber walls. Therefore, crevices and leaks tend to increase un-burnt fuel through the exhaust or blow-by gases, thus increasing total losses. They are shown to trap up to 8% of in-cylinder mass leading to a similar order of losses [4]. This is highlighted in Figure 5, subfigure 2. Further, the real combustion needs finite time for its completion rather than the infinitely fast ideal process of heat release. This finite rate of heat release also adds to the losses of engines. This can be identified in Figure 5, subfigure 3. It is difficult to estimate the loss due to the finite rate of heat release. However, researchers reported the combustion losses to account for <5% of the total fuel energy [5].

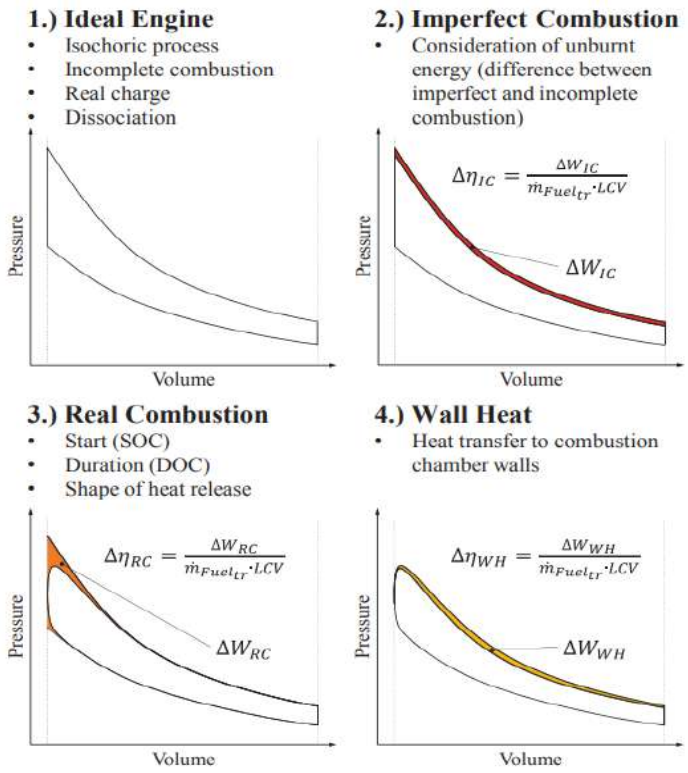

Figure 5: Some losses in constant volume heat addition combustion cycles [5]

The second category of losses is mechanical losses. Mechanical losses take place during the transmission of power from the engine to the wheels. It includes friction losses, inertia losses, transmission losses, etc. It accounts for <3 % of total fuel energy [7, 9]

The third category of losses is due to exhaust gases. Exhaust losses are due to the incomplete expansion of combustion gases to allow scavenging and reducing pressure during the early part of the exhaust stroke. This results in the reduction of work extracted during the latter part of expansion stroke and hence an increase in losses. Exhaust losses account for ~25% of total fuel energy [9–11]. A major portion of the heat of the gasses at the end of combustion stroke is practically not useable due to limited time available for the expansion of gases. In some cases, it is also vital for the exhaust gases to have hotter temperatures for the after-treatment system to function or to provide energy for the turbocharger [4].

The last losses category is wall heat losses. During combustion, the gases inside the chamber reach high temperatures above 1000°C while wall temperatures remain lower (~200°C). This temperature difference persists for some time, during the expansion stroke after combustion. During this time, heat transfer (heat flux) occurs from the hot gases to the walls, which is termed heat loss. This heating of the walls during combustion stroke, accumulated over many cycles leads to heat transfer from the engine chamber walls to the coolant. This is shown in Figure 5, subfigure 4.

Figure 6 shows a comparative analysis of energy distribution for gasoline and diesel engines, highlighting the dominance of heat losses [9]. In this study, the combustion is modeled to be complete, so combustion losses are absent. From this figure, we can see heat losses are predominant for different engines simulations. Similar results are found in another study analyzing the engine energy distribution of a pickup truck driving on the EPA urban fuel economy drive cycle (Figure 7) [7]. In this figure, both heat loss to the walls and exhaust loss are combined to form thermal losses. The distribution in Figure 7 indicates the dominance of thermal losses. These results demonstrate that heat losses to the walls, along

with exhaust losses, are the major sources of loss accounting for over 50 % of total fuel energy in some cases. Of the total heat losses, losses to the wall during combustion are the major portion [9, 11–15]. Hence, the efficiency of engines can certainly improve if heat losses are reduced. In this direction, it is important to understand the mechanism for the different modes of combustion encountered in engines.

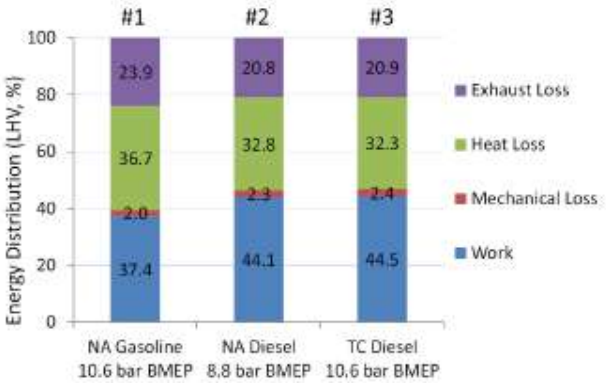

Figure 6: Energy balance in different engines using models with zero combustion losses [9]

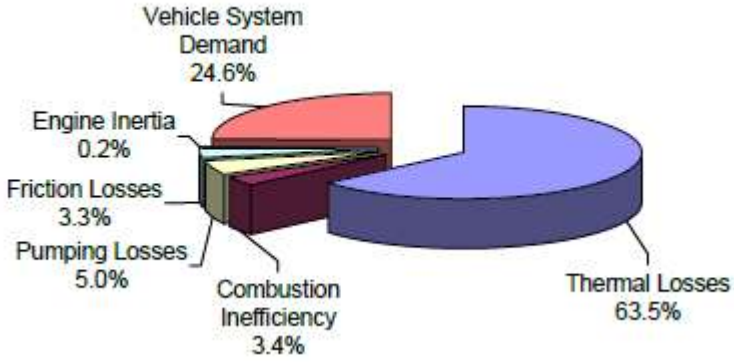

Figure 7: Energy distribution in engines [7]

1.1.3. COMBUSTION MODES

Two major modes of combustion are involved in conventional engines, i.e., propagative, and diffusive. These are discussed in this section.

1.1.3.1. Propagative flame

Propagative flame is encountered in premixed fuel-air mixture where a controlled ignition initiates the flame. The flame propagates by increasing the temperature of un-burnt gases in its vicinity to the point of ignition. The rate of propagation of the flame front is called flame speed. The flame speed at laminar aerodynamic conditions is called laminar flame speed (S_L). Laminar flame speed is dependent on the thermodynamics of the fuel-air mixture. Propagation of flame front in an engine depends not only on the laminar flame speed but also on the turbulence in the flow. Turbulence plays an important role in spreading the flame's influence (transporting heat and reactive flame fronts) in a small zone called preheat zone, located near the flame in fresh gases. The turbulent flame surface is wrinkled with many local curvatures in contrast to the laminar flame which is flat. Hence the turbulent flame propagates as a fast propagating wrinkled flame [4, 16]. The wrinkled flame is thought of as a turbulent flame brush. A turbulent flame brush in 1D is shown in Figure 8. S_T is the turbulent flame brush speed which is also referred to as turbulent flame speed. Various definitions of turbulent flame speed exist to characterize turbulent combustion [17]. In a SI engine, the flame speed is related to the turbulence level [3]. Thermodynamic conditions along with the fuel properties play their role not just in the ignition but also in the propagation of the flame. This stage of flame propagation has been studied widely in literature through both experimental and numerical work [4]. The last stage of flame propagation is when it approaches the chamber walls. During this stage, almost all the fuel is combusted, and the flame slows down and eventually quenches. A detailed explanation of the SI mode of combustion is available in chapter 9 of the book [4].

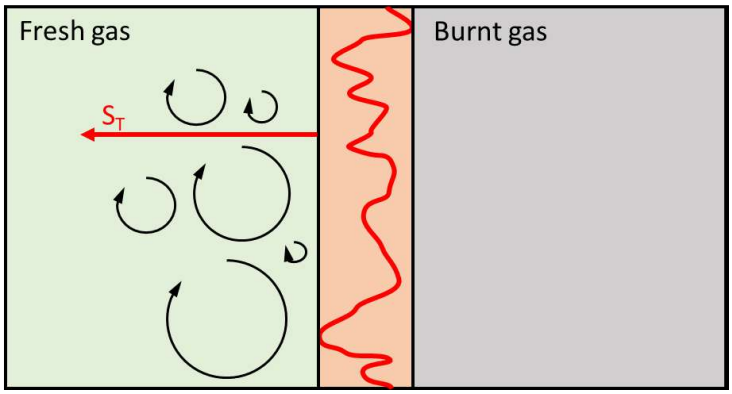

Figure 8: Turbulent flame brush

Traditionally a spark ignition is used to initiate the premixed flame. Alternatively, prechamber ignition can be used as a replacement for the traditional spark ignition. A prechamber is a small chamber inside the main combustion chamber of the engine. It consists of a hollow cavity with several holes and one spark plug. Prechambers can be active or passive. An active prechamber has a separate fuel injection for air-fuel mixture preparation inside the prechamber. A passive prechamber has no separate mixture preparation inside the prechamber, rather the air-fuel mixture in the main chamber is pushed into the prechamber through air motion due to a piston. Inside the prechamber, the spark initiates the combustion. Due to the pressure difference between the main chamber and prechamber, flame jets come out of the holes in the prechamber and initiate faster combustion through multiple ignition locations. It is unknown how the flame jets due to the prechamber affect the heat loss to the walls. A prechamber ignition system has the potential to increase the efficiency of engines [18].

1.1.3.2. Diffusive flame

Another important combustion mode is diffusive combustion. Diffusive flame in modern automotive engines relies on the autoignition of a high-pressure spray injected in hot air [19]. Hence, it is also called spray combustion or non-premixed combustion. This method of combustion is commonly found in CI or diesel engines. CI engine uses specific fuels favoring auto-ignition and high compression ratio to maximize temperature inside the chamber. Once the spray is introduced into the chamber, fuel starts mixing with

the air. After a suitable mixing is achieved, leading to the formation of the stoichiometric air-fuel mixture, it combusts releasing heat. Figure 9 gives a temporal description of the diesel diffusive flame development [19]. We can identify the premixed combustion by the first peak in heat release rate. The ignition is achieved in premixed conditions, which are characterized, typically by chemiluminescence emission. The time taken by the fuel spray to form an ignitable mixture by entraining air and igniting is called ignition delay (***ID***). ***ID*** can be identified as the time between the start of injection (start of needle lift) and heat release in Figure 9. The distance from the point of injection to the point of ignition is called lift-off length (***LoL***). A schematic of spray structure during combustion and the different stages is shown in Figure 10 [19]. ***LoL*** can be identified in Figure 10 as the distance from the point of injection to the chemiluminescence region. ***ID*** and ***LoL*** are the two main macroscopic physical values used to describe diesel sprays. If ***LoL*** is too long compared to the distance between the injector and combustion wall surface then it can lead to impingement of a liquid spray, degrading the combustion process.

A small-time after the premixed air-fuel combustion, the spray flame stabilizes into a diffusive flame (see Figure 10 and Figure 9). This part of combustion is also called mixing-controlled combustion. It is then slowly consumed in a diffusive flame shown using different colors in Figure 10. The different stages are also seen in Figure 9, where two-stage heat release is found corresponding to the premixed stage and diffusive stage of the flame (shown in light grey and dark grey). Over the years, a model of the spray combustion interacting with the wall is also developed [20]. Wall helps to achieve better premixing by affecting the velocity field [21, 22]. A detailed explanation is available in chapter 10 of the book [4]. Injection features like the pressure of injection, the size of nozzle holes, etc. affect the mixing, and hence the combustion [23]. Spray mixing and combustion show spatial variation globally as spray only distributes the fuel in its local vicinity. From this point, this mode of combustion will also be referred to as spray combustion in the report.

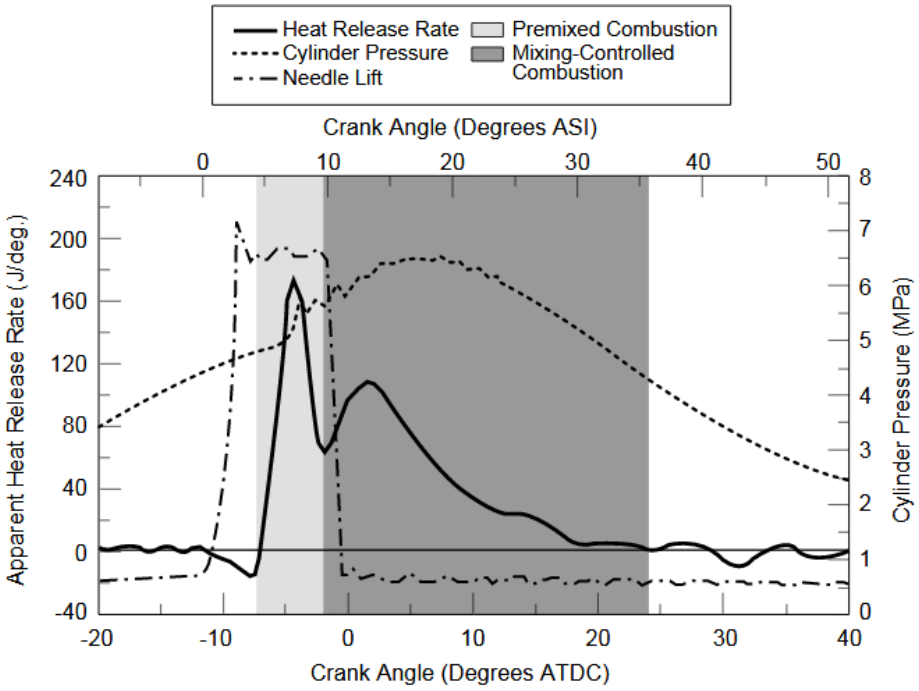

Figure 9: Different stages of spray combustion [19]

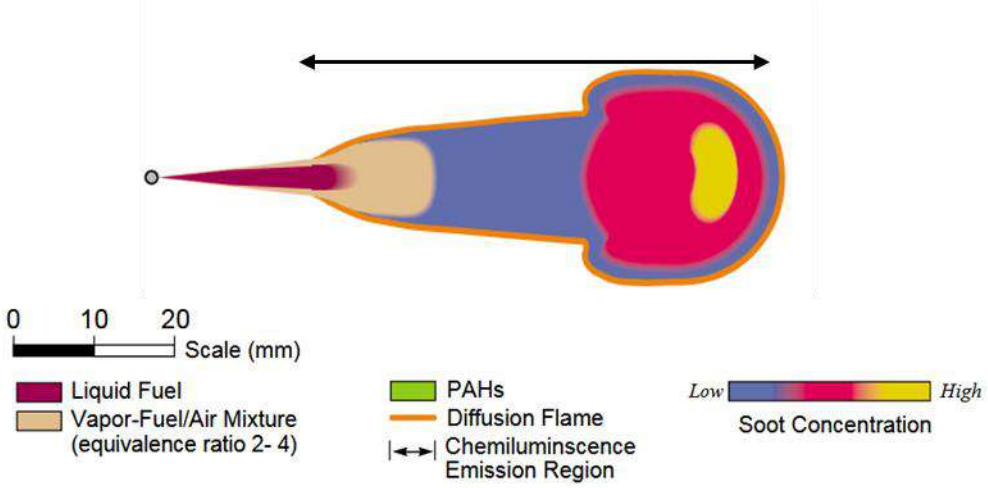

Figure 10: Spray combustion [19]

1.2. HEAT FLUX MEASUREMENTS

Heat flux measurements are critical to understand heat transfers and provide valuable data for developing an accurate description of heat losses in engines. Such measurements have been carried out since the 1940s [24]. This section will present the results of such measurements in an engine for the

premixed propagative and diffusive combustion modes. Further measurements performed in other combustion environments are also explored. This section will also detail the heat flux measurement strategies commonly used in engines.

1.2.1. MEASUREMENTS IN ENGINE

In this section, heat flux measurements reported in the literature for both premixed propagative and diffusive modes of combustion in engines are discussed. A comparison of global heat loss measured to that of local heat flux measurements carried out by other researchers finds that both the global and local heat loss are linearly correlated [25]. Local heat flux measurements provide heat flux with a high temporal resolution to resolve heat loss during combustion stroke. In this thesis, we will only present and analyze local heat flux measurement data.

1.2.1.1. Propagative flame in SI engine

In literature, one of the first reported measurements of heat flux in SI engines was carried out in cylinder head in 1969 [26]. Figure 11 shows the three locations of the surface thermocouples on the cylinder head. The corresponding heat flux traces are shown in Figure 12, for two different swirl conditions. These heat flux curves are typical of heat flux profiles in SI modes. A peak value is defined as the maximum of the heat flux trace. A rise time is defined which is the time taken by the heat flux curve to rise from the traditional motoring heat flux trace to the maximum value. The peak values are ~4-5 MW/m^2 and the rise time is of the order of 2 ms. Figure 13 shows the heat flux traces at the three different locations for a given swirl configuration. The heat flux profiles are spatially variable in both peak value and rise time. There is a difference in phasing which was deemed due to non-uniformity in combustion i.e., flame arrival near the sensor. Similar observation on the correlation of heat flux to flame front arrival is also found by other researchers [27]. Further large-scale charge motion like tumble or swirl is found to increase the peak values. These observations are consistent with other researchers [28]. There

is a tendency of increase in heat flux peak with an increase in intake pressure, air flow like swirl and tumble, and load. Airflow variations cause variation in velocity and turbulence intensity near the engine wall surface. These parameters have a multifold impact on heat loss. First, they change the pressure evolution and the hot gas temperature in the engines, and then they have their effect on the heat loss. It appears that it is necessary to decouple the effect of pressure from the other individual parameters to understand their respective influence on heat transfer.

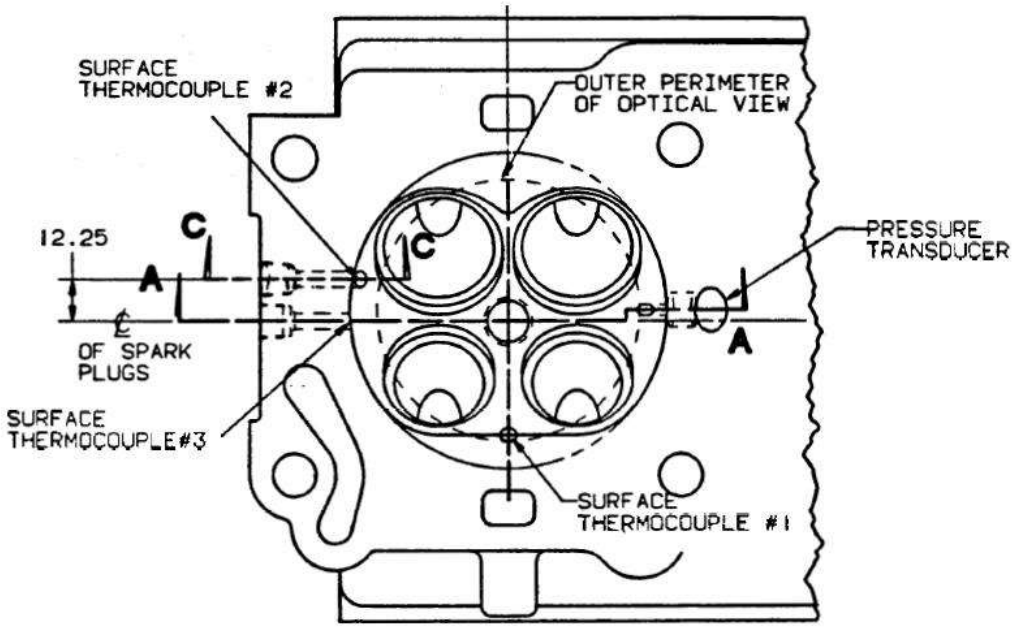

Figure 11: TC location for surface temperature measurements [26]

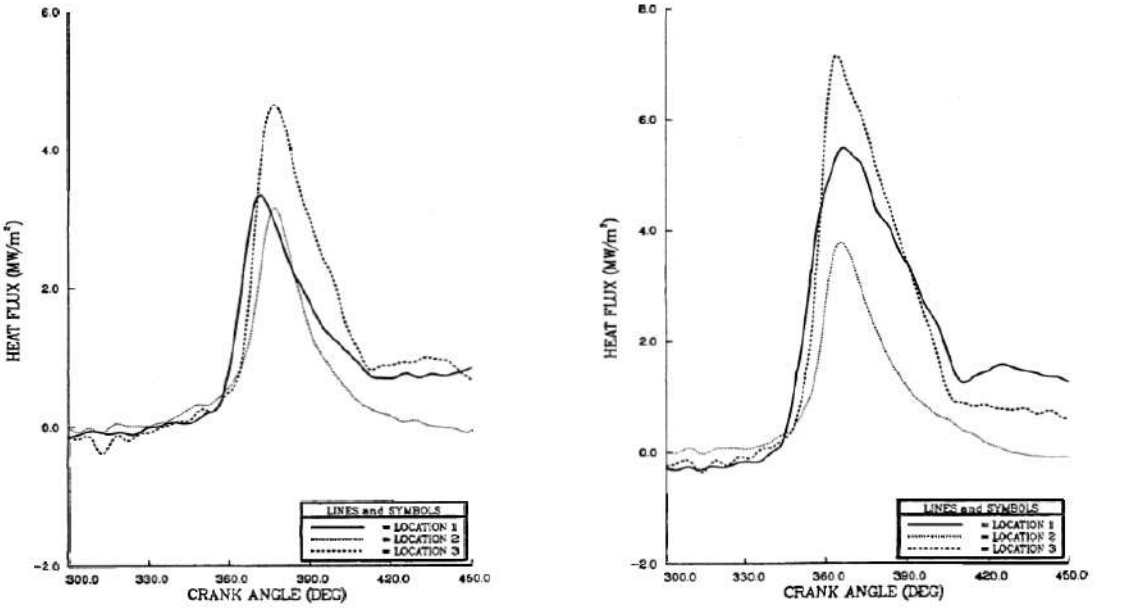

Heat-flux histories at three chamber locations for the baseline flow configuration.

Heat-flux histories at three chamber locations for the low-swirl flow configurations.

Figure 12: Heat flux trace at a different location for baseline and swirl condition [26]

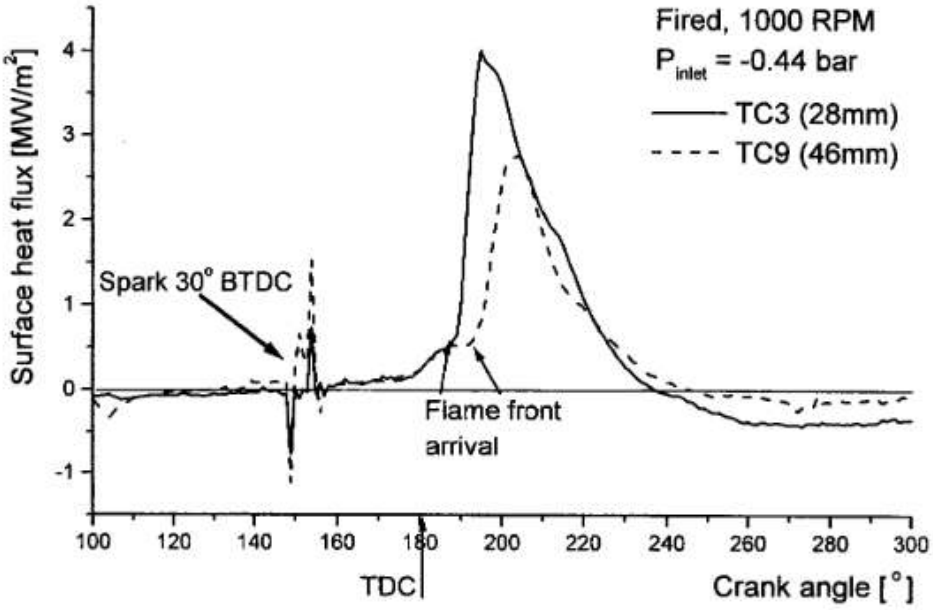

Surface heat flux dependence on location in the cylinder when firing

Figure 13: Heat flux rise correlated to flame front arrival [26]

Other heat flux measurements were carried out to study the heat flux in cold conditions [29]. This study used two wall temperatures i.e., 20°C and 80°C, and found that the effect of variation in wall temperature is insignificant on the heat flux profiles. Thermopile measurements were used to measure the heat flux in SI engines operating with hydrogen and methane [30]. Figure 14 shows the heat flux profiles for hydrogen and methane fuels measured on the cylinder liner near the cylinder head. In the top figure (a), methane cases present a heat flux peak of ~2 MW/m^{2}and a rise time of 15 CAD (~3 ms). In the bottom figure (b), hydrogen has a peak heat flux of ~4 MW/m^{2}and a rise time of 5 CAD (~1.5 ms). Although if we compute a duration based on a cut-off of 0.5 MW/m^2(shown by the yellow arrow in Figure 14), both the fuels have a similar duration of 50 -55 CAD (light red double arrow in Figure 14). These results appear very similar in broad characteristics to the measurements discussed earlier. Cycle-to-cycle variation is significant for cases with methane. Hydrogen is found to be less affected (both cycle-to-cycle and spatial variations) by the bulk in-cylinder flow which the authors hypothesize is due to its high burn rate of hydrogen compared to methane. The heat flux profile is sensitive to variations in ignition timing, equivalence ratio, and compression ratio. Ignition timing and compression ratio adjust the conditions inside the engine and the equivalence ratio directly affects the heat flux. Heat flux with hydrogen is higher in comparison with methane but it was possible to achieve high thermal efficiency with hydrogen as fuel in comparison to methane. The authors' reason that faster propagation can lead to higher efficiency. Heat loss is larger than the loss due to slow combustion (combustion losses in section 1.1.2). The observation that hydrogen has high heat losses and can lead to high efficiency in comparison with methane, highlights the lack of knowledge of heat loss in engines. There could be a multifold impact of fuel variation on heat losses i.e., pressure evolution, flame speed, burnt gas temperature, fresh gas properties change with different fuels. We will need to isolate the effect of important parameters (among those listed) to understand the effect of fuel variation. Moreover, the researchers also find that the existing heat flux correlations for engine applications exhibit discrepancies with hydrogen-fueled combustion [31].

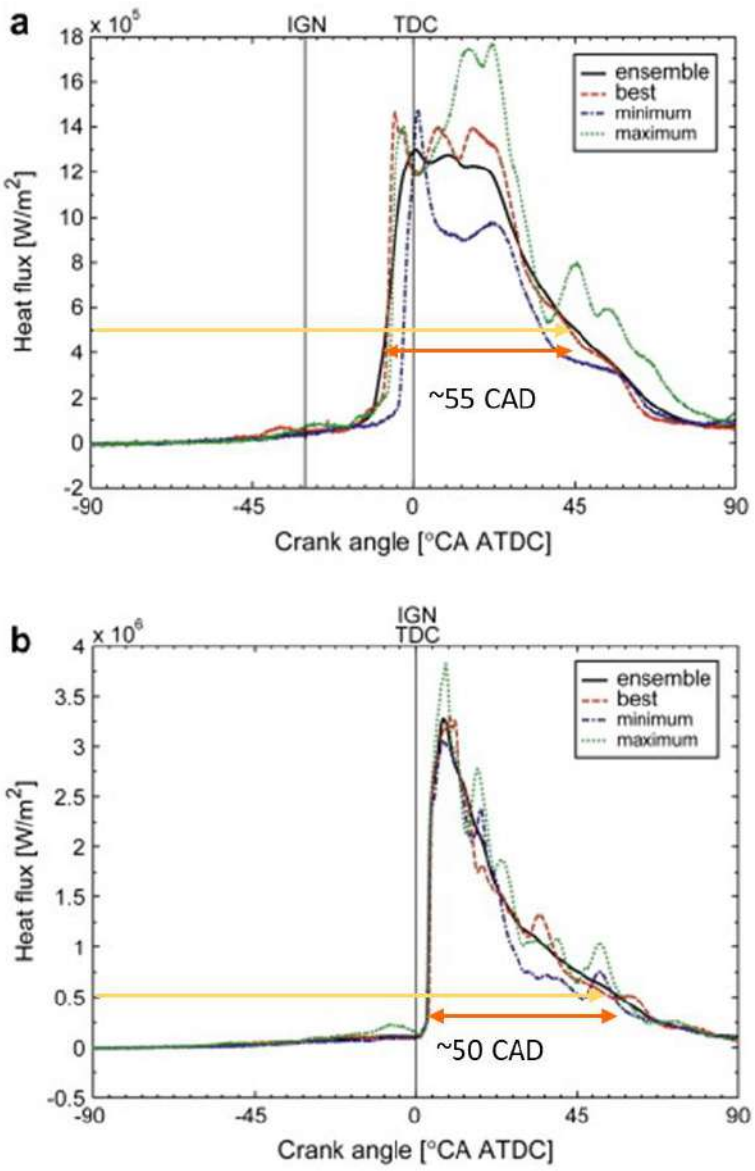

Figure 14: Heat flux profiles in SI engines at 600 RPM, stoichiometric mixture for two fuels a. methane b. hydrogen [30]

A wireless telemetry system, developed in the 2000s for engine application, enabled the use of TC on the piston surface [32]. This is an improvement over linkage systems used with wired thermocouples in some of the earlier works [24]. Researchers used nine TC at different locations to study the spatial uniformity of heat flux [32]. Figure 15 shows heat flux profiles on the piston and cylinder head. Ensemble averaged temperature measurements conducted in SI engine using thermocouples (TC) find that the heat flux trace has a heat flux peak of 1-5 MW/m^2 with a rise time to the peak of ~15 CAD (~1.25 ms) at 2000

RPM, stoichiometric conditions, 14% external EGR and gasoline as fuel. The head side measurements were conducted in the squish region. The measurements highlight the spatial non-uniformity of SI combustion, not only in peak location but also in the overall profile (heat flux vs. CAD). The non-uniformity is in broad locations of the measurements. Piston side measurements are close to each other, and head side measurements are also close to each other. However, piston side measurements differ significantly compared to head side measurements. This plants some uncertainty on using spatially averaged correlations commonly used to describe engine heat loss at the walls [33].

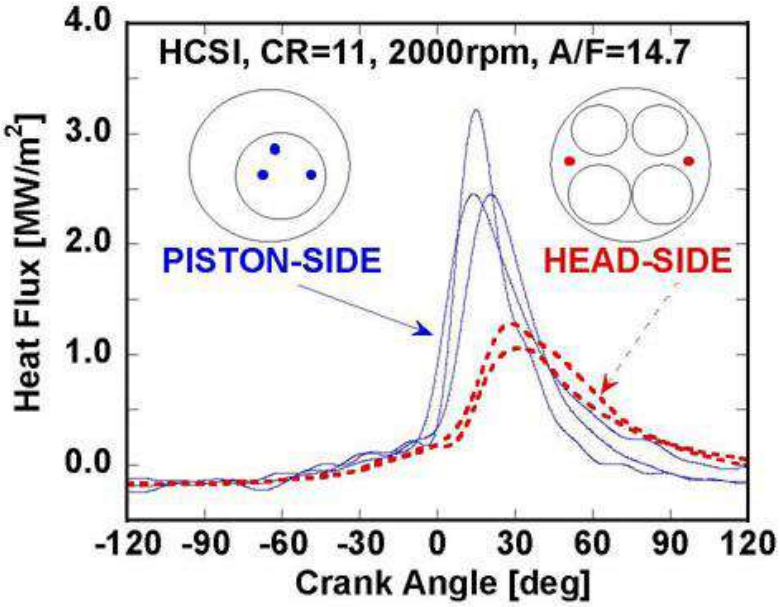

Figure 15: Heat flux profiles in an SI engine [32]

Heat loss in engines is fundamentally a transfer phenomenon where heat from hot gases is transferred to the engine wall surface. In such a simplistic model of heat transfer, the temperature of hot gas, the properties of fresh gas, and the thermal boundary layer thickness control the flow of heat [34]. Pressure can affect the properties of fresh gas, the flame temperature, and boundary layer thickness. The parametric variation was conducted in engines (Fuel, Tumble, RPM, intake pressure, equivalence ratio, swirl, etc.) to study the heat loss affects the pressure evolution, temperature, and the thermal boundary layer simultaneously. Hence it is difficult to provide quantification on the effect of each different

parameter on the engine. For this purpose, we will need to approach this problem fundamentally, to untangle the effect of each parameter. Towards this goal, fundamental studies of heat loss measurements during flame-wall interaction are carried out in literature which will be discussed in upcoming section 1.3

1.2.1.2. Spray combustion in diesel engines

One of the first measurements of heat flux in spray combustion is reported in [26]. The TC locations used in this study are shown at top of Figure 16. They are located on the head and the liner. The corresponding heat flux traces are shown at the bottom of Figure 16. The peak heat flux is ~1-4 MW/m^2 with a rise time of ~5-10 CAD (~0.4-0.8ms). Other studies employ measurements at multiple locations on the piston where significant dependencies of the heat flux on the spatial location of the sensor are seen [35]. The spatial variations may be attributed to the arrival of spray or hot gas at the location of the sensor. In engines, there exist multiple sprays and so studying the spatial variation of heat flux due to one spray is difficult. Similarly, the timing of injection affects the start of the heat flux. It is found that an earlier injection has an earlier heat flux peak and vice versa [35]. These effects are evident in the heat flux profiles measured using surface TC by other researchers [25, 36–39]. One example is shown in Figure 17 [39]. In this figure, we can see the heat flux traces for different injection timings which represent different mean gas temperatures ($\boldsymbol{T_m}$). The heat flux profiles presented in this article have a peak of 4-5 MW/m^2 and rise time ~5-10 CAD, ~0.4-0.8 ms. The rise times of heat flux trace in spray combustion engines are almost equal to rise times of heat flux trace during SI engines. In this article, spatial variation is highlighted and the heat flux trace is found to depend on the injection timing [39]. Swirl is found to not affect the heat flux trace strongly.

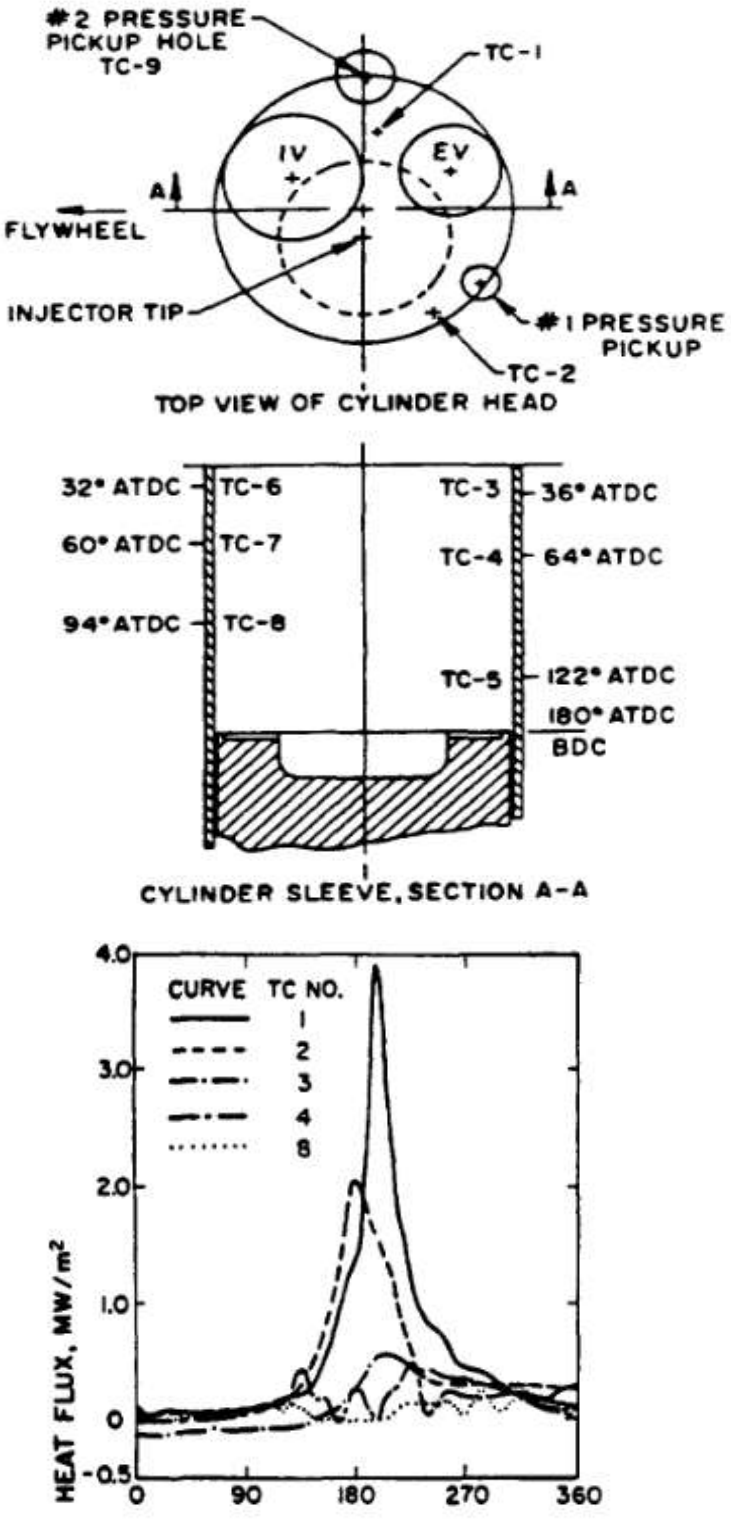

Figure 16: TC locations for heat flux measurement in diesel engine and the heat flux trace [26]

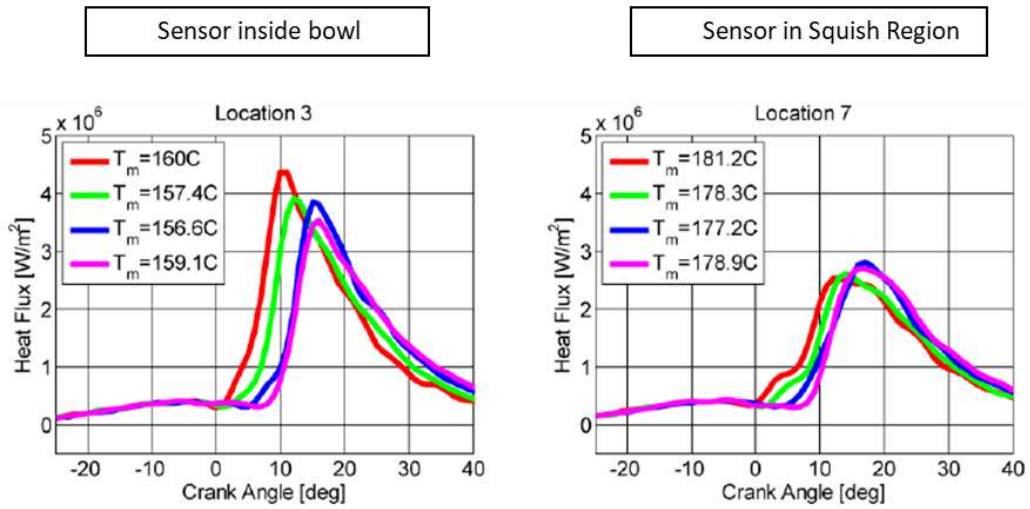

Figure 17: Cycle averaged heat flux at two different locations on the piston, with different injection timings represented by different mean gas temperature (T_m), during spray combustion in a diesel engine [39]

Like in the SI engines section, it appears necessary to decorrelate the individual effect of the parameters to explain the fundamental heat loss in spray combustion. Indeed, the high-pressure spray dictates the combustion and aerodynamics near the wall. This subject is further discussed in section 1.3

1.2.2. HEAT FLUX MEASUREMENT IN OTHER COMBUSTION CHAMBERS

Despite being able to measure the instantaneous heat flux in engines, the heat flux dependency on controllable parameters is not understood. Removing the degree of cycle-to-cycle variations and decoupling different parameters induced by engine operation could help to understand the independent effect of different parameters. Hence many combustion experiments are found in the literature carried out in controlled chambers, constant volume chambers (CVC), and rapid compression machines (RCM). These experimental devices are easier to operate than engines and provide optical access for multiple advanced diagnostics. These closed chambers with simplified working environments are aimed at reproducing engine conditions.

Several studies were conducted in CVC focusing on measurements of wall heat flux for premixed flames (methane-air) with high-speed thermocouple-based wall surface temperature measurements. In these studies, the combustion chamber was quiescent mimicking laminar flame with peak pressures of 1-2 bars. The heat flux is found of the order of 1 MW/m^2 and the interaction time defined by the rise of the second half of heat flux is found to be of the order of 1 ms [40]. A chamber to represent the pent-roof engine enabled the study of the influence of turbulence to a certain level using heat flux measurements and PIV in FOV of 7mm×7mm near the TC [41, 42]. Two different timings of ignition provided laminar and turbulent conditions for combustion to study the heat loss. However, the dependence of heat flux on turbulence could not be established as in this study, the variation of turbulence was coupled with a variation of the mean velocity. The study was also extended in RCM at high pressures during interaction (from 100kPa to 15 MPa) showing the heat flux traces obtained in such a test bench are representative of heat flux obtained in engines with peak heat flux ~6 MW/m^2 [43]. The peak of heat flux depends on the pressure during the interaction through a power-law relationship [43, 44]. The experimental results with the power-law fit are shown in Figure 18.

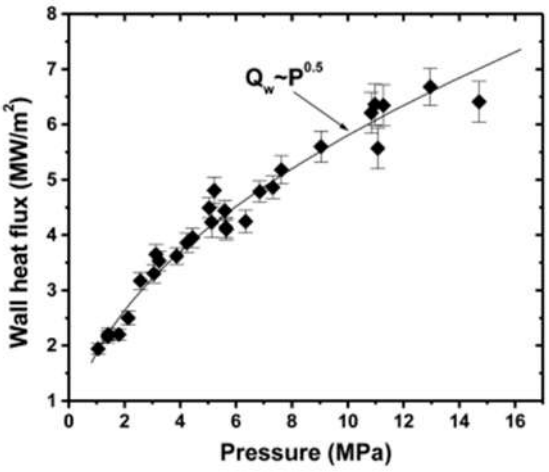

Figure 18: Power-law dependency of the peak of heat flux ($\boldsymbol{Q_w}$) on the pressure during interaction [44]

Heat flux during spray combustion was also studied in CVC and RCM. Researchers measured high-speed surface temperature during impingement of a single spray on a wall, in an RCM in reactive and non-reactive conditions using several TCs on the wall [45]. The position of TCs on the wall opposite the injector is given in Figure 19. Figure 20 shows a heat flux trace for spray experiments in reactive conditions (Figure 20, a) and non-reactive conditions (Figure 20, b) in a RCM [45]. The numbers in the legend correspond to the location of measurements. Apart from 1,2 and 3, there were several other TCs located in the head of the RCM. The measured heat flux traces are presented in Figure 20. The trace represents a characteristic heat flux profile for spray combustion, where a wide peak (like a plateau) of heat flux is observed (3-20 MW/m^2) with a rise time~0.5 ms. Such heat flux trace is also observed in non-reactive spray wall interaction. In non-reactive conditions, the peak is of the order of 1-5 MW/m^2 and a rise time~0.5 ms. Position 2 has the highest peak for all measurement locations. We can also see that the peak appears first in position 2 followed by 1, 3, and other positions which the authors correlate with the arrival of the spray at the location of measurement. The heat flux peak is found to increase with an increase in injection pressure, ambient density, ambient gas temperature, and distance of the injector from the wall. Researchers conclude that the dependency of the heat flux peak on the injection pressure and the distance of the injector from the wall indicate the dependency of heat flux on turbulence generated by spray injection [45, 46].

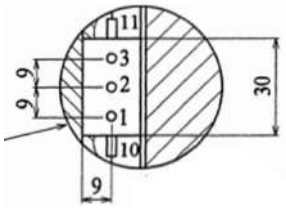

Figure 19: TCs on the wall opposite to injector used in [45]. '2' TC lies exactly opposite to the injector. Dimensions are given in mm.

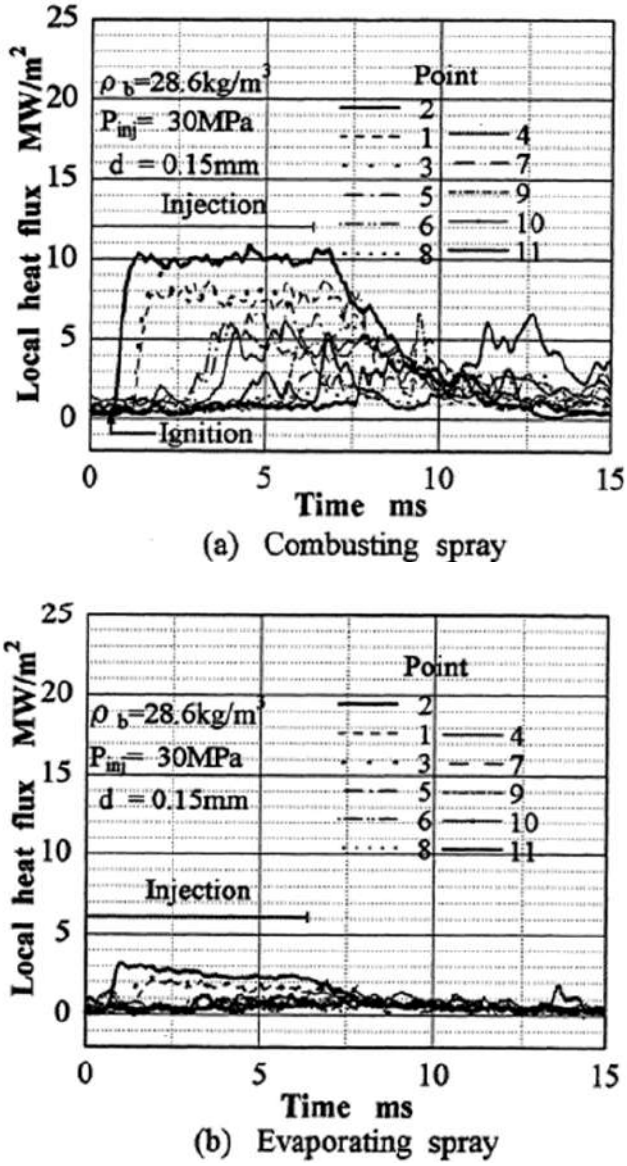

Figure 20: Typical profile for spray wall interaction for combusting and non-combusting spray at an injection pressure of 30 MPa and density of 28.6 Kg/m3 at the different spatial locations

A two-step heat flux is observed in low ambient density conditions when spray reaches the wall before autoignition which is also shown in Figure 21. This two-step heat flux is also reported by other researchers [46]. The authors deem the first step is due to the heat transfer from the non-reacting spray-hot ambient gas mixture to the wall. Then the heat flux trace rises to the plateau value in a second step which is due to hot gases resulting from combustion. However, no work shows both two-step and one-

step heat flux in the same experimental conditions to clarify this phenomenon. If the two types of heat flux could be observed in one setup with a similar thermodynamic condition, there lies a potential to compare the two types of heat flux. The researchers found that the heat flux plateau duration is approximately equal to the duration of combustion, which is close to the duration of injection. After the plateau, the heat flux trace drops due to the end of combustion. Moreover, the experiments for measuring the heat flux in spray combustion across the literature were carried out in varying conditions and setups. The research community now has well-defined ECN spray A boundary conditions to study spray combustion [47]. Such heat flux data in ECN conditions (for both reactive and non-reactive spray combustion) would be of interest so that the scientific community can incorporate the works of other researchers to develop the knowledge of spray wall interaction.

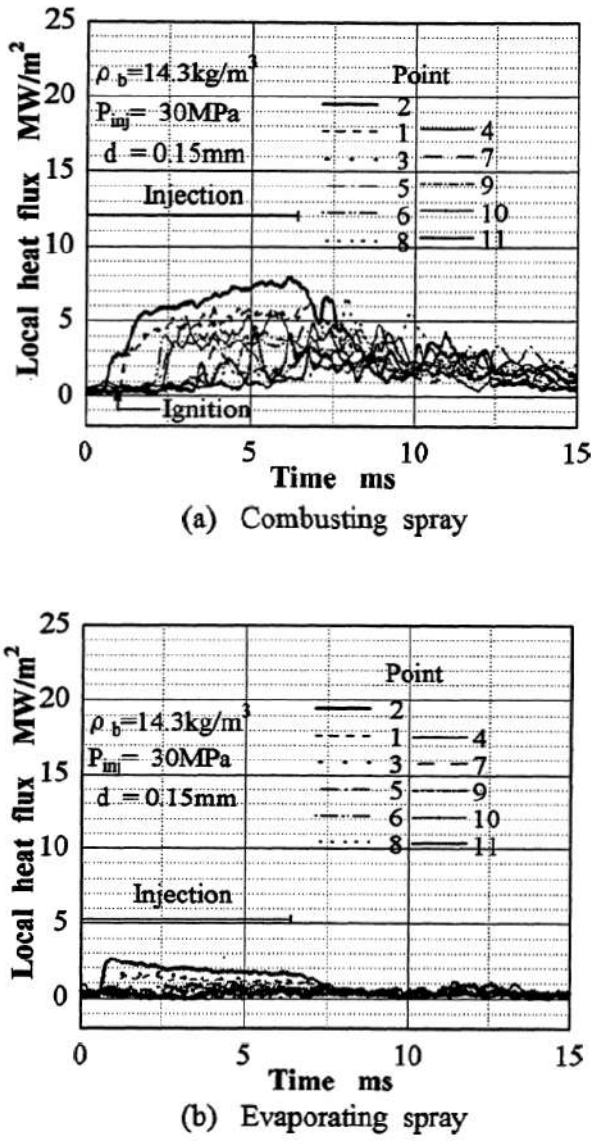

Figure 21: Typical profile for spray wall interaction for combusting and non-combusting spray at an injection pressure of 30 MPa and density of 14.3 Kg/m^3 at the different spatial locations

1.2.3. HEAT FLUX MEASUREMENT STRATEGIES

In an engine wall surface, the radial direction of temperature gradient (~1K/mm) is very low in comparison to the normal direction (~20K/mm) relative to the surface experiencing combustion [48]. It is found that the radial flow of heat is also the least at the surface [37]. Hence, the heat flux at the engine

surface can be considered normal to the surface. Surface temperature measurements are used to compute heat flux at the engine wall surface using a 1D semi-infinite heat conduction model. [24, 37, 46]

1.2.3.1. Thin Junction thermocouples

A detailed analysis of the temperature measurement techniques suitable for calculating heat flux at the engine wall surface is provided in the literature [46]. In this thesis thermocouples (TC) are used. TCs are junctions formed from two standardized metallic thermoelements which generate a voltage (function of the temperature of the junction) at the open end based on the principle of the Seebeck effect [37, 46, 49]. Junction thickness is found to affect the response time of the TC. To capture the rise of temperature due to fast heat transfer phenomena, a thin junction is required. Thin junction TC of junction thickness ~µm is generally used to measure wall heat flux in engines [46, 50, 51]. It has been found that the characteristic time of the heat flux (~1ms) is larger than the response times of thin junction TC (junction ~µm, response times~µs) making thin junction TC suitable for the study of heat flux during combustion [37, 46, 50, 51]. A type of thin junction TC, coaxial thin junction TC (shown in Figure 22), has been widely used in the measurement of surface temperature in engines [37, 49].

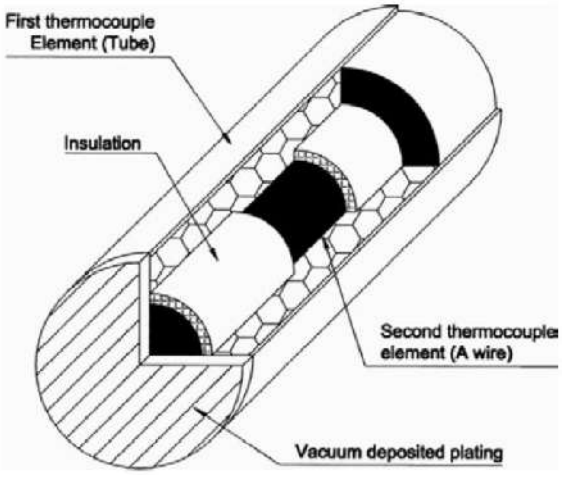

Figure 22: Coaxial thin junction TC used in surface temperature measurements

1.2.3.2. Processing of temperature to heat flux

After the surface temperature (***T***) is measured, it is used to calculate the heat flux. A comprehensive review of the processing of the temperature data is provided in the literature [37]. In this thesis, we will focus on the heat flux which occurs during the short duration of combustion. Duhamel integral is the most commonly used analytical method to obtain the heat flux from surface temperature measurements using the 1D heat flow model (Equation 1). ***Q*** represents the heat flux, ***k*** is the thermal conductivity, ***ρ*** is the density and $\mathbf{C_P}$ is the specific heat of the TC material.

Equation 1: $$Q=\sqrt{\frac{k.\rho.C_p}{\pi}}\int_{\tau=0}^{t}\frac{\partial T(\tau)}{\partial \tau}.\frac{d\tau}{\sqrt{t-\tau}}$$

The Duhamel integral is solved using Cook-Felderman Technique [50, 52, 53]. The numerical implementation of this equation is given in Equation 2. This processing can be applied directly to measure the heat flux in engines. More details can be found in the reference [37].

Equation 2: $$Q(t_n)=2.\sqrt{\frac{k.\rho.C_p}{\pi}}.\frac{1}{\Delta T}\sum_{K=1}^{n}\frac{T(t_K)-T(t_{K-1})}{\sqrt{n-K+1}-\sqrt{n-K}}$$

The mathematical problem of using surface temperature to derive the heat flux is an inverse problem. Small noise in the temperature data can lead to large oscillations on the heat flux trace, making it an ill-posed inverse problem. Since the temperature signal, especially from a TC is noisy, a regularization is needed to remove unwanted fluctuations in the calculated heat flux. For this purpose, Tikhonov regularization is used in this thesis which is successfully demonstrated in the literature [37, 46].

1.3. FLAME-WALL INTERACTION

The majority of the heat loss happens during the combustion stroke when the temperature of in-cylinder gases is hot. During the phenomena, called Flame-Wall Interaction (FWI), high heat flux, of the order of MW/m^2 is observed. This section will discuss the physics of FWI, in the context of wall heat flux.

1.3.1. LAMINAR FLAME WALL INTERACTION AND HEAT LOSS

In this section, we will discuss the laminar FWI and the heat loss associated with laminar FWI. A simple picture of FWI can be studied as laminar FWI, where a laminar flame interacts with the wall. Laminar FWI is a coupled process where a laminar flame and a wall affect each other. FWI can be described with three distinct phases [17, 40]. The first phase corresponds to the flame approaching the surface. Then the combustion is quenched (second phase). Finally, the third phase is the post quenching. A schematic diagram explaining FWI for laminar flames is given in Figure 23. The fresh gas mixture temperature (***T1***) is equal to the initial wall temperature (T_W). t_1 denotes the time before FWI. t_2, t_3, and t_4 denote the three distinct phases of FWI mentioned above.

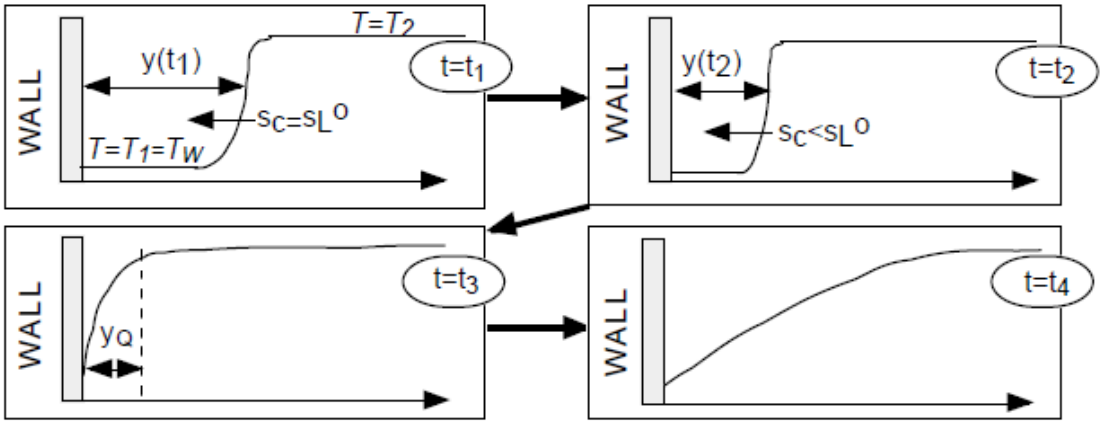

Figure 23: Temperature profiles showing FWI during quenching of laminar flame by a cold wall [17].

The Top-left image ($t=t_1$) of Figure 23 represents a laminar flame far away from the wall. It is therefore not affected by the wall yet. It consumes the load and spreads its influence (temperature rise and turbulence), typically with flame speeds equaling laminar flame speed.

At some point during its propagation, the flame starts to lose heat to the wall which can be considered the starting point of FWI shown in the top right ($t=t_2$) in Figure 23. This point can be different

on a quantitative scale depending upon the direction of flame propagation relative to the wall [17, 54]. The FWI can then be classified based on the direction of flame propagation relative to the wall as:

1. Head on Quenching (HOQ)
2. Sidewall Quenching (SWQ)

Figure 24(a) shows the figure of HOQ where the flame is approaching normal to the wall and (b) shows SWQ where the flame is approaching parallel to the wall [51]. The arrows show the direction of flame propagation relative to the wall.

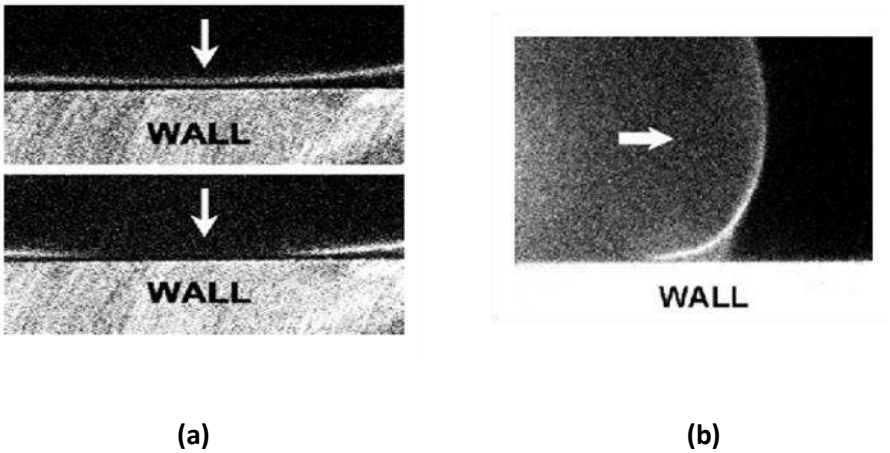

(a) **(b)**

Figure 24: Classification of FWI with respect to the orientation of FWI (a) head-on quenching (b) sidewall quenching [51].

Heat loss to the wall rises as the flame approaches closer to the wall. The flame starts to slow down (decrease in flame speed). Eventually, the heat loss reaches a maximum after which the energy released by the flame is not able to sustain the heat losses and its propagation. Hence, the flame quenches, as shown in the bottom left image, denoted t_3, in Figure 23. A typical heat flux profile for HOQ during laminar flame wall interaction is given in Figure 25 [40]. In the literature, several researchers have used Q_P to describe total heat loss during FWI [42, 44, 51, 55]. This is due to the fact the Q_P is linearly correlated with the total heat loss in one condition [42]. In this figure, we can identify the peak of heat flux where quenching occurs and the steep rise in the heat flux near the peak. The peak heat flux and the rise time

are identified as important characteristics of the heat flux trace. The flame stops at a minimum distance from the wall called the quenching distance ($\boldsymbol{\delta_q}$) [40, 56]. This phase of flame propagation can be described using the Peclet number (***Pe***). ***Pe*** is the ratio of heat transferred by convection to the heat transferred by conduction. It can be estimated from the ratio of the flame-wall distance (***y***) to the flame thickness ($\boldsymbol{\delta_F}$) which is given in Equation 3 [17, 40]. Flame thickness ($\boldsymbol{\delta_F}$) is given by Equation 4 where laminar flame speed in fresh gas is $\boldsymbol{S_L}$, the density of the fresh gas mixture is $\boldsymbol{\rho_1}$, the specific heat capacity of fresh gas is $\boldsymbol{c_{P1}}$. At quenching distance, ***Pe*** reaches a minimum value. Minimum ***Pe*** is ~3 for HOQ and ~7 for SWQ for hydrocarbon fuels, typically at 1 bar of pressure during interaction [17]. The flame during this phase of FWI gives a large amount of heat flux to the wall (~1 MW/m^2) in a relatively short period (fraction of 1ms, ~0.5ms in SI cases) [40].

Equation 3: $$Pe = \frac{y}{\delta_F}$$

Equation 4: $$\delta_F = \frac{k_1}{(\rho_1 c_{p1} S_L)}$$

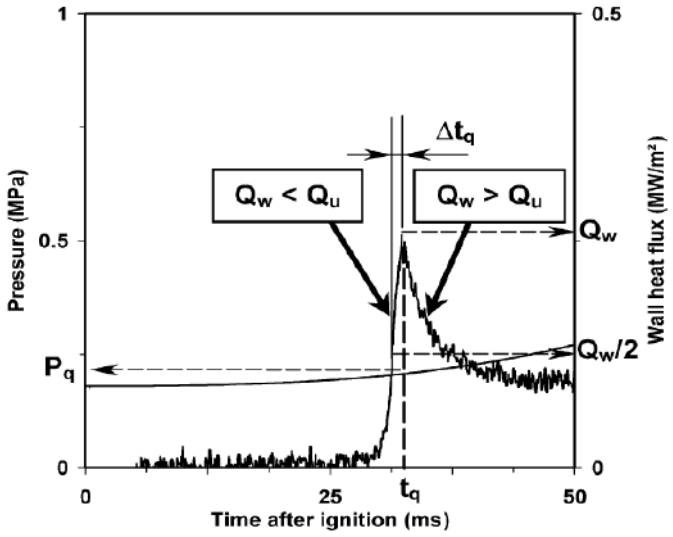

Figure 25: Typical heat flux profile in laminar FWI of methane-air at 0.7 equivalence ratio showing important characteristics of peak heat flux ($\boldsymbol{Q_w}$) which is denoted as $\boldsymbol{Q_P}$ in this thesis and rise time ($\boldsymbol{\Delta t_q}$) [40]

After the flame is extinguished, the FWI is in the post quenching region denoted by t_4 in Figure 23. Burned gases exchange heat to the wall, which eventually decays to minimum levels over a relatively long period (compared to the scales of FWI) [42]. It is important to note that the heat flux before FWI (t_1 timing in Figure 23) and after the FWI (t_4 timing in Figure 23) is considerably lower than the heat transfer occurring at quenching (t_3 in Figure 23).

The heat flux from the flame to the wall is approximated by conduction in the quenching layer [40]. The conduction is represented by Equation 5, where k is the conductivity of the gas in the quenching layer. δ_q can be correlated quantitatively to Q_P using Equation 5, where ΔT is the temperature gradient near the wall during quenching and $\Delta y = \delta_q$ [40].

Equation 5: $$Q = -k\frac{\Delta T}{\Delta y}$$

It is found that δ_q is dependent on the amount of energy contained in the flame, the pressure during the interaction, and the temperature of the wall. Flame Power (Q_Σ) is the measure of the amount of energy contained in the flame given by Equation 6. It is calculated from the laminar flame speed of fresh gas (S_L), fuel mass fraction (Y_F^1), the heat of reaction (Q_H), burnt gas temperature (T_2), and un-burnt gas temperatures (T_1). These quantities can be derived by calculations using thermodynamic conditions [40]. By going from lean to the stoichiometric ratio of fresh gas mixtures we increase the Q_Σ as S_L and T_2 increase. Figure 26 shows the effect of the equivalence ratio at 0.7 and 1.0, (hence Q_Σ) on δ_q [40]. Researchers have also found that δ_q decreases with an increase in wall temperature [57]. We can see that increase in Q_Σ leads to a decrease in δ_q. High pressure during the FWI can lead to a smaller and compressed δ_q which can be also seen in Figure 26. The effect of decreasing δ_q results in increasing Q_P as shown in Figure 27 [40]. Q_P is found to be dependent on the pressure during the interaction, P_{int} ($\sim P^{0.5}$, $P^{0.4}$) [42, 43]. Q_P is also found to increase with an increase in Q_Σ.

Equation 6: $$Q_\Sigma = [\rho_1 Y_F^1 S_L Q_H] = [\rho_1 c_{p1} S_L (T_2 - T_1)]$$

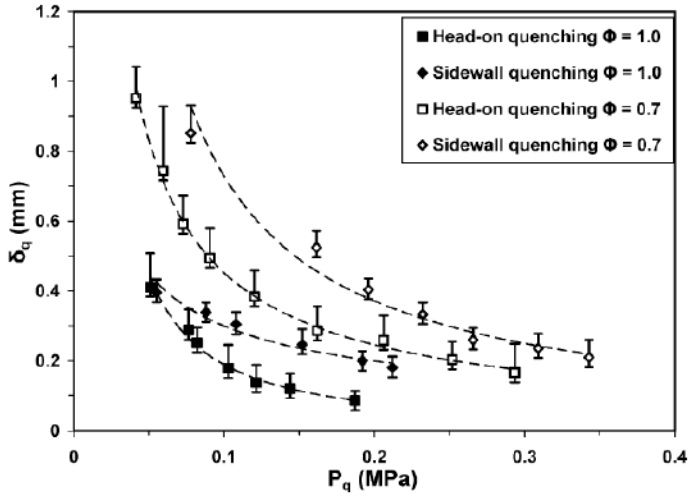

Figure 26: Variation of quenching distance of methane-air flame with respect to pressure during interaction (P_q) which is denoted as P_{int} in this thesis and equivalence ratio(Φ) at 1.0 and 0.7 [40]

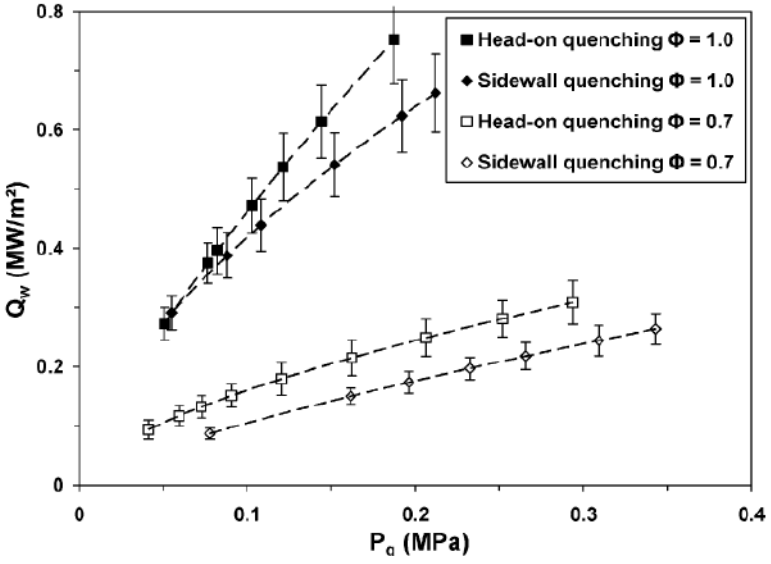

Figure 27: Variation of peak heat flux (Q_W, which will be referred to as Q_P in the rest of the thesis) of methane-air flame versus pressure during interaction (P_q/P_{int}) and equivalence ratio (Φ) = 1. 0, 0.7 [40]

Normalizations are used in literature to model heat loss providing non-dimensional heat flux ($\frac{Q_P}{Q_\Sigma}$) from non-dimensional local quenching ***Pe*** [40]. This is shown in Equation 7 and Equation 8. Normalization

of the heat flux in some cases leads to the heat flux traces obtained during FWI with different conditions to fall together to a coincident curve (renormalization) [40, 51].

Equation 7: $$\frac{Q_P}{Q_\Sigma} = \frac{|Q_P|}{[\rho_1 Y_F^1 S_L Q_H]} = \frac{|Q_P|}{[\rho_1 c_p S_L (T_2 - T_1)]}$$

Equation 8: $$\frac{Q_P}{Q_\Sigma} \sim \frac{1}{1+Pe}$$

Two important parameters, $\boldsymbol{Q_\Sigma}$, and $\boldsymbol{\delta_q}$ can be used to characterize the laminar FWI. Heat flux can be represented by $\boldsymbol{Q_P}$. Even though laminar FWI is an artificial condition representative of simpler, far from realistic FWI, it is widely studied to develop our understanding of FWI.

In conclusion, Figure 28 draws a schematic diagram of the important parameters affecting the physics of laminar FWI and the parameters characterizing the heat flux. Nevertheless, describing FWI in an environment such as engines is more complicated. Indeed, turbulence during practical FWI is hardly negligible and will be the subject of the next section.

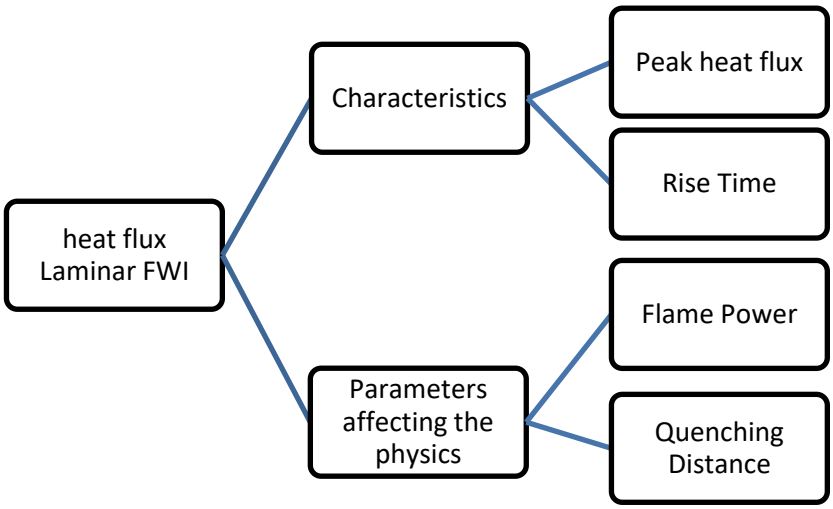

Figure 28: Important parameters affecting the heat flux during laminar FWI

1.3.2. TURBULENT FWI

Turbulent FWI is a complex coupled process involving flame, wall, and turbulence as presented in Figure 29. Flame affects the heat flux transferred to the wall and the turbulence near the wall during the

FWI. Wall can affect the heat flux and the turbulence in the near-wall region during the FWI. Flame and turbulence interact, affecting each other. The difference from the laminar FWI model lies in the characteristics of turbulent flame. The following section aims at describing the remaining part of turbulent FWI from the literature.

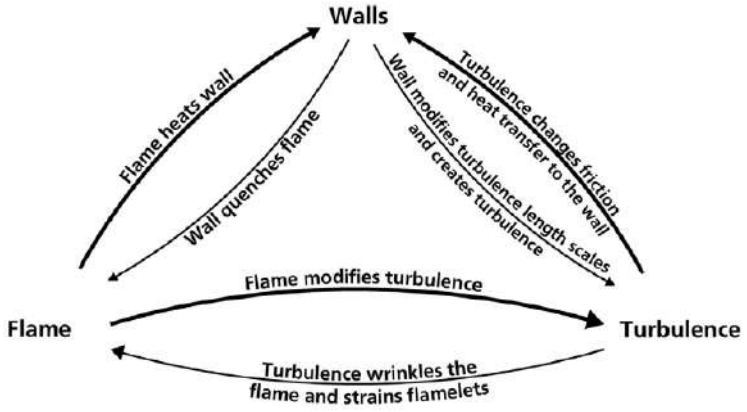

Figure 29: Coupled interaction of flame, wall, and turbulence during turbulent FWI [17]

1.3.2.1. Flow-flame interaction

Due to the effect of turbulent eddies, a laminar premixed flame behavior changes[17]. A schematic showing turbulent eddies affecting the flame front and the transport is shown in Figure 30, which highlights the wrinkling of flame in presence of eddies (in the unburnt mixture). It is important for FWI studies to identify the important parameters that govern flow-flame interaction.

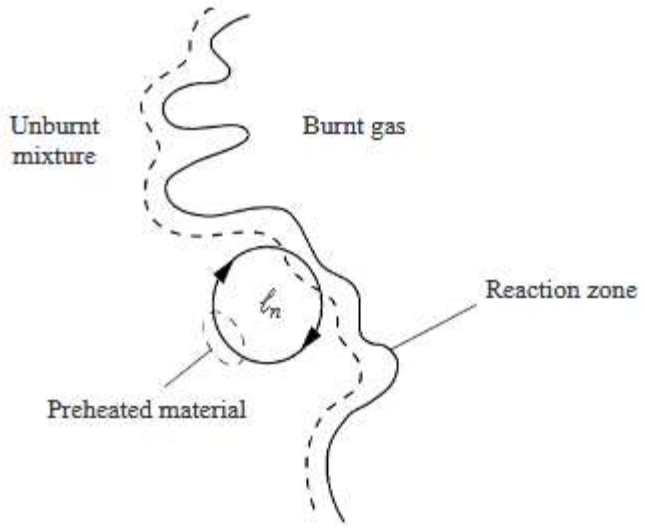

Figure 30: Eddies transport during propagation of turbulent premixed flame. l_n shows the length scale of the turbulent eddies

The flame front propagation speed is termed turbulent flame speeds (***S_T***). ***S_T*** is dependent on the turbulent scales and conditions existing inside the chamber. Usually, a factor multiplied by laminar flame speed represents the turbulent flame speeds. The turbulent scales existing in the chamber are relevant to transport. Hence these eddies could be relevant in transport during FWI. Integral length scales are the length of representative eddies near the flame front, while integral time scales are the turnover times of these eddies. The gas velocity is represented by '***U***'. Fluctuations of gas velocities (***u'***) are due to the eddies. In general, the gas velocity can be decomposed by Equation 9, which is the sum of an averaged part ($\overline{U}$) and a fluctuation component (***u'***). The fluctuations can also be represented by an intensity computed by the RMS value (Equation 10). These fluctuations are characteristic of the existing turbulence field. The integral scales of turbulence can be obtained from autocorrelations of ***u'*** which is a function of space and time [42]. RMS of ***u'*** can be used to calculate turbulent intensity (***q***) shown in Equation 11.

Equation 9: $U= \overline{U}+u'$

Equation 10: $u'_{RMS}=\sqrt{\overline{u'^2}}$

Equation 11: $$q=\sqrt{\frac{u'_{x,RMS}{}^2+u'_{y,RMS}{}^2+u'_{z,RMS}{}^2}{2}}$$

The impact of turbulent eddies-flame is studied by the impact of vortex structures on the laminar flame front. The strength of eddies is represented relatively, by the RMS of velocity fluctuations while the size of the eddies is represented by the integral length scales. Turbulence contains a full spectrum of vortices starting from the smallest scale (Kolmogorov scales, $\boldsymbol{\eta_k}$) to macroscopic scales of length (integral length, $\boldsymbol{L_{u\_t}}$). Flame propagation, size, ignition/extinction criteria, fuel effects, gas expansion, chemical reaction rate and time scales, baroclinic effects, gravity effect, and turbulence properties (length scale, intensity, etc.) can affect the flame-turbulence interaction [58].

Five regimes are identified based on flame-turbulence interaction [58]. A regimes diagram can be drawn based on these observations as shown in Figure 31. The scales represented here are relative and their limits are approximate. Chemical time scales ($\boldsymbol{\tau_c}$) represent the time scales for the chemical reaction to occur. $\boldsymbol{K_a}$ corresponds to the ratio of chemical timescale to the timescale of Kolmogorov length ($\boldsymbol{\tau_k}$), see Equation 12. To explain the different regimes, the Karlovitz number ($\boldsymbol{K_a}$) is used.

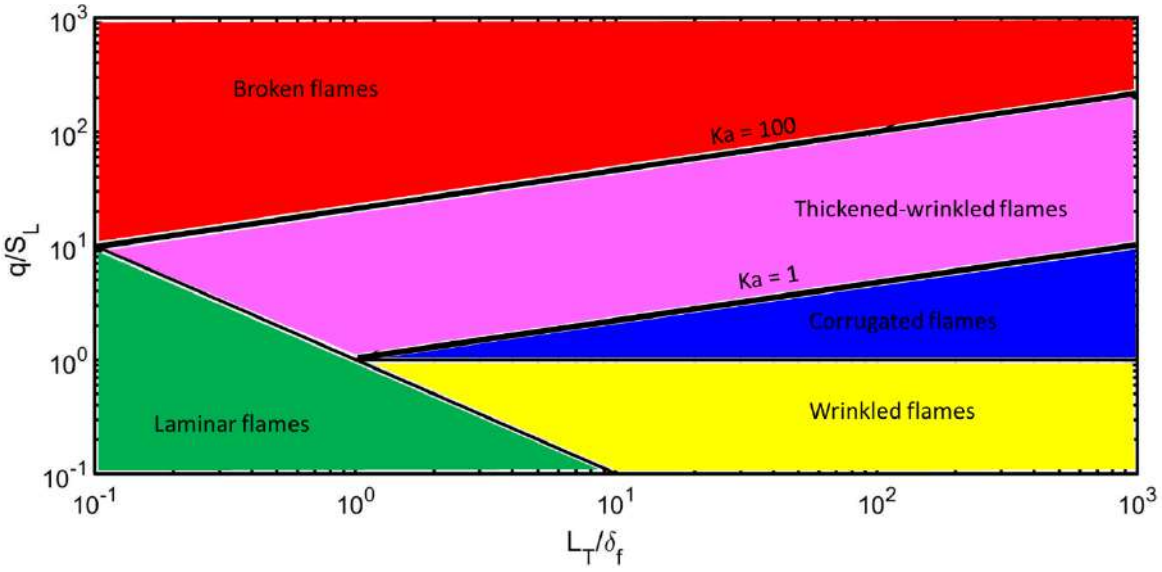

Figure 31: Regimes diagram for premixed combustion

Equation 12 $$K_a = \frac{1}{D_a(\eta_k)} = \frac{\tau_c}{\tau_k}$$

The five regimes are

1. Laminar flame regime: When the eddies are too small and too low in strength, they do not affect the flame front and hence flame stays in laminar flame regimes. Typically, there is not much turbulence, and the laminar flame is intact.

2. Wrinkled flame regime: As eddies grow in strength, they become relevant to affect the flame front, leading to a wrinkled flame front. However, the fluctuations are not strong enough to cause significant distortions to the chemistry. The wrinkled flame front retains the internal structure of the flame front. This flow-flame interaction is in the wrinkle flame front regime. This regime is represented by $K_a<1$, $u'<S_L$. When the flame is too small compared to the turbulent eddies the flame is referred to as flamelets.

3. Corrugated Flame regime: If the eddies grow stronger while being relevant to the flame thickness so that they start affecting the chemistry (at a lower scale, creating wrinkling at small scales of the order of a few times the flame thickness). Turbulent eddies lead to the transport of gases while they are reacting,

leading to wrinkling both in large and small scales relevant to the flame thickness. However, the chemistry is still fast compared to turbulent time scales. The reactants are therefore consumed before turbulence affects them. This is represented by $K_a<1$, $u'>S_L$.

4. Thickened-wrinkled flame regime: The eddies further increase in strength the chemistry is affected by the smaller scales. This condition is represented by $K_a>1$, $\tau_k<\tau_c<\tau_l$. In this regime, the flame is thicker than wrinkled flame regime, hence this regime is called the thickened-wrinkled flame regime. Flame is not identified by a laminar flame front but by a wide wrinkled flame, where turbulent eddies start affecting the preheat region.

5. Broken flame regime: If the eddies become very strong, they can significantly affect the flame front leading to dispersed flame fronts called broken flame regimes. In this regime, the eddies are so strong that there is high turbulent mixing, and the reaction is spread out evenly, like a bulk reaction. It is also called a well-stirred reactor as all the mixing is faster compared to reaction.

In engines, we encounter wrinkled flame regimes, corrugated flame regimes, and thickened wrinkled flame regimes. Studies on turbulent FWI need to be in engine combustion regimes to be relevant to the FWI in engines. Figure 32 shows the combustion regimes encountered in engines are shaded in the regime diagram (in red) [59, 60].

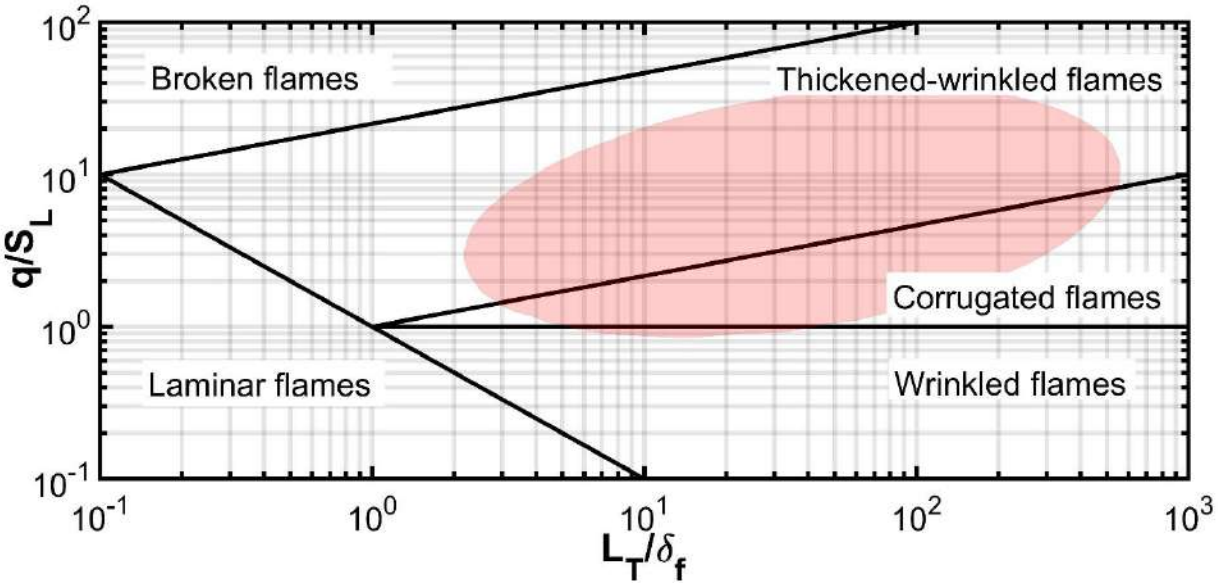

Figure 32: Combustion engine encountered in engines (in red)

As much as the turbulent eddies can affect the flame front, the flame front can also affect the turbulent eddies [61]. It is found, during FWI in an engine, that the turbulent fluctuations are amplified near-wall before FWI because of velocities and the interaction of the flame front with the fresh gases [56]. It is important to note that these phenomena are always present during FWI as expanding burnt gases compress the fresh gases and burning fresh gases needs a way out of the pressure and expansion. The researchers also identified that the quenching at the wall is not due to the stretch effects as, near the wall, the stretch is close to zero [56].

Since laminar FWI has given us knowledge on the interaction of laminar flame and wall, the next step is to correlate how turbulence affects the physics of an otherwise laminar flame and wall interaction. Important parameters that can be used to characterize the turbulence during flame-turbulence interaction are the characteristics of turbulent fluctuations i.e., the length scale of the turbulent eddies compared to the laminar flame thickness, and the velocity fluctuations compared to laminar flame speeds induced by it. A schematic diagram of the important properties of flame flow interaction and the

parameters that affect the interaction is provided in Figure 33. Turbulent FWI also involves wall-turbulence interaction, which will be discussed in the next section.

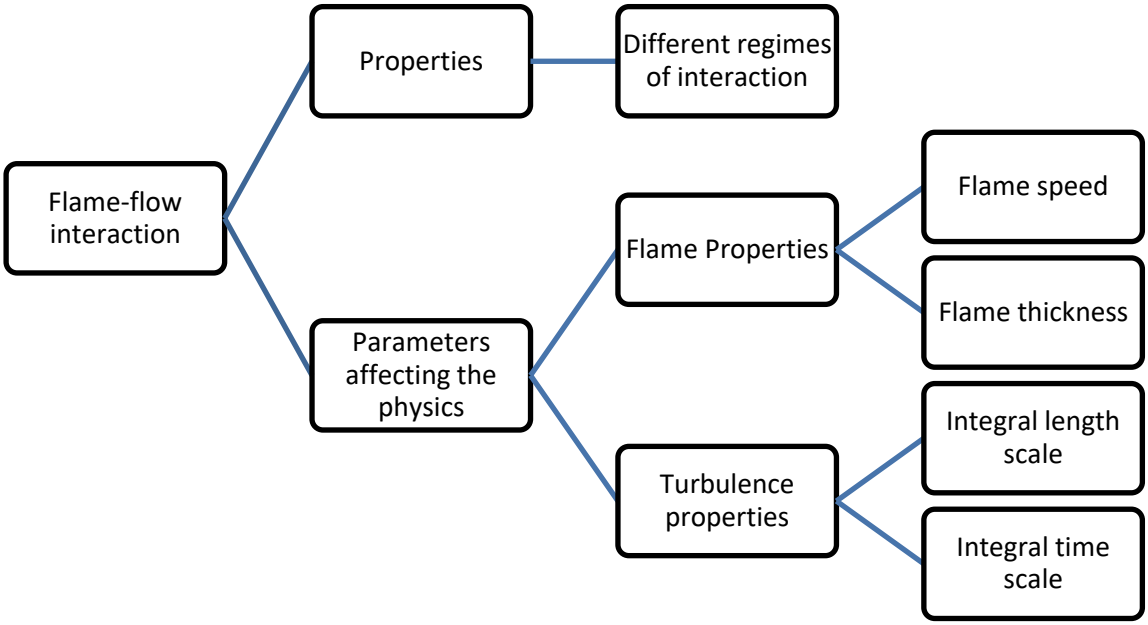

Figure 33: Important parameters during flame-flow interaction

1.3.2.2. Wall-flow interaction

Near wall flows, create a boundary layer (***BL***) which can be characterized by laminar ***BL*** leading to turbulent ***BL***. In the context of momentum transport, ***BL*** is called momentum ***BL***($\boldsymbol{\delta}$) and for thermal transport, it is called thermal ***BL***. A simplistic understanding of the wall-flow interaction is developed by studying the flow over a flat plate. Figure 34 shows the development of momentum ***BL*** in the laminar flow over a flat plate leading to turbulent flow. $\boldsymbol{u_\infty}$ is the free stream velocity, $\boldsymbol{x}$ is the distance from the leading edge and $\boldsymbol{x_c}$ is the critical distance at which the flow transitions into turbulent flow. Both the momentum ***BL*** and thermal ***BL*** are related by the Prandtl number (***Pr***) which is defined by the ratio of momentum diffusivity to thermal diffusivity of the fluid (see Equation 13) [34]. ***BL*** from here on refers to momentum ***BL*** and thermal ***BL*** will be explicitly stated as thermal ***BL***. Inside laminar ***BL***, the fluid is slow

almost sticking to the surface, leading to gradual conduction in layers that can be lumped into convection heat transfer coefficient. Figure 35 shows the variation of convection heat transfer coefficient (***h***) in laminar and turbulent flows. T_∞ is the free stream temperature. As ***BL*** becomes thin, ***h*** increases. The turbulent ***BL*** has a much larger ***h*** compared to laminar ***BL***. Notice the significant increase in ***h*** at the transition zone.

Equation 13: $$\frac{Thermal\ BL\ thickness}{Momentum\ BL\ thickness} = Pr^{-1/3}$$

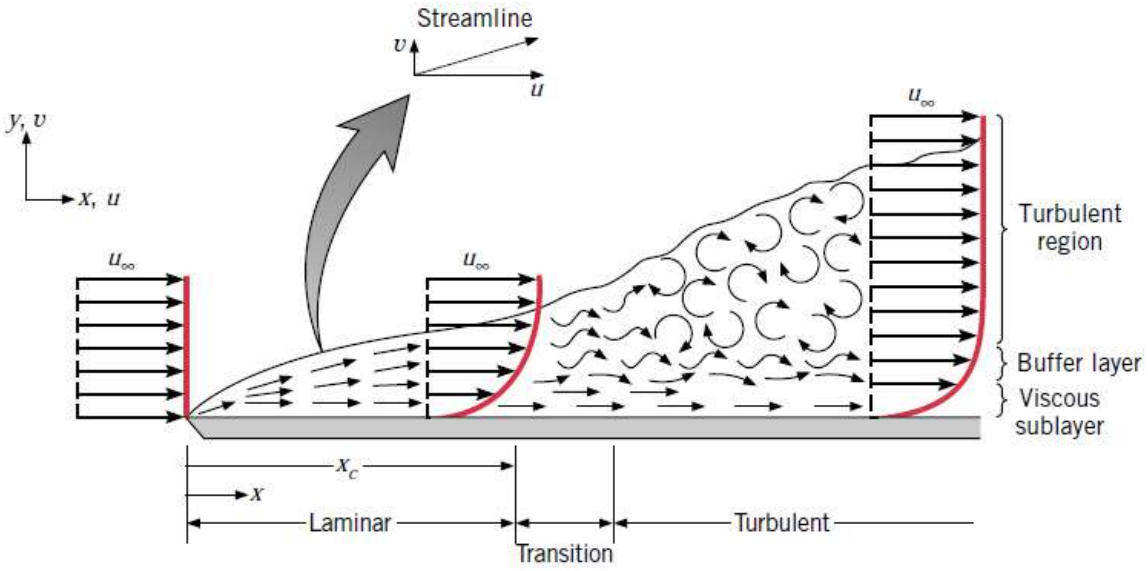

Figure 34: Momentum ***BL*** of flow over a flat plate [34]

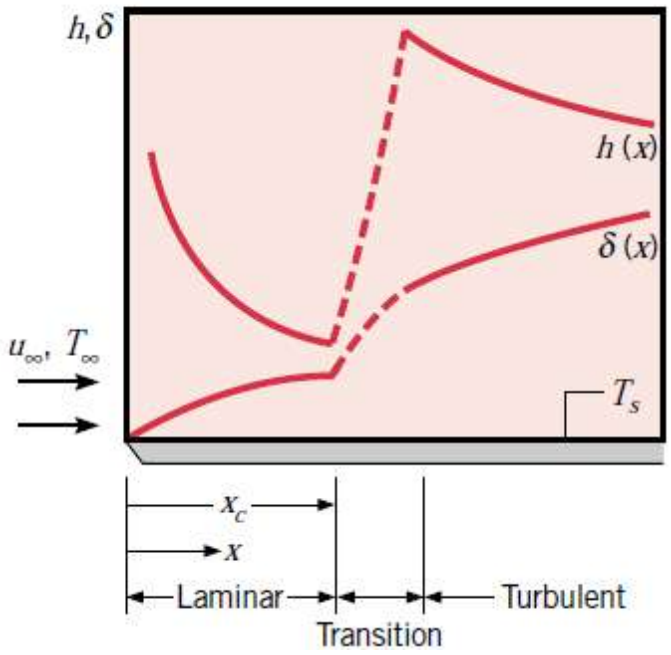

Figure 35: Convection heat transfer coefficient variation with laminar and turbulent regimes during flow over an isothermal flat plate [34]

A brief description of the various sub-layers inside ***BL*** developed near a flat plate is given in Figure 36. y^+ represents the normalized distance from the wall. U^+ represents the normalized velocity parallel to the wall. In this figure, we can see the inner layer of momentum ***BL*** consisting of a viscous layer and the outer layer of ***BL*** consisting of the logarithmic layer and wake region. Near wall, flows in turbulent conditions can contain turbulent coherent structures i.e., organized fluid elements. Near wall streaks, hairpin vortices/horse shoe vortices, large-scale-motion (LSMs), and very large-scale-motion (VLSMs) are identified as different structures existing near-wall [62]. These coherent structures mix the bulk fluid and the fluid in the BL through a motion of sweep and ejections. The consequential augmentation of heat transfer due to vortex structures is widely documented in the literature [63–65]. A study was conducted to understand the heat flux during the impingement of hot non-combusting gas on a flat plate [66]. The authors found that high turbulence has a high probability of forming vortices, which are transported close

to the wall affecting ***BL***. It was concluded that the heat flux contribution of such vortices is up to 12.5% of total heat transfer.

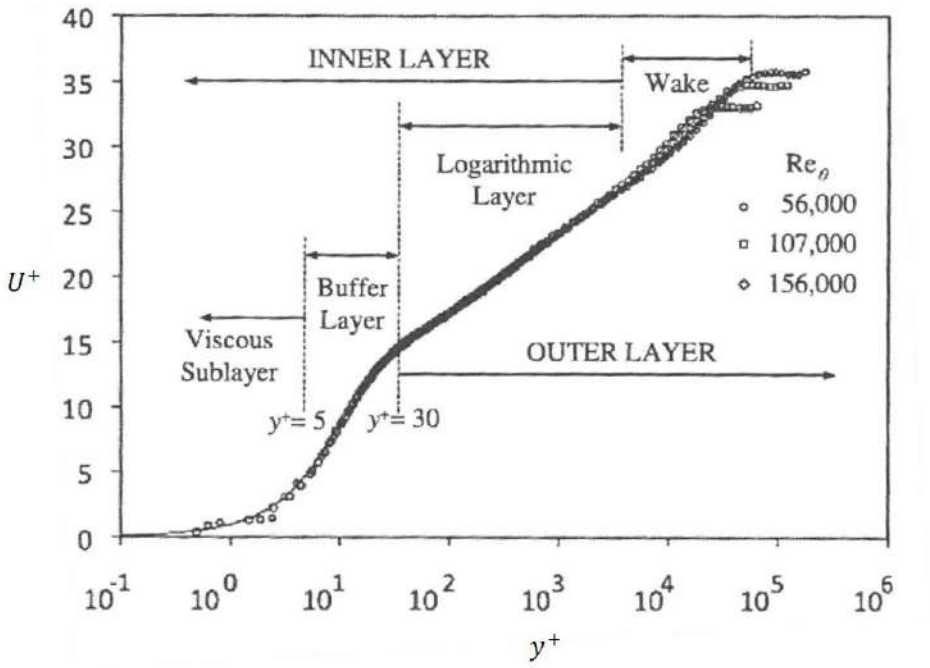

Figure 36: ***BL*** profile of flow over a flat plate

Now we can compare ***BL*** developed in engine with that of ***BL*** over a flat plate. ***BL*** developed inside engines differ from ***BL*** over flat plate, especially in the outer layer. Turbulence near the wall surface of an engine is found to be inhomogeneous where it is found to increase in both fired and non-fired cases [67]. The ***BL*** is turbulent in nature which is affected by not only large-scale turbulent structures but also small turbulent vortices which enter ***BL*** [68]. Velocity measurements in engines at motored conditions (using PIV and LDV) highlight this frequent interaction of turbulent structures in ***BL*** [69, 70].

Such structures are identified to increase the wall heat flux during FWI in other non-engine combustion environments [71, 72]. The heat flux is found to correlate with the presence of near-wall coherent vortices structures in a V-flame–wall interaction [71]. The temporal pattern of the heat flux fluctuations correlates well with the time scale and length scale of such vortices. The authors conclude

that the strong correlation of the vorticity structures with the heat flux fluctuations indicates the role of turbulence in augmenting heat flux in the specific experiment. We expect that the turbulence will influence the heat flux during FWI in closed chamber combustion i.e., engines, CVC, RCM. However, attempts on separating the influence on heat flux in CVC have not been successful [42, 51]. It is still unclear how turbulence affects the heat flux during the FWI in closed chambers including engines.

The velocity measurements carried out in engine by several researchers show that the turbulent structures are found inside ***BL*** in engine. One example of interacting turbulent structure inside ***BL*** in a motored engine is shown in Figure 37 [69]. In this figure, we can see turbulent eddies very close to the wall (the wall is at ***y*** = 0 or vertical axis = 0). Figure 38 shows ***BL*** for different engine speeds and positions of a piston in a motored engine [69]. The authors find differences in the position of piston and engine speed lead to changes in the magnitude of mean velocities and ***BL*** thickness. The authors conclude that ***BL*** is not fully developed. A comparison with ***BL*** in engine with that of a fully developed flow on the flat plate is presented in Figure 38. ***BL*** over a flat plate is given as a dashed black line with label law of the wall, whereas the ***BL*** at different positions of the piston is given as different colors with CAD as the label. ***u+*** is the dimensionless horizontal velocity parallel to the wall and ***y+*** is the dimensionless distance from the wall. We can see that there is significant variation in the logarithmic layer and wake region of outer ***BL***. Further, ***BL*** near the wall in an engine with combustion shows significant fluctuations [68]. Several researchers concluded that ***BL*** is not fully developed both in fired and motored test cases [68–70]. The differences in ***BL*** in engines and ***BL*** due to flow on a flat plate could be due to a lack of time to form well-developed ***BL*** in engines. Flame accelerates the gas velocity normal to the piston leading to an increase in the mass and momentum transport to the wall [68]. Breakdown of the processes near the wall could include identifying changing regimes due to piston speed, pressure variation due to the location of the piston, and of course the interaction of turbulent structures.

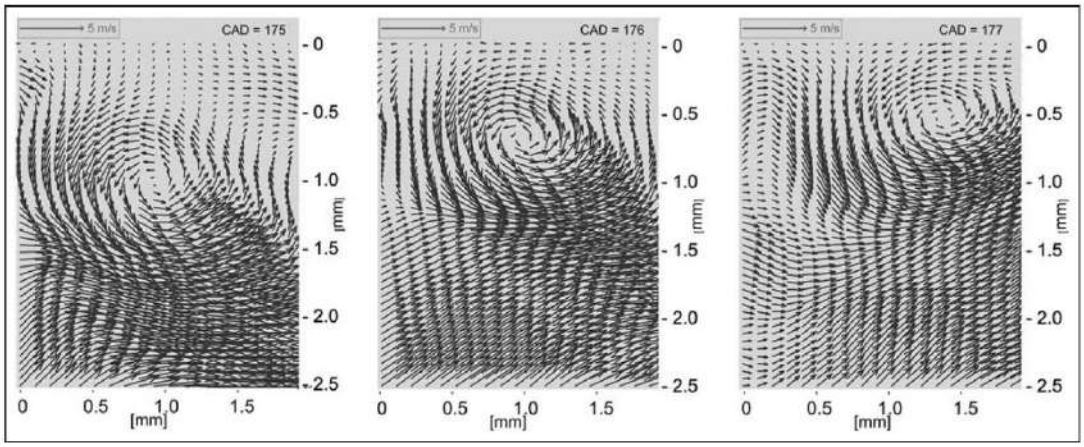

Figure 37: Small vortex structures near the wall (***y***=0, or vertical axis = 0) using high-speed high-resolution PIV in a motored engine at 400 RPM [69]. Resolution-100µm and the first measurement at 50 µm.

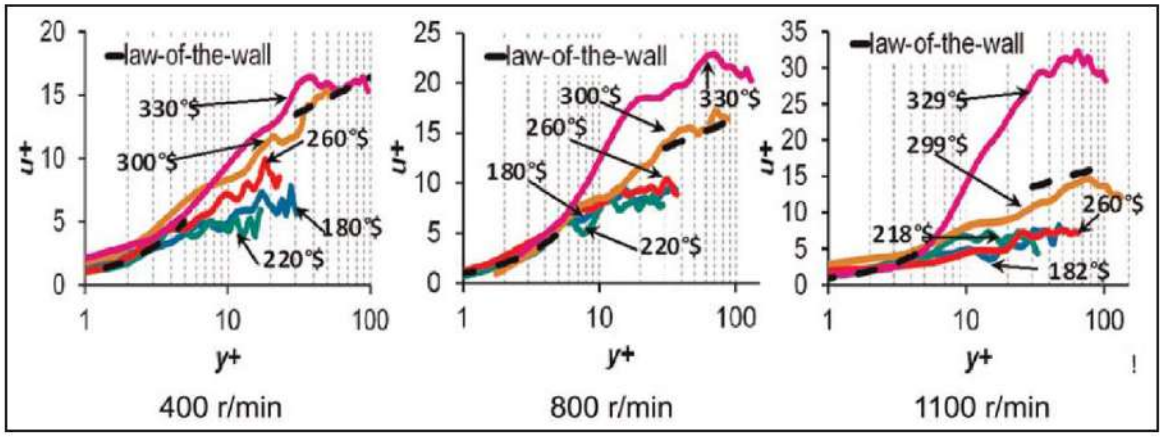

Figure 38: ***BL*** determined using experiments compared to ***BL*** over flat plates at different speeds of engine and different instants in the cycle (CAD) [69]

To understand ***BL*** development in engines, this bibliographic survey shows there is a critical need to understand ***BL***. This advance could lead to improving the understanding of the thermal ***BL***, which is a key factor in heat flux measurements in engines. Further, near-wall characteristics of relevant turbulent structures (length scales and time scales) are also important. Their relationship in increasing heat transfer will also be important in understanding heat losses. A schematic diagram of wall-flow interaction is presented in Figure 39.

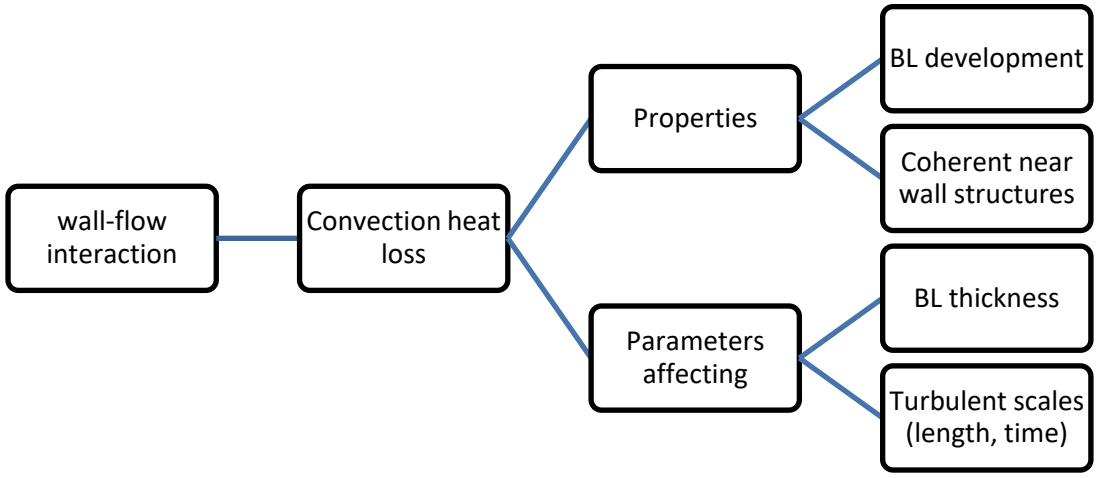

Figure 39: Important parameters during flow-wall interaction

1.3.3. SYNTHESIS OF TURBULENT-FLAME-WALL INTERACTION

Heat loss during FWI is due to the presence of flame near the wall. The parameters that are sufficient to understand the heat loss are the hot gas temperature near the flame and the convection coefficient of heat to the wall. The hot gas temperature near the flame is directly related to the flame. The flame is characterized by a combustion regime and flame properties such as flame power and flame thickness. In order to determine the combustion regime, we need to determine the laminar properties and the turbulence properties i.e., integral length scale and integral time scale. The local flame power is a property which is derived from the flame speed, flame thickness, and fresh gas properties.

The convection heat transfer coefficient is dependent on the thermal BL and properties of fresh gas. Researchers have found that the thermal boundary layer is of the order of quenching distance in a side wall quenching of burner flame [73]. Since the temperature falls continuously from the flame across the quenching distance until the wall, the quenching distance is equivalent to thermal ***BL***. So, we will use the hypothesis that the quenching distance represents the thermal ***BL***. Moreover, turbulent structures near

the wall can affect the convection heat transfer coefficient. A schematic diagram of this simplistic model of turbulent FWI is given in Figure 40. This figure is a synthesis of Figure 28, Figure 33, and Figure 39.

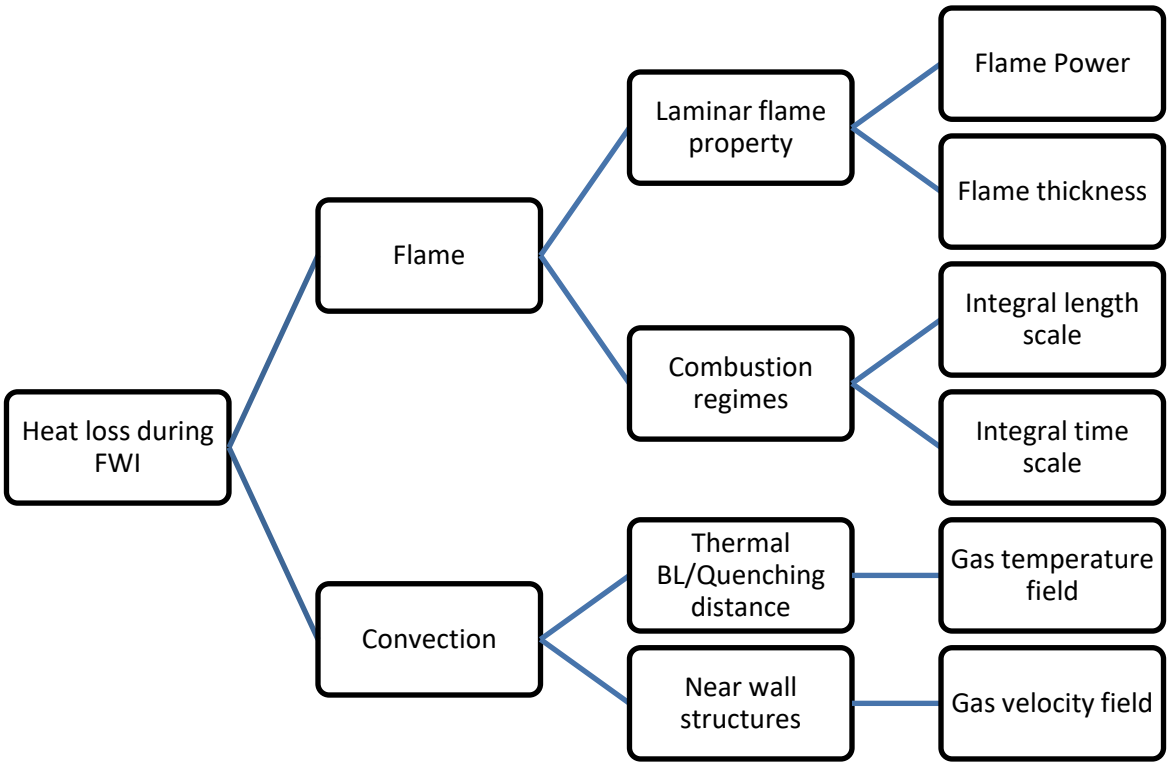

Figure 40: FWI simplistic model

Thus, to describe the heat loss mechanism, in addition to heat flux, flame power, flame thickness, integral length scale, integral time scale, gas temperature field, and gas velocity field are simultaneously required. Given the complexities of simultaneous measurements, we will use a mix of experimental measurements and numerical calculations to obtain the required data. Calculating flame properties and gas temperature field is possible using numerical methods. More discussions on these methods and the associated assumptions are presented in Chapter 2. Experiments can be used to determine the velocity field simultaneously with heat flux measurement, which will give information on the combustion regimes and near-wall structures.

1.3.4. SPRAY FWI

Along with propagative FWI, spray FWI is studied in this thesis to understand heat loss during spray-FWI. In this sub-section, we will explore the literature to gather important knowledge on spray FWI.

The spray FWI is expected to be different from propagative FWI as it's a non-premixed flame that interacts with the wall. The high temperature of the ambient atmosphere along with high levels of turbulence introduces another layer of complexity [74, 75]. Detailed study of the heat transfer during spray FWI is not present in the literature in the same light as premixed FWI. We can decompose the process of spray FWI into two interaction steps:

- Non-reactive spray-wall interaction: Measurements in literature present the heat flux due to non-reacting spray interacting with the wall [45]. The heat flux peak is in the order of half of the heat flux peak measured during reacting spray interacting with the wall signifying significant heat flux just due to non-reacting spray-wall interaction. Researchers also observe a two-step heat flux during the reactive spray-wall interaction [46]. They hypothesize that the two-step heat flux is due to the non-reactive spray-wall interaction and the spray FWI occurring sequentially in a short time. Significant heat flux due to non-reactive spray-wall interaction and evidence of two-step heat flux provide the need to quantify the heat flux due to non-combusting spray wall interaction.

- Turbulent spray FWI: Turbulent spray FWI can be observed as spray flames starts to develop due to auto-ignition and subsequent interaction with the wall. This part of the FWI could be found, analogous to that of turbulent FWI in premixed cases as there is a flame interacting with the wall. The spray flame interacting with the wall is studied in literature where the structure of the spray flame is found out[20]. There is a need to quantify the separate effect of spray FWI on the heat flux.

There are many differences existing in turbulent spray FWI, in comparison to premixed FWI, especially in the flame properties, turbulent ***BL,*** and flow properties near the wall. Premixed flame in the combustion regimes found in engines has a well-defined flame front with a well-defined temperature and species gradient. In comparison, the spray FWI presents a thicker flame, with different stages of diffusive combustion. The turbulent ***BL*** is also different for spray FWI as the major turbulence generating mechanism in spray-FWI is the high-pressure spray jet, whereas the turbulence during premixed FWI is generated by the existing flow field. There exists no study that explains the ***BL*** developed during spray-wall interaction. We hypothesize that the ***BL*** developed during spray FWI is similar to the ***BL*** developed during gas jet wall impingement obtained in other studies [34]. Figure 41 shows a schematic of ***BL*** in such a flow [34]. Although differences exist between gas jets (typically gas jet has a larger jet diameter compared to spray-wall interaction, with no flame near the wall) such a hypothesis can act as a starting step in our analysis. In Figure 42, we can see that ***BL*** thickness at the center (near the stagnation zone) is smaller which grows in thickness in the radial direction. Figure 42 shows the variation of the Nusselt number i.e., the ratio of convection coefficient (***h***) to the conductivity (***k***) on the radial axis. This figure shows the reduction in convection (aligning with ***BL*** thickness) as one moves away from the center of the jet [34].

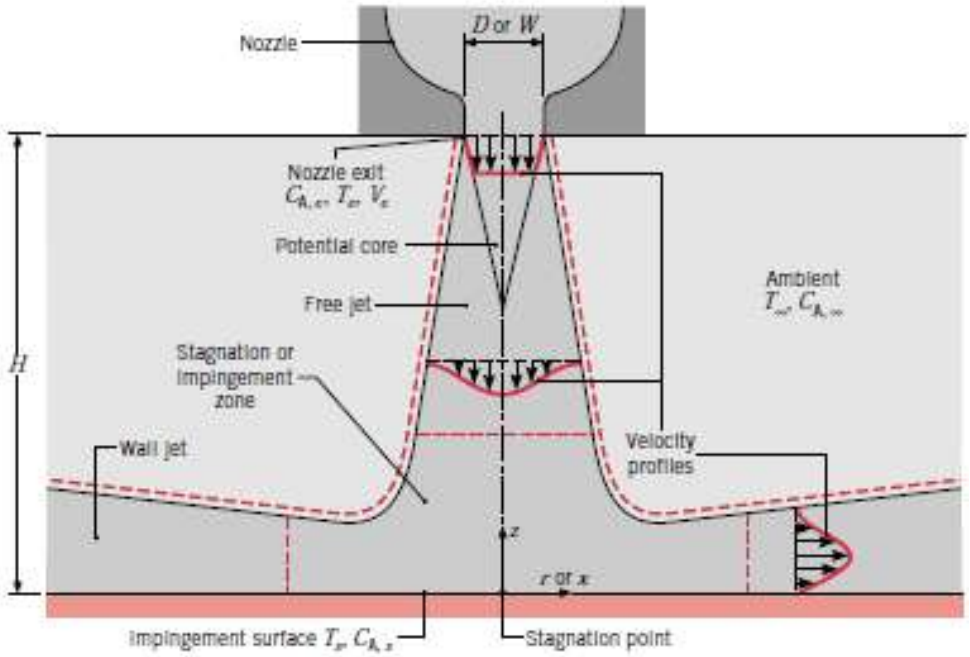

Figure 41: Spray ***BL*** development [34]

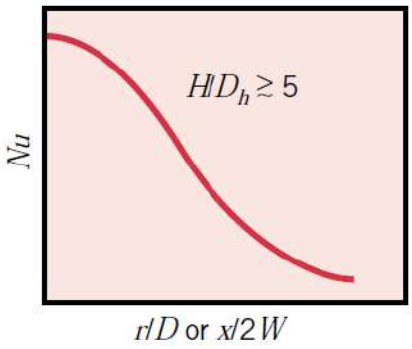

Figure 42: Nusselt number variation with radial distance(***r***) [34]

1.4. KEY ISSUES

In this section, we will discuss the key issues arising from the literature review and analysis presented in this chapter. Further, the strategy adopted in the thesis to answer these issues is discussed. The section is divided into three subsections based on premixed FWI, spray FWI in the CVC and premixed FWI in the engine.

1.4.1. PREMIXED FWI IN CVC

In this subsection, we will present the important issues that we have identified in this chapter pertaining to premixed FWI in the CVC.

Turbulent FWI is a coupled phenomenon involving many parameters (see section1.3). To understand the effect of each parameter we need to study FWI in such a way that we can decouple the effect of each parameter. For this purpose, we need to conduct experiments in engine as well as controlled simple combustion chambers like CVC. The use of a CVC also facilitates optical diagnostics through its various optical access, to conduct optical diagnostics like PIV to determine the gas velocity field.

Pressure during interaction (P_{int}) is an important parameter that is found to have an effect on the peak of heat flux (Q_P) during FWI. There is data from literature for the influence of pressure on the heat flux in laminar conditions where the dependency of Q_P on P_{int} is in the form of power-law ($Q_P \sim P_{int}^{b}$). It could be possible that the power-law coefficients of the dependency of Q_P on P_{int} is dependent on many other parameters including experiment configuration. Hence, we need to evaluate the effect of P_{int} during FWI in our setup, through a variation of P_{int} conducted during Laminar FWI. Such results of the dependency of Q_P on P_{int} can be compared with literature. Moreover, this dependency can be used to decouple the effect of other independent parametric variations whenever suitable.

Turbulence increases S_T, hence researchers look to develop engine designs with high turbulent flows in order to achieve higher efficiency. However, there is no information (in literature) on how turbulence intensity affects the heat flux during FWI. In this thesis, we will explore the turbulent FWI encountered in CVC at high pressure and high density, close to the conditions encountered in engines. Usually, CVCs has provision for fans or high-pressure injection flows to increase the turbulence intensity inside the CVC. We will measure the surface temperature (to derive the heat flux) and the flow field simultaneously (to get

information on the turbulence scales and turbulence intensity). Comparing the heat flux in laminar and turbulent conditions could give us the effect of turbulence intensity on $\boldsymbol{Q_P}$.

There have been results for heat flux in turbulent and laminar cases while varying equivalence ratio, density, and fuel. Although such a variation induces variation in flame power ($\boldsymbol{Q_\Sigma}$), the achieved variation is not completely independent due to the coupling of changes in $\boldsymbol{Q_\Sigma}$ (through equivalence ratio, density, and fuel type) to changes in chemistry, the density of the air-fuel mixture and fuel properties. Carrying out the variation of $\boldsymbol{Q_\Sigma}$ at a similar equivalence ratio, density, and fuel could yield the direct effect of $\boldsymbol{Q_\Sigma}$. Such knowledge could help us optimize the engine operation or design engines for low heat loss.

Modern engines employ or plan to employ EGR for achieving high performance and low emissions. However, there is no data on how dilution affects the heat flux. Hence, the effect of dilution can be studied in a CVC by varying the composition of inert gasses in the fresh gas mixture, like CO_2 and N_2.

Further, in some experiments, it has been found that $\boldsymbol{Q_P}$ in propagative FWI is non-homogenous in space. We will evaluate the above observations by comparing $\boldsymbol{Q_P}$ evaluated at different locations in CVC.

Understanding the effect of fuel properties on the heat flux is important to designing the engines and fuels of the future. Even though there is data in the literature for comparison of heat flux for different fuels these comparisons are not in similar conditions. Typically, there is a large variation in $\boldsymbol{Q_\Sigma}$. We can compare the heat flux during FWI in CVC for different fuels (CH_4, C_2H_2+H_2, and H_2) at similar orders of flame power. This can be achieved by adjusting N_2 fraction in the air to obtain the target $\boldsymbol{Q_\Sigma}$ while keeping the density of fresh gas, fuel, and O_2 concentration the same.

1.4.2. SPRAY FWI IN CVC

In this subsection we will present the important issues that we have identified in this chapter pertaining to spray FWI. In order to obtain a reproducible experiment condition, we need a CVC to conduct experiments on spray FWI. Recently, a standardized spray A condition is defined within ECN framework to bring together contributions across the research community. Not much data is available for heat flux during spray FWI in ECN spray A conditions. Hence, we have chosen to use ECN spray A condition to conduct surface temperature measurements in the CVC during FWI. ***LoL*** evaluated through OH* visualization is compared with ***LoL*** of the Spray A to ascertain that the Spray A conditions are achieved.

Spray FWI is expected to show variation in heat flux due to ***BL*** development similar to the jet-wall interaction shown in section 1.3.4. Location of measurement is varied to understand the spatial variation in heat flux during spray FWI. Ambient temperature variation is also conducted to understand its effect on heat flux during FWI. High turbulence near the wall due to non-reactive spray-wall interaction is expected to cause significant heat flux. Hence, heat flux due to reacting and non-reacting spray A is measured in the same setup to separate the contribution of spray momentum and spray FWI on the heat flux during spray-wall interaction.

There have been reports of 2 step heat flux for a spray FWI in various experiment configurations. Researchers hypothesize that the two-step is due to non-reactive spray wall interaction followed by reactive spray wall interaction occurring in a very short time. In this thesis, we will attempt to reproduce 2 step heat flux by controlling the order of the sequence jet arrival at the TC and autoignition in the same thermodynamic conditions.

1.4.3. PREMIXED FWI IN ENGINE

In this subsection, we will present the important issues that we have identified in this chapter pertaining to premixed FWI in the engine. In order to study the FWI in an engine the IMEP of the engine need to be constant so that we can conduct variation of targeted parameters and understand its effects independently.

PC ignition is shown to have the advantages of faster combustion with the potential to achieve efficiency gains in engine applications. We will measure the heat flux during FWI, with a prechamber ignition system to compare the heat losses with a conventional spark-ignition system in order to compare the heat flux. This comparison will give us insight into whether the heat flux varies in the different ignition systems or not.

We plan to evaluate the relationship of $\boldsymbol{Q_P}$ vs $\boldsymbol{P_{int}}$ for FWI obtained in the engine and compare the qualitative features of $\boldsymbol{Q_P}$ vs $\boldsymbol{P_{int}}$ with the dependency found in CVCs. We expect the high turbulence intensity inside the engine will lead to natural variation in $\boldsymbol{P_{int}}$ which will lead us to obtain $\boldsymbol{Q_P}$ vs $\boldsymbol{P_{int}}$ for FWI in an engine.

Turbulence intensity and fresh gas properties change based on the position of the piston. Hence, we will conduct a variety of ignition timing to understand its effect on the tendency of $\boldsymbol{Q_P}$ vs $\boldsymbol{P_{int}}$.

Since PC ignition is due to flame jets from PC, we expect to see high $\boldsymbol{Q_P}$ due to the effect of the flame-jet during FWI [18]. Hence, we need to understand the difference in the heat flux trace measured near the tip of the flame-jet and compare it with the case where the effect of flame-jet is minimum. Such knowledge of the heat loss can help us, to proceed further in optimizing the PC operation in an engine.

In the next chapter, we will discuss the experiment setups, diagnostics and postprocessing in detail which is used in this thesis.

Chapter 2: Experiment methodology

In this thesis, FWI is studied through combustion in a constant volume chamber (CVC) and a piston engine at IFPEN. The wall heat flux is measured through the evolution of surface temperature measurements using a wall-TC assembly. This chapter presents five different sections. In first section we present the experiment setups. In the second section we present the diagnostics used to measure wall surface temperature, gas velocity and OH* emissions. In the third section we present the complimentary thermodynamic gas property calculations and postprocessing of the heat flux to derive important properties for our analysis. In the fourth section we present the postprocessing the PIV velocity field. In the fifth section we present the methods of calculation of turbulence properties from the velocity field. The objective of this chapter is to understand the details of the experiment setup, limitations and advantages of each diagnostic, the methods of postprocessing the measurements, and how they fit into the study to probe FWI.

2.1. Experiment Setup

In this section, we present the experiment setups used in this thesis i.e., CVC and the engine at IFPEN along with their major components.

2.1.1. Constant volume chamber at IFPEN

HPHT cell at IFPEN is a high pressure-high temperature CVC (HPHT cell) used to study both premixed propagative and spray FWI. In a CVC, the initial and boundary conditions (temperature, the composition of combustion gases, etc.) are well controlled to study combustion, providing high repeatability of the experiments. Further, it is easier to conduct simultaneous diagnostics, especially optical diagnostics like

PIV, LIF, etc. through the numerous optical accesses of the HPHT cell. In this section, the basic building block along with its instrumentation i.e., spark plug, fan, and pressure measurement are discussed.

2.1.1.1. Basic block

The HPHT cell is carved out of a cube with approximately 100 mm of edge, with optical access through all its faces, shown in Figure 43. The total volume is 1.4 liters. The vessel has 8 corners and 6 faces. The optical accesses are provided with circular optical windows on each face (80 mm in diameter), made of sapphire, to conduct optical diagnostics like PIV or LIF. During the experiment, the cell is maintained at 200 °C (±3.6 °C) using heating coils. This temperature ensures water formed as a product of combustion is not condensed after the reaction. The cell can withstand combustion peak pressures found in naturally aspirated SI engines. It is designed to withstand pressure larger than 120 bars. The leak standards are 20 mbar in 20 seconds in vacuum and 200 mbar in 30 seconds in pressure at 40 bars.

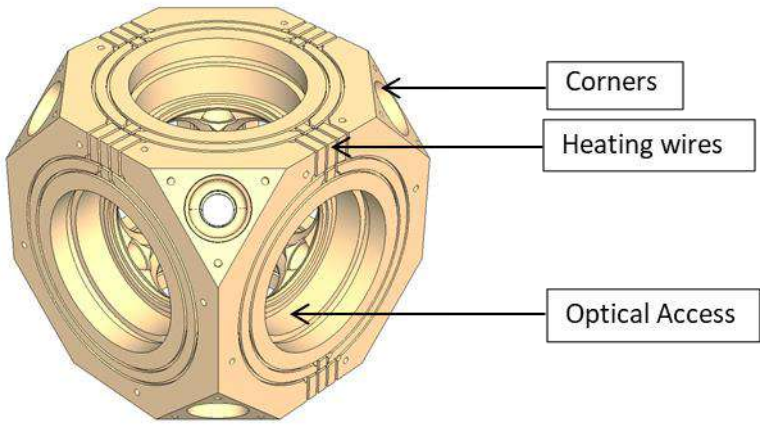

Figure 43: HPHT cell basic block

2.1.1.2. Gas exchange

A vacuum pump ensures that before the start of the experiment all the gasses inside the HPHT cell and lines are removed. Before filling the HPHT cell, the inlet gas pressure is precisely measured by a high-precision pressure sensor. For fuels, Keller type pressure sensor with model PAA-33/80794.4 is used which has a pressure measurement range of 0-10 bar with a least count of 0.001 bar. For nitrogen and oxygen,

Keller-type pressure sensor with model PAA-33X/80794.4 is used which has a pressure measurement range of 0-100 bar with a least count of 0.01 bar. The exact amount of gas as per the experiment design is allowed into the HPHT cell through the electronically controlled inlet valves by measuring gas partial pressures sequentially. These valves consist of high flow rate and low flow rate valves which take feedback from the pressure sensors to reach the set gas composition. The tolerance limit on gas pressures achieved during filling of HPHT is given in Table 1. Exhaust valves remove the burnt gas after the combustion. A schematic of the gas introduction process is given in Figure 44. The operation sequence is as follows

- Vacuum the HPHT cell (up to 0.05 bars) to remove any gases present in the HPHT cell
- Purge with nitrogen gas (up to 5 bars)
- Vacuum HPHT cell (up to 0.05 bars) to remove nitrogen gas
- Meter and fill gasses (fuel, oxidizer, and diluents) sequentially one after another

Table 1: Tolerance of different gas pressures during filling of CVC

Gas type	Tolerance (%)
C_2H_2, CH_4	0.8
H_2	0.25
N_2	0.15
O_2	1.5

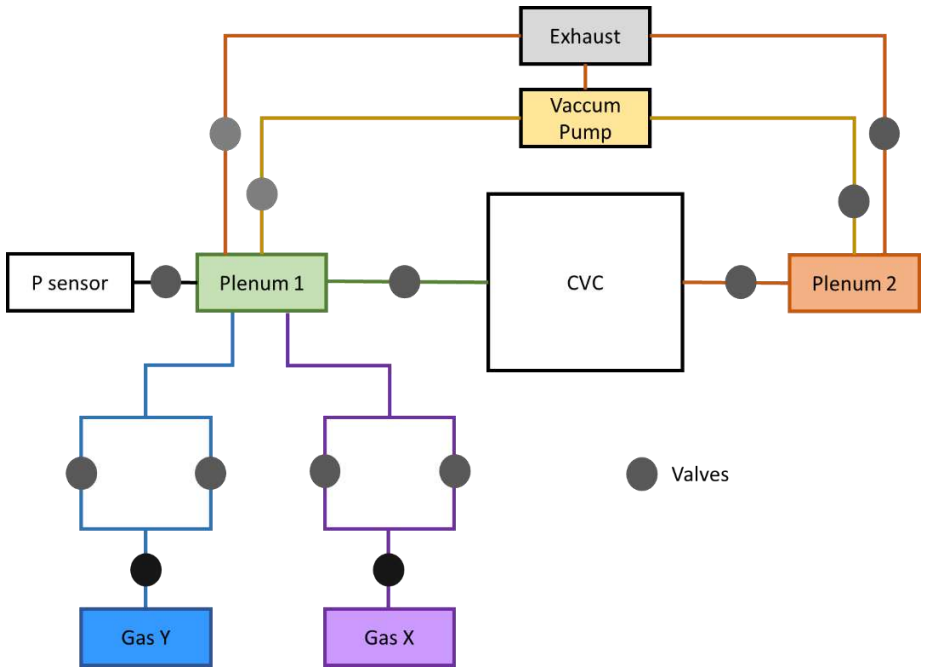

Figure 44: Schematic of gas exchange in HPHT cell

2.1.1.3. Fans

After the filling of gases inside the HPHT cell, the gases need to be mixed to achieve homogenous composition. For this purpose, a fan (or multiple fans) is introduced inside the HPHT cell through one of the corners (or multiple corners) of the HPHT cell. The CVC could accommodate a maximum of 6 fans. However, we have used 1,2, or 3 fans depending on target experiment configurations. The fan enhances mixing to achieve homogenous composition inside the HPHT cell by introducing turbulence. This feature of introducing turbulence inside the HPHT cell through a fan is quite common in literature [76, 77]. A simplified representation of a fan inside HPHT cell is given in Figure 45 and Figure 46. In this thesis, two different types of fan blades are used in order, along with the various mode of operations, to obtain various turbulence intensities. A schematic of the blades is presented in Figure 47. Drawings containing all the dimensions are given in Annex 1. The fans are rotated using a motor shaft connected to a 12-volt motor. A calibrated voltage is supplied to the motor through a voltage controller to maintain the target rotation speed (0, 3000, 4000 RPM). Since the calibration is done at constant pressure i.e., initial pressure,

the fan speed may vary during combustion when the pressure increases. However, the objective of fan-induced turbulence and mixing in the cold flow (before combustion) is achieved through the fan operation.

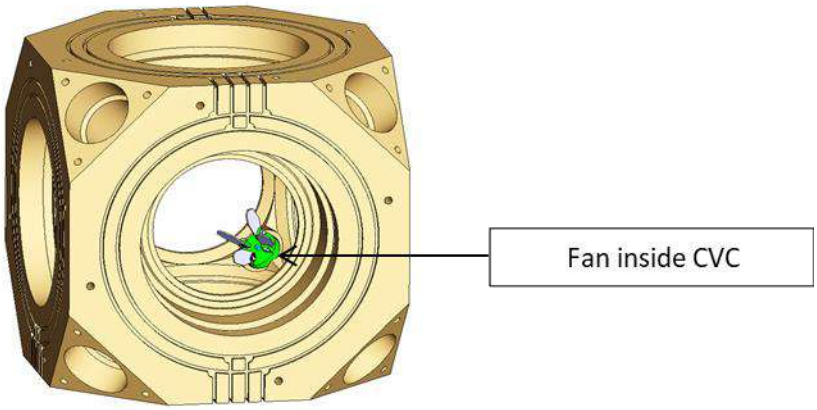

Figure 45: CVC Basic block with the Fan

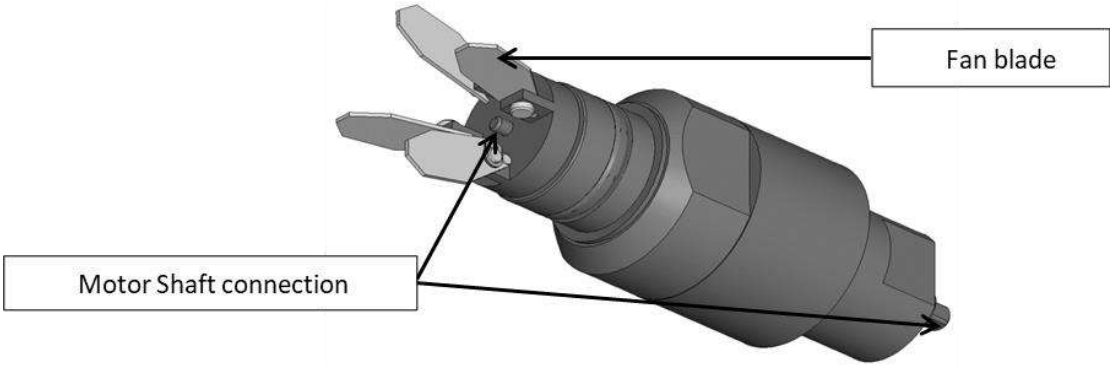

Figure 46: Fan used in HPHT cell shown in Figure 45

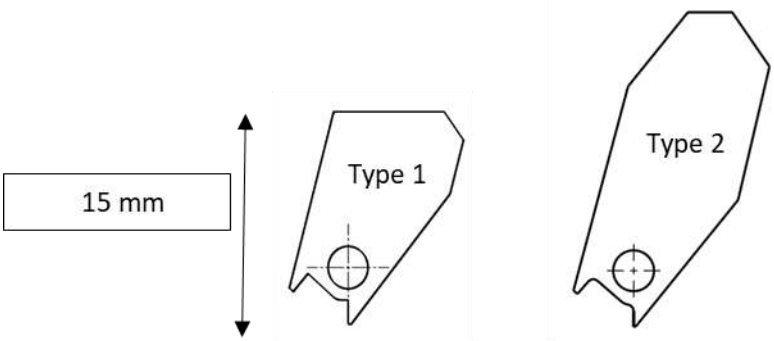

Figure 47: Different Fan blades used in this thesis

2.1.1.4. Spark ignition

Conventional spark plugs with one electrode are used to initiate the combustion (Denso 5344 IKH20 Iridium Power Spark Plug with 12 V standard coil on plug ignition coil). Spark plugs can be mounted on one of the faces of HPHT cell or on the corner of HPHT cell with a suitable insert. For premixed propagative FWI experiments only one spark plug is used in one of the faces of HPHT cell. For spray FWI experiments, 3 spark plugs are used. More details are provided in the setup details.

2.1.1.5. Pressure measurement

A piezo-electric pressure sensor is mounted on a corner of HPHT cell to record the pressure during the combustion. AVL GU21D along with Kistler single channel (Type 5011 B) charge amplifier is used for pressure measurements in all the experiments presented in this work. Such pressure readings enable accurate calculation of the unburnt gas temperature inside HPHT cell. Knowing the gas composition, initial gas density, transient gas pressure, and initial gas temperature we can accurately define the thermodynamic state of the gas inside HPHT cell assuming a homogeneous pressure across the chamber. A similar one-point measurement has been commonly used in literature to record pressure during FWI. A sample of time-pressure evolution during combustion in HPHT cell is shown in Figure 48. $\boldsymbol{t} = 0$ corresponds to the spark timing and then the pressure rises induced by the combustion.

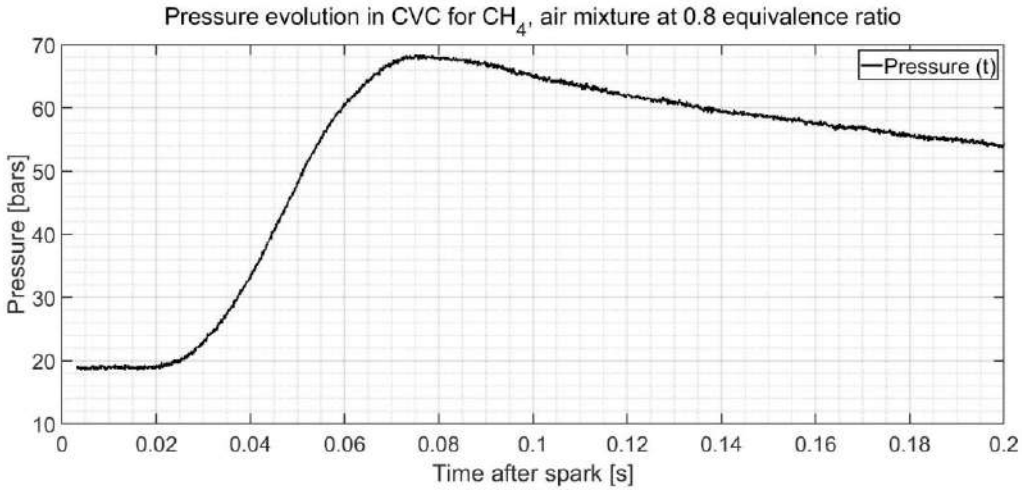

Figure 48: Sample Pressure evolution during the combustion in HPHT cell

2.1.1.6. Combustion events

In this CVC two combustion modes can be studied, premixed flame and spray combustion. For premixed FWI studies, the direct combustion of filled gases is used to generate a flame. However, the non-premixed spray type of combustion needs high temperature and pressure, encountered in diesel engines. To achieve high temperature and pressure, the premixed combustion (also called precombustion) event is used, which takes advantage of the high pressure and temperature in the burnt gas to reach the target conditions. The initial gas composition is set such that even after the pre-combustion, the resultant burnt gas composition simulates the target gas composition of the spray combustion. After the precombustion, the pressure inside HPHT cell starts to decrease (after 0.015 s in Figure 48). During this decrease, at a target pressure (temperature), a high-pressure spray is injected to recreate spray combustion. A schematic of various events (gas filling, spark, precombustion, injection, and spray combustion) is given in Figure 49.

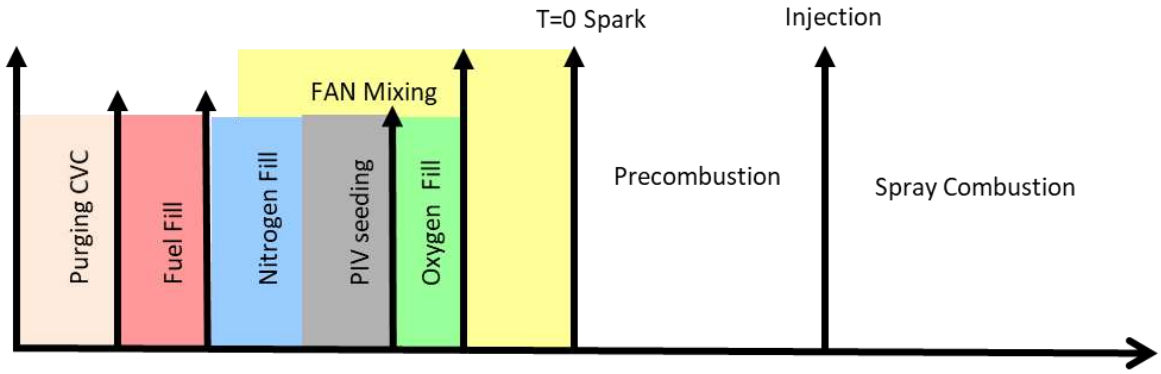

Figure 49: Schematic of various events during operation of HPHT cell

2.1.1.7. Spray A Injector

During the spray combustion, an ECN spray A injector is used. This solenoid injector is a single hole axial orifice with a nozzle diameter of 0.09 mm used with a common rail with nozzle temperature maintained at 363 K. A schematic is shown in Figure 50. More details about the injector can be found in [78]. This CVC is well characterized and has been used in fundamental studies of spray combustion [47]. HPHT cell and injector system are well-calibrated to obtain ECN conditions (injection pressure, timing, duration of injection, ambient temperature) [47]. In this thesis, all the spray experiments are carried out with an injection pressure of 1500 bars.

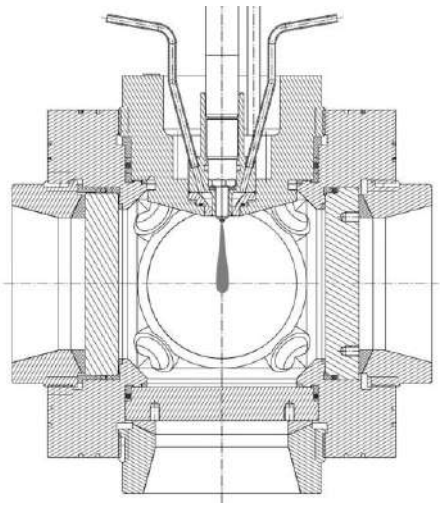

Figure 50: Single hole injector inside CVC

2.1.1.8. Laser ignition

To force ignition at a desired time and location a laser ignition can be used. Laser of high energy, when focused on a small region such that energy density is very high, can force ignition. However, the energy of the laser must be sufficient, and the location of ignition must contain an air-fuel mixture in vapor form. Laser ignition is already been carried out in the CVC at IFPEN [79]. The energy usage and the experiment setup are exactly like the earlier experiment. Figure 51 shows the schematic of the laser ignition setup and the timing diagram when used in CVC. At a wavelength ($\boldsymbol{\lambda}$) of 1064 nm an energy density of ~38 kJ/cm^2 is obtained using a laser pulse of 600 mJ per pulse, from Quantaray YAG PIV 400.

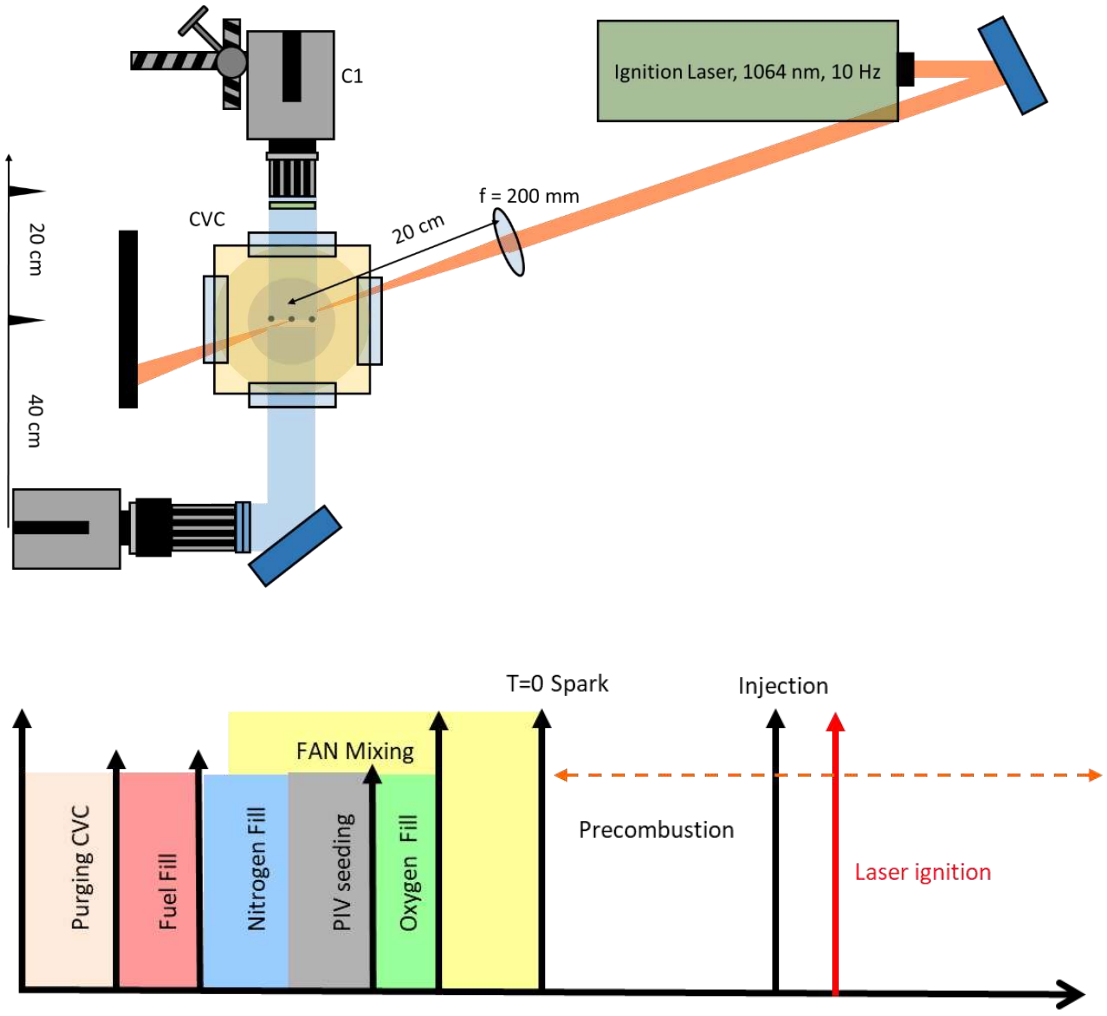

Figure 51: Schematic and synchronization of Laser ignition (in red line). The dashed red line shows that laser ignition can happen at any time after Fan mixing.

2.1.2. ENGINE

During this thesis, heat flux measurements are also carried out in an engine during premixed propagative FWI. In this section, the engine, pressure measurement, tumble variation, and ignition system variations are discussed.

2.1.2.1. Engine description

At IFPEN, a piston engine has been used as a combustion chamber in this thesis. It is 4 strokes single-cylinder engine, with 4 valves. The displaced volume is 400 cc with a compression ratio of 10.5:1. This engine has been studied with both conventional and pre-chamber ignition systems in previous work at IFPEN [18]. A schematic of the engine is shown in Figure 52. Details of the experiment are given in Table 2. The engine is operated at 1200 RPM for all the experiments in this thesis. For each set of experiments, the engine starts operating at a wall temperature of 90° C and each experiment consists of 200 cycles.

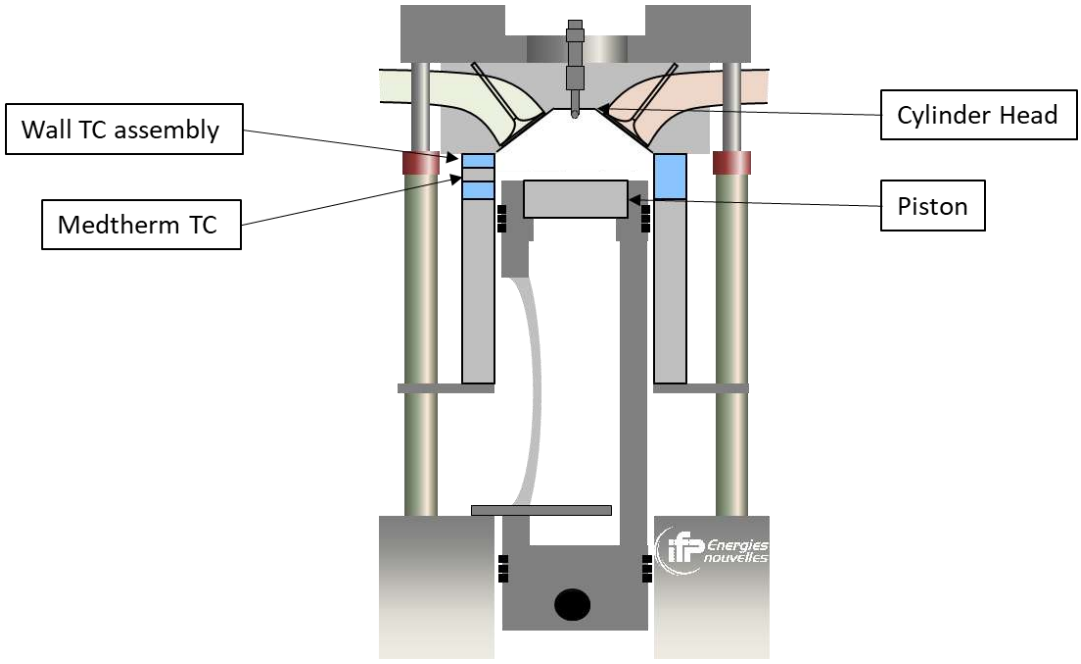

Figure 52: Schematic of the engine used in this thesis.

Table 2: Engine at IFPEN information

	Engine
Type	Single cylinder, 4 valves
Capacity	400cc
Bore x Stroke	77 x 85.8 mm
Compression Ratio	10.5:1
Fuel	Commercial Gasoline E10
Injection Strategy	Port fuel
Equivalence Ratio	0.9, No EGR

2.1.2.2. Pressure measurement

A piezo-electric pressure sensor is mounted on the cylinder head to record the pressure during the combustion. AVL QC34D along with Kistler single channel (Type 5011 B) charge amplifier is used for pressure measurements in all the experiments. This pressure sensor is used in past studies and is capable of recording pressures during knock which has a faster characteristic time compared to FWI [80, 81]. Hence it is suitable to measure pressure during FWI.

2.1.2.3. Ignition system

Two types of ignition systems are used in the study on the engine i.e., conventional spark ignition and prechamber spark ignition. The prechamber has a volume of 1.5% of the TDC volume of the engine. The holes in the prechamber are 1mm in diameter. The passive, 6-holes pre-chamber ignition system has been used before, and details are provided in [18].

2.1.2.4. Tumble variation

The tumble is the ratio of the angular speed of the flow to the angular speed of the crankshaft of the engine. The engine has 2 variations of tumble, that are used in this thesis. Original tumble in the engine is

measured at 1.1 using an internal procedure. With an insert in the intake, the tumble can be increased up to 1.5. This engine with tumble 1.5 is used in a previous study [18].

2.2. DIAGNOSTICS

In this section, we will present the different experiment diagnostics that were employed to study FWI. First, we present the method of determining heat flux from surface temperature measurements. Then we present the particle image velocimetry (PIV) used to determine the velocity flow field and laser-induced fluorescence used to determine the flame front surface near the wall.

2.2.1. HEAT FLUX FROM SURFACE TEMPERATURE MEASUREMENT

Wall surface temperature is measured during the FWI (premixed or spray) using thin junction thermocouples to calculate the heat flux to the wall. This section provides details of this setup, the acquisition methodology for surface temperature measurement, and the postprocessing of these measurements to determine the wall heat flux.

2.2.1.1. Wall-TC assembly

Surface temperature measurements are carried out using a fast thermocouple (TC) manufactured by the Medtherm corporation (TCS244KUKU1567211340). The TC is a coaxial, K-type, thermocouple with a junction thickness of 1-10 µm and a response time of 1-10 µs (given by the manufacturer). These TC have been used before for surface temperature measurements in engines and CVC [4, 5]. The output of the TC is amplified using the AD624 amplifier, gain = 500, and filtering all measurements <10 kHz with an inbuilt filter. The final signal is collected using the Lecroy oscilloscope, sampled at 100 kHz. In an earlier study [46], a calibration was carried out to determine the response time of the complete surface temperature acquisition chain and it was found that the response time is 0.093 ± 0.006 ms. This response time is considered sufficient to characterize FWI, which has a characteristic time of 0.5-1 ms. This TC also consists

of a slow speed backside TC to record the temperature at a distance of 3.96 mm from the surface. In this thesis, we will only focus on the heat flux due to FWI which is the instantaneous heat flux derived from only the surface temperature.

The TC is embedded in the flat wall, designed to mimic the wall during FWI. Two designs of wall-TC are available for use in HPHT cell and one for the engine. Both wall-TC assemblies designed for HPHT cell are shown in Figure 53. Type 1 was previously used for surface temperature measurements during FWI [46]. The type 2 design was made to use multiple surface TCs (3 slots).

Both the wall-TC have provisions to move the wall axially, through hollow support and spacers (see Figure 53). These spacers come in different thicknesses, to reach a target distance from the spark plug or injector. In this thesis, the wall-TC is used in HOQ configuration only. The TC and surface of the wall are sealed along with the hollow support and face of HPHT cell. This results in minimum leakage from the surface of the flat wall (overall leakage of HPHT cell remains within the operating limits). This setup of CVC and wall TC assembly creates a closed CVC where combustion is carried out. Both walls have a passage on the backside of the assembly through the hollow support. This passage is open to the atmosphere, hence remains cooler than the body. The passage enables the TC wires to connect with the oscilloscope.

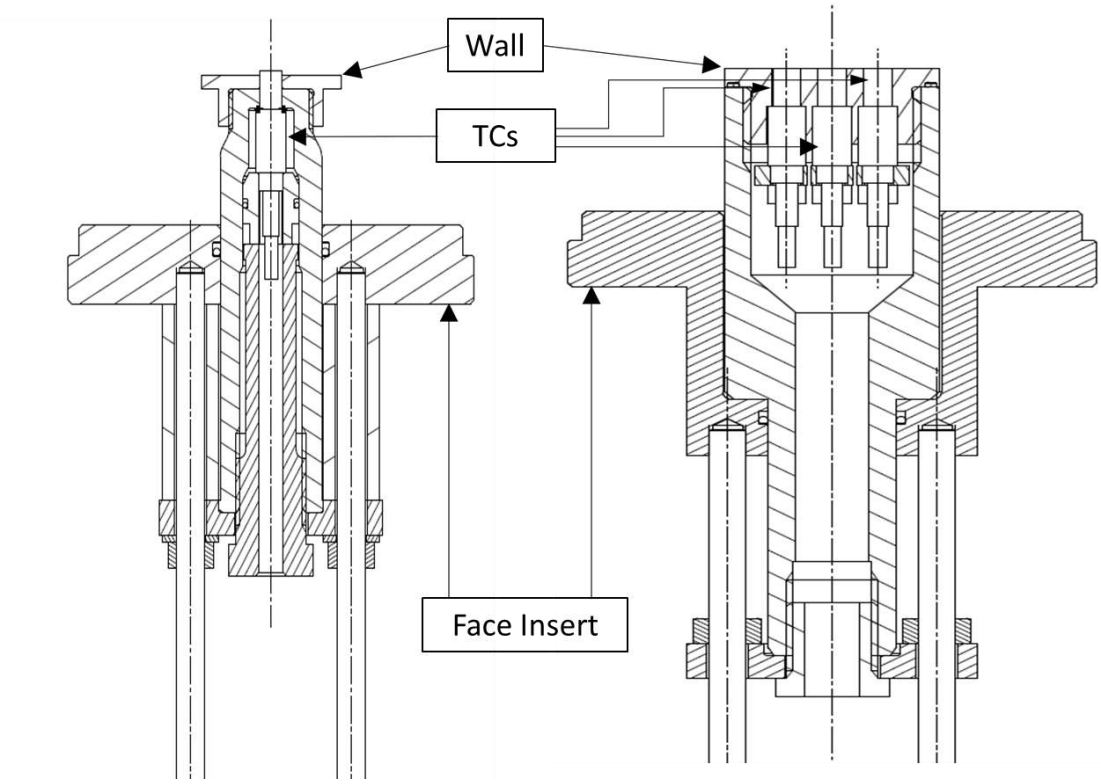

Figure 53 : Left: Old Wall-TC assembly (Type 1), Right: New Wall-TC assembly (Type 2)

In the engine, a wall-TC assembly is designed to measure the surface temperature on the cylinder wall. Figure 54 shows the TC-wall assembly used as an insert between the cylinder head and cylinder. The objective of this experiment is to measure the surface heat flux during FWI with the use of two different ignition systems i.e., prechamber and conventional spark ignition. The prechamber ignition system has a flame jet exiting the prechamber holes after the ignition inside the prechamber [18]. The TC position is such that the flame jet is geometrically normal to the TC, where we expect that jet influence will be significant. An alternative position of the TC is also available, in between two flame jets, where jet influence will be minimum.

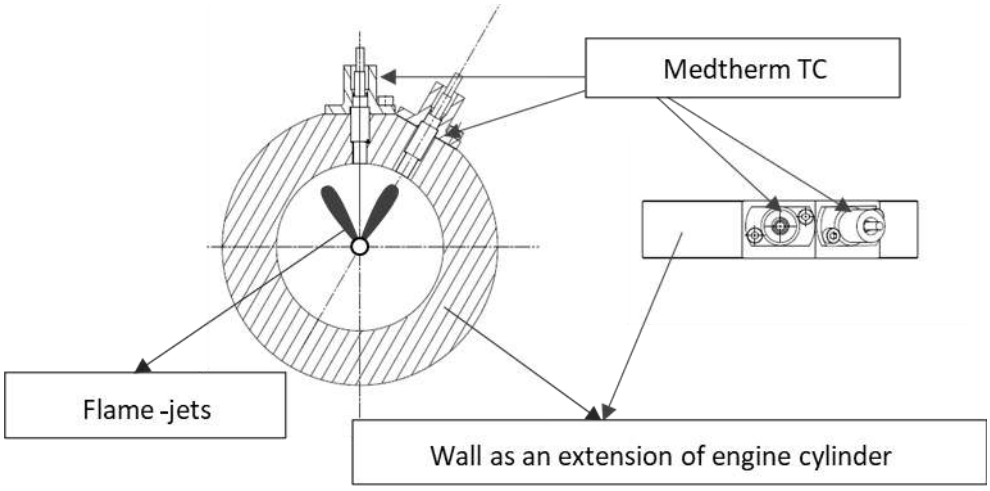

Figure 54: Wall-TC assembly for heat flux measurement in the engine

2.2.1.2. Calculation of Heat Flux from Surface Temperature

Instantaneous heat flux is calculated from the surface temperature measurement using the 1D semi-infinite model of heat conduction. The heat flux is given by the Duhamel integral. The derivation of the Duhamel integral is given in Chapter 16 of the cited book [82]. The Duhamel integral is numerically evaluated as per earlier works [52, 83]. This is shown in Equation 14. $\boldsymbol{Q}$ is the heat flux as a function of time, $\boldsymbol{t_j}$. $\boldsymbol{T_j}$ is the surface temperature as a function of time $\boldsymbol{t_j}$. $\boldsymbol{T_{j-1}}$ is the surface temperature at time $\boldsymbol{t_{j-1}}$. $\sqrt{\boldsymbol{k\rho C_p}}$ is the effusivity of the material of TC. Equation 14 is used in this thesis to compute the heat flux [46].

Equation 14: $$Q(t)= \frac{2\sqrt{k\rho C_p}}{\sqrt{\pi}} . \sum_{j=1}^{n} \frac{(T_j - T_{j-1})}{\sqrt{t_n - t_j} - \sqrt{t_n - t_{j-1}}}$$

The noise in the acquired temperature introduces complications in the calculation of surface heat flux. Such problems where one must go from $\boldsymbol{T}$(temperature) to $\boldsymbol{Q}$(heat flux) through $\boldsymbol{T_j - T_{j-1}}$(differential of temperature) is called an inverse problem. The noisy time derivation of temperature creates peaks in heat flux that is not real, hence making the problem ill-posed. In some studies, a median filter has been used to filter the noise [42, 51]. In other studies, Tikhonov regularization is used owing to its advantages of only keeping the relevant time derivative of temperature intact which otherwise would be affected by median

filters [37, 46]. In this thesis, Tikhonov regularization is used. The use of Tikhonov regularization is validated in literature [37]. The Tikhonov coefficients of 10 and 0.1 are used similar to the literature [46]. Variations in Tikhonov coefficients (±10%) yielded no change, so we have used Tikhonov coefficients as used in the literature. A sample representation of the noisy raw signal and the Tikhonov regularized signal is shown in Figure 55. From this point onwards Tikhonov regularized surface temperature will be used to refer to surface temperature. The corresponding computed heat flux is shown in Figure 56. In Figure 56 multiple peaks can be seen in the heat flux trace. The first peak corresponds to the time at which the flame reaches the wall, hence it is attributed to FWI. The peaks after the first peak are attributed to burnt gas-wall heat exchange. Burnt gas-wall interaction is separated from the FWI by a few ms. The focus of the current thesis will be on the first peak due to FWI.

Figure 57 presents a characteristic surface temperature trace along with the calculated heat flux. Different regions are identified in the heat flux trace. Overall, we can observe that the heat flux before FWI is negligible (Region 1) and when flame approaches the wall, a slow rise is observed (Region 2). This slow rise could be attributed to the compression of fresh gases by flame, leading to an increase in the temperature of the fresh gas. This slow rise is followed by FWI where high heat flux of the order of 1 MW/m^2, is observed (Region 3). Soon after the peak, the heat flux falls to an intermediate level higher than the initial level. This is due to the high temperature of burnt gas (Region 4). After region 4 we see fluctuations in the heat flux trace (Region 5) due to turbulence.

Post quenching the gas temperatures are high, which leads to high viscosity and thick BL [42]. The measurements from several researchers indicate that the first peak of heat flux trace always occurs after the peak pressure location. The time scale of fluctuations in heat flux trace (~5-20 ms after FWI) in region 5 indicates that the fluctuations will take place later in the combustion stroke when the pressure will be low. At low pressures, the amplitude of heat flux fluctuations (Region 5) is expected to dampen further

due to thick BL resulting from the combined effects of high-temperature gases and low pressures. Hence, we hypothesize that heat flux fluctuations will not play a major part in heat loss.

The FWI interaction does not always happen at the same point in time even though all the controllable parameters are kept the same. This could be due to the initial growth of turbulent flame and cycle to cycle variations. To draw meaningful statistics for an experiment condition (average and standard deviation), we have synchronized the heat flux trace based on the location of the peak of heat flux in time[46]. Figure 57 presents the result of this synchronization methodology for the two repetitions presented in Figure 56.

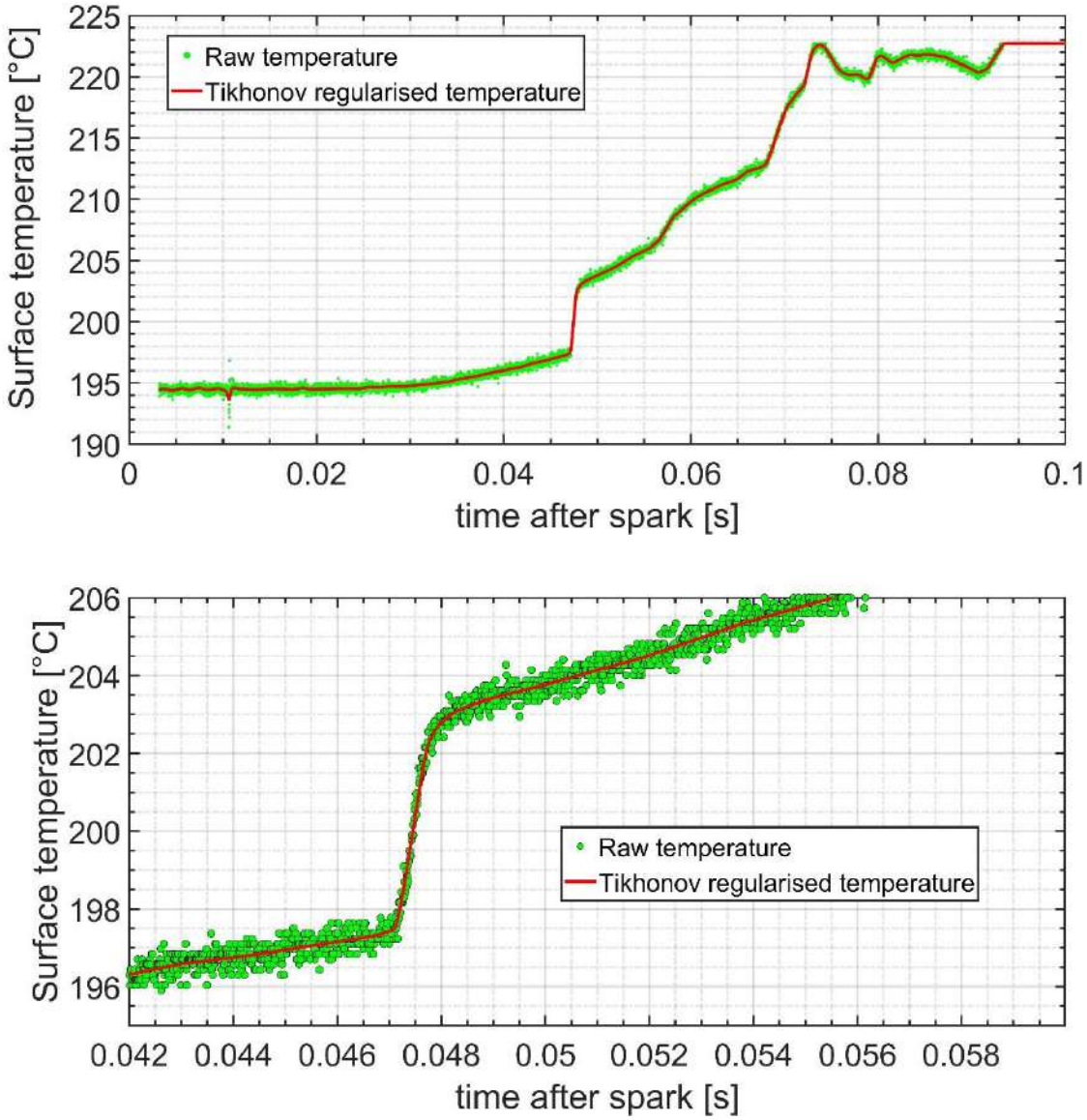

Figure 55: Comparison of raw and filtered temperature. Top: the comparison of raw and regularized temperature. Bottom: zoomed version of the comparison of raw and regularized temperature with a focus on noise in the raw temperature signal

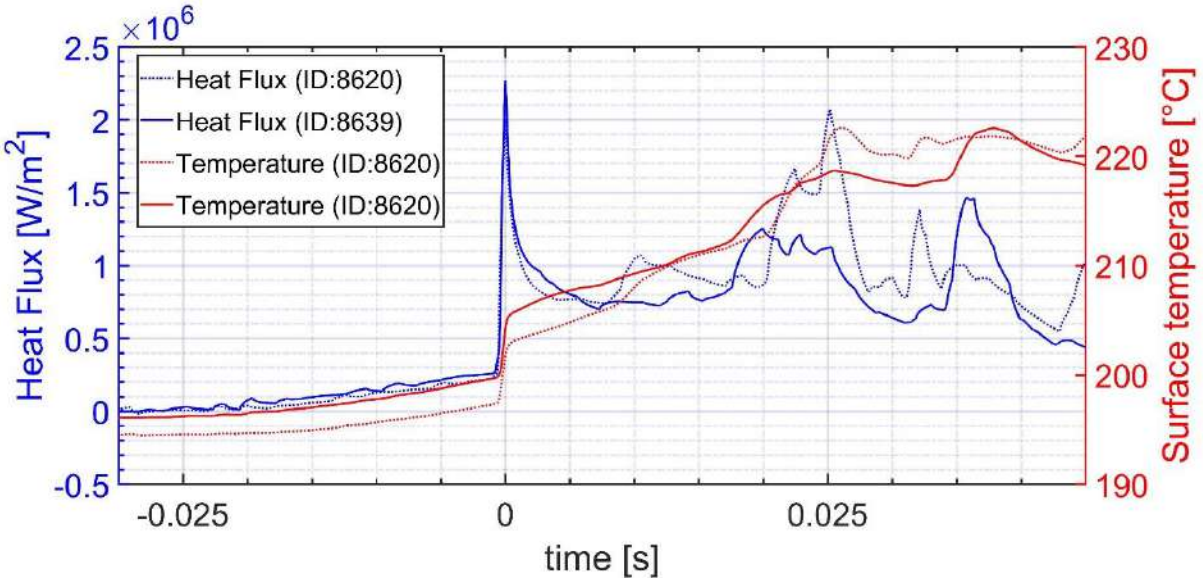

Figure 56: Calculated heat flux trace and the corresponding surface temperature trace for two tests in same conditions.

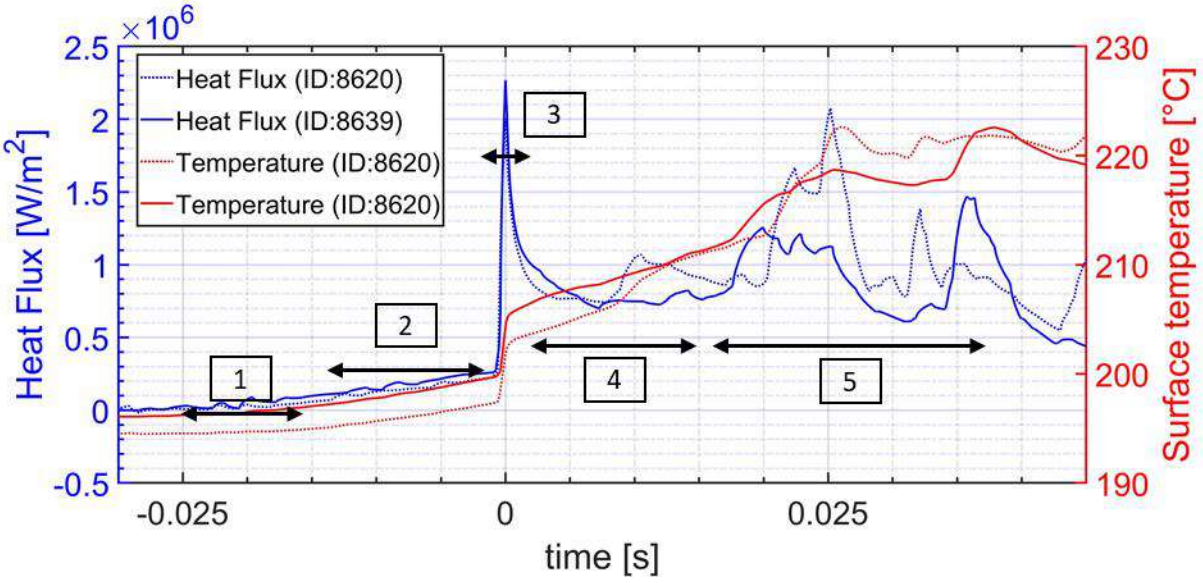

Figure 57: Heat flux and surface temperature trace synchronized with respect to the Q_P of FWI.

In the engine, the TC signal has an additional noise due to the signal for spark ignition. A raw voltage signal of TC in the engine is shown in Figure 58. The noise due to spark is captured in both the surface and backside TC, blue and red curves respectively. With a subtraction and adjustment of the two signals, this noise is removed. Further, the heat flux increase due to compression is also captured by this method.

Once the surface TC signal is corrected it can be used to compute the instantaneous heat flux due to FWI in the same way as in CVC. The heat flux and corresponding regularized temperature is shown in Figure 59. In this case, the heat flux has a sharp rise and fall corresponding to the beginning and end of the combustion stroke respectively. The different stages are also highlighted in Figure 59. Region 1 denotes the time where the heat flux is negligible. Region 2 shows the rising heat flux after compression of fresh gas by the piston and flame. The heat flux in this region is low, insignificant compared to the heat flux due to FWI. Region 3 shows the FWI which happens over a period of ~ 20 CAD (~ 2.7ms) where high heat flux ~ 1 MW/m^2 is observed. Region 4 denotes the burnt gas wall exchange region which in this case, has hardly any significant peaks. This is unlike the heat flux trace in CVC where multiple heat flux peaks are observed after the FWI. This is due to the evolution of pressure in the engine. In CVC the pressure is still high for several ms after the FWI. However, in the engine, the pressure falls due to the expansion of gases. Hence post-FWI, the heat flux trace in engines shows no peaks or severely reduced peaks.

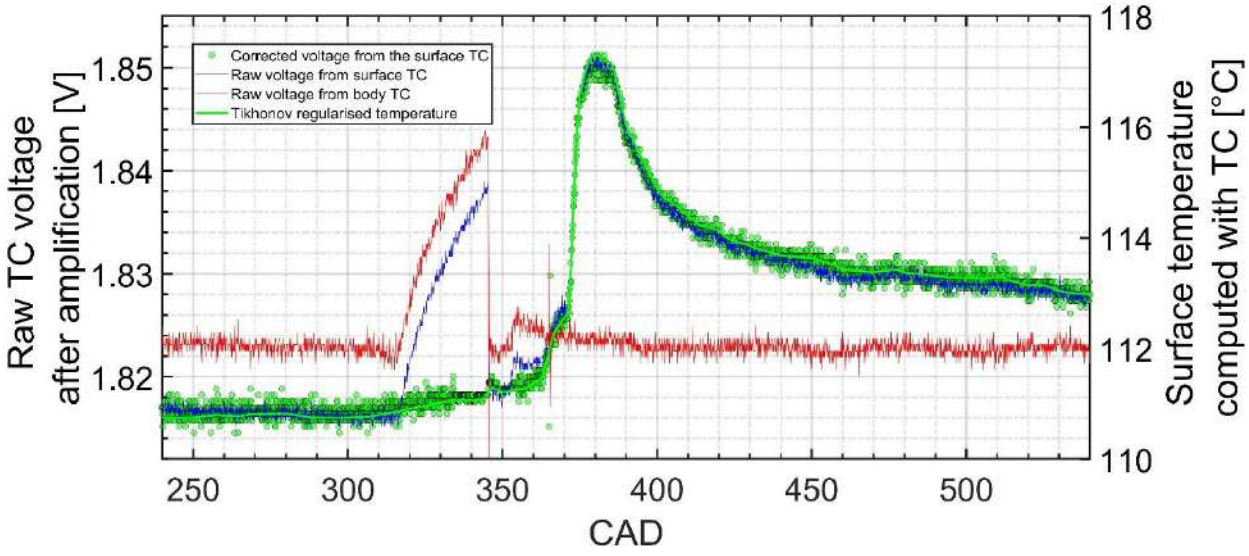

Figure 58: Raw voltage from surface TC, backside TC, the corrected signal, and the temperature

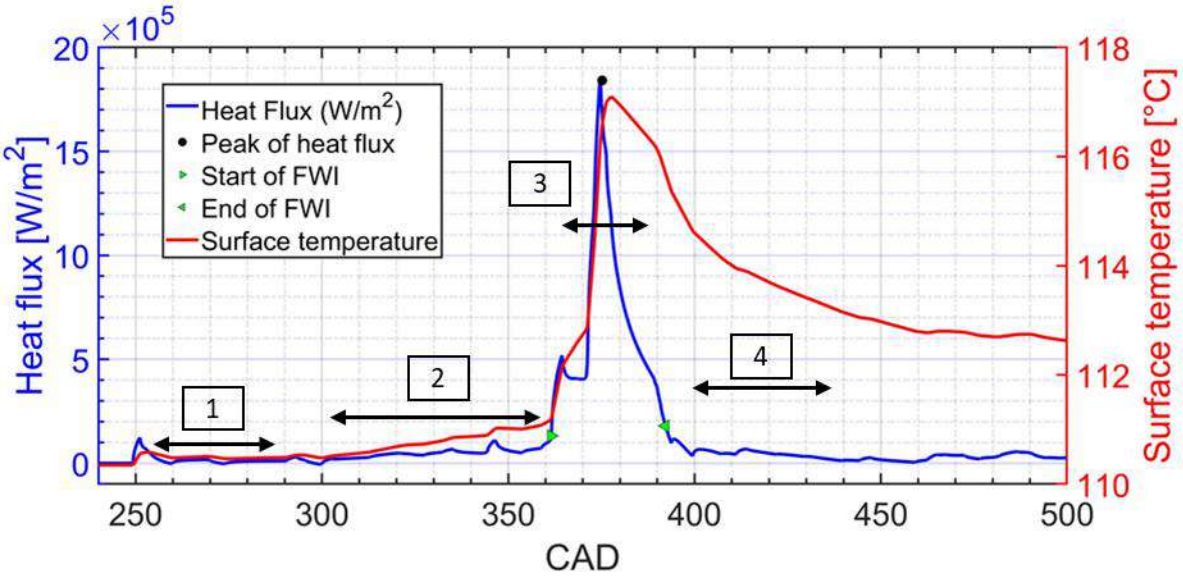

Figure 59: Sample heat flux trace calculated from surface temperature measurement in the engine

2.2.2. FLOW FIELD BY PARTICLE IMAGE VELOCIMETRY (PIV)

PIV is used to characterize the velocity field in this thesis. In a PIV setup, particles are suspended in a fluid flow. The suspended particles track the flow by moving along with the flow. The position of the particle at one instant of time is obtained, through the scattered image of the particles suspended in the flow. A laser sheet and a high-speed camera are used to obtain a 2D scattered image such that two or a series of two images of a known time interval are obtained. Using cross-correlation (with a suitable spatial window) of the two or sets of two images, the particle displacement can be obtained, which can be used to get particle velocity on the 2D field. More details of a PIV system can be found in [84, 85]. In this thesis, a 2D PIV is used to measure the gas velocity field near the wall-TC assembly. In this subsection, the design of PIV experiments along with the processing of raw PIV images into velocity field is discussed.

2.2.2.1. Experiment setup

Quantronix Hawk Duo laser is used to generate a laser sheet at a wavelength of 532 nm. Later it will be found that for a series of variations conducted in this thesis time delay of 0.1 ms is enough. Hence a single laser at 10 kHz is used to obtain a time series. The advantage of using a single pulse from the PIV

laser is the uniform power and the exact alignment of the laser sheet. A set of lenses and a slit of the thickness of 1 mm is used to get a laser sheet of thickness ~0.5 mm. A Photron SAZ camera is placed perpendicular to the laser sheet (exposure of 10 microseconds) to record the PIV signal. A 50 mm objective with a 14 mm ring with f2.8 is used in the setup. An optical filter is used at 532 (±4) nm to reduce noise from the flame. The whole camera setup is placed on a 3D micrometer screw to adjust the camera position. A schematic of the PIV setup and synchronization of the signals is provided in Figure 60.

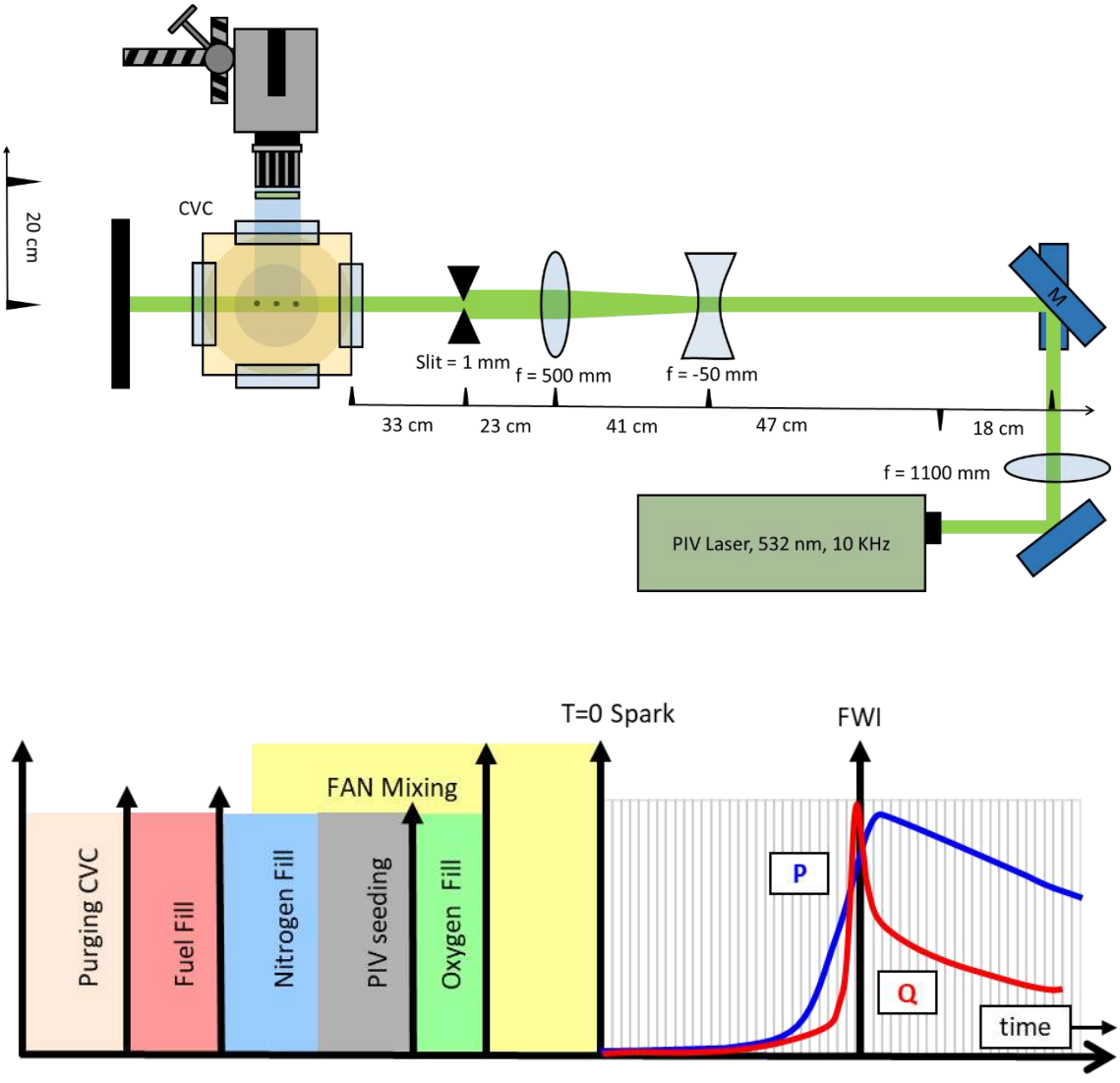

Figure 60: Schematic and synchronization for high-speed PIV

We are going to check if the PIV particles used in this thesis fall within the suitable range of PIV particle size for our experiment setup. The PIV particles move with the flow due to drag induced by the flow. The characteristic time of drag, t_p, of a particle is given by Equation 15, where ρ_p denotes the density of the particles, d_p denotes the diameter of the particle, μ denotes the viscosity of the flow and g denotes the acceleration due to gravity [42]. To trace the velocity of the flow effectively the particles used in PIV should have a low characteristic time of drag compared to the characteristic time of the turbulent flow. The ratio between the characteristic time of drag on the particle and that of the turbulent flow is called the stokes number (St). A low stokes number means the particles will react to the turbulent flow efficiently allowing us to trace the flow. We will calculate the range of stokes numbers later in this section.

We do not have information on the characteristics of the turbulent flow, prior to doing experiments. So, we will use estimates from the literature to obtain suitable PIV particle size. For experiments near the wall, the characteristic time for turbulent eddies (t_t for the largest and t_Δ for the smallest) can be estimated from the literature [42, 84]. The largest turbulent eddies length scale (L) is estimated at 1 mm (similar to the scale of clearance dimension at TDC in the engine) and the smallest scale (Δ) is estimated at 0.01 mm (from Kolmogorov scale estimates). Correspondingly the estimate of turbulent fluctuation intensity (u'_{RMS}) is ~1 m/s. The time scale for large eddies can be calculated by Equation 16. The time scale for small eddies can be estimated by Equation 17.

Equation 15: $$t_p = \frac{\rho_p {d_p}^2}{18\mu g}$$

Equation 16: $$t_t = \frac{L}{u'_{RMS}}$$

Equation 17: $$t_\Delta = t_t.(\frac{\Delta}{L})^{2/3}$$

Based on these guidelines stokes number can be calculated for particles of different densities and sizes. Solid PIV particles of density 800 Kg/m^3 and size 2 µm are used in this setup same as in literature [74, 75]. Small scales (estimated ~ 10 µm) are too small to be captured by PIV particles of size 1-2 µm,

considering the magnification in the PIV image. Hence, small-scale eddies are not resolved in this thesis. Figure 61 shows the evolution of stokes number for different turbulence intensities, large length scales, and average gas temperature. For the estimated large-scale eddies, ***St*** is <0.01 (***L***= 0.5 mm, $\boldsymbol{u'_{RMS}}$~1 m/s). Later in Chapter 3, it can be found that the range of turbulence is ~0-1.2 m/s and the range of length scales is (0-3 mm). For this range of length scales and turbulent intensity, ***St***<0.05 (the black box in Figure 61). Hence, the solid PIV particles used in these experiments are good enough to correctly represent the flow. The introduction of these particles is carried out by a motorized seeder system. This seeder is connected to the N_2 supply and HPHT cell so that N_2 passed through the seeder carries the suspended PIV particles.

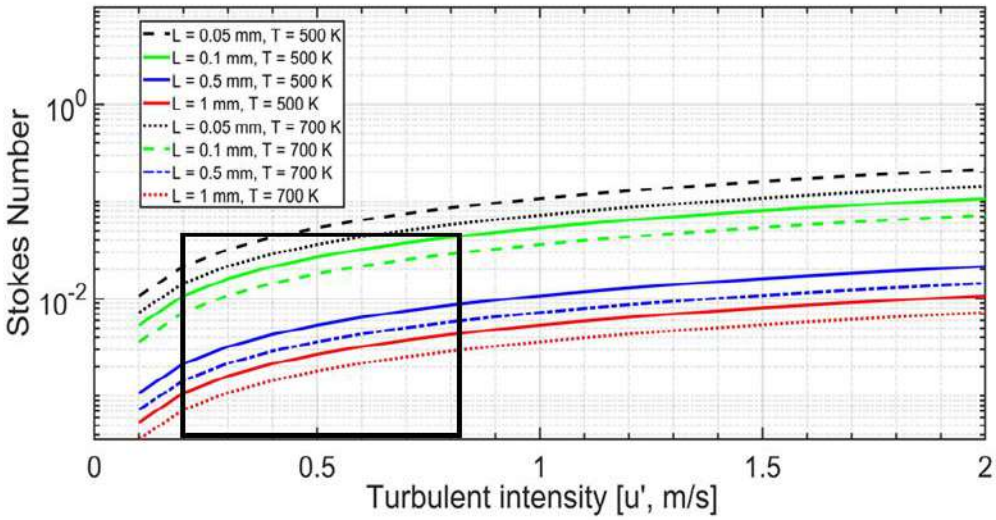

Figure 61: Stokes number for the PIV particles used in experiments

2.2.2.2. Instantaneous velocity field from PIV

PIV setup explained earlier, is used to obtain raw images of the laser scattered by PIV particles. Correlating two PIV images can yield velocity. A sample PIV raw image is shown in Figure 62. In this figure, we can see the three TCs, the surface of the wall, the limits of optical view, and the fan. The PIV image is composed of bright spots of particles that can be 1-9 pixels in diameter. There is a minor background reflection on the edge and center of the image. A MatLab scheme is developed to extract a relevant section of the raw PIV image. The advantage of this code is to remove unnecessary calculations on the

regions outside the laser sheet and optical view. This is advantageous to save time and clearly define the RoI. The resulting image is processed with Davis software (commercial postprocessing software of Lavision) to obtain velocity vectors. The set of operations carried out in Davis is provided in Annex 2.

After these operations, the raw image is converted to velocity vector over space and time i.e. $\vec{U}(x,y,t)$, shown in Figure 63. The Davis output files are then managed for post-processing and analysis through open-source PIVMAT MatLab codes [86]. Although velocity vectors are obtained, the accuracy of such vectors needs to be evaluated.

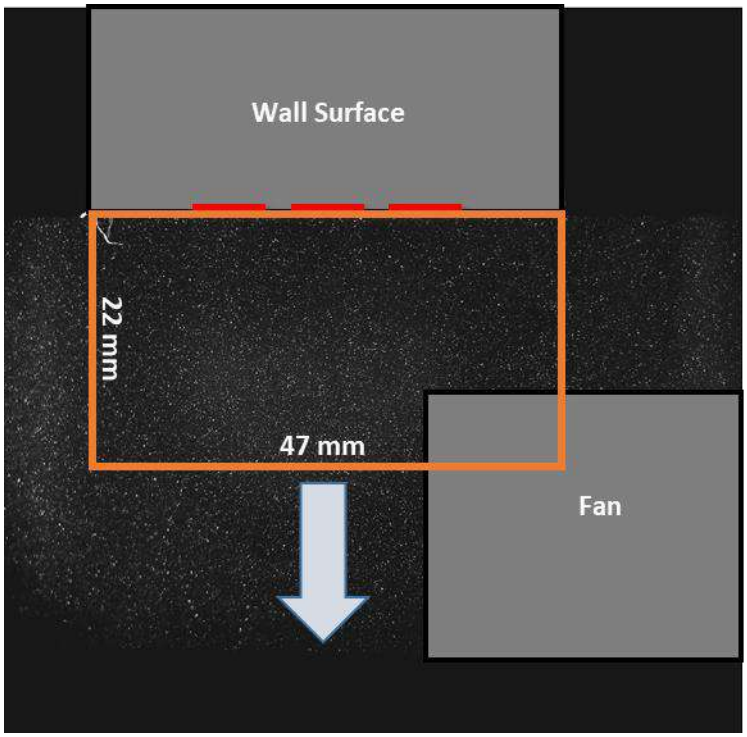

Figure 62: Sample PIV Raw image

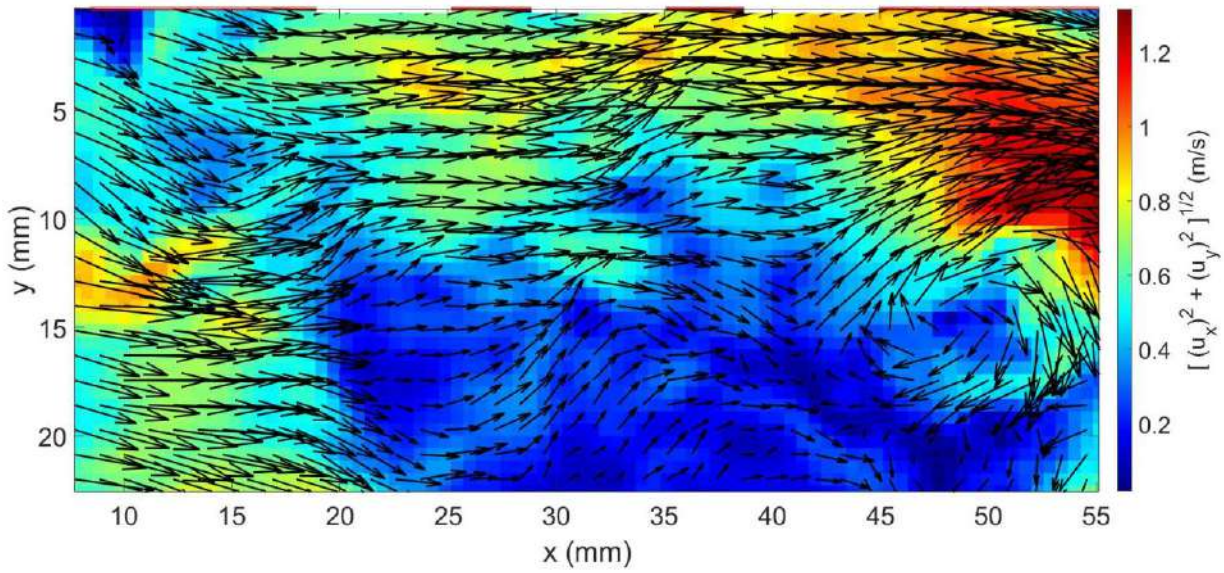

Figure 63: Sample velocity vector obtained from Davis

2.2.3. FLAME FRONT DETECTION BY LASER-INDUCED FLUORESCENCE (LIF)

Laser induced fluoroscence (LIF) is a method used to detect flame shape (wrinkling) near the wall. LIF tracks target species, called tracers (molecules are inserted in small quantities like acetone, SO_2 etc.) or target molecules produced in-situ during combustion (like OH, HCHO etc.) that can be used to detect flame front during combustion [56, 68, 87]. These molecules are excited by light energy sources of a certain wavelength, they absorb the light energy and move to a higher energy level from their ground state, a phenomenon called excitation. This excitation is immediately followed by spontaneous fluorescence emission when the molecule returns to its ground state. Different species have a different band of absorption and emission based on their energy levels. Typically, lasers at a specific wavelength (or band of wavelength) are used, as a light source targeting a specific tracer, hence the technique is called LIF (OH~283 nm, acetone at 266 nm, etc.). The emission signal(***S***) is proportional to species concentration (***c***), Quantum yield (***Qy***, which is characteristic of the molecule), the energy intensity of exciting laser (***I***), and the number density of the fluorescent atom(***n***), see Equation 18. More details can be found in [88].

Equation 18: $S \sim n.c.I.Qy$

This signal is generally used to determine species concentration. In our case, we have used acetone LIF to determine flame front location marked on one side by the presence of acetone and the other side by the absence of acetone. In the following section, the detailed experiment setup for LIF flame front tracking is discussed.

2.2.3.1. Experiment setup

In this study a high-speed frequency-doubled 355 nm Laser (GSI Mesa 355 40M, in KHz regimes) and 266 nm frequency quadrupled Laser at 10Hz (Quantaray PIV 400 series Nd: YAG) is used. High-speed Laser excitation provides an exciting opportunity to trace the evolution of flame front by LIF. Bi-acetyl (at 355 nm) and acetone (at 266 nm) are suitable tracers available to us at 355 nm and 266 nm [21, 56, 89, 90]. Upon a careful examination of the signal intensity, it was found that the LIF signal intensity count with acetone as a tracer is superior to the LIF signal of Biacetyl. Hence, Acetone is chosen to trace the flame front near the wall (0.05g/1.4litres). Details of the experimental setup are presented in Figure 64. Because of the variability of flame arrival at the wall, a PIV laser is used at 266 nm. This ensures there are two simultaneous flame front images for each shot, increasing the chances of capturing the flame close to the wall. However, the shot-to-shot variation in the flame arrival at the wall makes it difficult to keep a constant timing on the LIF. Hence the flame front images are not at same distance from the wall. The duration between the two lasers is 0.5 ms. The laser sheet has a thickness of <0.5 mm. A Photron high-speed camera with a high-speed intensifier at signal amplification of (700-900) is used at 2000 FPS is used to capture the two images. A zoomed-in view is provided with a screen resolution of 55 pixels per mm (determined using a calibrated target object) in a field of view of 1.8 cm X 1.8 cm.

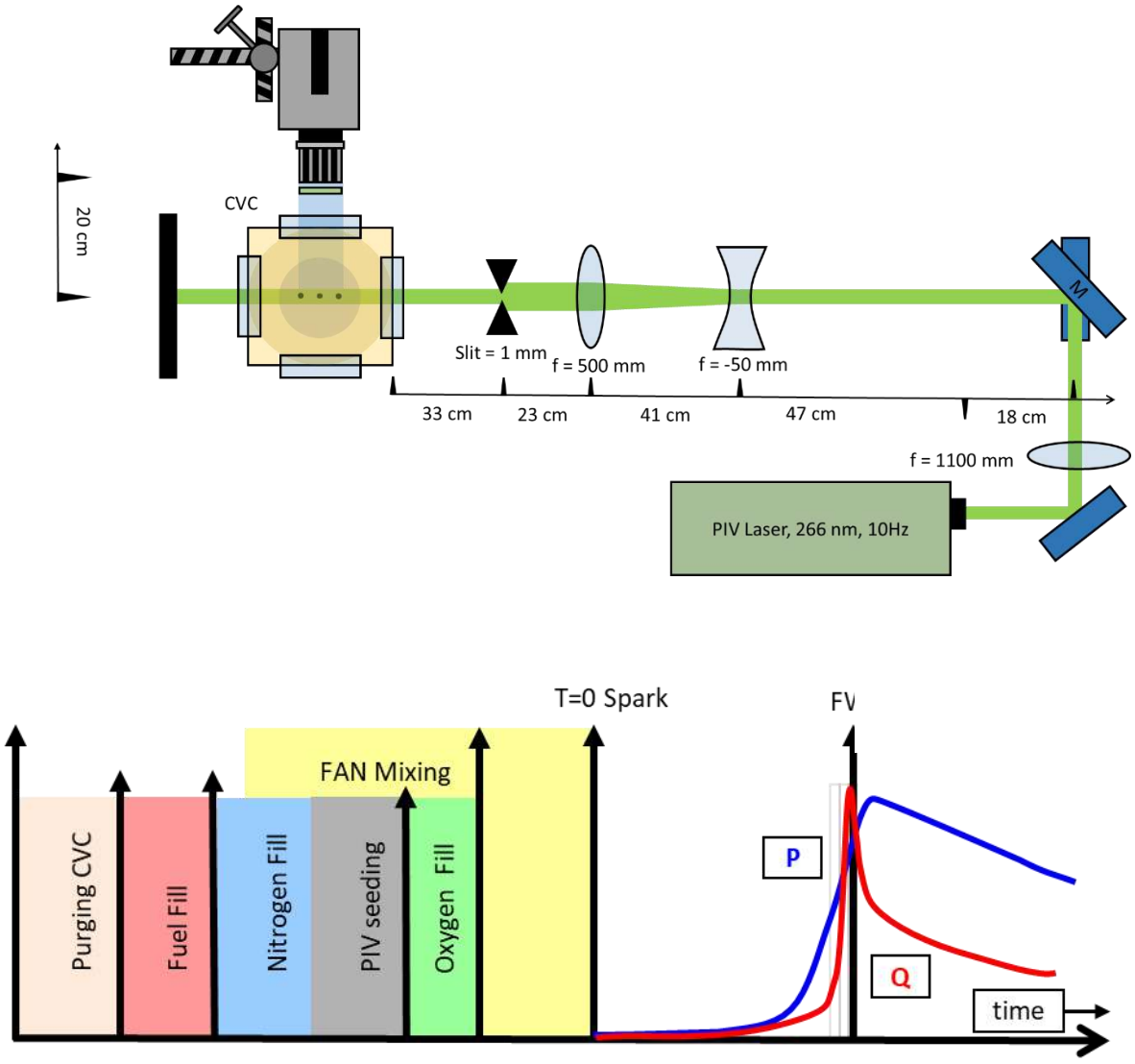

Figure 64: Schematic setup for Acetone LIF

2.2.3.2. Image processing to determine flame front wrinkling

The raw images with LIF signal (Figure 65, left image) enables us to detect the flame front edge by using image processing tools. The high magnification used in this experiment targeting the scales of FWI implies the usage of high gain. The LIF images then suffer from high noise due to high gain and flame luminosity. To detect the flame front, we need to binarize the LIF image. Further, the shot-to-shot variability in laser energy presents the challenge of determining a suitable threshold to binarize the LIF image. This means that a variable threshold method is applied to derive the flame front edges from the

LIF signal. The raw image (shown on left, Figure 65) is flat field corrected and then binarized using a suitable threshold. The binarized image then undergoes a morphological operation to remove edge errors. Then the processed image undergoes edge detection and connection. A sample image with edge detection is shown in Figure 65. This figure of the flame front is used to understand the experiment conditions qualitatively to identify laminar or turbulent flames before FWI.

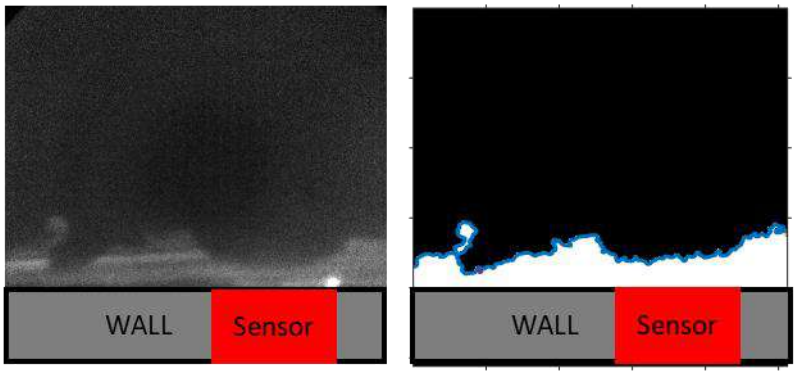

Figure 65: Sample image and edge detection. Bright portion is unburnt region and no signal is burnt region

Once the edge is detected near the wall, the flame front image can then be used to find the relative flame front wrinkling (***RFW***). This can be done by finding the length of the flame front and then dividing the length of the wall in RoI, see Equation 19. The turbulent flame will be wrinkled leading to the high length of the flame front and high ***RFW***. The laminar flame will be flat leading to a low length of the flame front and low ***RFW***. ***RFW*** can be used as a qualitative comparison of turbulence.

Equation 19: $$\mathrm{RFW} = \frac{\text{Length of the flame front}}{\text{Length of the wall in RoI}}$$

2.2.4. OH* IMAGING

The onset of combustion is always accompanied by the spontaneous production of excited OH molecules (OH*). OH* molecules emit light in a narrow band near 310 nm, which is called chemiluminescence. Hence several researchers detect OH* emission qualitatively to measure the lift-off-

length (***LoL***) in the spray conditions [47, 91–94]. In this thesis, a high-speed camera (Photron SA1) at 10KHz is used with 100 mm UV objective with 8 mm ring. High-speed hiCATT intensifier is used along with a band pass filter of 300-320 nm (Semrock, FF01-315/15) with 800 gain and 20 microseconds of gate width. A sample of the OH* emissions observed for ECN spray A is shown in Figure 66. In this figure, we can see the intensity of the OH*signifying reaction region during a spray A combustion. Notice the lack of signal close to the injector, attributed to a lack of chemical reaction close to the injector. The distance between the injector and the appearance of OH* is used as ***LoL***.

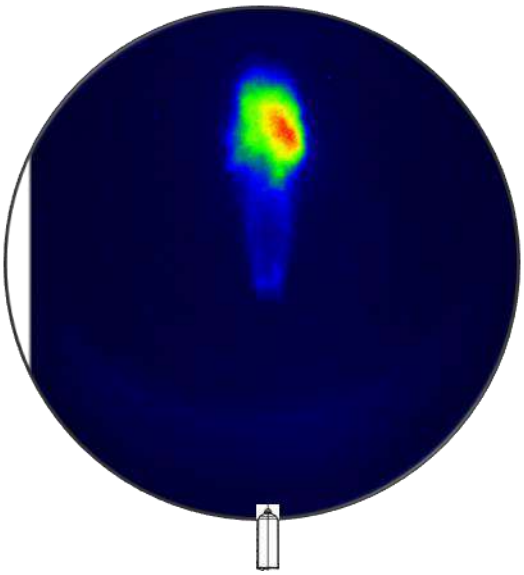

Figure 66: Sample OH* image from ECN spray A

2.3. POSTPROCESSING

In this section, we will present the numerical scheme to compute complimentary fresh gas properties which will be used for our analysis. Further, we also present the scheme to compute the heat flux from surface temperature measurements.

2.3.1. LAMINAR FLAME PROPERTIES USING 1D CANTERA CODES

When Flame wall interaction is studied, it is used to compare wall heat flux to the wall with laminar flame power. Hence 1D laminar flame characteristics must be determined. Knowing the initial pressure of the gas, the initial temperature of the gas, and the transient evolution of pressure we can determine the evolution of the temperature of the gas through the adiabatic relationship.

Using the pressure and temperature data, different properties of a laminar flame can be found from 1D Cantera calculations (freely propagating 1D flame). The FFCM-1 mechanism file is used as this mechanism is validated at higher pressure [95]. The initial conditions of the gas (composition, initial temperature, initial pressure) used in experiments are used to define the thermodynamic state of the gas. Then a 1D adiabatic flame is simulated to propagate in space where a grid of various initial pressure is used to determine the flame properties. At different instants, the flame properties are recorded as a function of the pressure of the fresh gas. A database of various properties is obtained through Cantera is shown in Table 3. Lewis number of air-fuel mixture is computed by a weighted average of different components [96]. Thermal flame thickness is calculated based on the method prescribed in chapter 2 of the book [17].

Table 3: Flame properties calculated from Cantera

The output of 1D flame propagation in Cantera			
1.	Pressure (bars)	2.	Flame Power (W/m^2)
3.	Fresh gas density (Kg/m^3)	4.	Lewis number of fuel-air mixture
5.	Fresh gas temperature (K)	6.	Adiabatic flame temperature (K)
7.	Flame speed (m/s)	8.	Specific heat capacity of fresh gas (J/KgK)
9.	Thermal flame thickness (m)	10.	The conductivity of fresh gas (W/mK)
11.	The characteristic time of flame (s)		

Using this table of properties, the flame property can be obtained based on the measured pressure in the experiments at the instant of quenching. These properties can then be used for the analysis of the heat flux measurements during FWI with parametric variations.

2.3.2. POST-PROCESSING OF HEAT FLUX TRACE

In this section, the heat flux trace is analyzed to extract the important properties of the heat flux trace that will be utilized for the comparative study of various parameters.

2.3.2.1. Heat flux trace premixed FWI in CVC

To explain the post-processing of the heat flux trace and PIV data we will use a few experiments. The notations and details of these experiments are presented in Table 4. In this table the distance between the spark plug to the TC in the wall-TC assembly is X_D.

Table 4: Experiments and notations used for postprocessing

Reference composition (Methane-Air, equivalence ratio=0.8, density = 10 Kg/m^3)					
X_D (mm)	Fan type	Number of Fans	Fan speed RPM	Fan operation	Notation
60	1	1	3000	OFF 60s before the spark	LT-60
60	1	1	3000	ON always	Reference
60	2	2	4000	ON always	HT2-60
60	2	3	4000	ON always	HT3-60

In this section, we will identify and derive the important properties of a heat flux trace. Heat flux traces can be described using three main characteristics: the maximum of heat flux (Q_P), the duration of

FWI ($\boldsymbol{\Delta t}$), and the average heating rate($\boldsymbol{Q_{HR}}$). Based on the variation of $\boldsymbol{Q_P}$ we will also find out the number of repetitions necessary for convergence.

$\boldsymbol{Q_P}$ is the maximum heat flux that occurs during the FWI. In most of the experiments carried out in this thesis, it's the first peak in the heat flux trace, in the order of 1 MW/m^2 or more. This peak is well separated from other peaks (by a few ms) in time, due to burnt gas-wall exchange. For more details see section 2.2.1.2. In a few cases, instead of one prominent first peak, there is a group of multiple heat flux peaks close to each other (< 1 ms of separation in time). Two examples of deformed heat flux are shown in Figure 67. In such cases, the highest peak in the group of closely spaced peaks is chosen as $\boldsymbol{Q_P}$ during FWI.

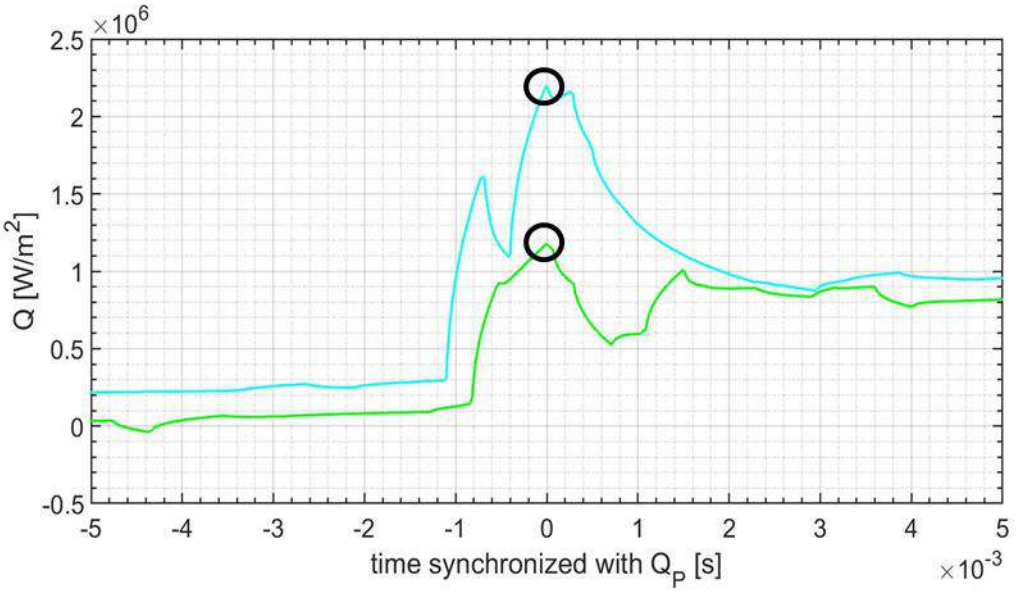

Figure 67: Examples of deformed heat flux trace, with highlighted $\boldsymbol{Q_P}$

To find the average we need to know the sufficient number of repetitions necessary for convergence of $\boldsymbol{Q_P}$. The evolution of $\boldsymbol{Q_P}$ for different repetitions of Reference case is studied. Figure 68 shows the evolution of the mean and standard deviation of $\boldsymbol{Q_P}$ with several repetitions for the Reference case (Table 4). The mean of $\boldsymbol{Q_P}$ is relatively flat with <10 % variation on the mean for any number of experiments. The

standard deviation of Q_P of experiments stabilizes at ~12 experiments. We can see that from the 12th experiment onwards the standard deviation achieves convergence, varying within 5%. Hence, the number of repetitions necessary for one set of experiments to achieve convergence in Q_P is set at 15 (>12).

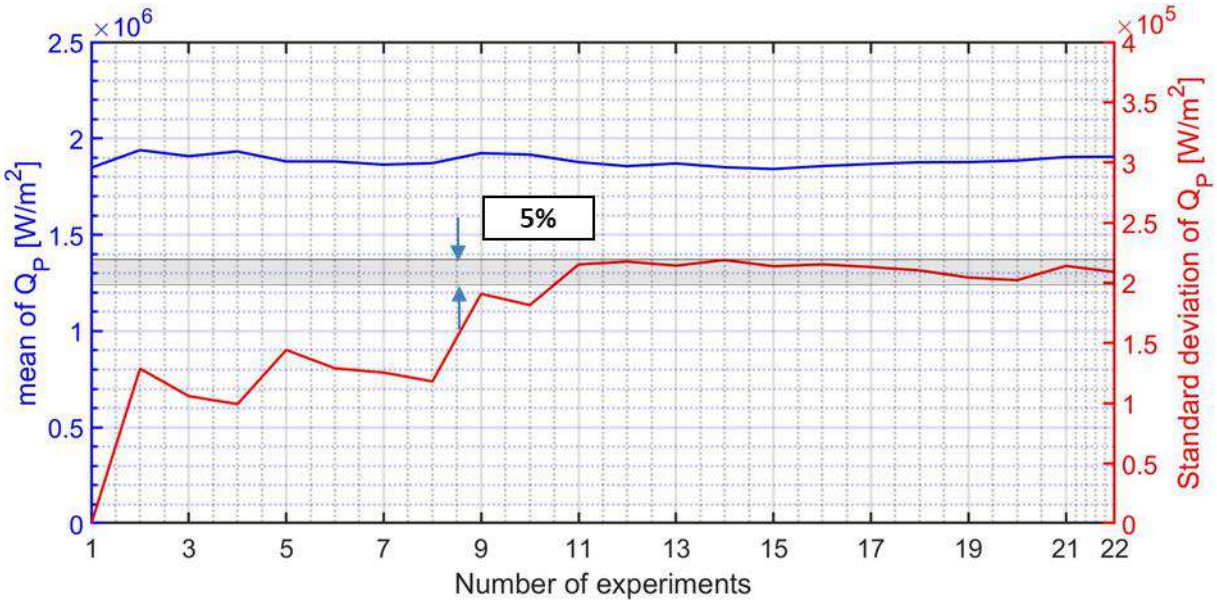

Figure 68: Number of repetitions necessary to achieve convergence in the average peak of heat flux (Reference case)

After the synchronization of the heat flux trace of all repetitions with Q_P, the mean and standard deviation of the heat flux trace can be calculated with 15 or more repetitions. Figure 69 shows the average heat flux for one experiment which has 15 repetitions.

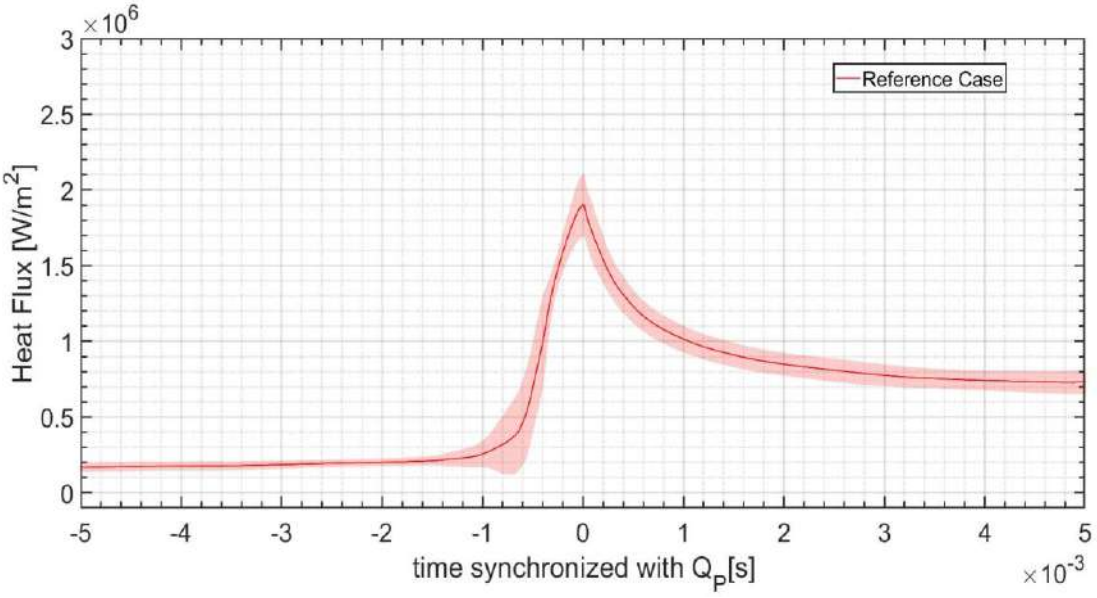

Figure 69: Average and standard deviation of heat flux trace for a set of repetitions for one experiment (Reference case)

The duration of FWI, noted Δt, is the sum of rise time (Δt_r) and fall time (Δt_f). We will define $\Delta t_r(X)$, as the time taken by the heat flux trace to rise from X% of Q_P to Q_P. It is important to come to a fixed value of X to define Δt_r that can be applied to all experiments. A criterion is found by studying the standard deviation of Δt_r for X = 1% to 100%. Figure 70 shows the evolution of the standard deviation of Δt_r, in blue curves, for reference and LT-60 cases. When X is too small, it leads to a small value for X% of Q_P, which lies in the noise of the heat flux trace prior to FWI. We can see that the blue curve in Figure 70 consists of largely 2 slopes shown by dotted lines. The first slope is due to X being too small. We want to choose a value of X such that X% of Q_P is larger than the noise. Hence the point at which the first slope ends determines the optimum X that can be used for the determination of Δt_r. For Δt_f the noise is due to post FWI heat flux due to burnt gas wall heat exchange. Similar to Δt_r, Δt_f is calculated. We have carried out this analysis for Reference and LT-60 cases to determine X. The resulting value of X is fixed for all other experiments. Using this analysis, a choice is made for the rise time (Δt_r), which is the duration of the heat flux to rise from 20 % of Q_P to Q_P. Similarly, the choice for fall times (Δt_f) is made, which is the duration for the heat flux to fall from its peak, i.e., Q_P to 70 % of Q_P. The total duration of FWI (Δt) is the sum of the

rise time and the fall time. The computed ***Δt*** still needs subjective evaluation due to special heat flux traces with extremely low Q_P which tends to select ***X*** such that ***X***% of Q_P lies in the noise. Such problems in determining ***X*** in experiments with significantly different Q_P lead to a subjective interpretation of the comparison of ***Δt***.

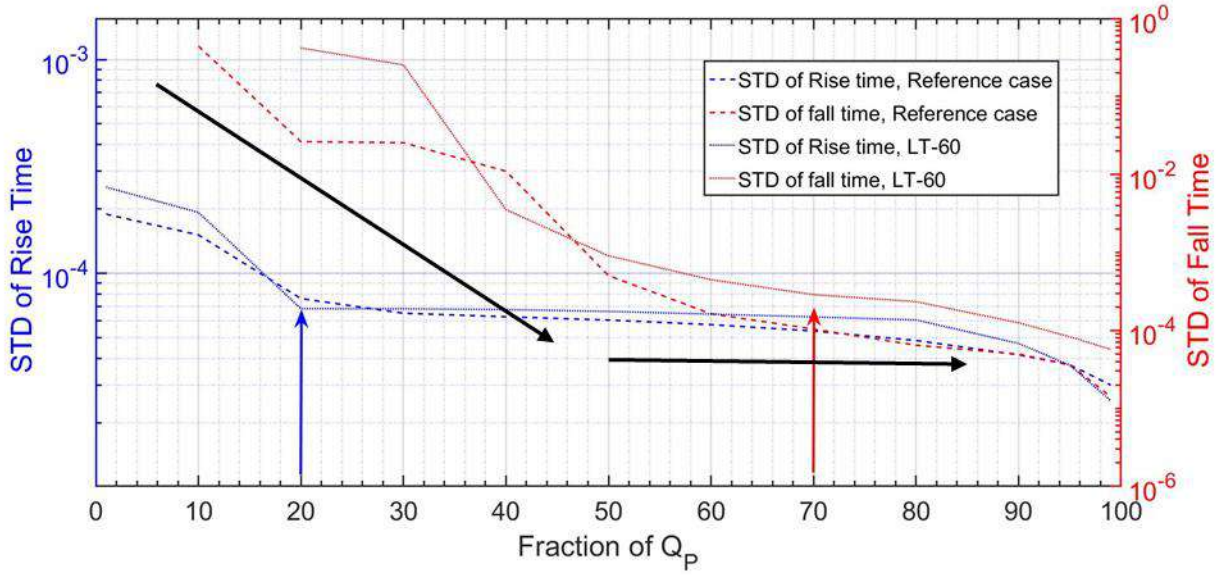

Figure 70: Standard deviation of the heat flux trace, used to choose the criterion for calculating the rise and the fall times

The purpose of obtaining Q_P and ***Δt*** is to evaluate the integrated heat loss. The heat flux trace can be integrated with this duration of FWI to obtain the integrated heat loss. The subjective interpretation of ***Δt*** translates into a subjective interpretation of integrated heat flux. A work around the problem is to find an integrated quantity, is to obtain average heating rate (Q_{HR}). By dividing the integrated heat flux with ***Δt*** we will obtain Q_{HR} (shown in Equation 20). The experiments with low Q_P where the starting point lies in the noise will compensate for the long ***Δt***.

Equation 20 :
$$Q_{HR} = \frac{\int_{\Delta t_r}^{\Delta t_f} Q}{\Delta t}$$

A comparison of Q_{HR} and Q_P is carried out to check if one of the parameters is redundant. For this purpose, different conditions are tested, and the corresponding Q_P and Q_{HR} are compared and shown in

Figure 71 where both Q_P and Q_{HR} follow the same trend. This comparison shows that irrespective of the conditions either Q_P or Q_{HR} can be representative of the heat loss during FWI. As Q_P is convenient to derive, Q_P will be used as a measure to compare the different experiments. Note that Δt is also redundant as Δt is also used to obtain Q_{HR}. Overall, the important characteristic of the heat flux trace is Q_P. A heat flux trace and its corresponding important property, Q_P is shown in Figure 72.

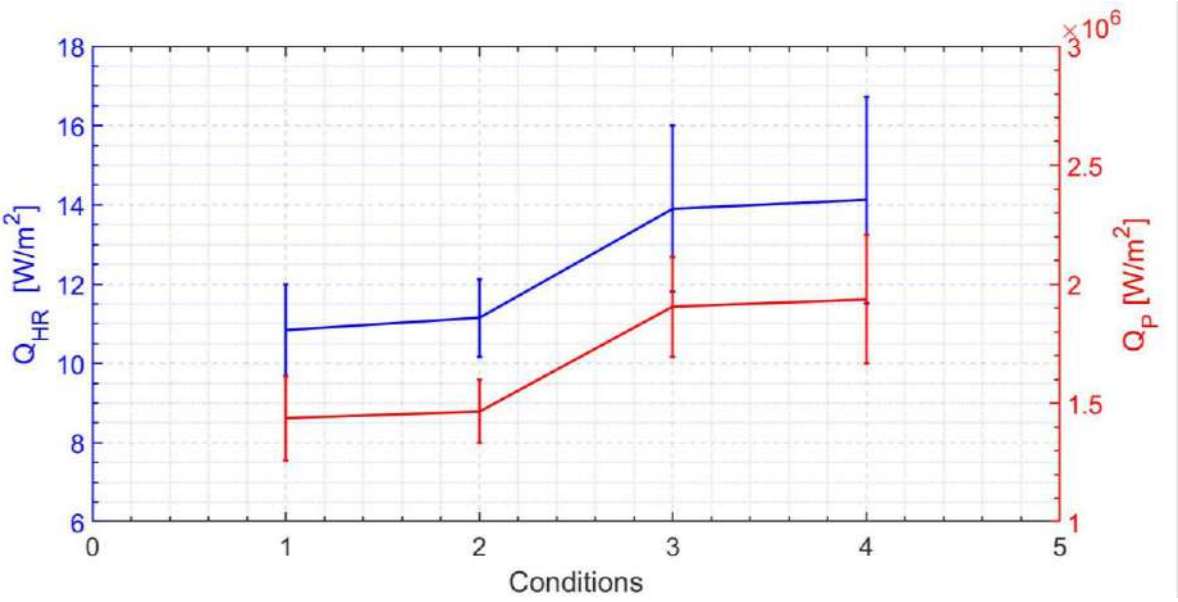

Figure 71: Comparison of Q_{HR}, and Q_P. Condition 1: LT-60, Condition 2: 1 LT-60 with X_D = 75 mm, Condition 3: Reference, Condition 4: HT2-60 with 1 Fan

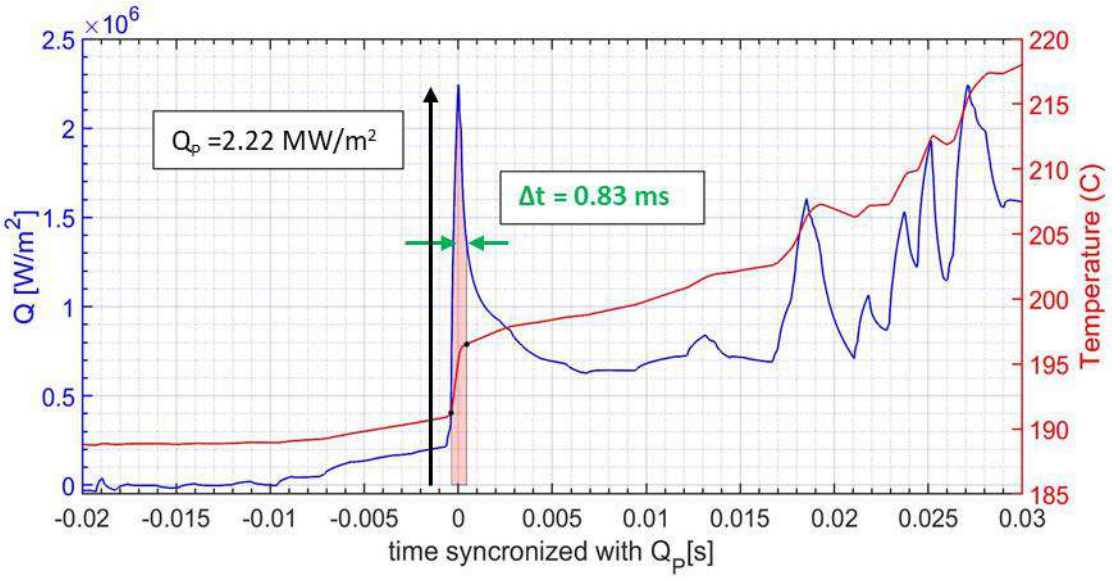

Figure 72: Illustration of a sample heat flux trace with important characteristics (***Δt*** and Q_P during FWI)

Heat flux fluctuations after the FWI can be correlated with the turbulence scale existing near the wall. To determine the characteristics of heat flux fluctuations in the burnt gas, the heat flux trace post flame wall interaction can be analyzed in Fourier space. In this section, we will define the method to calculate high-frequency heat flux fluctuations from the heat flux trace for Fourier analysis. Fluctuations in the heat flux trace are seen in region 5 of the heat flux trace (different regions are explained in section 2.2.1.2). The high-frequency heat flux trace is obtained by subtracting the moving mean on the instantaneous heat flux trace over 10 ms (shown in Equation 21 where ***Q***(t) is the heat flux trace) from the instantaneous heat flux trace. The high-frequency heat flux so obtained is then analyzed in Fourier space to find an approximate time scale of the turbulent fluctuations near the wall after the FWI. An example of PSD distribution of individual repetitions for the Reference case is shown in Figure 73. We can see from this example that there exists a global peak around 1000 Hz.

Equation 21: $Q_{HF}(t)=Q(t)-\text{moving mean}\,(Q(t), \text{window} = 10\ \text{ms})$

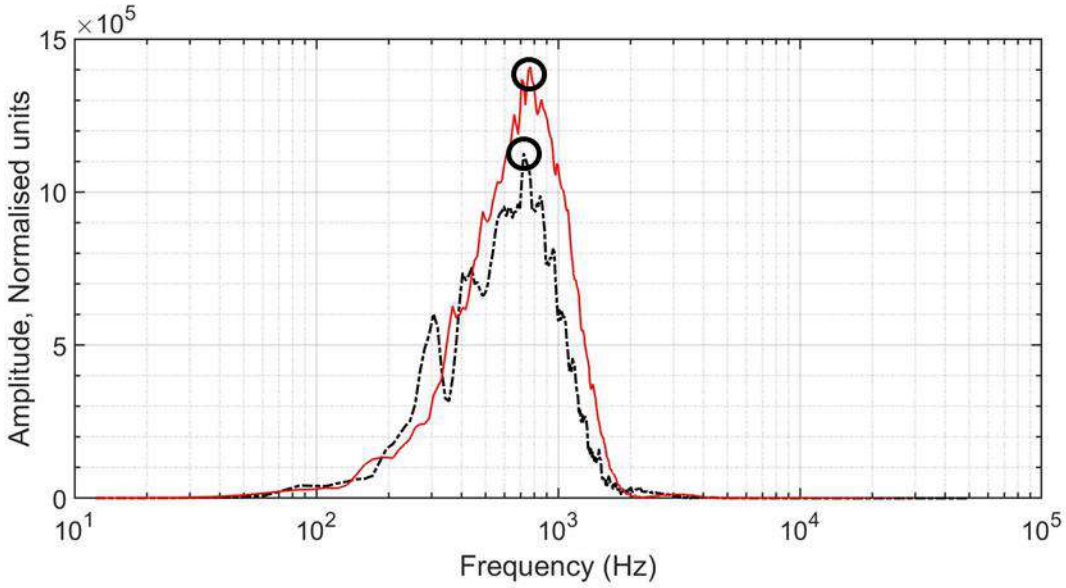

Figure 73: PSD spectrum of Q_{HF} for one repetition of Reference case

2.3.2.2. Heat flux trace-spray FWI in CVC

The heat flux is calculated from the surface temperature as is given in Chapter 2. The heat flux trace is synchronized at the first peak of heat flux (Q_P). The heat flux trace is very repetitive between the different repetitions of an experiment (standard deviation of Q_P<10% of its value for all experiments). To understand the differences between the heat flux trace of spray FWI and propagative FWI, a sample heat flux trace for spray FWI is given in Figure 74. Unlike propagative FWI, the spray FWI does not have a distinct peak but a plateau-like square signal. Though the duration of this plateau may differ from one experiment condition to the other. The duration of the plateau matches the duration of the combustion (as in [45]). The important property of the spray FWI is the magnitude of the plateau of the heat flux trace which is synonymous with the peak in propagative FWI. In this thesis, the average of the plateau of the heat flux peak can be used for comparison as well, shown in the green arrow. In that case, it will be mentioned explicitly.

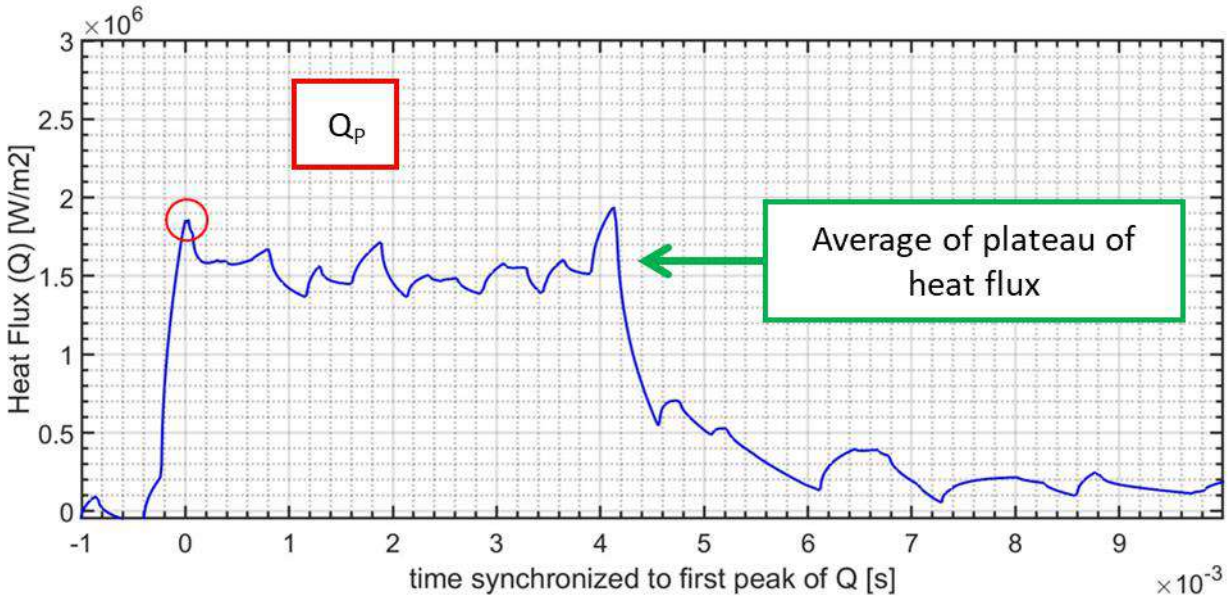

Figure 74: Sample heat flux trace for spray FWI

2.3.2.3. Heat flux trace premixed FWI in engines

In this section, we will discuss the processing of the surface temperature measured from TC in the engine leading to the important property of the heat flux trace, similar to Chapter 2. The rate of acquisition in the optical engine is 72kHz, different from the rate of acquisition in CVC (100 kHz). This rate of acquisition is related to the engine speed (1200 RPM) at which measurements are carried out. The surface temperature measurement is carried out in synchronization with crank angle degrees. Data is acquired from the engine in sets of 200 repetitions. Typically, we measure $\boldsymbol{Q_P}$ of the order of 1 MW/m^2. However, in others, we measure $\boldsymbol{Q_P}$ of the order of 0.1 MW/m^2. At this point, we don't know why such a discrepancy is observed. However, looking at the TC signal it is clear that TC recording is physical. We hypothesize that sometimes, FWI does not occur at TC. Further studies are needed for validating this hypothesis. For our analysis, we choose a cutoff at 0.8 MW/m^2, which separated FWI and no FWI. All the results presented in this thesis comprise cycles where $\boldsymbol{Q_P}$>0.8 MW/m^2.

A sample heat flux trace computed is given in Figure 75. Like in the CVC, $\boldsymbol{Q_P}$ is an important property of the heat flux trace. It seems that burnt gas wall exchanges are significantly reduced in their

peak values and occur towards the end of the combustion stroke (430-500 CAD). The peak and subsequent decrease in the heat flux trace resemble the heat flux trace in CVC, only this time, in engines, it is affected by decreasing pressure trace. Unlike in CVC, the pressure trace is somewhat constrained by the engine so we can directly compare the integrated heat loss (Q_{integ}). Both Q_P and Q_{integ} are shown and explained in Figure 76. It is well known that both Q_P and Q_{integ} are linearly related [42, 97]. To compute Q_{integ} we use the duration from the start of ignition to the end of combustion stroke TDC (360 -540CAD). A similar relation is also found in our experiments, shown in Figure 77. In Figure 77 we see that the overall trend of Q_{integ} as a function of Q_P is linear. For our purpose, the important characteristic of the heat flux is identified as Q_P.

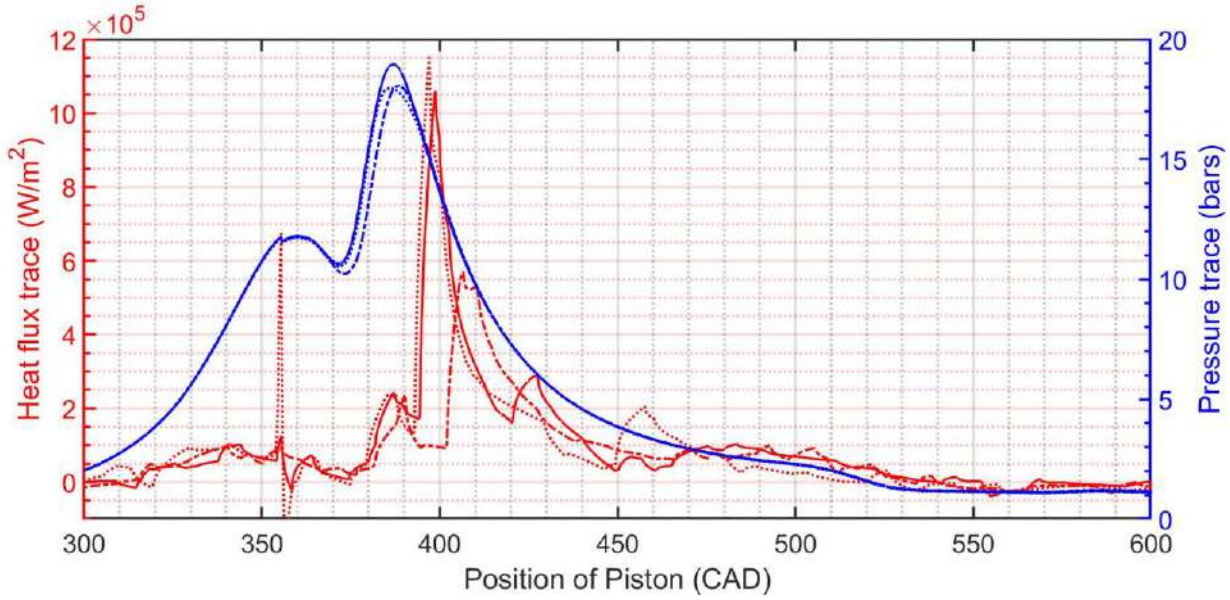

Figure 75: Sample heat flux trace measured in the engine, ignition at 355 CAD

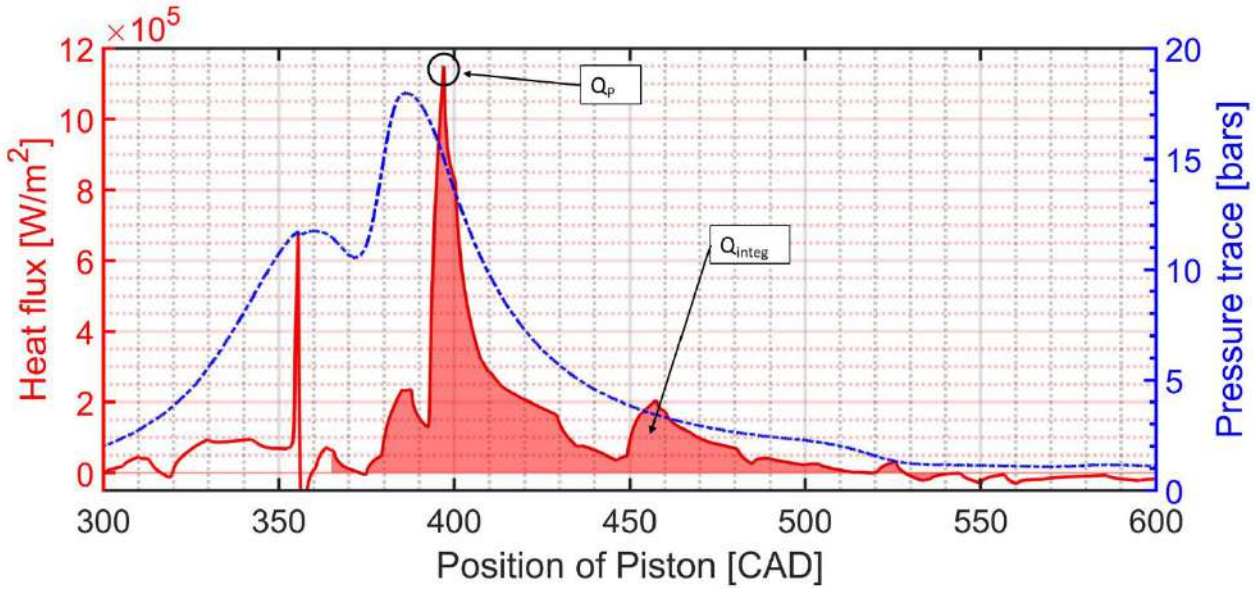

Figure 76: Important properties of the heat flux trace in engine

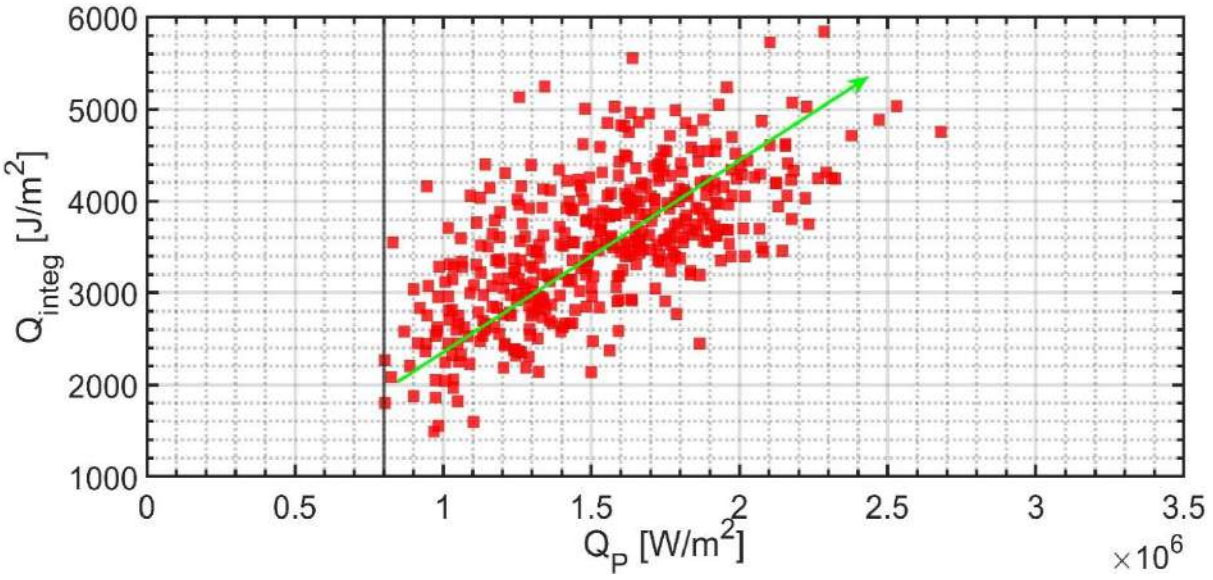

Figure 77: Correlation between Q_P and integrated Q_{integ} over full cycle (ignition at 345 CAD– 540 CAD) during combustion stroke for one experiment.

2.4. POST-PROCESSING OF PIV VELOCITY FIELD

In this section, we will present the post-processing of the velocity field derived from the PIV experiments to introduce the required mask and reduce the noise in the PIV field.

2.4.1. IMPROVING THE ACCURACY OF PIV RESULTS

Continuing with $\vec{U}(x,y,t)$ derived from the PIV calculations, in this section, we will present the method to evaluate and improve the accuracy of $\vec{U}(x,y,t)$ wherever possible.

Evaluating the accuracy of $\vec{U}(x,y,t)$ is complicated, beyond the scope of this thesis. However, particle density, out-of-plane velocity, and average displacement can be checked as per recommendations based on literature [98]. Particle density is checked for one case (as per the sample shown in Figure 62). With an evaluation by sampling, the particle density in different experiments in this thesis is found ~12 particles per interrogation window of 64×64 pixels. Some variation is expected from one experiment to another. The particle density also suffers near the wall. The spatial resolution of the current experiment, i.e. the distance between 2 vectors is ~ 0.5 mm which is lower than typical high-resolution near-wall experiments in literature (~ 0.04-0.1 mm in [84, 99]). This ensures that low particle density near the wall is not a major concern. Accurate estimation of out-of-plane velocity components is not possible. However, by tracking a single particle from its emergence on the PIV image till it vanishes from the PIV sheet, an estimate of the average third component velocity could be made. Using information that the laser sheet thickness is 0.5 mm, it is estimated that the third component displacement is <0.25 times the laser sheet thickness. The average displacement for time delay of 0.1ms is <0.25 of the interrogation window size (<16 Pixels). Hence, we conclude that the PIV particle density, out-of-plane velocity, and average displacement are as per recommendations in the literature.

PIV field can be affected by the peak locking effect [100], which induces bias towards integral displacement in pixels. In this paragraph, we will evaluate the degree of peak locking observed in the experiments carried out in this thesis. In this thesis, turbulent fluctuations are an important parameter that will be derived from the PIV. Turbulent fluctuations are severely affected by peak locking [101]. Hence the degree of peak locking must be evaluated and minimized. The evaluation of the degree of peak locking

(***C***) is based on the histogram distribution of the fractional part of displacement computed from two PIV images. To evaluate ***C***, first, the displacement is decomposed into integral and fractional parts. Equation 22 shows the decomposition of velocity into fractional and integral parts. In Equation 22, the $|\boldsymbol{x}|$ operator yields the highest integer (***I***) such that $\boldsymbol{I}<\boldsymbol{x}$. The distribution of fractional parts is approximated by a normal distribution. A high degree of pixel locking will have a prominent peak at zero indicating a strong bias of displacement to integer values. A low degree of pixel locking will have a flat distribution indicating no bias to integer values. Once the distribution of the fractional part of velocity is found, ***C*** can be evaluated by Equation 23. To evaluate ***C*** in our experiments, the zero vectors in both dimensions ($\boldsymbol{X_x(x,y,t)}$=0, $\boldsymbol{X_y}(\boldsymbol{x,y,t})$=0), induced by flame mask (explained in upcoming section 2.4.2) are removed. The distribution of fractional part of both $\boldsymbol{X_x}$and $\boldsymbol{X_y}$, for the time delay between two PIV images with a time interval = 0.1 ms, for one repetition of the Reference case is shown in Figure 78. ***C*** of $\boldsymbol{X_x}$ is >0.4 indicating severe peak locking [101]. It has been found in the literature that severe peak locking has a minor effect on the mean velocity while the turbulent fluctuations can be significantly overestimated.

Equation 22: $$X_f(x,y,t)=\{X(x,y,t)-|X(x,y,t)|\}$$

Equation 23: $$C(t)=1-\frac{\{\text{expectation of } X_f(x,y,t)=0.5\}+\{\text{expectation of } X_f(x,y,t)=-0.5\}}{2\times\{\text{expectation of } X_f(x,y,t)=0\}}$$

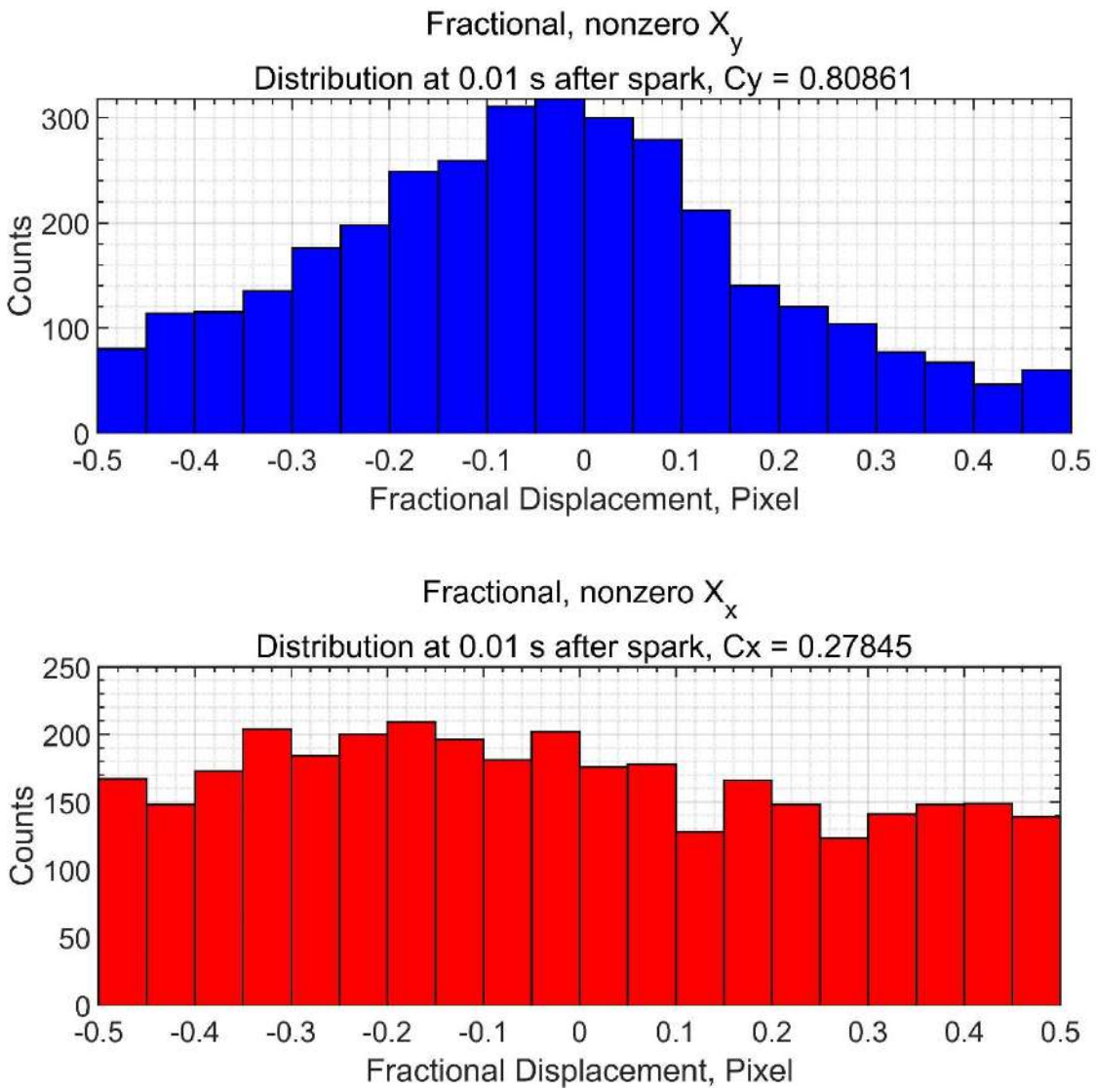

Figure 78: Histogram distribution of fractional part of ***X(x,y,t)*** at ***t*** = 10 ms for one repetition of Reference case (ID 8618), with PIV of time interval = 0.1 ms

In this paragraph, we will show the method used in the thesis to reduce the degree of peak locking. Increasing the dynamic range of displacement increases the resolution in velocity (or the displacement between 2 PIV images). Dynamic displacement can be improved by increasing the time delay between two PIV images. 10 kHz PIV carried out in these experiments provides us with the advantage that the time delay between two PIV images can be varied. The uncertainty in velocity computation is shown in Table

5. For the Reference case (category 2), the fractional part of both $\boldsymbol{U_x}$ and $\boldsymbol{U_y}$, with a time interval between two PIV images of 0.3 ms is shown in Figure 79.

Table 5 : Uncertainty for different categories to evaluate degree of pixel locking

Category	Notations	Uncertainty (m/s)
1	LT-60	0.014
2	Reference	0.024
3	HT2-60, HT3-60	0.071

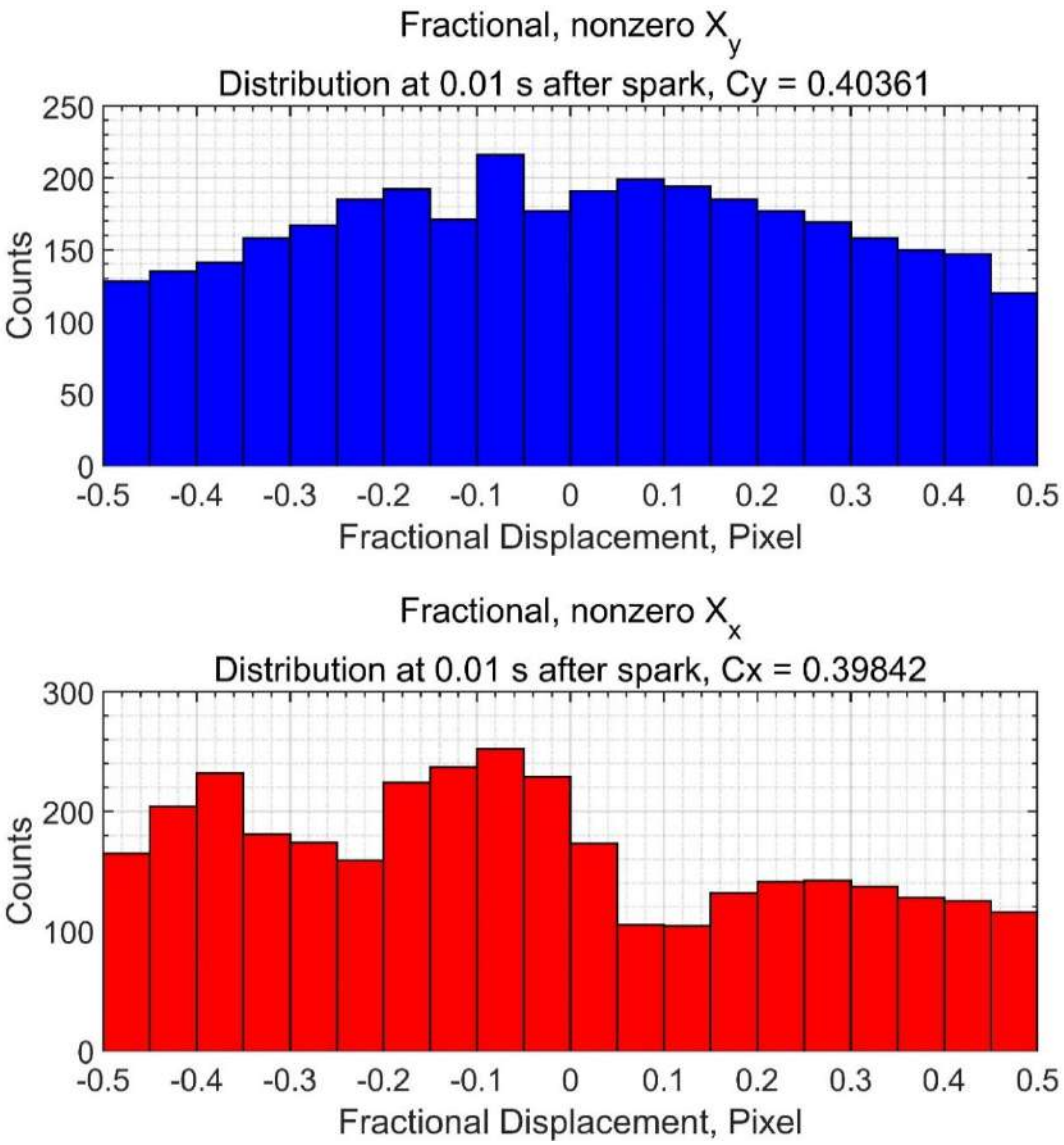

Figure 79: Histogram distribution of ***X(x,y,t,i)*** at ***t*** = 10 ms for one repetition of Reference case (ID 8618) with PIV of time interval = 0.3 ms

A comparison of Figure 78 and Figure 79, indicates that the tendency of the fractional displacements to near-zero reduces as the time interval between two PIV images is increased (from 0.1 ms to 0.3 ms). Going from a time interval of 0.1 ms to 0.3 ms between two PIV images results in stretching of the dynamic displacement leading to the reduction of the degree of pixel locking. Figure 80 and Figure 81 shows the evolution of the degree of pixel locking for one repetition of the Reference case (category 2) with different time delays between two PIV image for both the ***x*** and ***y*** component of displacement. It is seen that

increase in time delay leads to a fall in ***C***, from severe peak locking (***C*** > 0.4) to mild peak locking (***C***~0.3-0.4) [101]. This reduction is visible significantly on the ***y*** component of velocity for ***t***<15ms. Using a different time interval doesn't affect the spatial mean of velocity, shown in Figure 80 and Figure 81. On one side, we want high dynamic displacement to avoid the peak locking effect, while on the other side we want to stay well within the recommendation of maximum dynamic displacement ($<\frac{1}{4^{th}}$ of interrogation window). The upper limit on the dynamic displacement is set at $\frac{1}{8^{th}}$ of the interrogation window size. Hence for the Reference case with 1 fan, shown in Figure 80 and Figure 81, a time delay of 0.3ms is chosen to be optimum. For all the experiments in category 2, the time delay chosen is 0.3ms. Using a similar analysis for other categories, for category 1 the time delay chosen is 0.5ms and for category 3 the time delay chosen is 0.1ms. With this optimum time delay, $\vec{U}(x,y,t)$ is computed for different experiments (and repetitions).

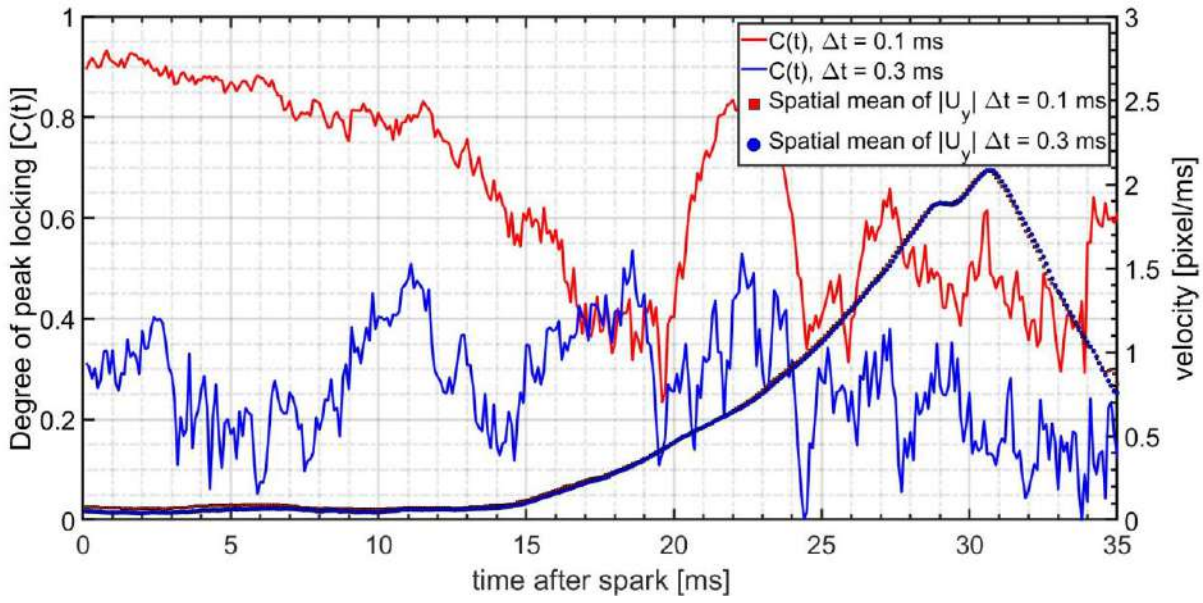

Figure 80: Evolution of degree of peak locking (***C***) over time in U_y for Reference case (ID 8618)

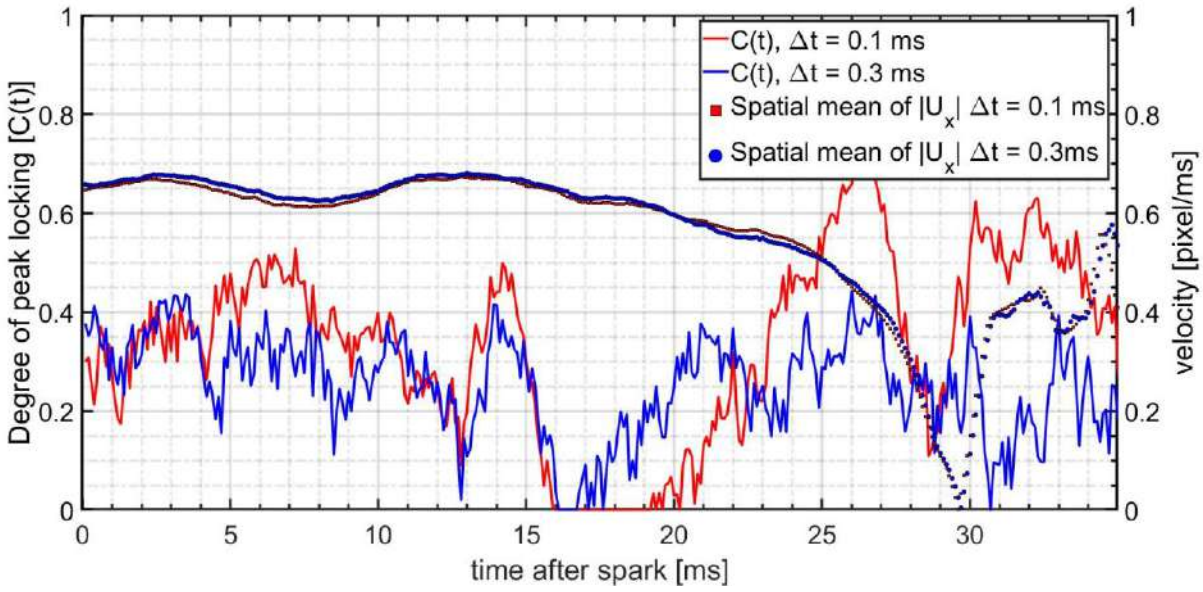

Figure 81: Evolution of degree of peak locking (***C***) over time in $\boldsymbol{U_x}$ for Reference case (ID 8618)

Evaluating uncertainty in the PIV measurements is a task that is beyond the scope of the current thesis. We have used recommended setting for the PIV experiments, which allows us to use the uncertainty estimate for these recommended settings[85]. For these settings, an uncertainty of 2-5% on the mean pixel displacement is reported in the literature [84, 102, 103]. In other reports, 0.1 pixels of uncertainty is also considered an estimate for the displacement computed from PIV [104]. In our experiments, 0.1 pixels of uncertainty gives the maximum uncertainty hence is considered for analysis throughout the thesis (given in m/s in Table 5).

2.4.2. MASKING OF BURNT GAS

Although PIV can yield $\vec{\boldsymbol{U}}\boldsymbol{(x,y,t)}$, it is not accurate over all space ***(x,y)*** especially, in the vicinity of the flame. This is primarily due to the density gradients affecting the scattered PIV signal which is seen as bands in the PIV signal near the flame. This noise creates erroneous vectors near the flame front. Hence it is of utmost importance to separate the erroneous vectors from the good vectors. This can be achieved if the flame front (and other reflections) is masked. In this section, we will discuss the masking of burnt gas.

The experiments can have shot to shot variations in the intensity due to PIV particles sticking to the optical window or variation in the density of PIV particles in the combustion chamber. These problems add to the noise in the PIV signal leading to a non-uniform signal in the burnt and unburnt zone. Hence a universal threshold is not directly applicable to PIV images, to detect the flame accurately. Instead, an FFT filter is utilized to remove the noise in the PIV images, after which a threshold is used to binarize the image.

One example of the flame front mask of a raw image is shown in Figure 82. However, determining the mask from PIV images is not accurate, especially on the spatial scale of measurement in the experiments carried out in this thesis. Hence the flame front mask is a qualitative tool to rule out bad velocity vectors due to noise from the flame. Interpretation of burnt and unburnt zones near the wall is also tricky as the signal near the wall has deteriorated.

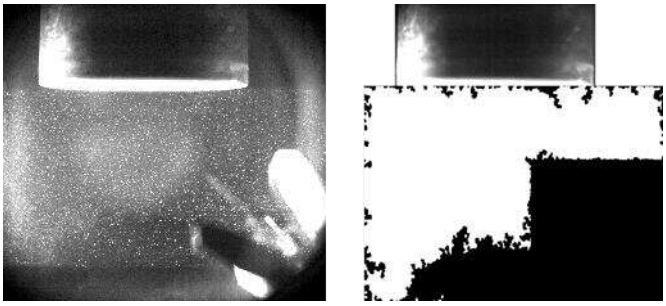

Figure 82: Sample image with flame and its corresponding mask

There is noise however from the fan and on the borders due to filtering, which needs to be excluded. In such a scenario, two ROI are determined for analysis, highlighted in Figure 83. Henceforth ROI2 refers to the smallest ROI and ROI1 refers to medium size ROI. With this flame front masking, we can achieve our objective of reasonably obtaining the time at which flame enters a particular ROI.

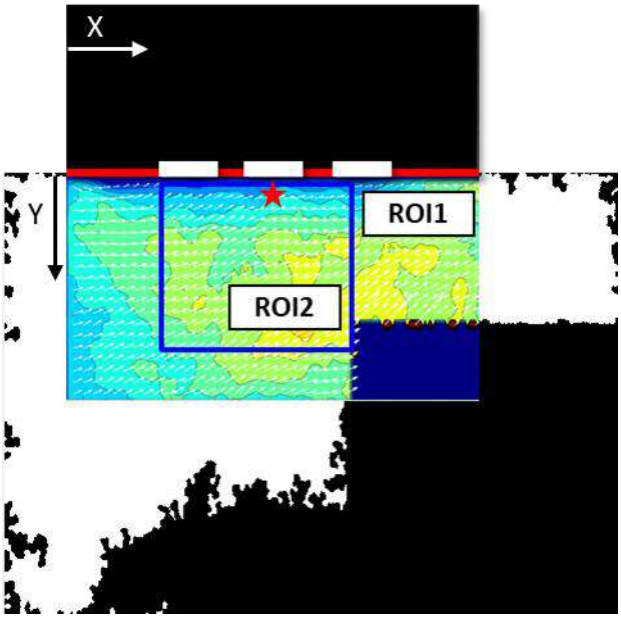

Figure 83: Schematic showing the location of ROI used for analysis, the relative location of sensor and wall in the ROI. The blue square represents the ROI2.

2.4.3. SYNCHRONIZATION OF THE VELOCITY VECTORS

We have seen in section 2.3, that the heat flux trace is synchronized to Q_P to determine the statistics from many repetitions of an experiment. PIV statistics of the turbulent flow field need a large number of repetitions to achieve convergence within satisfactory criteria [42]. In this thesis, 15 repetitions are used to characterize one experiment based on convergence on Q_P. The variation in the timing of Q_P, which is also the arrival of flame on the wall is denoted by $t(Q_P)$. There can be 2 methods of synchronization for the velocity vectors. In the first method, the synchronization of the velocity is done by taking spark as a reference which occurs at $t = 0$. While in the second method, the synchronization is done by taking the time of flame arrival on the wall, based on $t(Q_P)$. In the second method, an offset in time is introduced into the velocity field $\vec{U}(x,y,t+\Delta t)$. This offset is derived from the synchronization of Q_P for the individual repetitions shown in section 2.4.3. In this section, we will evaluate the sensitivity of the mean velocity computed by the two methods leading us to choose one of the two methods to proceed with the analysis.

For the Reference case, at a point that is 1.77 mm from the center of the wall, the temporal evolution of mean velocity computed using the two different synchronization methods is shown in Figure 84. By intuition, one would expect the mean velocity computed by the synchronization with the $\boldsymbol{Q_P}$ would have a lower standard deviation compared to the mean velocity computed by synchronization with spark. Through this figure, we can see that there exists only a minor difference in the mean velocity (and standard deviation) computed by the two different methods of synchronization. The second method introduces an additional computational step to determine an offset. Hence, based on convenience the first method is chosen to evaluate the mean velocity and the fluctuations.

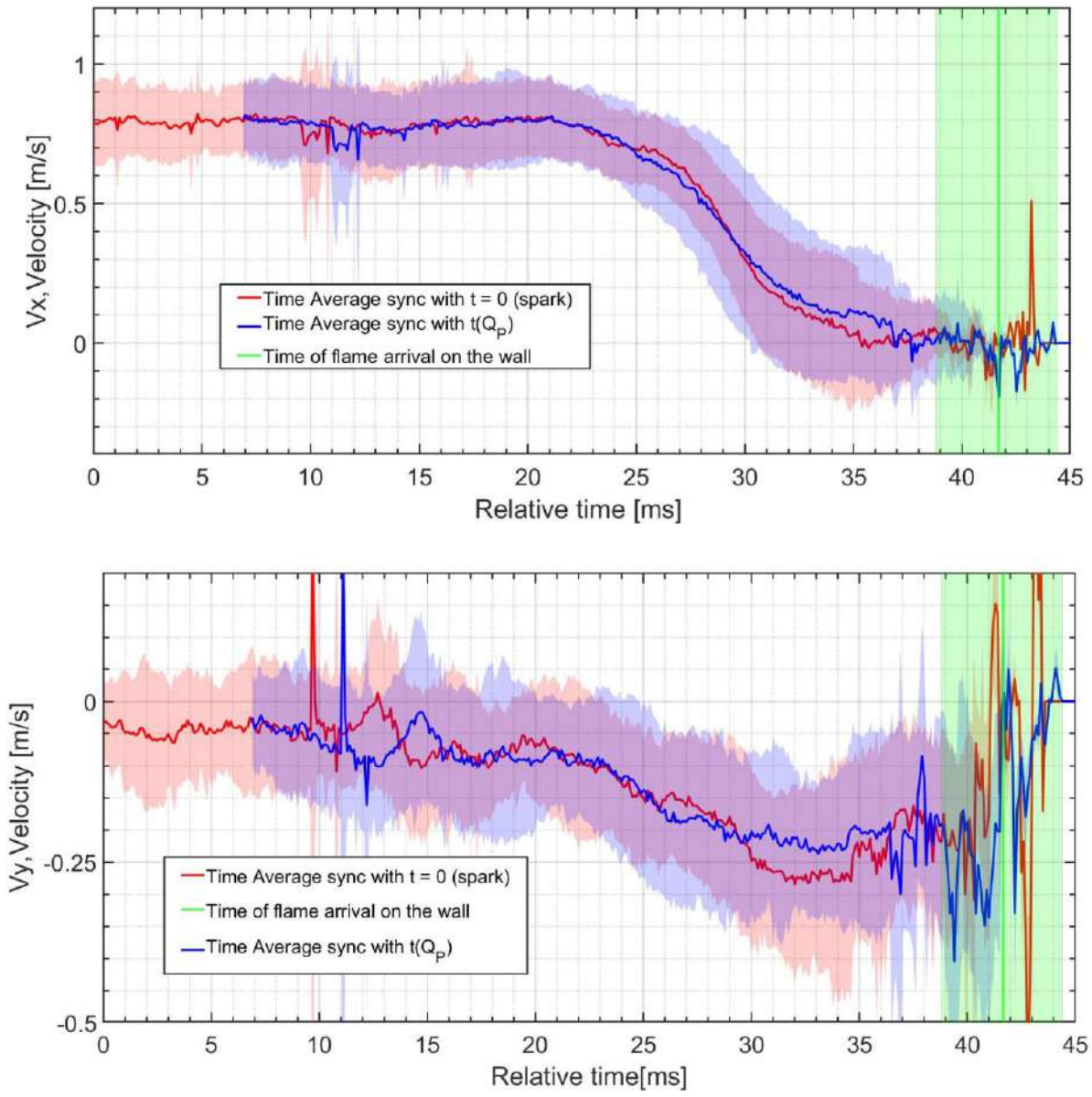

Figure 84: The comparison of the mean velocity of the Reference case (at 1.71 mm from the center of the wall), consisting of two different methods of synchronization. The time of Q_P is given by $t(Q_P)$.

The mean velocity is seen to be modified by the flame in Figure 84, at t>20 ms for the Reference case. This is evident from the change in the value of the mean velocity from its initial value which stays constant for t = 0 to t = 20 ms for the Reference case. This conclusion is needed for the calculation of the turbulence scale in section 2.5.3 revisited in chapter 3.

2.5. TURBULENCE CHARACTERISTICS FROM VELOCITY DECOMPOSITION

In this thesis, PIV measurements target characterization of the velocity flow field, $\vec{U}(x,y,t,i)$ and the turbulence intensity, $\vec{u'}(x,y,t,i)$ where '*i*' refers to the repetition number of an experiment. In this section, the decomposition of the velocity field into turbulent fluctuations and the calculation of turbulence properties will be discussed.

2.5.1. DECOMPOSITION OF VELOCITY TO DETERMINE TURBULENCE

To derive the turbulence statistics from $\vec{U}(x,y,t,i)$, the velocity field needs to be decomposed into average and turbulent components. In this section, we will explain the method of decomposition of the velocity field into turbulent fluctuations.

In literature, Reynolds decomposition of velocity (Equation 24) is frequently used, where instantaneous velocity, $\vec{U}(x,y,t,i)$ and ensemble average mean velocity, $\overline{\vec{U}(x,y,t,i)}$ is used to obtain Reynolds fluctuations $\vec{u'}_{reynolds}(x,y,t,i)$.

However, in applications like a closed combustion chamber, there can be cycle-to-cycle fluctuations in addition to turbulent fluctuations. In such a scenario, the velocity can be decomposed into mean and two types of fluctuations. The low-frequency fluctuations correspond to cycle-to-cycle fluctuations and the high-frequency fluctuations correspond to turbulent fluctuations [42, 103]. The decomposition is given in Equation 25 and Equation 26. u'_{HF} are the high-frequency turbulent fluctuations whereas $\vec{U}_{LF}(x,y,t,i)$ is the in-cycle mean velocity consisting of $\overrightarrow{u'_{cycle}}$, cycle-to-cycle fluctuations and $\overline{\vec{U}(x,y,t)}$, ensemble average velocity.

Equation 24: $$\vec{U}(x,y,t,i) = \overline{\vec{U}(x,y,t,i)} + \overrightarrow{u'_{reynolds}}(x,y,t,i)$$

Equation 25: $$\vec{U}(x,y,t,i) = \overline{\vec{U}(x,y,t)} + \overrightarrow{u'_{cycle}}(x,y,t,i) + \overrightarrow{u'_{HF}}(x,y,t,i)$$

Equation 26: $$\overline{\vec{U}(x,y,t)}+\overrightarrow{u'_{cycle}}(x,y,t,i)=\vec{U}_{LF}(x,y,t,i)$$

However, the separation in the frequency domain needs to be quantitative to form meaningful decomposition. Some researchers use a specific time window to perform a moving average on instantaneous velocity to split the high-frequency and low-frequency fluctuations [42, 44]. The moving window size is 1-10 ms, based on the literature on different experiment setups.

Another method is to determine the criteria by studying the effect of various window sizes of moving averages in the frequency domain[103]. Figure 85 show the PSD distribution of the moving average of instantaneous velocity at one point with various moving average window size. The Fourier power spectrum density (PSD) of moving average (different window sizes are represented as different colors, see Figure 85) of instantaneous velocity separates from the PSD of instantaneous velocity at a particular frequency (shown in the grey band in Figure 85). This frequency can be used as a frequency cut-off for determining high-frequency fluctuations. This method of frequency filtering is employed in the current thesis.

Conducting such an analysis on each point in space ***(x, y)*** for each experiment (and repetitions) can be a humongous task. Instead, we have used 6 points in space for one experiment (and repetitions) to yield a range of frequency where the PSD of instantaneous velocity separates from the PSD of moving average of velocity. The lowest frequency of the range of cut-off frequency obtained from analysis at different points is used as the cut-off frequency. This cut-off frequency is found as 100 Hz, corresponding to the 10 ms window for moving average. This cut-off frequency is similar to the order of cut-off frequency used in the literature [42, 103].

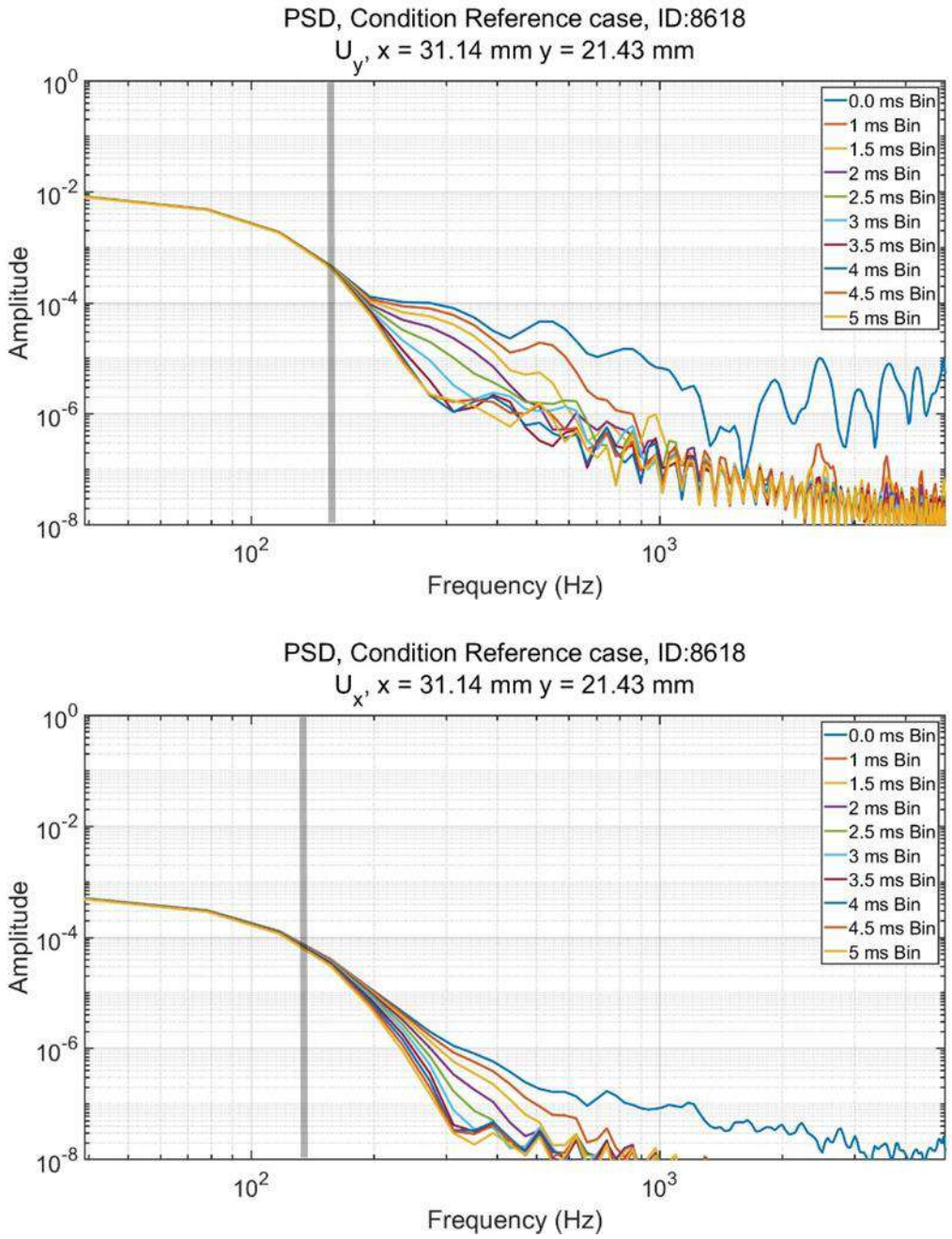

Figure 85: Fourier analysis at one point showing the cut-off frequency at which PSD of instantaneous velocity separate from PSD of binned averages. Top: for U_x, Bottom: U_y

The accuracy of determination of the cut-off frequency can be improved with high resolution in space (which would lead to larger particle size and low noise in correlation) and time (which would lead to adjustable dynamic displacement and high sampling frequency).

A low pass filter was designed in MatLab to separate the high frequency and low-frequency velocities from an instantaneous velocity trace. Figure 86 shows one example of the velocity field decomposition for the Reference case and Figure 87 shows the decomposition for HT2-60 (see for notation). In Figure 86 and Figure 87, we can differentiate high-frequency fluctuations (with a small time scale in red color) related to turbulence and the low-frequency instantaneous velocity (in-cycle mean velocity in black color). This observation attests to the effectiveness of such a method to split cycle-to-cycle fluctuations from turbulent fluctuations. There is noise at the start of the velocity trace obtained after filtering i.e., t<2 ms, due to the border effects of the filter. As flame nears the point of observation there is an increase in noise as well. These two types of noise are characterized by fast, large-amplitude fluctuations seen in the velocity trace and the high-frequency component of the velocity trace.

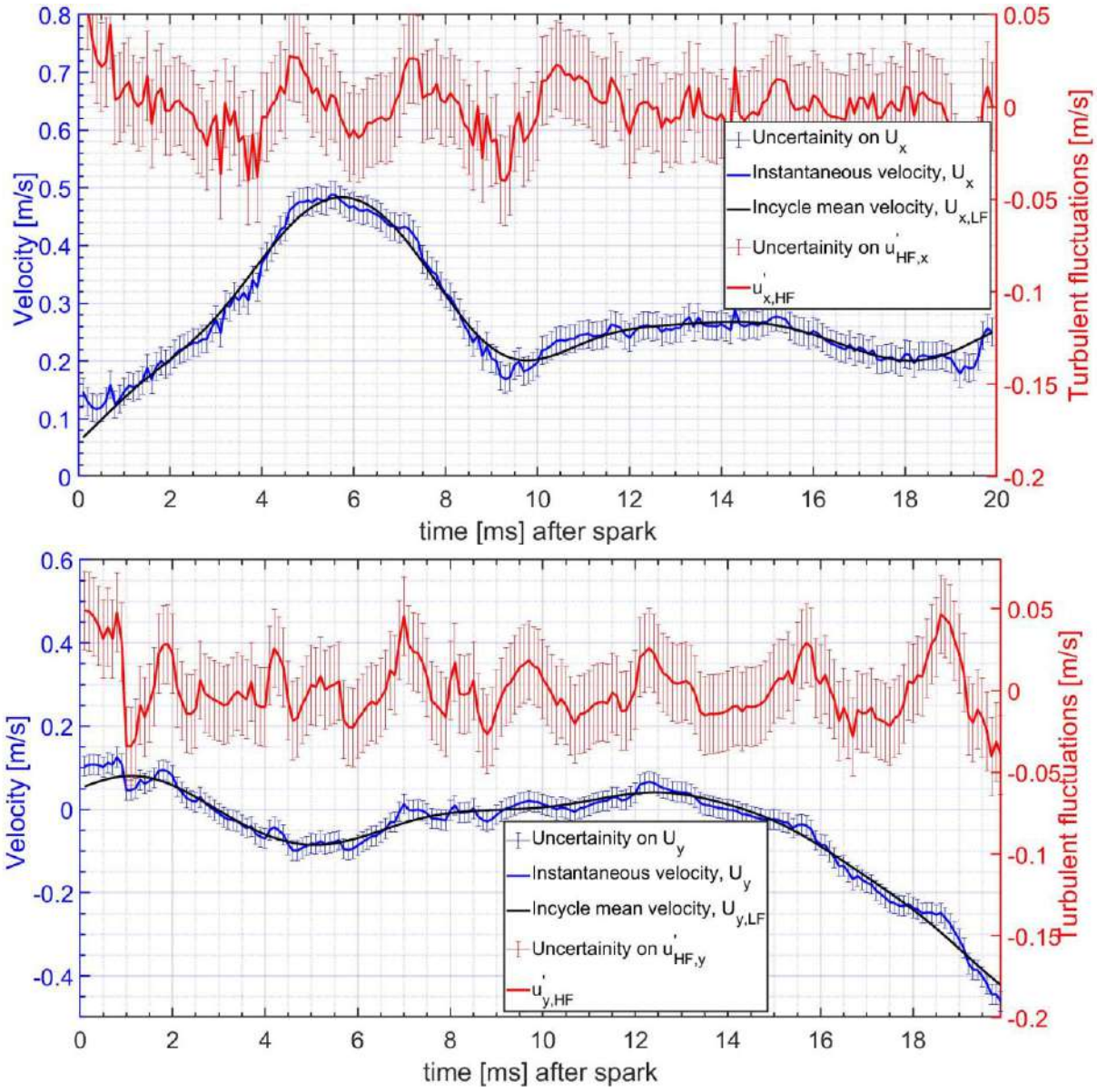

Figure 86: Instantaneous, low frequency, and high-frequency velocity components for one point (same as in Figure 85) for Reference case (ID 8618). Top: ***X*** component, Bottom: ***Y*** component

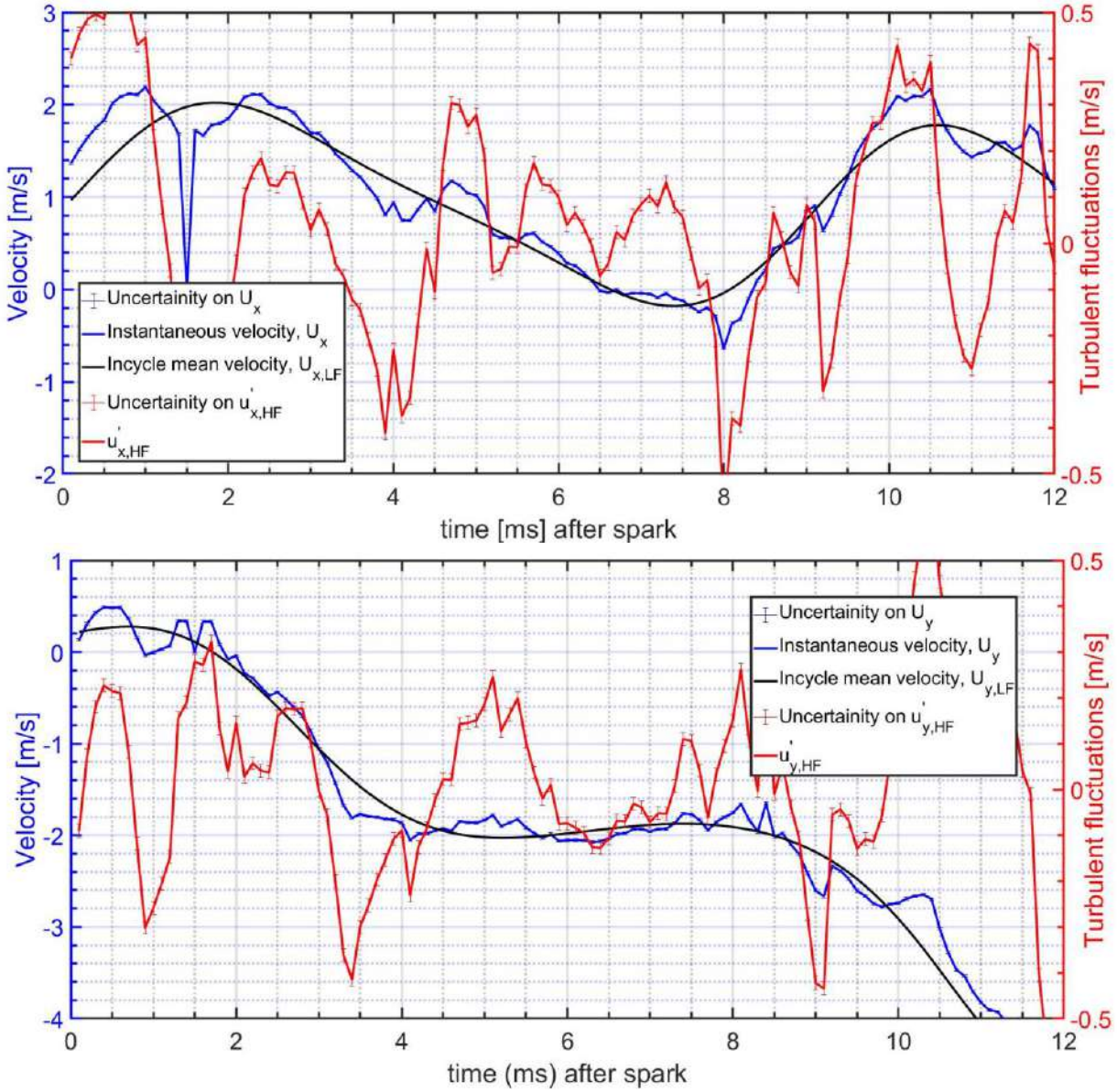

Figure 87: Instantaneous, low frequency, and high-frequency velocity components for one point (same as in Figure 85) for HT2-60 (ID 8859). Top: ***X*** component, Bottom: ***Y*** component

2.5.2. NATURE OF TURBULENCE

Turbulence is characterized by its length scale and time scale. If the turbulence is isotropic and homogenous then autocorrelation can be used to determine the turbulence characteristics i.e., time scale and length scale [105]. In this section, we check the nature of turbulence to determine if the turbulence is isotropic and homogenous.

Homogenous turbulence means the turbulence is invariant in space. Generally, homogenous turbulence is verified by a normal distribution of the turbulence in the space [76, 106]. Evaluation of normal distribution is not clear when the sample size is large, consisting of noise as in these PIV measurements. Usually, a normal distribution is characterized by skewness close to zero and kurtosis close to three. However, when the sample size is>300 the criteria for kurtosis or skewness are not rigid. Rather an evaluation of histogram distribution and a wide tolerance on skewness values lying from -2 to 2 and kurtosis values lying from 0 to 7 is used as per literature [107]. In our case, each ROI1 has 3360 samples and ROI2 has 1014 samples so we can use relaxed criteria.

$u'_{x,HF}$ and $u'_{y,HF}$ is used as turbulent fluctuations, hence also referred to as u' or u'_x and u'_y (for different components) in this thesis. Figure 88 shows the histogram distribution of u'_x and u'_y at one instant in time for ROI2, for the Reference case. The objective of presenting such a result is to understand the methodology without focusing on the specific result. At this instant the turbulence is homogenous. The distribution has a skewness (***Sx***, ***Sy***) of -0.39 and -0.5 along with a kurtosis (***Kx***, ***Ky***) of 4.32 and 4.13. The values of skewness and kurtosis lie within the relaxed criteria of normal distribution. Similarly, for ROI1, the histogram distribution is shown in Figure 89, with skewness (***Sx***, ***Sy***) of 0.27 and 0.42 along with a kurtosis (***Kx***, ***Ky***) of 6.22 and 6.84. The values of skewness and kurtosis also lie within the relaxed criteria of normal distribution. Visually, the overall distribution in ROI1 is close to normal, but the kurtosis is higher compared to ROI2. Nevertheless, we can use both ROI1 and ROI2 for our analysis.

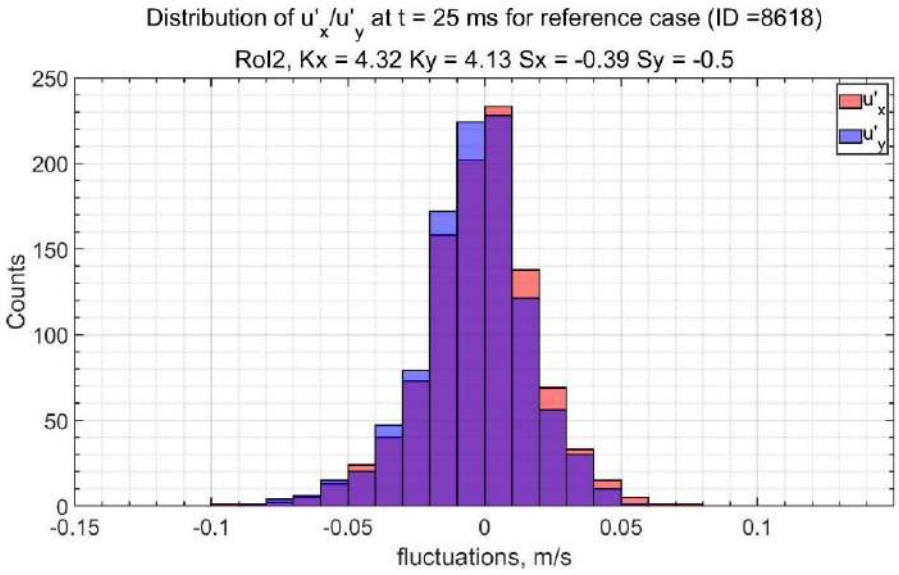

Figure 88: Histogram distribution of ***u'x*** and ***u'y*** for one experiment at one instant of time for Reference case, ROI2

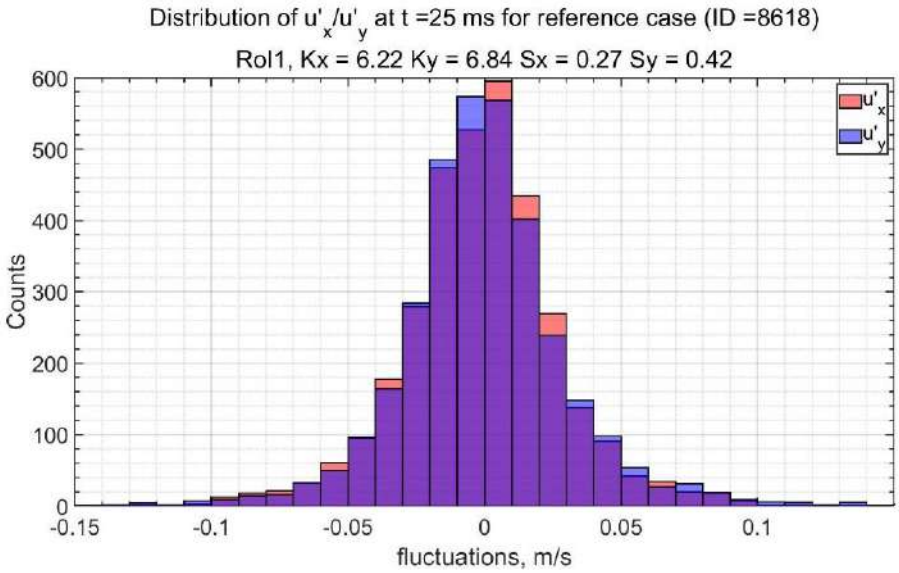

Figure 89: Histogram distribution of ***u'x*** and ***u'y*** for one experiment at one instant of time for Reference case, ROI1

Kurtosis and skewness can be evaluated for all times of one repetition and all repetitions for one experiment. This is shown as a kurtosis or skewness plot over a 2D space of time and repetitions in Figure 90 and Figure 91. Average skewness (***Sx***,***Sy***) is zero (***Sx***= 0.00, ***Sy***= 0.00) and Kurtosis is <7

(***Kx***= 4.39, ***Ky*** =4.18). The skewness and kurtosis values lie within the relaxed criteria of normal distribution. Our evaluation of the Reference case suggests that indeed the turbulence is homogenous.

There are noisy peaks in Figure 90 and Figure 91 which need further evaluation. The frequency filtering of velocity to yield fluctuations is not an absolute criterion (using cut-off frequency) to separate high-frequency fluctuations. Hence further insights on the cutoff frequency are needed. We believe, a small contribution of low-frequency fluctuation or noise in the measurement can distort the distribution and cause the peaks in Figure 90 and Figure 91. In this thesis, we will not focus on the noisy peaks. The mean of kurtosis and skewness for different turbulence conditions is shown in Figure 92. Within the criteria set earlier turbulence is found to be homogenous.

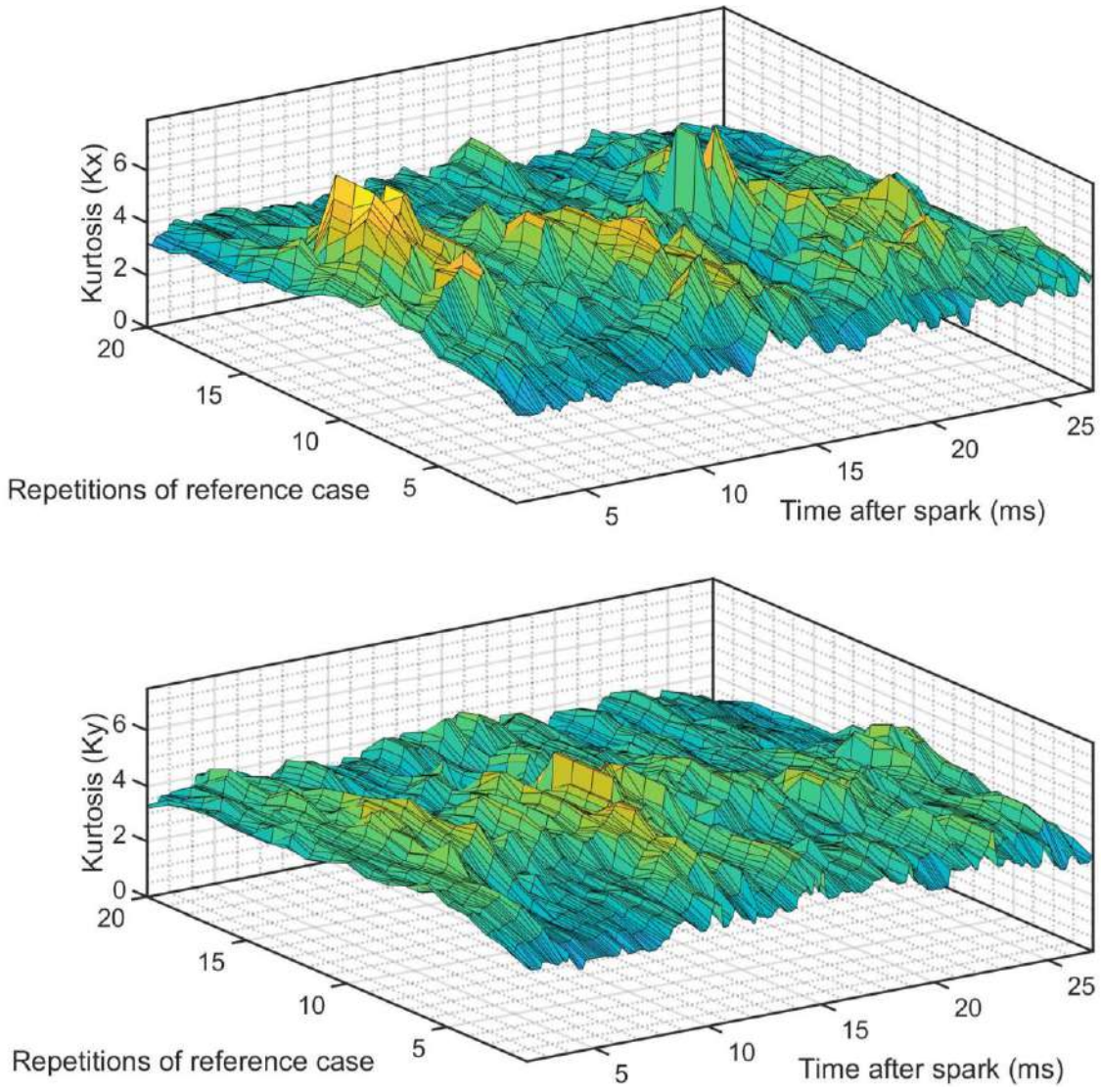

Figure 90: Kurtosis over 2D space of time and repetitions for ROI2 for the Reference case. Top: X component (***Kx***), Bottom: Y component (***Ky***)

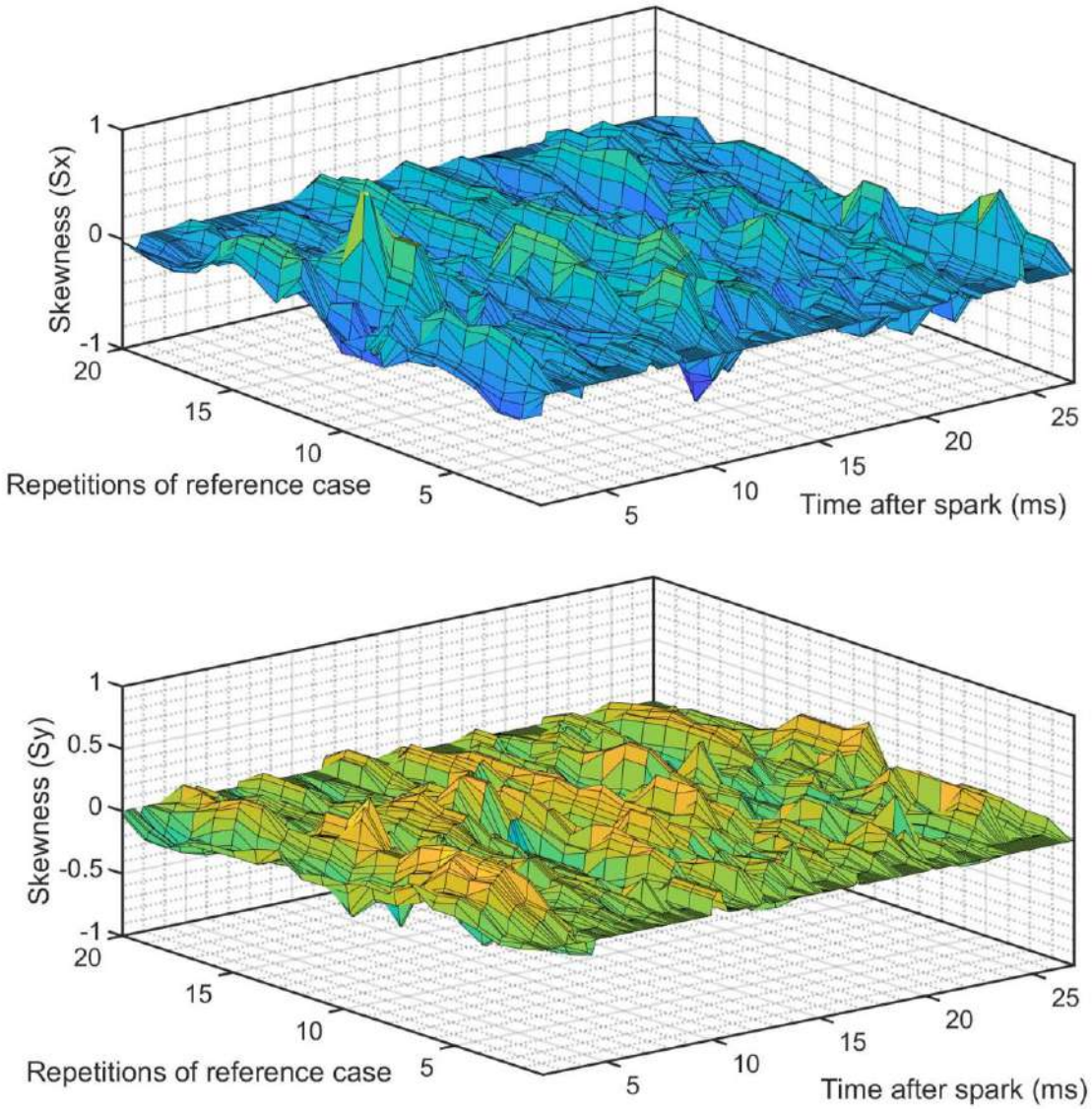

Figure 91: Skewness of u'_x over 2D space of time and repetitions for ROI2 for the Reference case. Top: X component (***Sx***), Bottom: Y component (***Sy***)

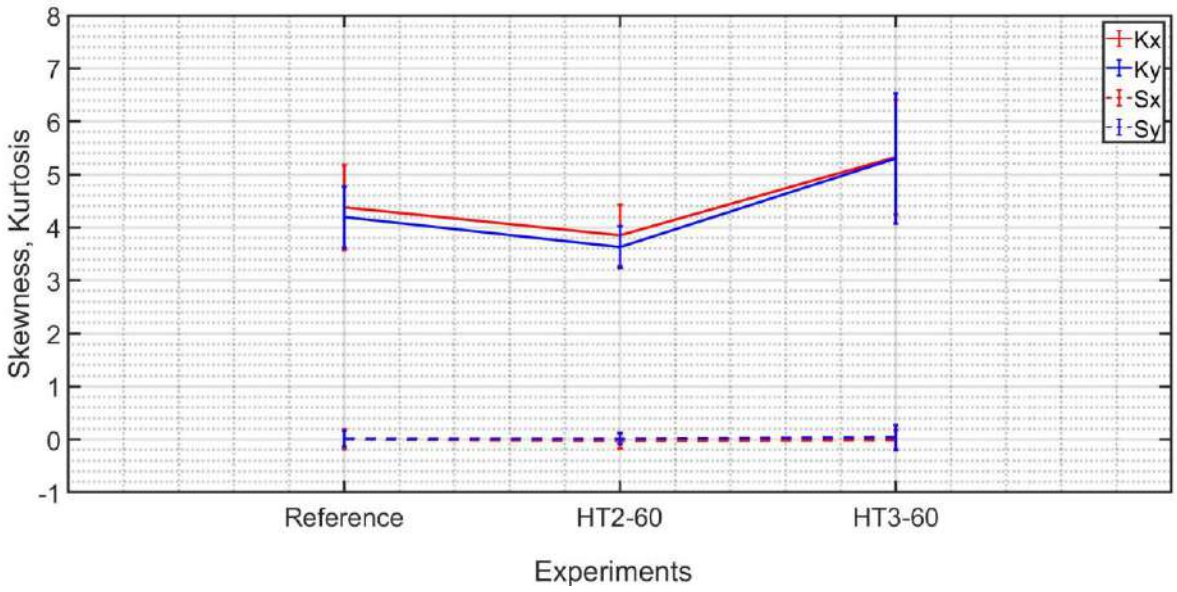

Figure 92: Mean Skewness and Kurtosis over different experiments in Table 4

Now, we need to test the isotropy of the turbulence i.e., turbulence is invariant to rotation. In the case of isotropic turbulence, there is no directional preference. Hence, $\overline{u'_x u'_y}$=0. In the case of anisotropy, u'_x is negatively correlated with u'_y leading to $\overline{u'_x u'_y}$<0. Figure 93 and Figure 94 plot the u'_x vs u'_y at different times (in different colors), for the Reference case and HT2-60 respectively. In Figure 93 and Figure 94, we observe the correlation of u'_x with u'_y at different times. Looking at all the plots, we can conclude turbulence is isotropic. Moreover, $\overline{u'_x u'_y}$ is less than 10% of u'_x and u'_y, which we can consider~0, suggesting that turbulence is isotropic.

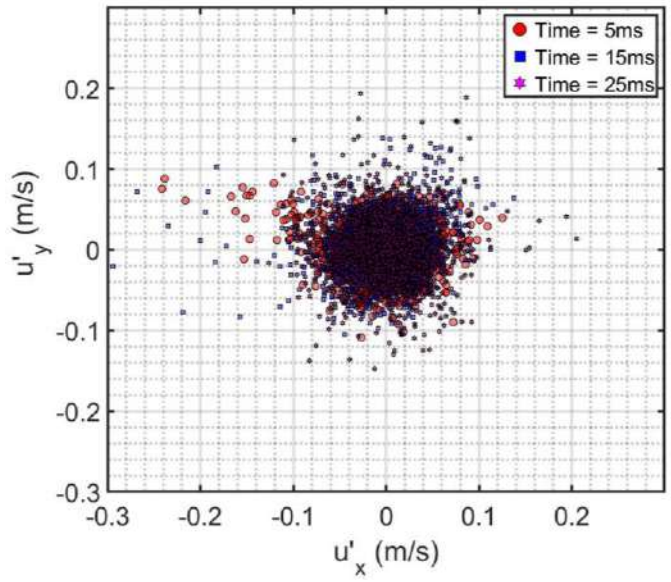

Figure 93: Evolution of isotropy test parameter over time for one repetition of Reference case (ROI2)

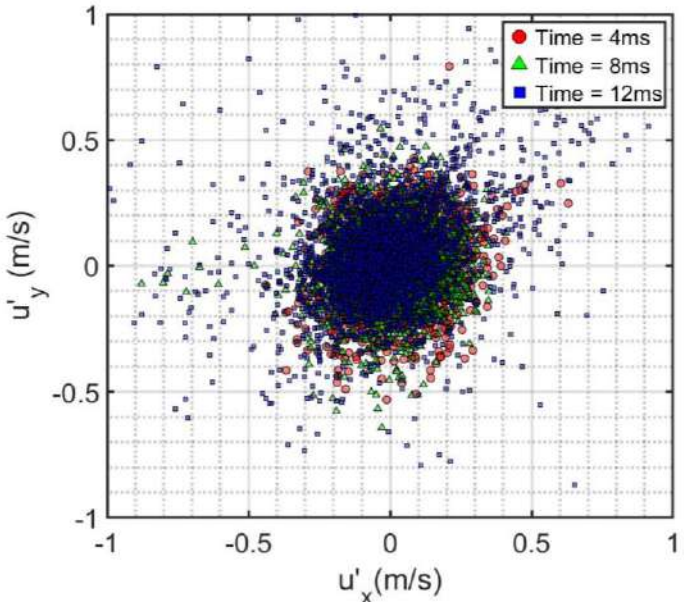

Figure 94: Evolution of isotropy test parameter over time for one repetition of HT2-60 (ROI2)

Turbulence can be statistically stationary or variable over time. We need to evaluate the variation of turbulence over time. Figure 95 shows turbulent fluctuation evolution over time for a non-reactive case for three different points of observation for the Reference case and HT2-60 respectively. In Figure 95, we see that the amplitude of turbulent fluctuations all lies within -0.06 m/s to 0.06m/s with no distinct change

in the distance between two peaks. For any duration after 2 ms, sufficient to contain few peaks the mean of u'_x and u'_y is less than uncertainty, which we will consider as zero. A similar observation is found in HT2-60 case. Hence, we conclude that the turbulence is stationary in non-reactive cases, i.e., turbulence does not change in time.

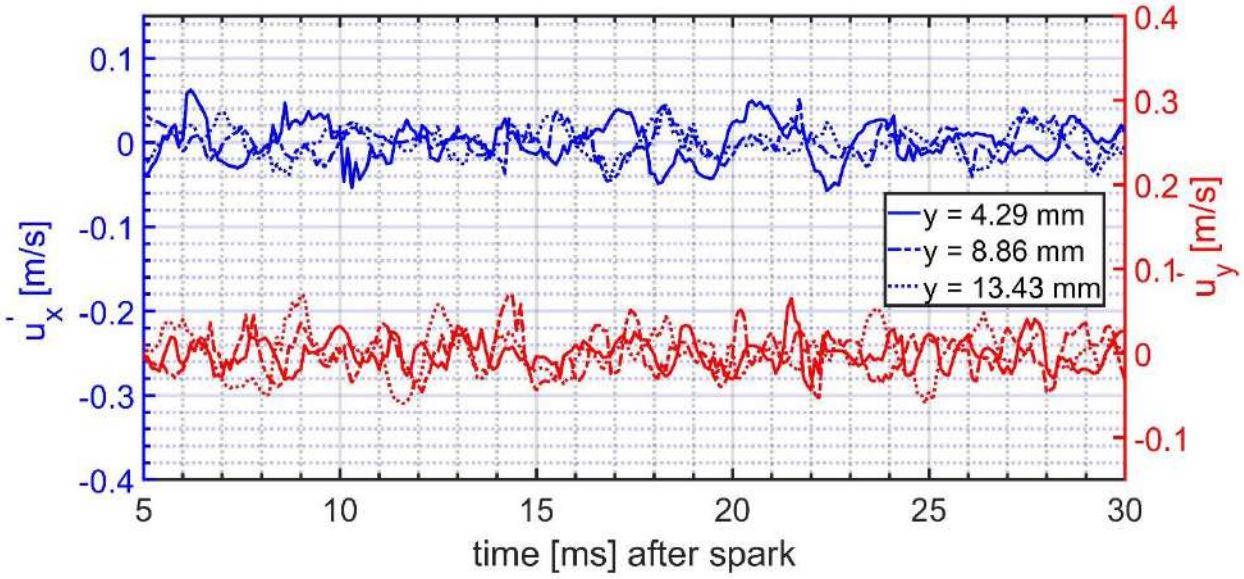

Figure 95: Evolution of turbulence(u'_x,u'_y) at several locations for Reference cases in non-reactive conditions. '***y***' denotes the distance of the point from the centre of wall

In literature, turbulence is found to change near the flame, both in CVC and SI engines by researchers [108, 109]. Overall, the researchers have found an increase in turbulence intensity near the flame ~2-5 times compared to turbulence far from flame or in the cold flow. The temporal evolution of the turbulent flow field for the reactive case for experiments conducted in this thesis, at several points of observation is shown in Figure 96. At the start, up to 2ms, the turbulent fluctuations are error-prone due to the border effects of filtering. The arrival of flame at the location of measurement is indicated by arrows. When the flame is close to the point of observation, there is significant noise due to flame arrival that is seen in the turbulence component (see section 2.4.2). Hence, in the current setup, turbulence can only be evaluated starting from 2ms until the point in time when noise appears in the temporal evolution of turbulence. Till

this point, no significant increase in amplitude of turbulent fluctuations is seen especially not in the order of 2-5 times.

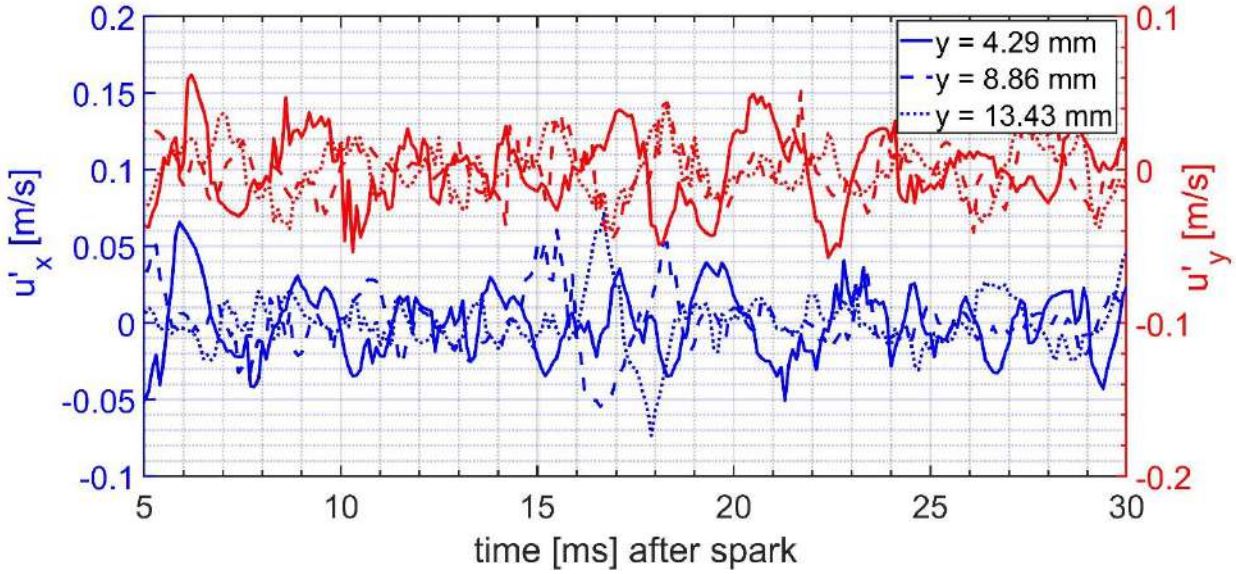

Figure 96: Evolution of turbulence (u'_x,u'_y) at 3 different locations for Reference cases in reactive conditions. '***y***' denotes the distance of point from the centre of wall.

A comparison of the reactive and non-reactive turbulent fluctuations at two points of observation is shown in Figure 97 for reference. This comparison shows indeed u'_x and u'_y is similar in reactive and non-reactive cases in amplitude, until the signal is distorted by flame arrival. We don't see a change in amplitude ~2-5 times that is seen in the literature. We conclude u'_x and u'_y is consistent in its amplitude prior to flame arrival.

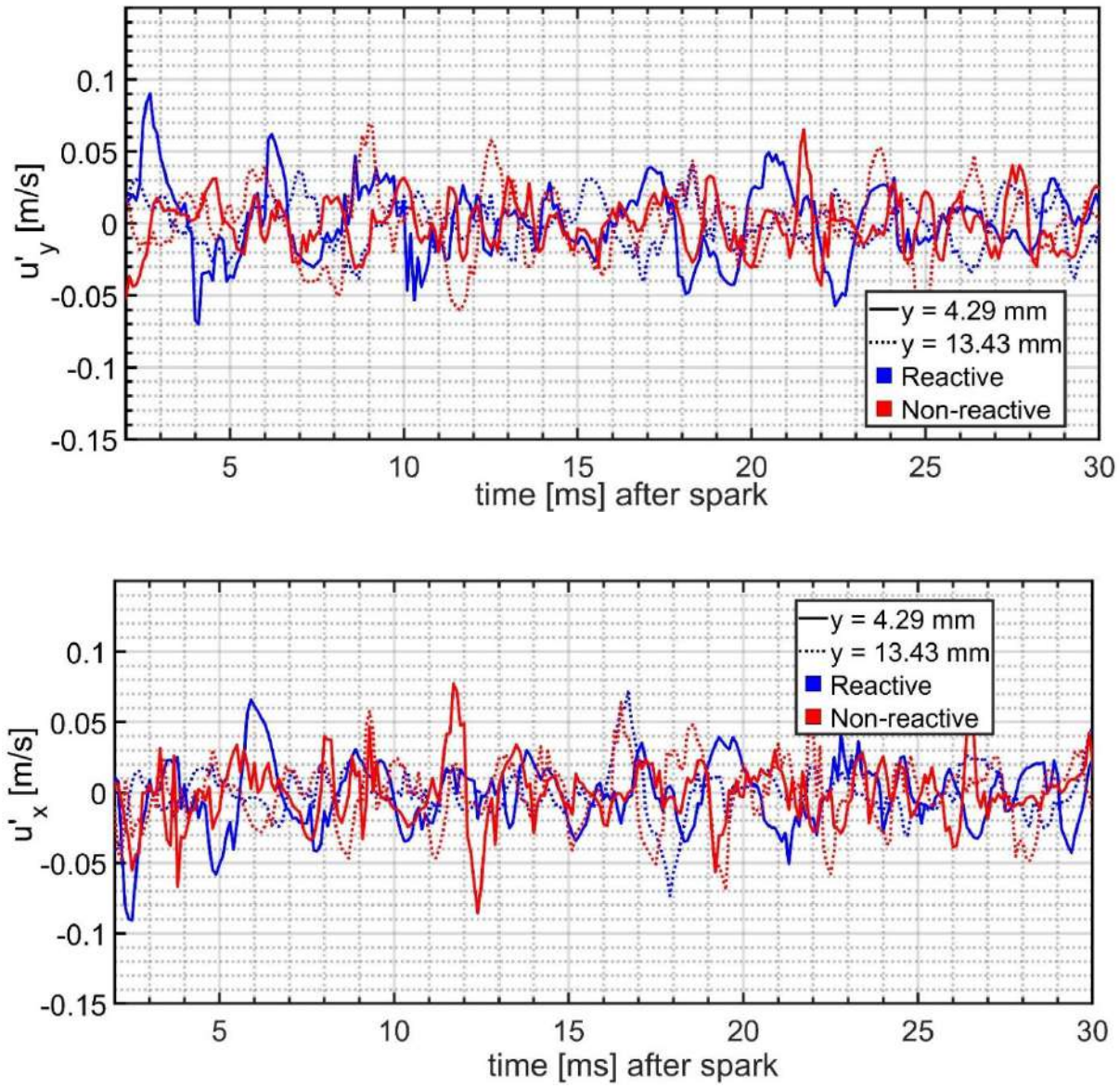

Figure 97: Comparison of turbulence in reactive and non-reactive conditions for the Reference case. '***y***' denotes the distance of point from the centre of wall. Top: ***x*** component, Bottom: ***y*** component

The u'_x and u'_y computed in this thesis, by frequency filtering, is constant until the noise (due to flame) interferes with the PIV signal. Hence the u'_x and u'_y is assumed to remain unchanged even during FWI. We conclude that the turbulence measured before FWI is representative of the turbulence during FWI.

2.5.3. CALCULATION OF TURBULENT PROPERTIES

To move from space and time-defined turbulent fluctuations to a representative value for one repetition or a set of experiments, we can obtain the RMS of turbulent fluctuations (u'_{RMS}) defined in space and repetitions coordinate as in Equation 27 or Equation 28, respectively. If the turbulent fluctuations are varying in time, then Equation 27 where ***i*** is the repetition number, is suitable [42]. Since the turbulence in our setup is invariant in time (as in our calculations, see Figure 97), we hypothesize that Equation 28 can also be used. In such a case, both methods (Equation 27 and Equation 28) should yield similar values. Figure 98 shows the trace of RMS of turbulent fluctuations computed in both methods. It is found that the RMS of fluctuation computed by Equation 27 is almost equal to the fluctuations computed by Equation 28. We conclude both the methods are applicable to our case. In this thesis, the fluctuation intensity is computed using Equation 28.

Equation 27: $u'_{RMS,x}(x,y,t)=RMS(u'_x(x,y,t,i)$

Equation 28: $u'_{RMS,x}(x,y,i)=RMS(u'_x(x,y,t,i)$

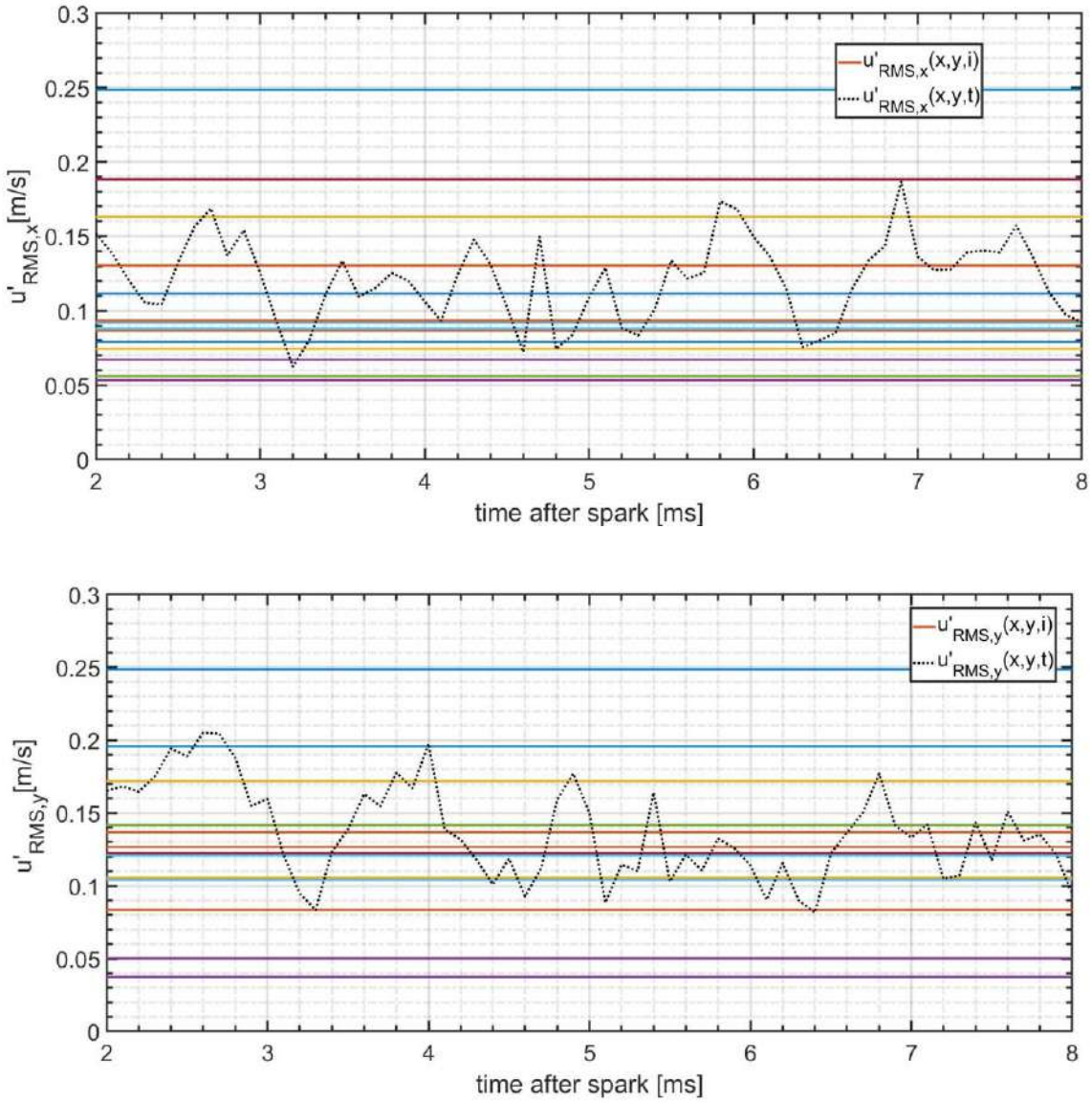

Figure 98: Comparison of $u'_{RMS}(i)$ and $u'_{RMS}(t)$ for all repetitions in HT2-60. Different colors represent different repetitions of one experiment. Top: ***x*** component, Bottom: ***y*** component. The observed point is at a distance of 13 mm from the center of the wall.

Figure 99 shows the spatial distribution of the RMS of turbulent fluctuations in one repetition of a set of experiments with HT2-60. We hypothesize that $u'_{RMS}(x,y,i)$ is flat enough that a space average can give us a representative RMS of turbulent fluctuations for one repetition in a set of experiments as per Equation 29. When we look at the spatial averages of the RMS of turbulent fluctuations in Figure 100 for

all repetitions in the same set of experiments, it shows that there is no significant variation in the spatial averages of the ***x*** component and ***y*** component, a sign of homogenous turbulence.

Equation 29: $$u'_{RMS,x}(i) = \iint_{x,y}^{RoI} u'_{RMS,x}(x,y,i)$$

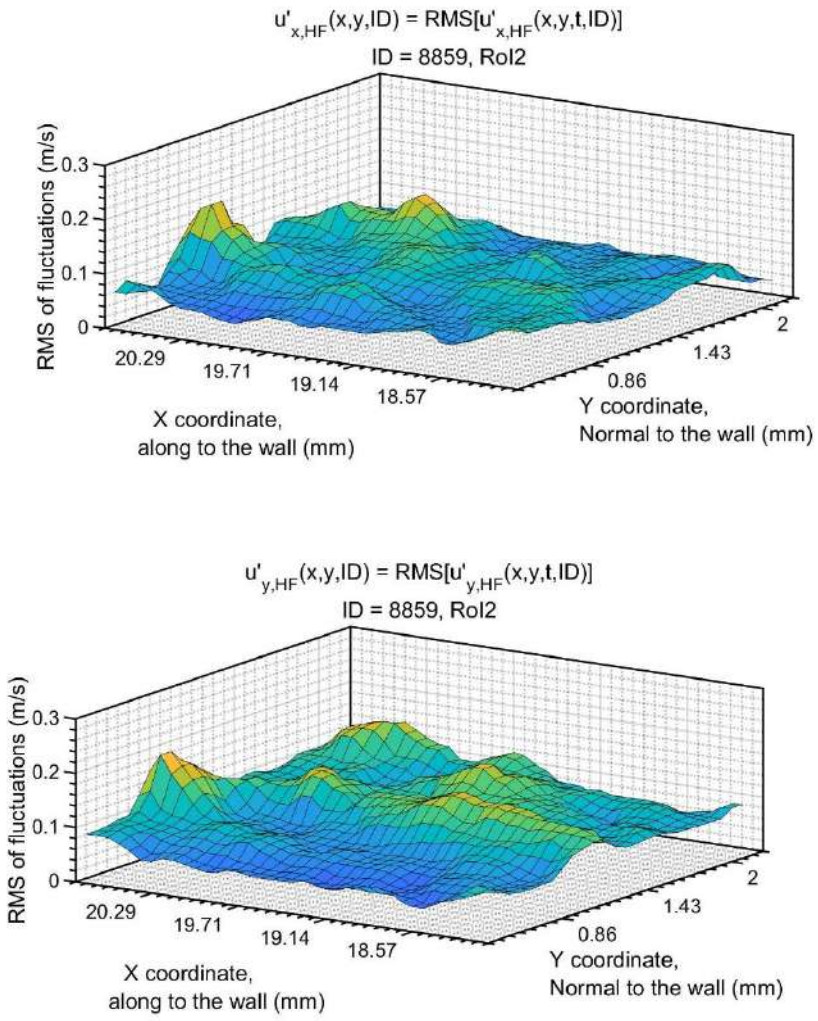

Figure 99: Turbulent fluctuation intensity as a function of space in one repetition for experiment with HT2-60 fans in ROI2

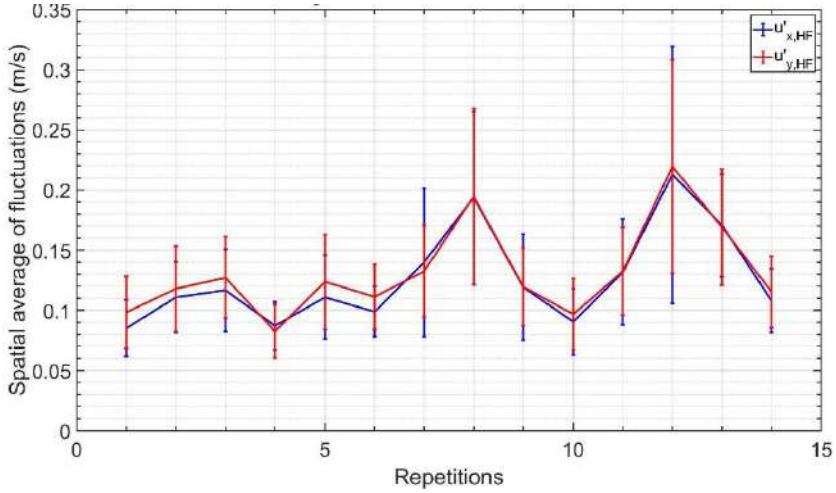

Figure 100: Spatial average and the standard deviation of the turbulent fluctuation intensity for all repetitions with HT2-60 case.

A turbulence intensity (***q***) can be computed from u'_{RMS} of both components shown in Equation 30. We assume $u'_{RMS,x} \sim u'_{RMS,z}$, which is an hypothesis used in 2D PIV experiments near the wall [42].

Equation 30:
$$q(i)=\sqrt{\frac{u'_{RMS,x}(i)^2+u'_{RMS,y}(i)^2+u'_{RMS,z}(i)^2}{2}}$$

The turbulence is demonstrated to be isotropic and homogenous. Hence, we can compute the integral time scales of turbulence ($L_{u,t}$) by autocorrelation [42, 76, 106]. The autocorrelation function, $R_{u,t}$ is shown in Equation 31. With the increase in the lag, the autocorrelation decreases and then oscillates around zero. Ideally, integration of the autocorrelation function till the whole length would lead to an integral time scale (Equation 32), however, it is not possible to integrate indefinitely. A cut-off is needed to find characteristic lag. Although many methods exist, the lag in this study is calculated by the method of zero-crossing [42]. The lag at the point when autocorrelation is zero corresponds to the timescale of the turbulence represented as $L_{u,t}$. Due to noise before 2 ms (border effects of filter) and noise after the flame arrival, only cold flow before the flame arrival in the RoI is used to compute the characteristic time scale at one point in space. Figure 101 shows the time scale computed on ROI2. We hypothesize that the

time scale over the ROI2 is flat enough for the spatial average to be representative of each repetition (see Equation 33). Spatial averaged integral time scale show that $\boldsymbol{L_{u,t} = L_{v,t}}$, shown in Figure 102.

Equation 31 : $$R_{u,t}(x,y,i) = \frac{u'_x(x,y,t,i) \times u'_x(x,y,t+\Delta t,i)}{|u'_x(x,y,t,i)| \times |u'_x(x,y,t+\Delta t,i)|}$$

Equation 32: $$L_{u,t}(x,y,i) = \int_0^{\infty} R_{u,t}(x,y,t,i)\, dt$$

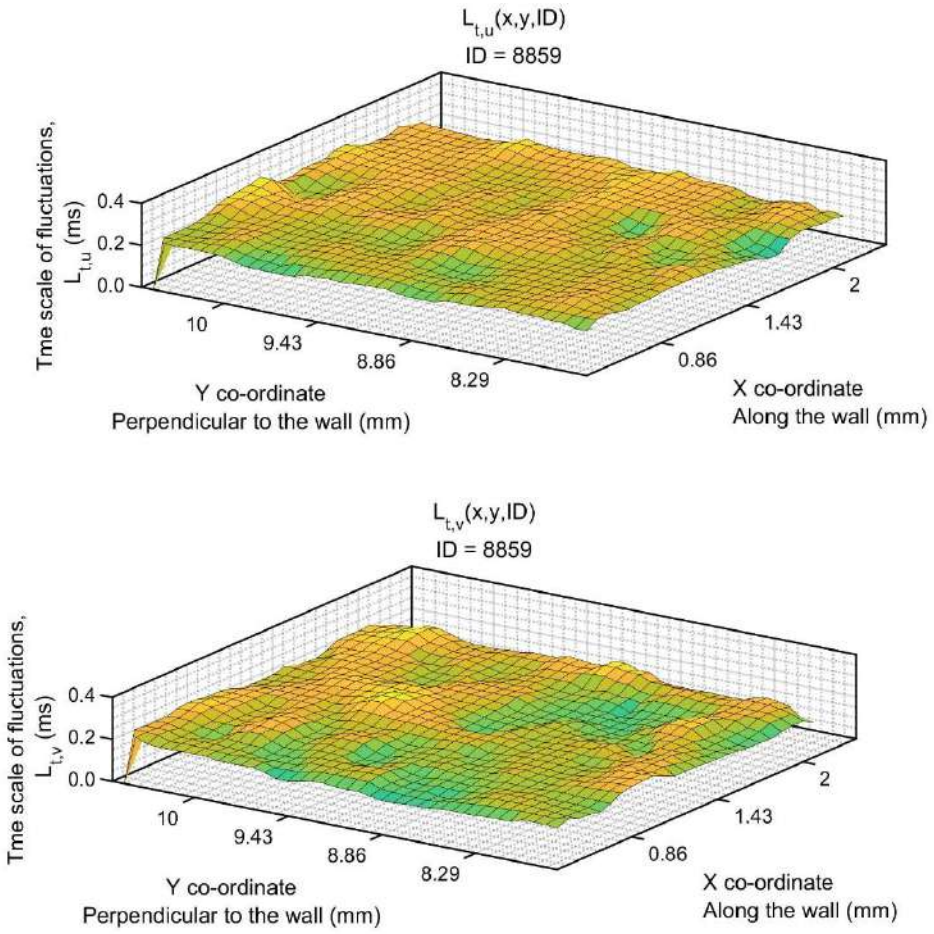

Figure 101: Integral timescale of turbulent fluctuations as a function of space in one repetition for experiment with HT2-60 in ROI2

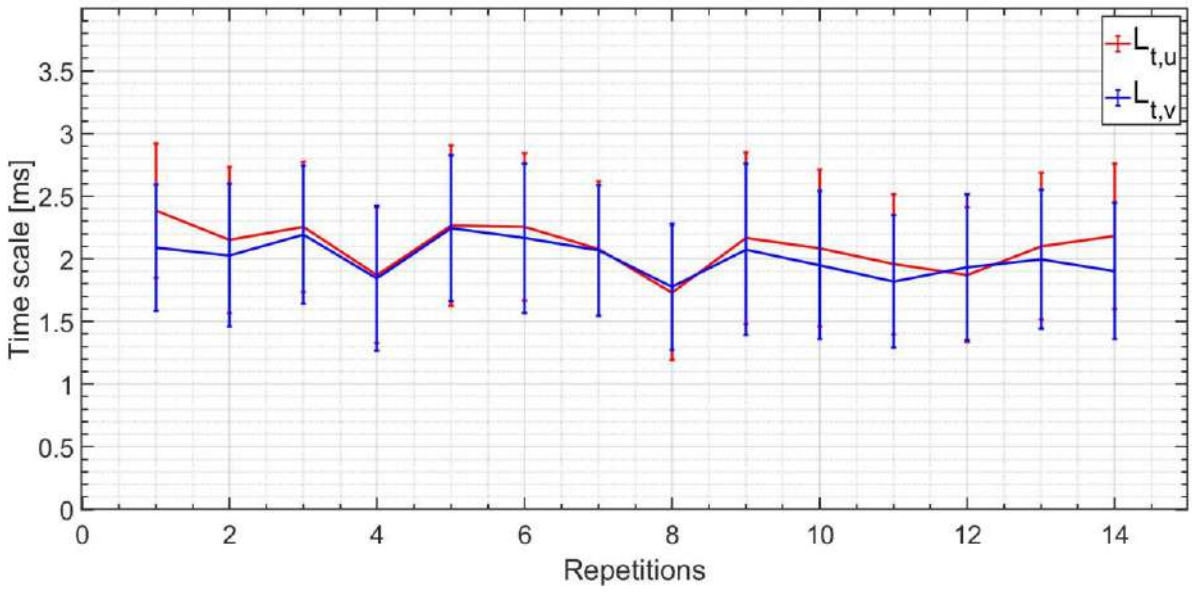

Figure 102: Spatial average and the standard deviation of the integral time scale of turbulent fluctuations for all repetitions with HT2-60 case

Equation 33: $$L_{u,t}(i) = \iint_{x,y}^{ROI} L_{u,t}(x,y,i)$$

It is determined that the spatial resolution of the experiments in this thesis is not sufficient to compute the integral length scale by autocorrelation. Alternatively, the length scale can be estimated from other relationships.

In homogenous, isotropic turbulence, Taylor's hypothesis relates the length scale with the time scale using the mean velocity (Equation 34). This hypothesis is also valid in a CVC setup during the study on FWI [42]. We have verified from the turbulence time history that the turbulent fluctuations are not affected by flame while the ensemble mean velocity is affected by the flame. Hence, we will estimate the integral length scales using the Taylors hypothesis, at a time, where the ensemble mean velocity is unaffected by flame i.e., ***t*** = 0 to 5 ms.

Equation 34: $$L_{u,x}(y,i) = L_{u,t}(y,t,i) \times \overline{u_x(x,y,i)}$$

2.6. CONCLUSION

In this chapter we discussed, the different experiment setups i.e., CVC and engine, and their instrumentation used to probe FWI. A Wall-TC assembly and a PIV system are used to measure surface temperature and instantaneous velocity field respectively. The wall-TC assembly is capable to obtain high-speed surface temperature measurements to resolve FWI. The computation of the instantaneous surface heat flux from surface temperature measurement is presented. Similarly, the PIV setup is presented with validation of the setup and postprocessing to derive the instantaneous velocity field. LIF of acetone is also discussed, which is used to differentiate between laminar and turbulent flame. Laser ignition is also used in this thesis to induce ignition in a spray during spray FWI. For our analysis, the properties of the laminar flame during FWI are determined from 1D Cantera codes.

Further, the method of postprocessing of the heat flux trace to determine important properties of the heat flux trace is presented. It is found that $\boldsymbol{Q_P}$ is the important property whereas 15 repetitions are enough to reach convergence. The method of decomposition of post-FWI heat flux into high-frequency heat flux is presented.

The method of post-processing of the PIV velocity field is discussed. Using a frequency filter of 100Hz, high-frequency turbulent fluctuations are obtained. The turbulence is found to be homogenous, isotropic, and statistically stationary until flame disrupts the PIV signal. Suitable methods are defined to compute turbulence intensity, turbulence time scale, and length scale for further analysis.

With this knowledge, we can go to the next chapter where the results of different parametric variations are analyzed.

Chapter 3: Results of propagative flame in CVC

In this chapter, the results of the experiments conducted in CVC undergoing premixed propagative FWI are analyzed to determine the influence of variation of key parameters on the heat flux during FWI. These parameters are pressure during FWI (P_{int}) turbulence intensity (q), dilution of the fuel-air mixture (with inert gas), increase in mole fraction of oxygen in fuel-air mixture, sensor location, and fuel type on the heat flux. Through the analysis of the effect of each parameter, new insights into FWI are obtained whose implications are also discussed in this chapter.

3.1. Effect of the pressure during laminar FWI (P_{INT})

P_{int} is an important parameter that affects the heat flux during FWI. First, we will discuss relevant literature regarding the effect of P_{int} on Q_P to identify the relationship between them. Then, we will present the experimental methodology to obtain a variation in P_{int}. Finally, we will present the influence of P_{int} on the heat flux and the implications of such effects on the interpretation of the results obtained for other parametric variations.

3.1.1. Brief discussion from the literature

As flame propagates inside the CVC, the gas pressure increases due to combustion. The change in pressure leads to a change in the temperature of the fresh and burned gas. With the increase of pressure and temperature of the gas, the laminar flame properties pertinent to FWI (flame power, flame speed, flame thickness) and the fresh gas properties (density, specific heat capacity, conductivity) also change. These changes can affect Q_P during the FWI. Hence it is important to derive the dependency of Q_P on P_{int} to understand the independent effect of other parameters on Q_P.

It is found in the literature that Q_P is related to P_{int} by power-law. This description has been built through experiments on a wide range of pressure from <1 bar up to 150 bars [42, 44]. This relationship is shown in Equation 35. The value of ***b*** is evaluated in laminar conditions in at least 2 studies conducted at ENSMA. In a CVC, CH_4-air mixture at 0.7 equivalence ratio (P_{int} up to 2.5 bars), ***b*** is found to be 0.4 whereas in RCM, CH_4-air mixture at stoichiometric conditions (P_{int} up to 140 bars), ***b*** is found to be 0.5. In RCM, the authors use a variation in density to achieve the target P_{int}. To our knowledge, in literature, it has not been established if the power-law coefficients (***a, b***) are dependent on any other parameters. Moreover, the coefficients are not fully characterized in different experiment setups with different boundary conditions. The difference in ***b*** obtained in the literature leads us to hypothesize that ***b*** can be sensitive to variation in the composition of the fuel-air mixture or different experiment setups as the studies cited here use different equivalence ratios and density of CH_4-air mixtures in 2 different setups.

Equation 35: $$Q_P = aP_{int}^{\ b}$$

The importance of determining such a relationship lies in the possibility it offers to separate the effect of pressure (and its other pressure-temperature dependent parameters) from parametric variations conducted in this thesis, without having to untangle the relationship of pressure-temperature dependent parameters. Hence, we will determine such a relationship for our experiment setup, specifically a power-law.

3.1.2. METHOD TO ACHIEVE VARIATION IN P_{INT}

In this section, we present the method to achieve P_{int} to study its effect on Q_P. P_{int} dependency in our experiments is evaluated with the reference operating condition, i.e., CH_4-air mixture at 0.8 equivalence ratio at initial pressure of 14 bars. The strategy to obtain different P_{int} consist of varying the duration between spark timing and timing of FWI. This is achieved by moving the wall towards or away from the

spark. Three positions of wall TC assembly are then selected that can result in three different P_{int}. Details of the experiments carried out to vary P_{int} for laminar conditions are shown in Table 6.

Table 6: Experiment details to achieve P_{int} Variation

Reference composition: CH_4-Air at 0.8 equivalence ratio at 10 Kg/m^3, initial temperature ~ 473 K, initial pressure ~ 14 bars, 1 Fan ON during mixing and OFF 60 s before the spark, Fan at 3000 RPM
X_D = 30 mm
X_D = 60 mm
X_D = 80 mm

To reach laminar conditions a specific operating strategy for the mixing fans is established. It consists in operating one fan only during the mixing of the gasses and switching it OFF 60s before spark timing. Therefore, we first need to characterize the aerodynamics for all X_D. Figure 103 shows the evolution of turbulent fluctuations at one point for all X_D. In this figure, we can see that barring a few noisy peaks, the turbulent fluctuations are within the range of -0.1 to 0.1 m/s with a mean ~ 0.0001 and RMS ~ 0.01 which is much less than the uncertainty on the measurement, for all the three different X_D. Calculating the turbulence intensity we obtain, for all distances, $\frac{q}{S_L} < 0.2$ and $\frac{L_T}{\delta_F} < 0.1$, where q is turbulence intensity, S_L is laminar flame speed, L_T is turbulence length scale and δ_F is laminar flame thickness. These calculations indicate that all three experiments lie in laminar flame regimes. Moreover, since the measured turbulent fluctuations lie within the measurement uncertainty, we conclude that the aerodynamics of the three test cases are similar and laminar.

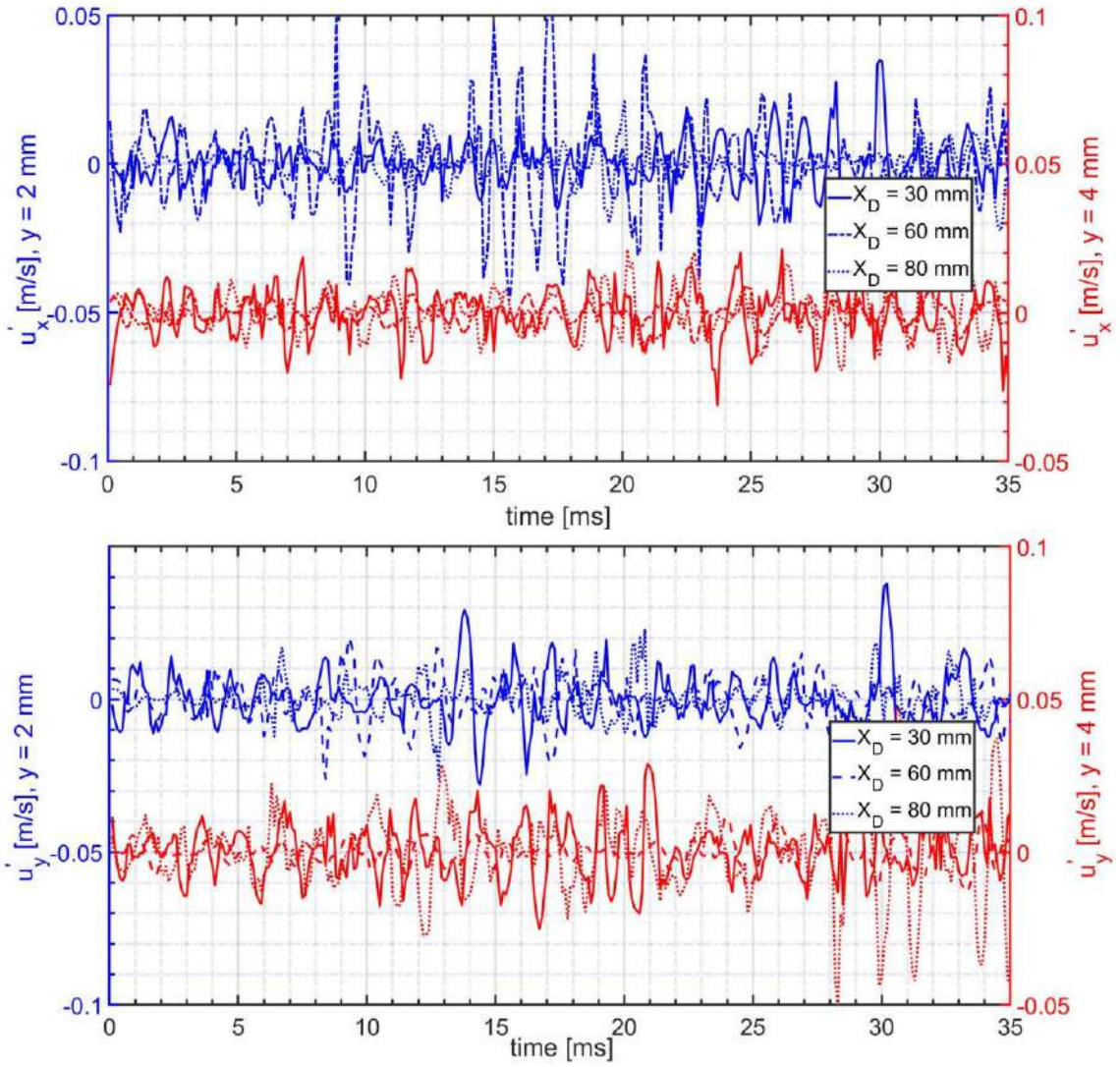

Figure 103: Turbulent fluctuations (u'_x,u'_y) at two different points in space (y = 2mm and 4 mm from the center of the wall) for the three-wall distance variation for the laminar case.

Now, the influence of the wall distance on P_{int} can be determined. Figure 104 presents the mean pressure evolution for all three cases along with the individual P_{int} for each repetition. It can be seen that P_{int} indeed varies with X_D. P_{int} for different X_D is shown in Table 7. These results confirm the strategy designed to vary P_{int}, keeping the aerodynamics constant.

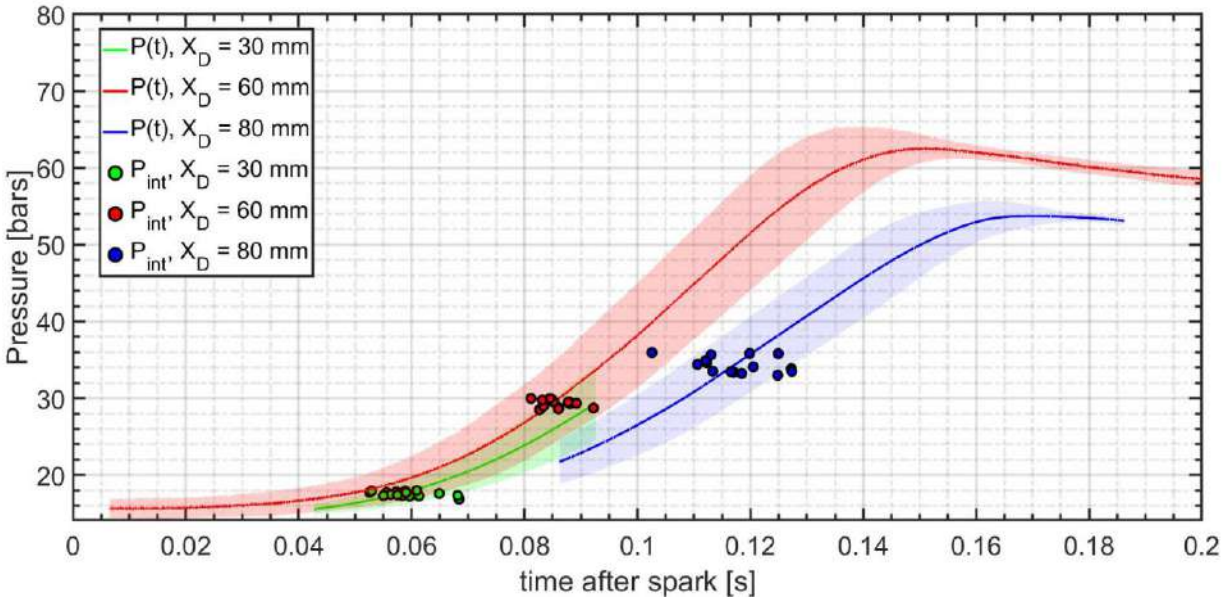

Figure 104: ***P(t)*** for the three variations in wall distances (***X_D***) for the laminar case

Table 7: Effect of ***X_D*** on ***P_{int}*** in laminar regimes

X_D, mm	***P_{int}***, bars
30	17.5±0.3
60	29.3±0.5
80	34.3±1.1

3.1.3. EFFECT OF P_{INT} DURING FWI ON Q_P

The effect of ***P_{int}*** on the heat flux for our experiments can now be determined. Figure 105 presents the heat flux traces obtained for the three previously discussed test cases shown in Table 7. It can be seen that ***Q_P*** increases with ***P_{int}*** between 17 and 34 bar.

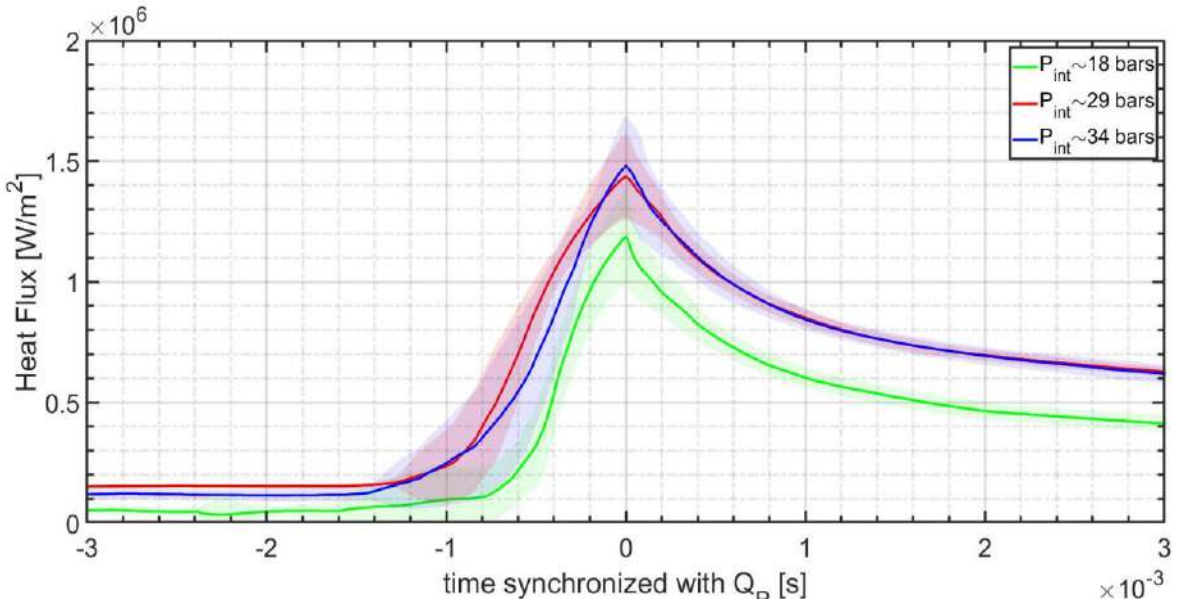

Figure 105: Effect of P_{int} on Q for different turbulence cases

Using a method of minimization of error, we can use these results to obtain the power-law coefficients discussed in section 1.1.1. shown in Equation 36 and Figure 106. The coefficient ***b*** obtained in our experiments (0.35) is different from the one obtained in the literature (0.5 at Φ=1 in RCM and 0.4 at Φ=0.7 in CVC). This difference can be attributed to different gas compositions, wall temperatures, and experiment configurations. The exact cause cannot be determined. However, for experiments where composition, experiment configuration, and wall temperatures are kept constant, the pressure dependency on Q_P is expected to remain the same. Therefore, for this thesis, as the experimental setup is the same throughout all experiments, the power-law relation established in Equation 36 can be used to separate the effect of P_{int} and isolate the effect of other parametric variations.

Equation 36: $$Q_P = 0.43 \times P_{int}^{0.35}$$

In this section 0we find the power-law dependency off Q_P on P_{int} in laminar conditions given in Equation 36. The variation in P_{int} is achieved by varying X_D.

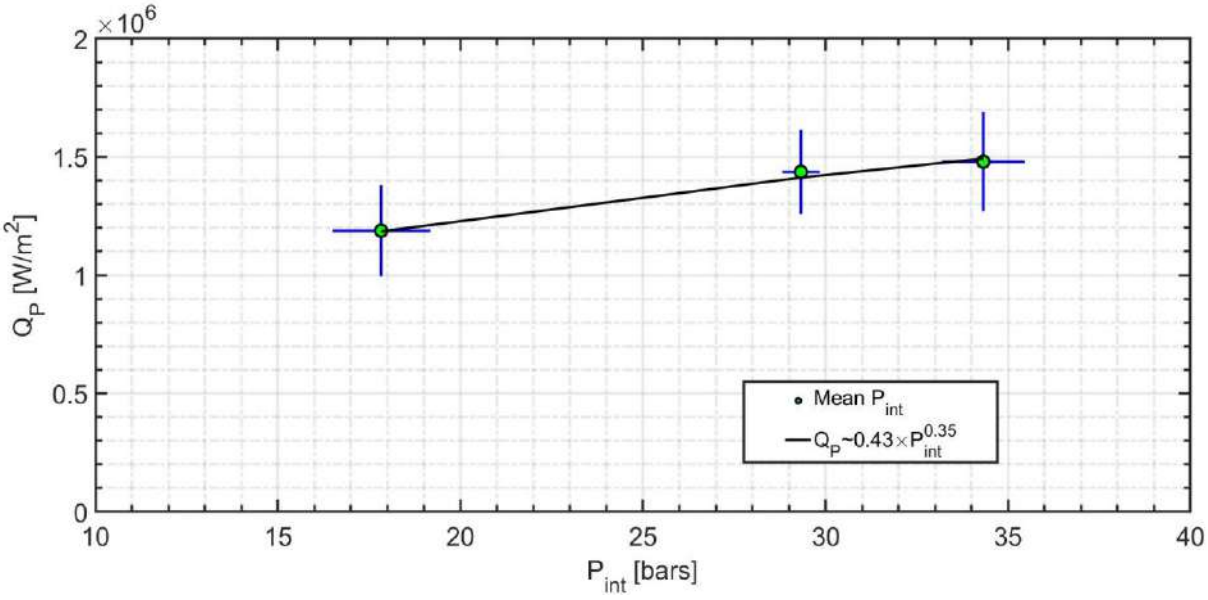

Figure 106: Power-law dependency of Q_P on P_{int} for laminar case

3.2. Effect of Turbulence variation

In this section, the influence of turbulence on heat flux is studied. First, the strategy to achieve turbulence variation in the CVC is presented. Then we characterize the aerodynamics and the turbulence intensity levels achieved. Finally, their effects on heat flux during FWI are analyzed.

3.2.1. Effect of fan operation on the flow field inside CVC

Four types of fan operation are used in this thesis to generate variations in aerodynamics inside the CVC. The details of the fan operation and the corresponding notation are given in Table 8. In this section, we will discuss the different large-scale mean flow fields arising from different fan operations.

At t~0 (spark timing), the flow is parallel to the wall for all cases, except for LT-60 where the velocity is too small to interpret as flow parallel to the wall. The flow behavior at different times after spark for HT2-60 for ROI1 is shown in Figure 107, Figure 108, and Figure 109. In Figure 107, at 3ms after spark, the flow field imposed by the fan i.e., flow parallel to the wall is seen. The velocity parallel to the wall (U_x) is decreasing in the order, HT3-60>HT2-60>Reference.

Table 8: Different Fan operations carried out in this thesis

Reference composition: CH_4-Air at 0.8 equivalence ratio at 10 Kg/m^3, initial temperature ~ 473 K, initial pressure ~ 14 bars, X_D = 60 mm				
Fan blade type	Number of Fans	Fan Speed in fresh gas (RPM)	Fan operation	Notation
Type 1	1	3000	OFF 60s before spark	LT-60
Type 1	1	3000	Always ON	Reference
Type 2	2	4000	Always ON	HT2-60
Type 2	3	4000	Always ON	HT3-60

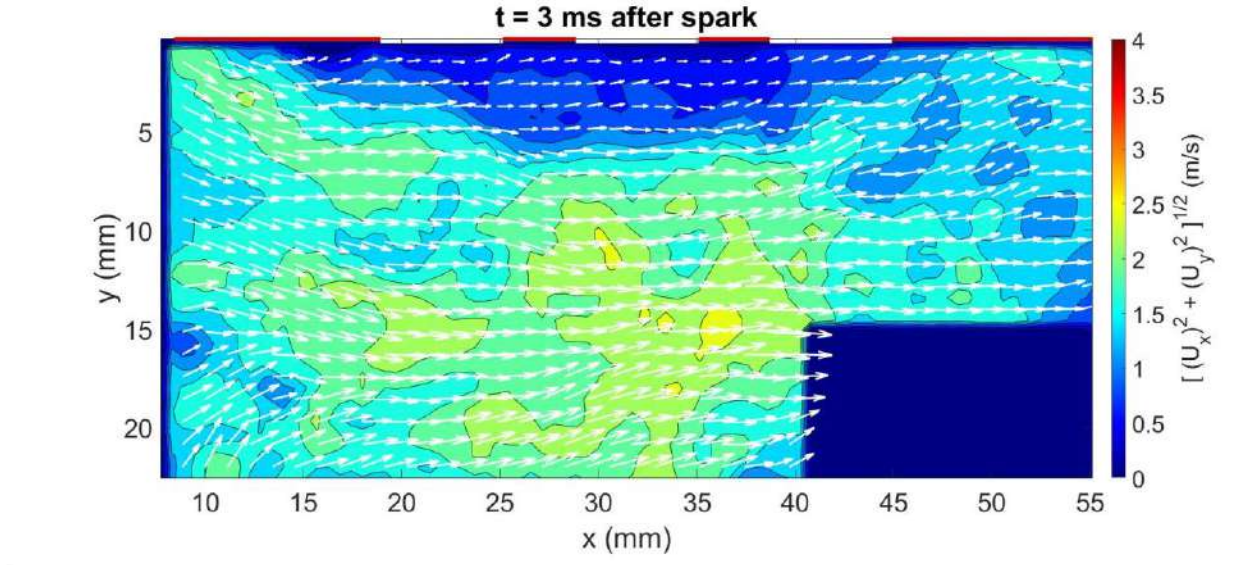

Figure 107: Flow field in HT2-60 case with 2 fans at ***t*** = 3ms after spark. The three white bars are the surface TCs

At ***t*** = 13 ms and 16.5 ms, in Figure 108 and Figure 109 respectively, the flow field appears to be affected by the flame leading to a jet-wall impingement type of flow. This result has already been observed in engines [99]. The velocity normal to the wall (U_y) increases during this time. This modification of flow velocity is common to all fan operations used in this thesis. This effect of flame takes action much before flame enters the field of view. After the flame affects the flow, the flow starts to become normal to the wall. The absolute velocities (U_y) may differ in order HT3-60>HT2-60>Reference>LT-60. The velocity parallel to the wall (U_x) rearranges to accommodate jet wall impingement flow.

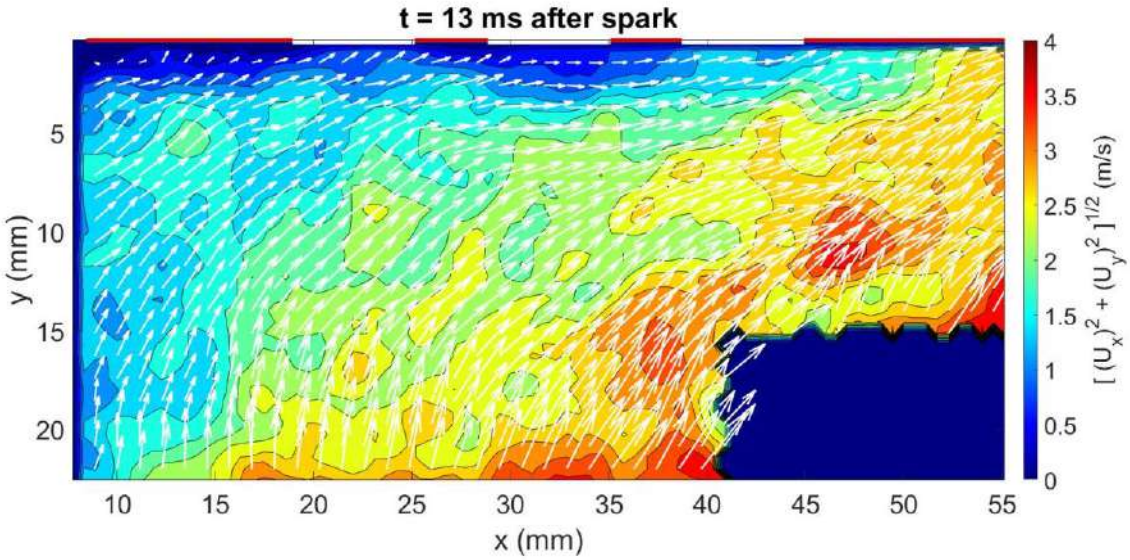

Figure 108: Flow field in HT2-60 case with 2 fans at ***t*** = 13 ms after spark.

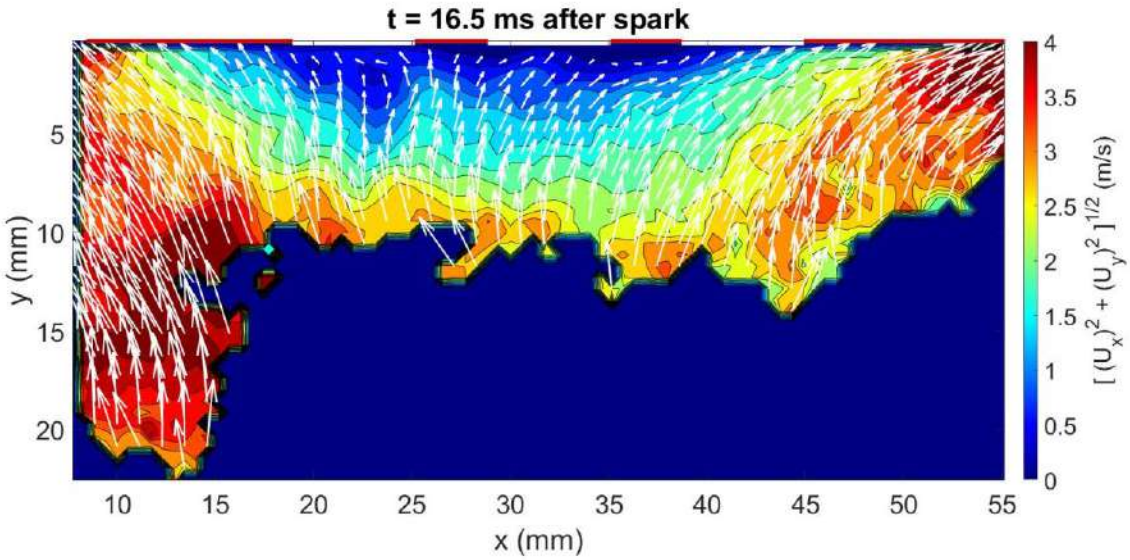

Figure 109: Flow field in HT2-60 case with 2 fans at ***t*** = 16.5 ms after spark.

As mentioned earlier LT-60 test case exhibits a different behavior at spark timing. At ***t***~0, the flow field is quiescent. Nevertheless, sometime after the spark, the flame-induced flow field is seen to be similar to what we discussed earlier for HT2-60 (cf. Figure 110 and Figure 111). Similarly, as for the previously discussed test case, the flow is significantly affected by the flame propagation.

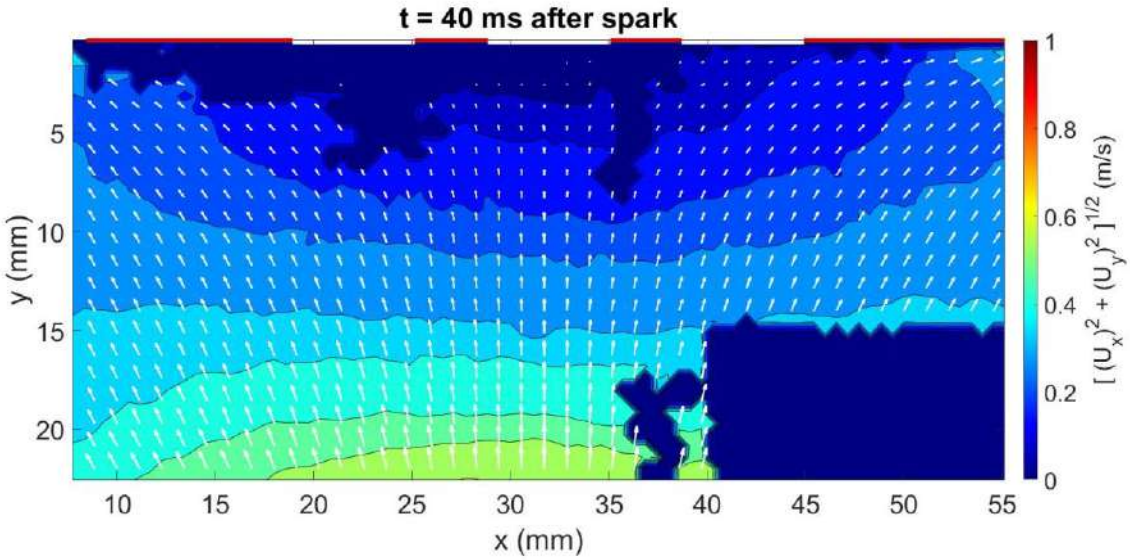

Figure 110: Masked flowfield for LT-60 after flame affects the flow field.

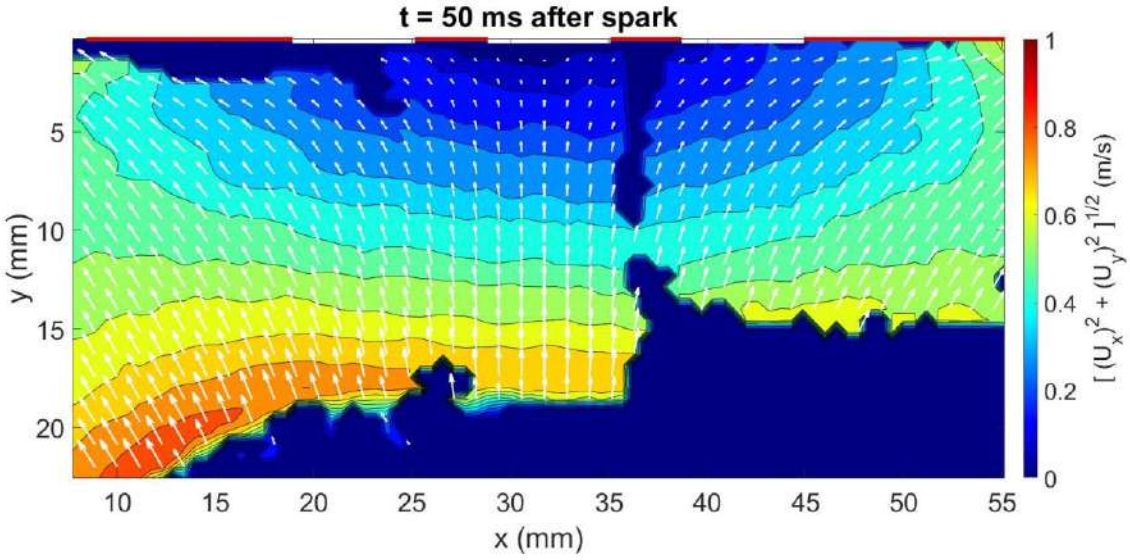

Figure 111: Masked flow field for LT-60 after flame affects the flow field and flame is in RoI 1.

Mean velocities ($\overline{U_x}$,$\overline{U_y}$) evaluated at two positions (2mm and 4mm from the wall) are shown in Figure 112 and Figure 113, for LT-60 and HT2-60, respectively. It is seen that the magnitude of $\overline{U_y}$ increases as the flame approach the wall. However, after a certain time, the magnitude of $\overline{U_y}$ decreases again. As reported in the literature, this can be attributed to the deceleration of the flame close to the wall [42, 51] A detailed discussion on this deceleration is carried out in section 3.2.2These observations are common

to both the points of observation (***y*** = 2 mm and 4 mm from the wall). We can also see that at ***y***=2 mm flame starts to affect the velocity trace at a timing later than for ***y***=4 mm. The trend observed at these locations is common for all locations in ROI1.

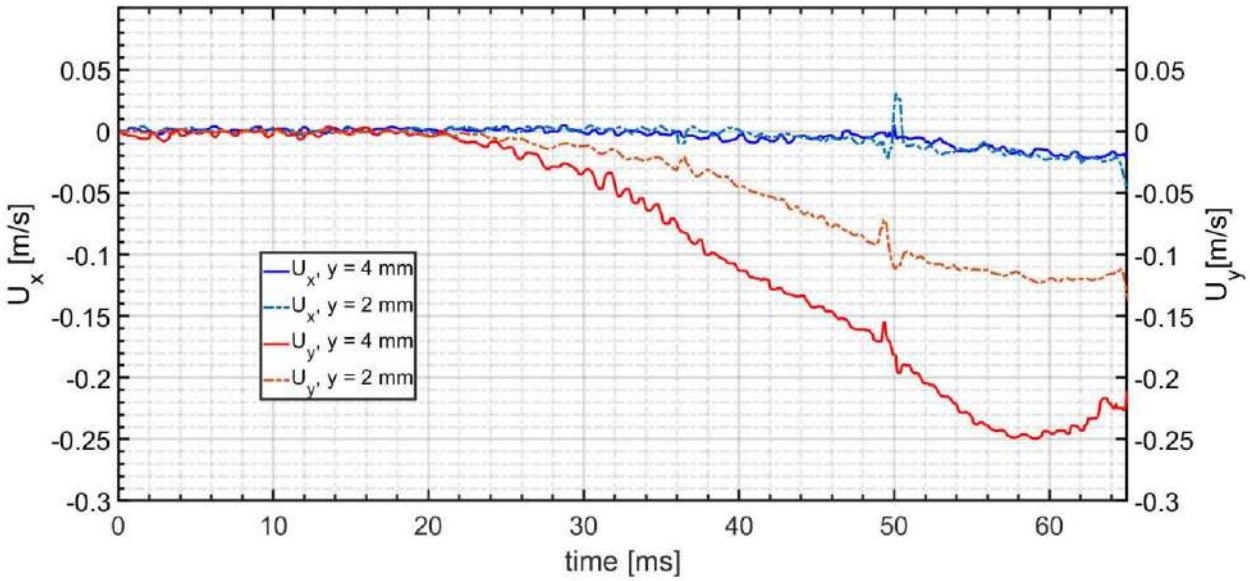

Figure 112: Average flowfield at one point in space with y distance from the center of the wall, for LT-60.

$\overline{U_x}$ for HT2-60 also shows a change (shown in Figure 113) while $\overline{U_x}$ for LT-60 does not have any big change (shown in Figure 112). There exists a region of low overall $\overline{U_x}$ and $\overline{U_y}$ (in magnitude), which is due to confinement of the flow by the wall (seen in Figure 109 and Figure 111) and flame. To accommodate for the strong jet wall impingement type of flow the magnitude of vectors $\overline{U_x}$ on either side of the confinement region also increases as shown in Figure 113. A schematic of the flow field is given in Figure 114. In this figure, we can see the region of confinement near the TCs.

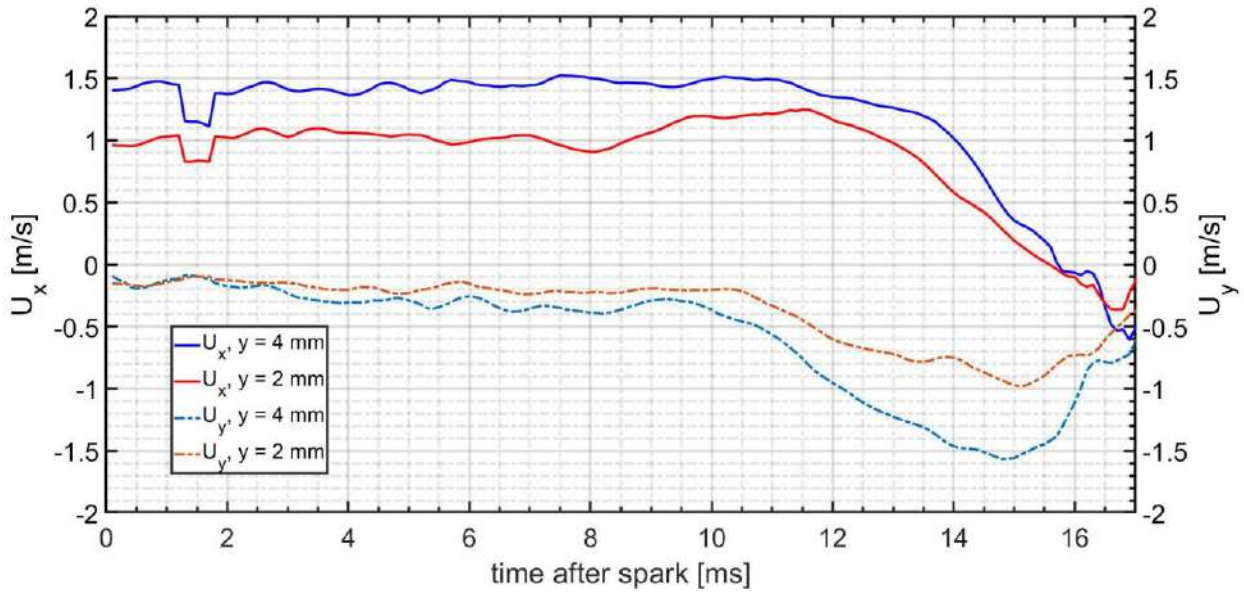

Figure 113: Average flowfield at one point in space, ***y*** is the distance from the center of the wall (HT2-60).

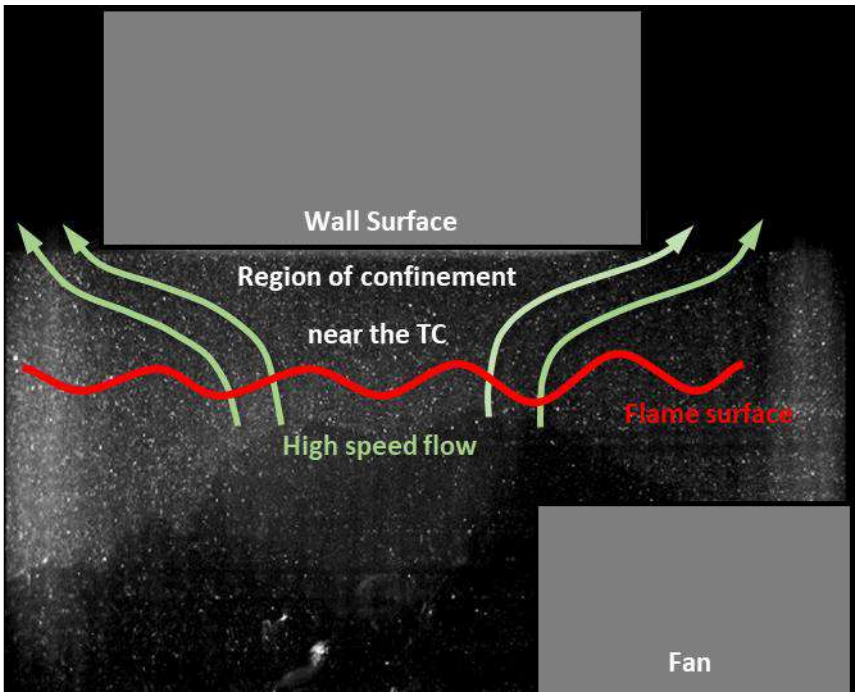

Figure 114: Schematic of the flow field prior to FWI

The turbulence intensities (***q***) are then evaluated for the four operating conditions. It can be seen in Figure 115, different levels of turbulence intensity are achieved thanks to the fan operation strategy. The

two extremes are LT-60 and HT3-60. The LT-60 leads to q~0.01 m/s while HT3-60 leads to q ~ 0.5 m/s. q for LT-60 is close to the uncertainty (0.014 m/s) indicating near-zero turbulence intensities. q for HT2-60, HT3-60 are significantly higher than the uncertainty for velocity (0.071 m/s).

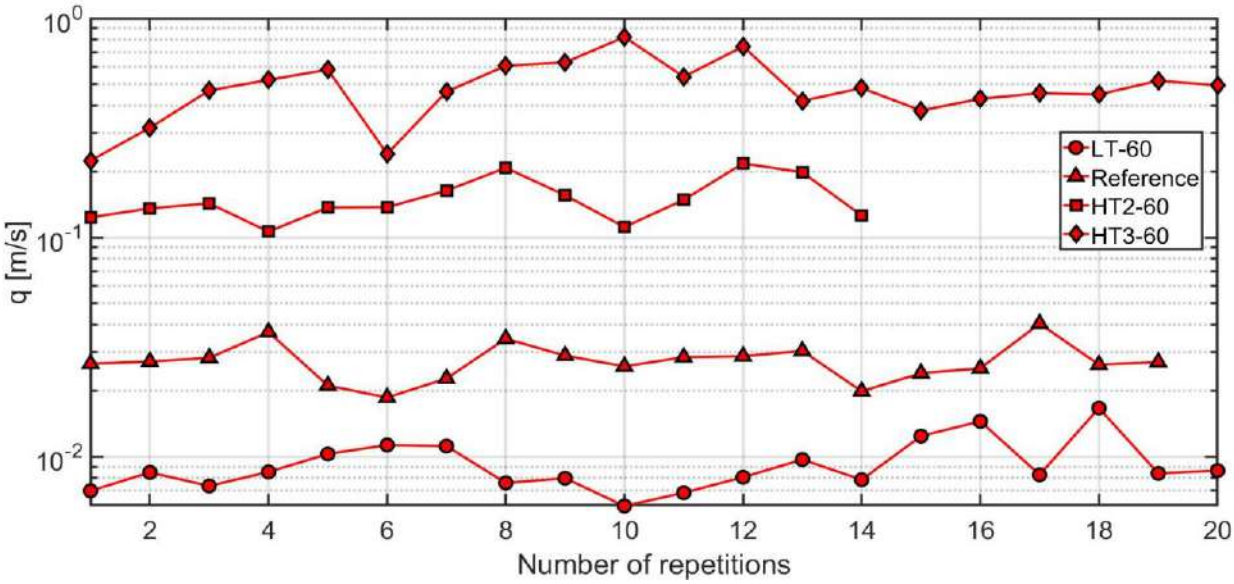

Figure 115: Turbulence intensity(q) for different experiments

3.2.2. CORRELATION OF Q_P WITH LARGE SCALE VELOCITY

To study the influence of the large-scale flow field on Q_P, we need to discuss the flow field just before FWI in detail. We will investigate this topic by tracing velocity till the instant of flame arrival at the point of observation.

For this purpose, we will evaluate the velocity profile at 2mm from the center of the wall (shown in Figure 116). To get a better location of the flame front when the flame is near the wall we use direct visualization of PIV, instead of the automatic mask discussed in the methodology section. In this figure, we can see a relatively high density of PIV signal on fresh gas compared to no PIV signal in burnt gas leading us to detect the flame front at the point of observation.

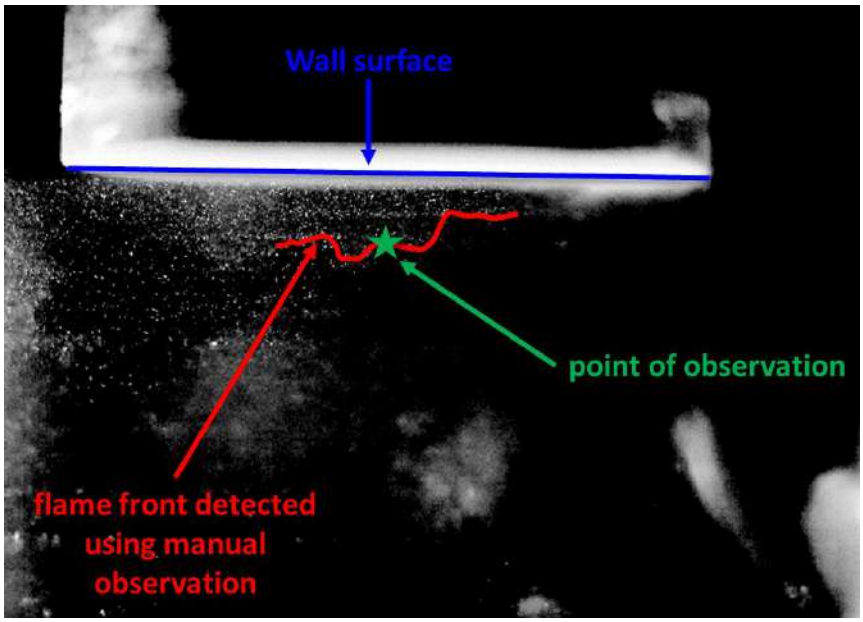

Figure 116: Sample of manual detection of the flame front

We choose to present the experiment HT2-60 to illustrate this analysis as this test case provides high velocity at t = 0 (U_x~1.5 m/s) and at an intermediate time (U_y~1.5 m/s) due to flame imposed velocity. The instantaneous velocity determined from the unmasked PIV flowfield, used for this analysis is shown in Figure 117. Different repetitions are shown as different colors in this plot. The flame's arrival in time is denoted by a circular marker. In this figure, we can see that both U_x and U_y show an increase in the magnitude as the flame approaches the point of observation. This increase starts between t = 10 ms and 14 ms. Immediately after this increase, we can see a decrease in the U_x and U_y magnitudes. This observation is common to all repetitions.

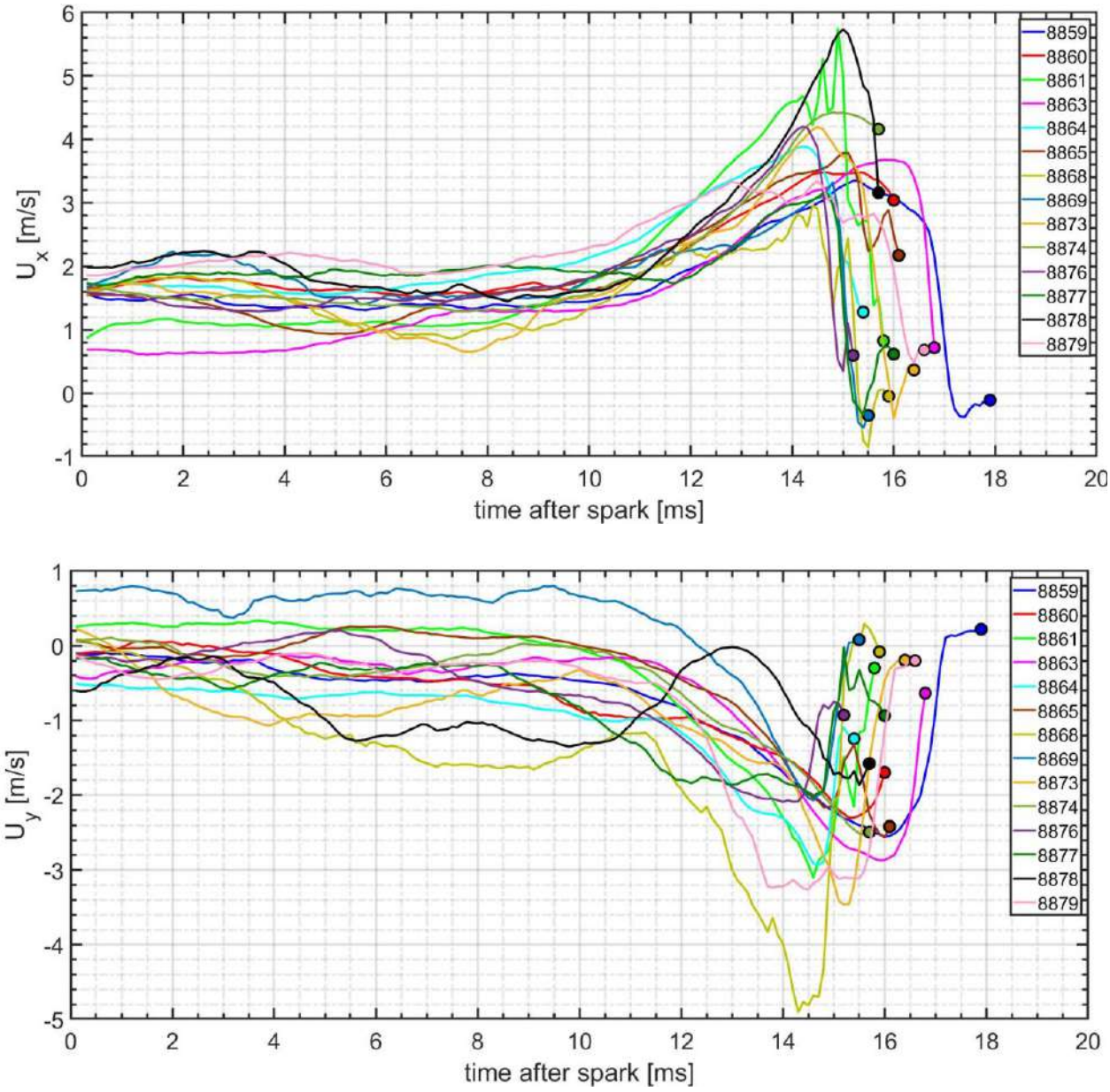

Figure 117: Instantaneous velocity at ***y*** = 2 mm from TC for HT2-60. Top, ***x*** component instantaneous velocity, U_x. Bottom ***y*** component instantaneous velocity, U_y.

For some of the repetitions (6/14 repetitions for U_y and 5/14 repetitions for U_x), we can trace the deceleration fully until the magnitudes U_x and U_y decreases below 0.5 m/s. For this operating condition, the amplitude of the turbulent fluctuations is~0.5 m/s. Hence, we can say the magnitude of U_x and U_y fall to the level of turbulent fluctuations. This decrease in the magnitude of large-scale velocity is attributed to the confinement of the fresh gas near the wall where they can only be compressed (rather than getting

pushed). There is no scope of increase in velocity, after reaching a minimum value until the FWI, as there is no scope of gas movement due to confinement.

For the rest of the repetitions, we can trace either only a part of the deceleration where U_x and U_y are falling in magnitude but not exactly down to 0.5 m/s (4/14 repetitions for U_y and 6/14 for U_x) or that the magnitude of U_x and U_y fell to < 0.5 m/s and then increased to a small value above 0.5 m/s (4/14 repetitions for U_y and 3/14 for U_x). We hypothesize that the noise in the PIV signal near the flame front as the flame front approaches the point of observation is the cause of noise in U_x and U_y which otherwise would continue to fall to well below 0.5 m/s (level of turbulent fluctuations). Combining this hypothesis, information from literature, and our observations we conclude that the magnitude of U_x and U_y for all experiments and repetitions likely reaches the magnitude of u'_x and u'_y in the region close to the wall just before the flame arrives at the wall. This implies a $\overline{U_x}$ and $\overline{U_y}$~ 0 m/s near the wall before FWI. Hence, we conclude that Q_P is not influenced by large-scale mean velocity for the different experiments of turbulence variation conducted in this thesis.

3.2.3. Effect of variation of Pint for non-laminar conditions

Different turbulence intensities affect the propagation of the flame in the CVC [17]. Hence, the different experiments corresponding to different turbulence variations shown in Table 8 lead to different pressure evolution in the CVC. A direct comparison is only possible if we obtain Q_P for a range of P_{int} for relevant turbulent conditions. The objective will be to reach a power-law relationship similar to the one discussed in section 0The strategy to achieve a variation in P_{int} is the same i.e., varying X_D. In this section, we, therefore, discuss the effect of variation of X_D on the turbulence intensity. Then we discuss the effect of P_{int} on Q_P for different fan operations. The complete experiment matrix is given in Table 9.

Table 9: Different Fan operations carried out in this thesis with variations in X_D

Reference composition: CH_4-Air at 0.8 equivalence ratio at 10 Kg/m^3, initial temperature ~ 473 K, initial pressure ~ 14 bars					
Fan blade type	No. of Fans	Fan Speed at t=0 RPM	Fan operation	X_D mm	Notation
Type 1	1	3000	OFF 60s before spark	30	LT-30
Type 1	1	3000	OFF 60s before spark	60	LT-60
Type 1	1	3000	OFF 60s before spark	80	LT-80
Type 1	1	3000	Always ON	60	Reference
Type 2	2	4000	Always ON	30	HT2-30
Type 2	2	4000	Always ON	60	HT2-60
Type 2	2	4000	Always ON	80	HT2-80
Type 2	3	4000	Always ON	30	HT3-30
Type 2	3	4000	Always ON	60	HT3-60
Type 2	3	4000	Always ON	80	HT3-80

The turbulence intensity, ***q***, is computed from PIV for all the experiments. The results are presented in Figure 118 and summarized in Table 10. We achieve major change (~3000-5000%) in ***q*** due to variation in fan operation (LT-XX to HT2-XX, HT3-XX). X_D variations induce change in ***q*** (~50-100%) which is small in comparison to the variation in ***q*** induced by different fan operations. The fan operation variation induces a significant change in ***q*** while, X_D induces a negligible change in ***q***.

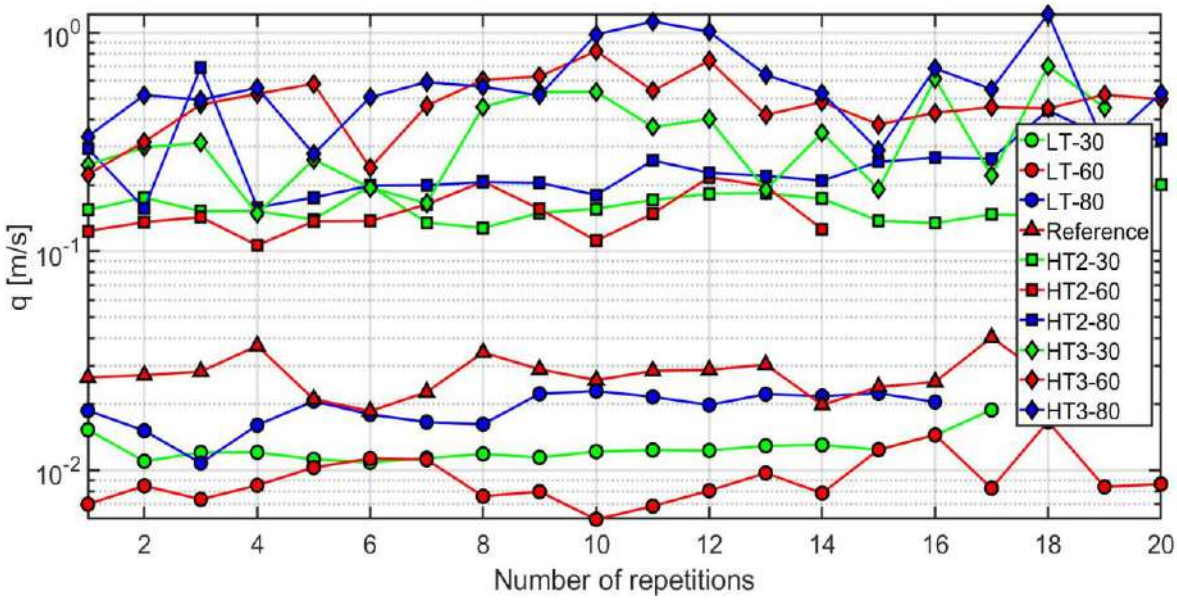

Figure 118: Turbulence intensity (***q***) for experiments in Table 9

Table 10: P_{int}, ***q***, and Q_P for experiments in Table 9

Experiment notation	P_{int} bars	***q*** m/s	Q_P MW/m^2
LT-30	17.5±0.3	0.013	1.17±0.18
LT-60	29.3±0.5	0.010	1.44±0.18
LT-80	34.3±1.1	0.019	1.45±0.18
Reference	37.6±3.3	0.028	1.90±0.21
HT2-30	31.3±4.6	0.159	1.76±0.30
HT2-60	46.2±3.9	0.151	1.91±0.28
HT2-80	55.4±5.0	0.266	2.76±0.41
HT3-30	34.0±4.7	0.350	1.86±0.27
HT3-60	49.4±4.6	0.500	2.04±0.38
HT3-80	58.3±3.1	0.560	2.80±0.35

The pressure evolution with P_{int} for HT2-XX and HT3-XX is given in Figure 119. The low turbulence cases results (LT-XX) are presented in Figure 104 and Figure 105. With the change in X_D we observe the change in P_{int}, although, there is scattering on P_{int}. P_{int} corresponding to experiments in Table 9 is given in Table 10. With the variation of X_D, P_{int} variation is greater than three times the standard deviation on P_{int}.

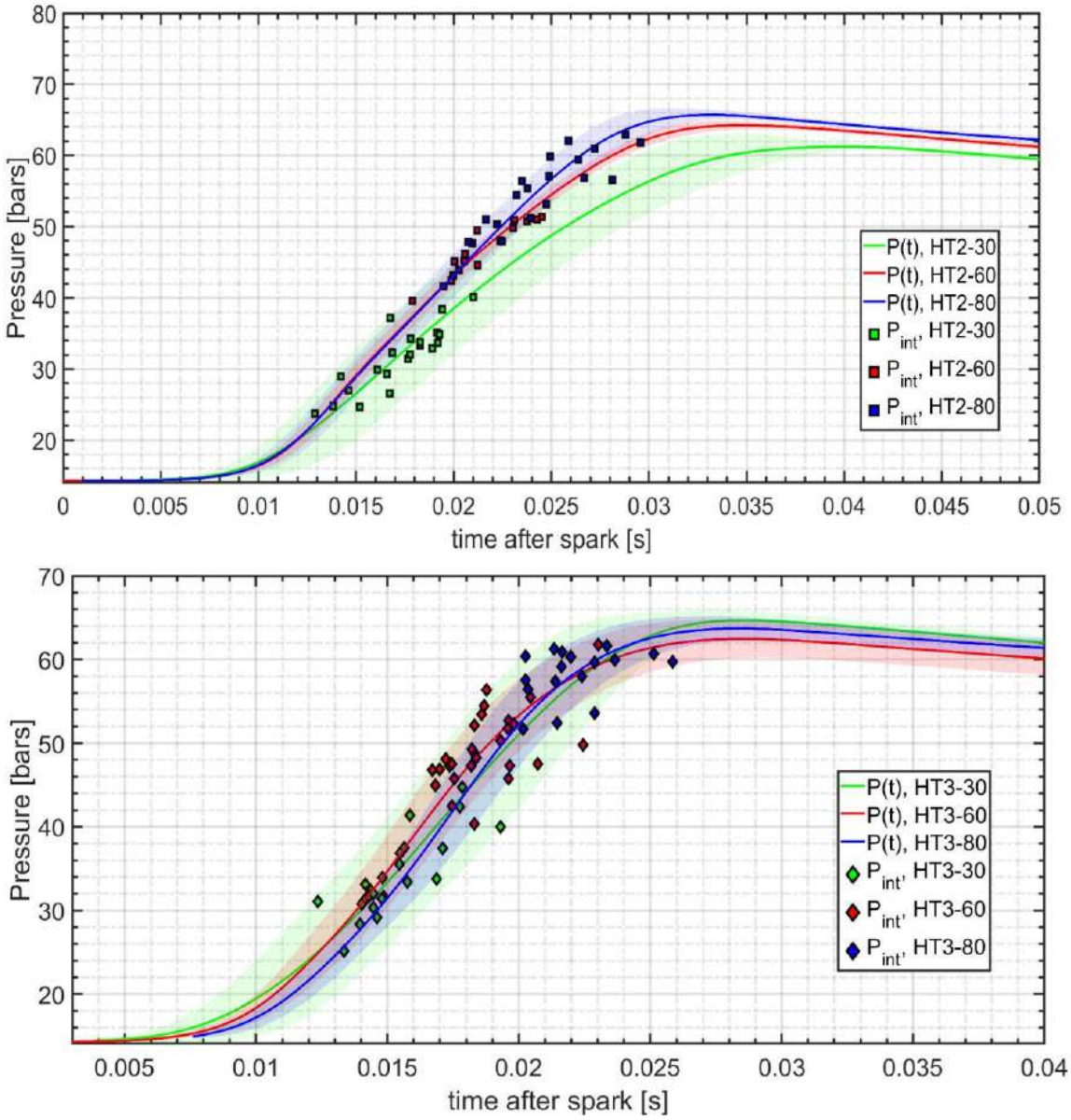

Figure 119: Pressure evolution: ***P(t)*** and P_{int} for experiments in Table 9. Top: HT2-XX experiments. Bottom H3-XX experiments

In this subsection, we verified that by changing X_D, there is no significant change in ***q*** in comparison to the change in ***q*** due to fan operation. The effect of ***q*** on the heat flux trace can be obtained at a similar P_{int}. Changing X_D there is a significant change in P_{int}, which can be used to study the dependency of Q_P on P_{int} for turbulent conditions.

3.2.4. COMBUSTION REGIMES

The relative strength of turbulence to that of laminar flame is used to define various combustion regimes. Based on our calculation of turbulence properties, i.e., integral length scale and turbulent intensity, all the experiments in Table 9 are placed in the combustion regimes diagram in Figure 120. The shaded portion indicates a turbulent combustion regime in engines. Placing our experiments in a combustion regime diagram we see that HT2-XX and HT3-XX are very close to the turbulent combustion regimes encountered in engines while LT-XX lies in laminar flame regimes.

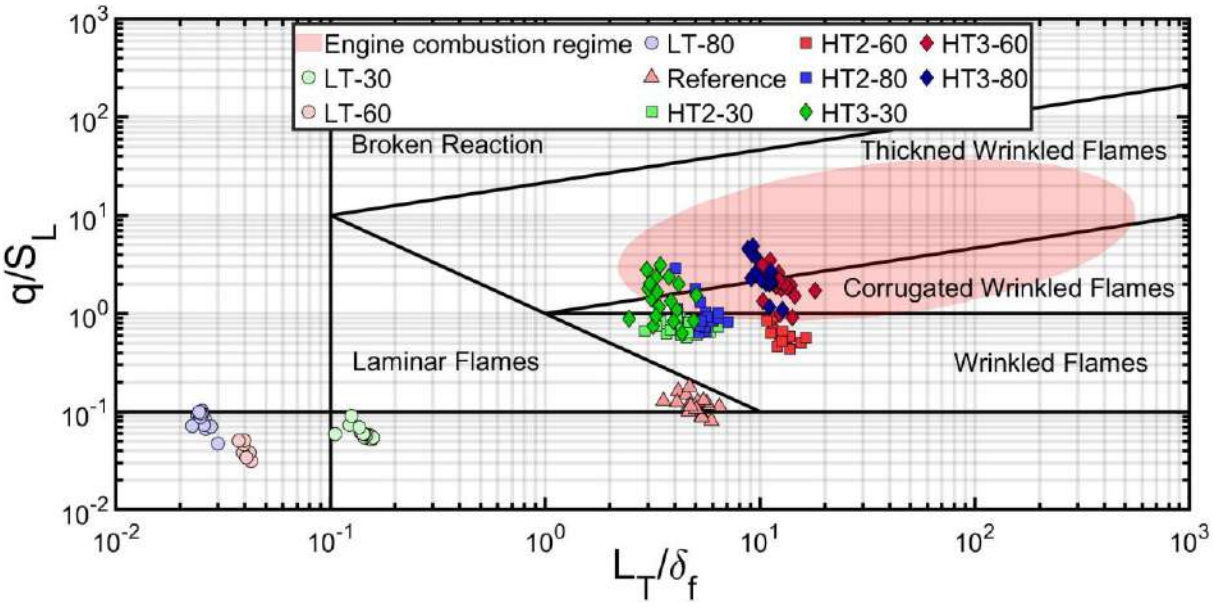

Figure 120: Different regimes of combustion achieved during experiments in CVC with different fan operations

To confirm this description, LIF images can be used to provide qualitative insight into the various combustion regimes. Such characterizations were carried out using type 1 wall TC assembly for LT-60 and reference test cases. For laminar regimes, a spherical flame front with no wrinkles is seen in the PIV image far from the wall while a flat flame front with no wrinkles can be seen (Figure 121). The relative flame wrinkling (***RFW*** cf. section 2.2.3.2 for calculation method) computed from LIF images yields 1.05±0.3 for LT-XX cases.

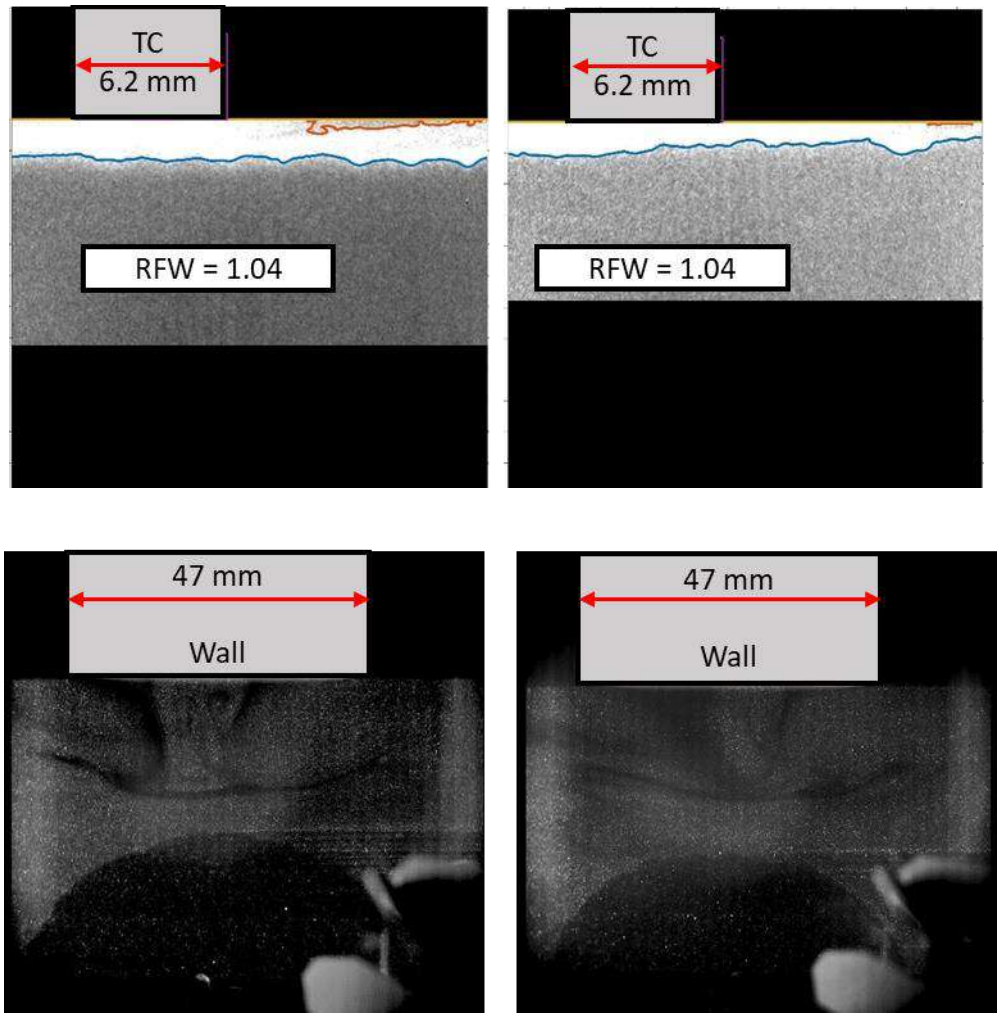

Figure 121: Non-simultaneous LIF images (Top) and PIV images (Bottom) showing the flame front in laminar regimes

The reference case lies in the border of the laminar and wrinkled flame regime (Figure 120). For the Reference case, a wrinkled flame front is seen in the PIV image, far from the wall, in Figure 122. Similarly, a wrinkled flame front is seen near the wall in the LIF image shown in Figure 122. ***RFW*** computed from LIF images yields 1.48±0.4 for the Reference case. This indicates that the turbulence intensity is higher for the Reference case than LT-60, which is in line with the calculation of ***q*** from PIV (***q*** for the Reference case is 0.028 m/s while ***q*** for LT-60 is 0.010 m/s, see Table 10).

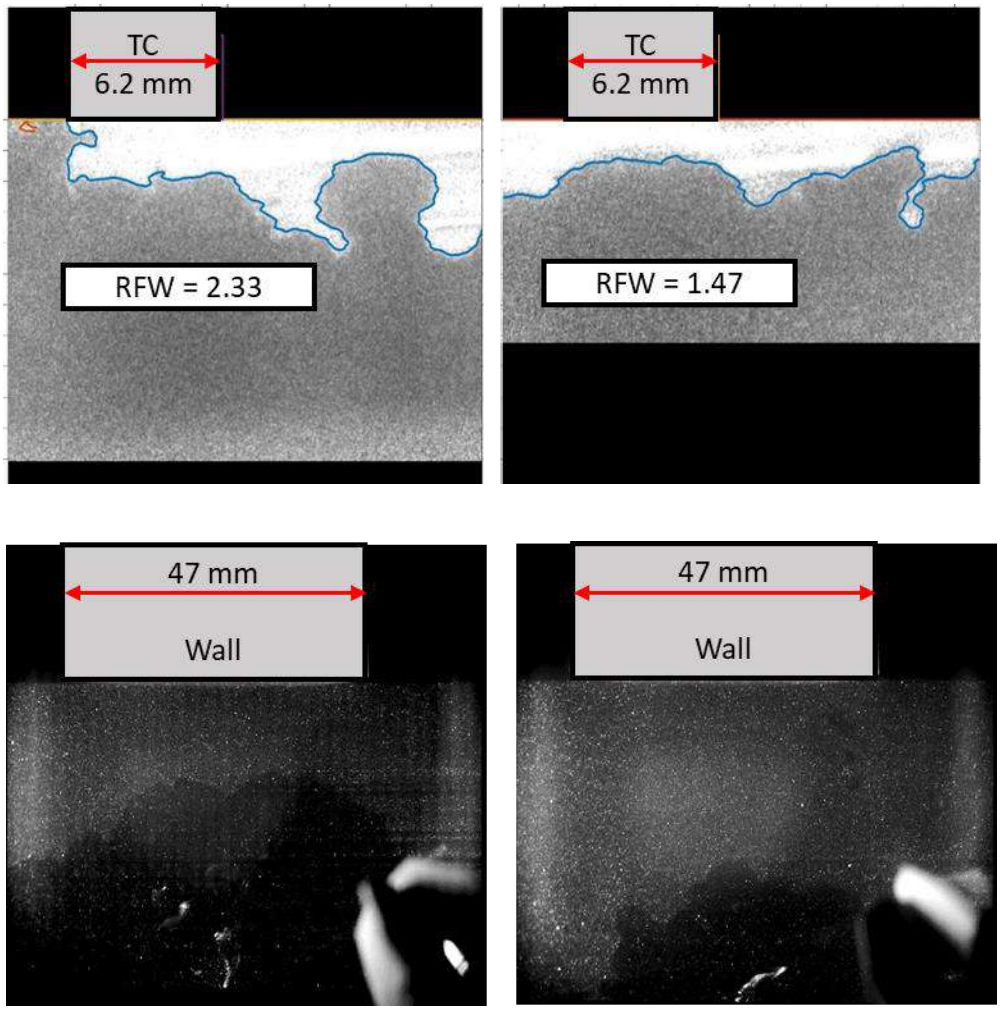

Figure 122: Non-simultaneous LIF images (Top) and PIV images (Bottom) showing the flame front in Reference cases

For higher turbulent intensity cases, a highly wrinkled flame front can be seen. Figure 123 shows the PIV images obtained for the HT2-60 case (LIF image for this experiment is not carried out). Even though the flame front for the Reference case shows wrinkles it is not strictly in the wrinkled flame regime as per Figure 120, as the boundaries of the combustion regimes diagram are not absolute.

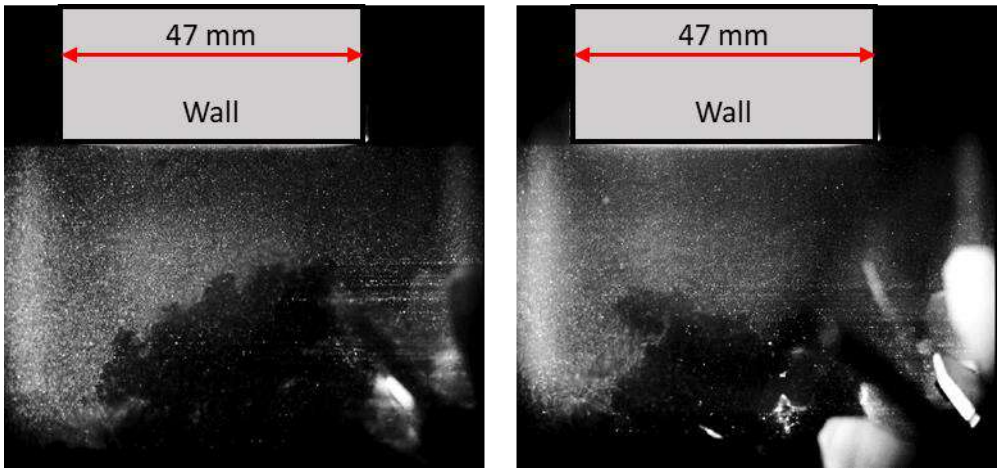

Figure 123: PIV images showing the flame front in high turbulence cases

Overall, the experiments conducted in this thesis range from laminar flame regimes (LT-XX) to turbulent combustion regimes (HT2-XX, HT3-XX). It is interesting to note that the levels of turbulence reached for higher turbulent intensity test cases lead to similar combustion regimes as those encountered in IC engines.

3.2.5. CORRELATION OF Q_P WITH HF TURBULENCE VARIATION

We now analyze the dependency of $\boldsymbol{Q_P}$ on $\boldsymbol{P_{int}}$ for the experiments presented in Table 9. The objective is to understand the influence of $\boldsymbol{q}$ on $\boldsymbol{Q_P}$. The dependency of $\boldsymbol{Q_P}$ solely on $\boldsymbol{P_{int}}$ can be evaluated using the power-law dependency determined for laminar FWI (Equation 36 in section 3.1.3). To analyze turbulent combustion, we study the dependency of $\boldsymbol{Q_P}$ on $\boldsymbol{P_{int}}$ shown in Figure 124. Compared to the low turbulent levels represented in green, $\boldsymbol{P_{int}}$ for turbulent cases is less well separated. Instead, a continuous scatter of $\boldsymbol{P_{int}}$ is obtained for the HT2-XX and HT3-XX series of experiments. From Figure 124 we can find that $\boldsymbol{Q_P}$ increases continuously with $\boldsymbol{P_{int}}$. At low $\boldsymbol{P_{int}}$, the difference between $\boldsymbol{Q_P}$ for turbulent FWI and $\boldsymbol{Q_P}$ for laminar FWI is small. This difference rises with an increase in $\boldsymbol{P_{int}}$ denoted by the double arrow. The mean values of $\boldsymbol{Q_P}$ for turbulent regimes is~24% higher than $\boldsymbol{Q_P}$ for laminar regimes at low pressure. However, as $\boldsymbol{P_{int}}$ increases, we can see the difference in $\boldsymbol{Q_P}$ between turbulent (from red and blue scatter) and

laminar regimes (from the power-law fit in green) rise to~55% on the mean values of Q_P. Although the amount of data for turbulent regimes is not perfect for determining a fit, the scatter seems to depend on an exponent b >1 if the data is to follow a power-law relationship.

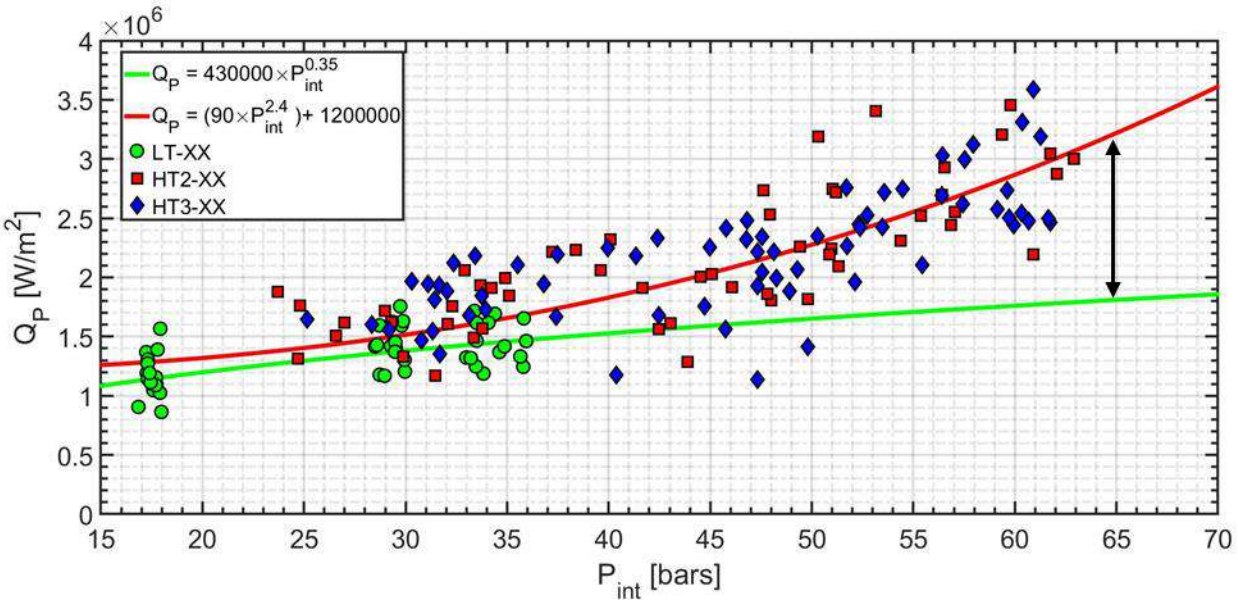

Figure 124: Dependency of Q_P on P_{int} for different regimes of combustion (scatter). Note the colors of the scatter are different from previous figures to improve the presentation

To distinguish the influence of P_{int} from the influence of q, this analysis is presented in a 3D plot in Figure 124. The green surface represents the power-law relationship obtained for laminar cases. It is clear from this representation that increasing the turbulence intensity leads to an increase in Q_P beyond the effect of P_{int} alone. To our knowledge, such effects of turbulence intensity on Q_P have not been reported in the literature in closed chamber FWI studies. It is widely accepted that flame tends to slow down and become laminar near the wall during FWI leading to question the role the turbulence intensity plays on the transport of heat flux during FWI in closed chamber combustion. The results from this thesis show that despite slowing down of flame, turbulence intensity plays a role to enhance Q_P. Further, it seems that the effect of turbulence could increase as P_{int} increases.

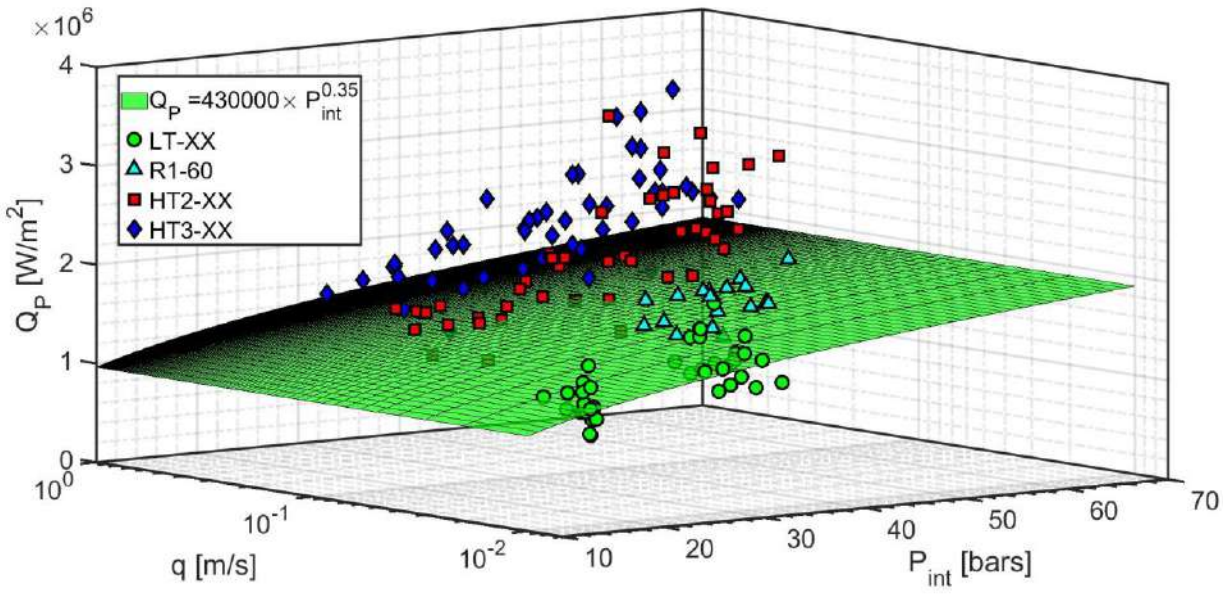

Figure 125: 3D Plot of Q_P as a function of P_{int} and q. The colors are similar to Figure 124.

3.2.6. OTHER EVIDENCE OF THE ROLE OF TURBULENCE DURING FWI

Although we can differentiate the effect of q independently from the effect of P_{int}, the data points are somewhat scattered (Figure 124 and Figure 125). One of the reasons for scattering on Q_P is the local FWI configuration which could be neither fully HOQ nor SWQ but a hybrid of HOQ and SWQ, leading to the scattering [42, 51, 55]. Another reason is the deformation of the heat flux trace which is seen in all experiments in this thesis.

A deformed heat flux may include multiple heat flux peaks close to Q_P due to FWI or contain a flat peak. Examples of deformed heat flux traces are shown in Figure 126. For cyan and blue heat flux traces, we can see multiple peaks in the heat flux trace while for others we see a flat peak. These deformations are present in all turbulence variations.

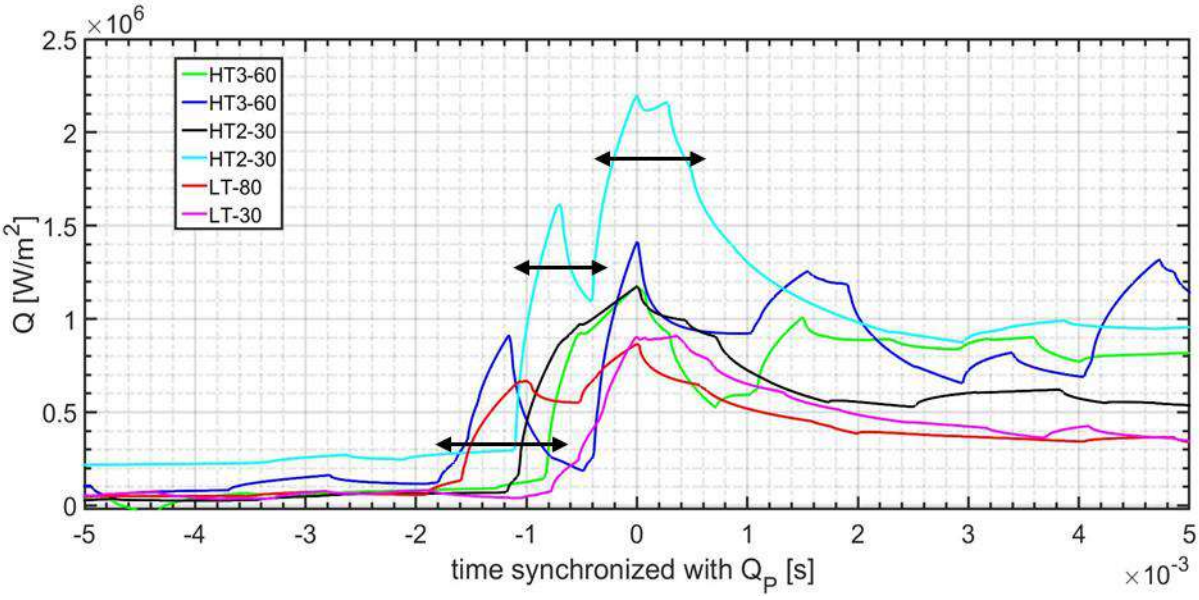

Figure 126: Deformed heat flux trace obtained during FWI

In this section, we will discuss another hypothesis that points to the possible role of turbulence during FWI. The heat flux traces shown in Figure 126, are studied in detail to conclude that the deformations are physical and not due to the acquisition or due to signal processing. Moreover, researchers obtain repetitive heat flux trace and $\boldsymbol{Q_P}$ in as little as 3 shots [51]. The thermocouples used in this thesis have a sensing element of diameter of 0.78 mm which approaches the integral length scales estimated from PIV for our experiments (~10 µm for LT-XX, ~100-300µm for HT2-XX and HT3-XX), especially for HT2-XX and HT3-XX series. Further, the time scale of these deformations is of the order of 0.2-1 ms. An example of this estimation is shown by the double arrow in Figure 126.

From the analysis of the nature of heat flux trace, heat flux trace fluctuations post FWI, and turbulent velocity fluctuations, some insights into the role of turbulence could be derived. To get an idea about the timescales of turbulent fluctuations near the TC, a Fourier analysis of the high-frequency fluctuations in the heat flux trace (post-FWI, region 5 in Figure 57) is carried out. The PSD spectrum for high-frequency fluctuations in the heat flux trace for different combustion regimes and repetitions for HT3-60 and LT-60 is shown in Figure 127. Peaks are observed between 500 Hz-1 kHz in all combustion

regimes which corresponds to a time scale ~1-2 ms. Similarly, the high-frequency turbulent fluctuations in the velocity (determined from PIV) also have a characteristic time scale of a fraction of 0.4ms to 0.8ms.

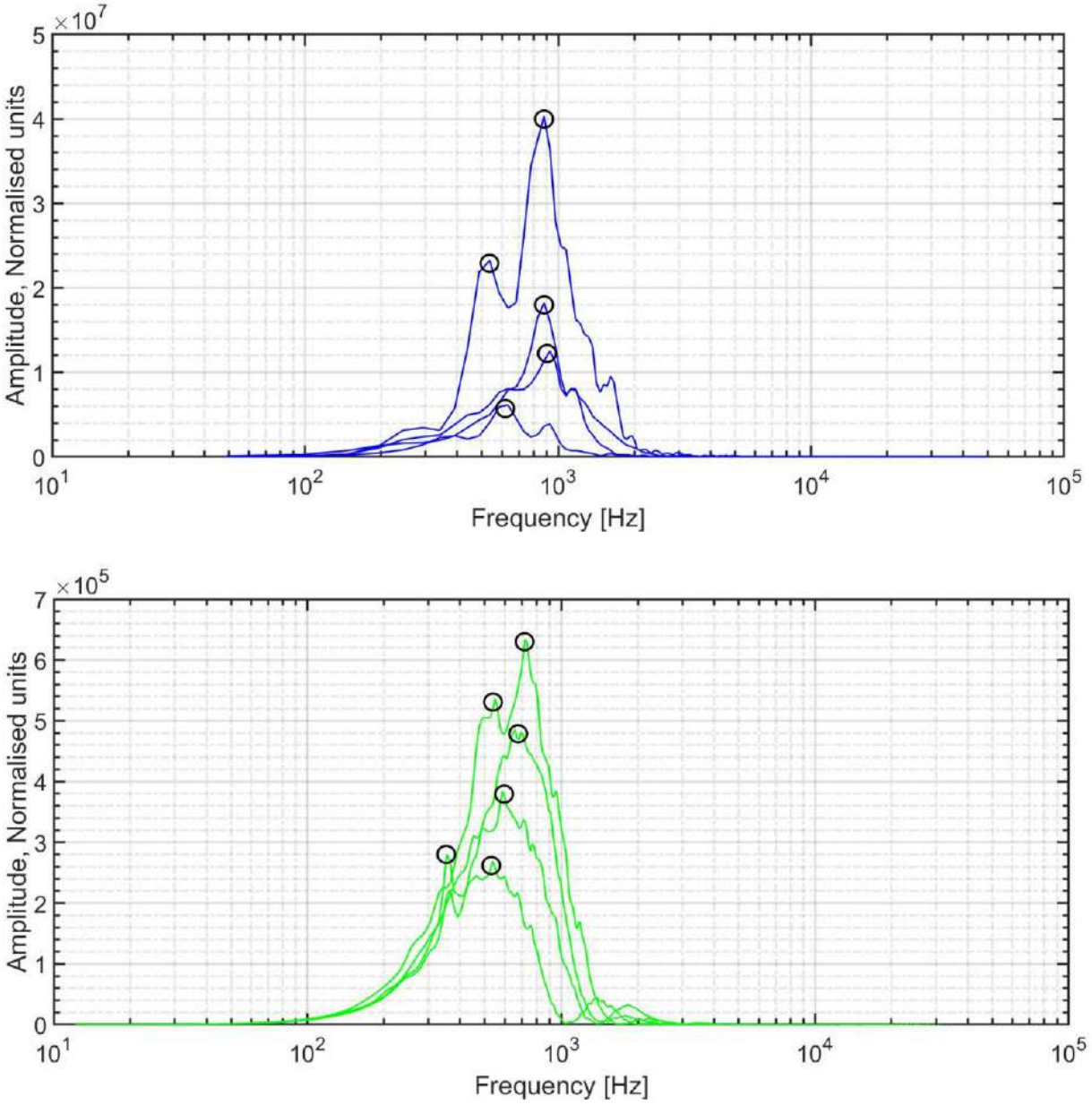

Figure 127: PSD spectrum of high-frequency fluctuations in the heat flux trace for HT3-60 (Top) and LT-60 (Bottom)

Considering that the deformation in the heat flux trace occurs over a fraction of ms (0.2ms-1ms) which is close to the timescale of turbulence near the wall and that the sensor element size is ~ 2-8 times the estimated turbulence length scale, we hypothesize that the deformations in the heat flux trace are

due to the coupling of heat flux during FWI with turbulent structures near the wall. More experiments are needed to support this hypothesis and uncover the mechanism of how turbulence affects heat flux.

In the section 3.2, we presented the variation of $\boldsymbol{q}$ inside the CVC, achieved by different fan operations. We were able to achieve laminar and turbulent combustion regimes like the combustion regimes found in engines. In our setup we concluded that the mean velocity vanishes near the TCs before FWI, hence has no effect on the $\boldsymbol{Q_P}$. By separating the influence of $\boldsymbol{P_{int}}$, we could identify the increase in $\boldsymbol{Q_P}$ due to an increase in $\boldsymbol{q}$.

3.3. EFFECT OF DILUTION VARIATION

In this section, the effect of dilution of the air-fuel mixture is studied. For this purpose, two diluents are chosen, nitrogen and carbon dioxide. This choice of diluents is relevant to EGR gas composition. Further variation in mole fraction of oxygen in fuel-air mixture is also presented in this section.

3.3.1. EXPERIMENT MATRIX

The complete experiment matrix of the experiments performed for the study of dilution is given in Table 11. Two levels of turbulence intensity are used in this section (LT-60 and HT2-60). In these experiments, the initial density of the mixture and air-fuel ratio is kept constant. Hence to accommodate the diluent, fuel quantity is slightly reduced.

Table 11: Experiment matrix for the effect of dilution on the heat flux during FWI

Dilution variation, equivalence ratio = 0.8, $\boldsymbol{X_D}$ = 60 mm, wall-TC type 2						
Fuel (CH_4) (bars)	O_2 (bars)	CO_2 (bars)	N_2 (bars)	Condition Refer Table 9	Other Diagnostics	Notation
1.10	2.76	0	10.38	LT-60/HT2-60	PIV	LT/HT
1.05	2.63	0	10.58	LT-60/HT2-60	-	LT-N_2-5%/HT-N_2-5%
0.99	2.49	0	10.77	LT-60/HT2-60	PIV	LT-N_2-10%/HT-N_2-10%
1.05	2.63	0.71	9.87	LT-60/HT2-60	-	LT-CO_2-5%/HT-CO_2-5%
0.99	2.49	1.43	9.87	LT-60/HT2-60	PIV	LT-CO_2-10%/HT-CO_2-10%

Flow fields were characterized using PIV for no-dilution and 10%-dilution (by mole) conditions. Turbulence properties were found to remain unchanged despite changes in the chemical composition of the gas, prior to combustion. Hence, we can conclude that the turbulence properties are a function of fan operation rather than the gas composition. However, the P_{int} changes due to different gas compositions leading to different laminar flame properties. The subsequent turbulent flame regimes were then determined. The results are plotted in the combustion regime diagram in Figure 128. It is observed that an increase in dilution leads to a displacement of the flame regime towards the left of the combustion diagram (arrows in Figure 128). This result is consistent with the literature [110, 111].

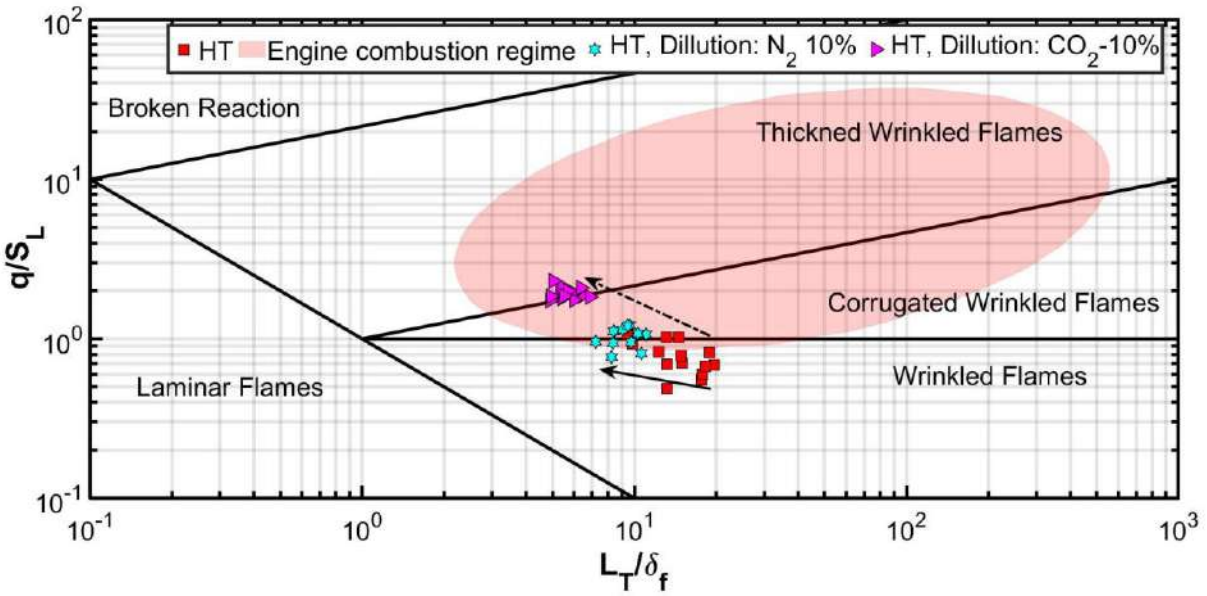

Figure 128: Experiments with dilution (CO_2 and N_2) in the combustion regime diagram

3.3.2. Effect of dilution of fuel-air mixture on Q_P

In this section, we will present the heat flux measurements for the experiments with dilution variation shown in Table 11. The average heat flux traces for dilution experiments with both N_2 and CO_2 are presented in Figure 129 and Figure 130, for low and high turbulence levels, respectively. It is found that Q_P is reduced with the increase in the dilution fraction, as expected. The reduction of Q_P is more for CO_2 dilution than with N_2 for both the turbulence variation. The differences in Q_P are shown in Figure 131.

We see that LT-CO_2-5% (HT-CO_2-5%) yields a reduction of $\boldsymbol{Q_P}$ by 39% (31%) and LT-CO_2-10% yields a reduction of 63% (48%) when compared to LT. Similarly, LT-N_2-5% (HT-N_2-5%) yields a reduction of $\boldsymbol{Q_P}$ by 17% (18%) and LT-N_2-10% (HT-N_2-10%) yields a reduction of 34% (33%) when compared to LT (HT).

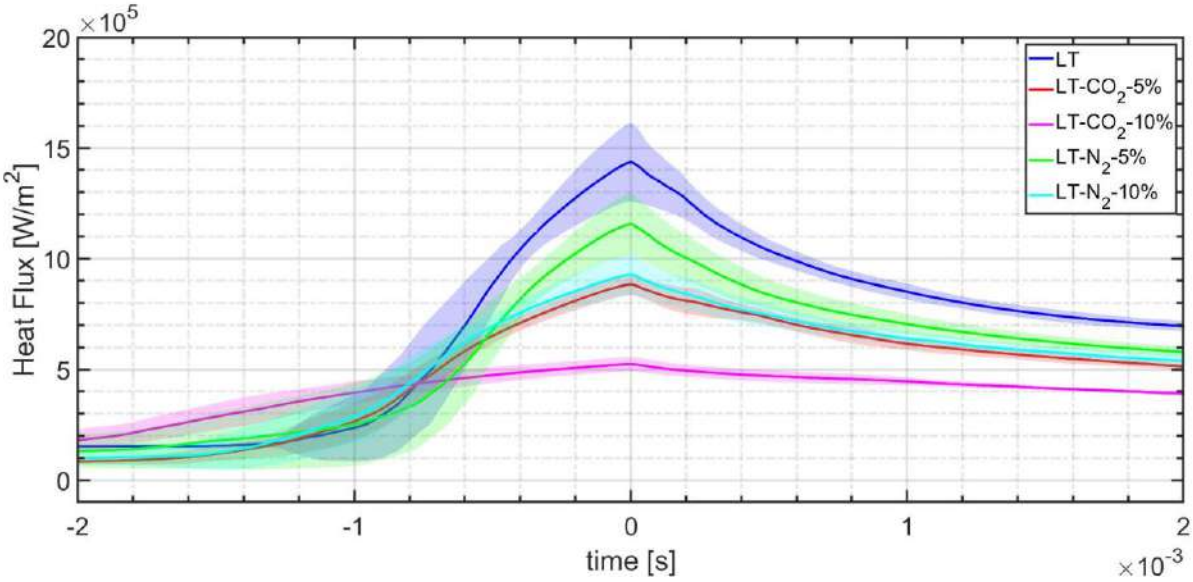

Figure 129: Average heat flux trace for LT case, $\boldsymbol{X_D}$ = 60 mm with dilution (CO_2 and N_2)

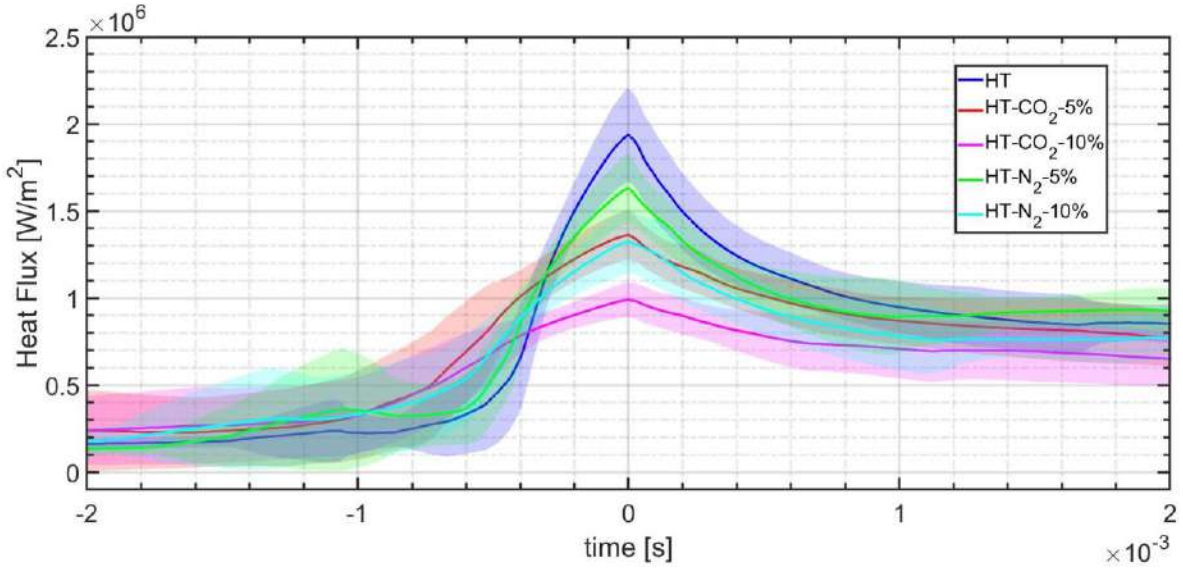

Figure 130: Average heat flux trace for HT case, $\boldsymbol{X_D}$ = 60 mm with dilution (CO_2 and N_2)

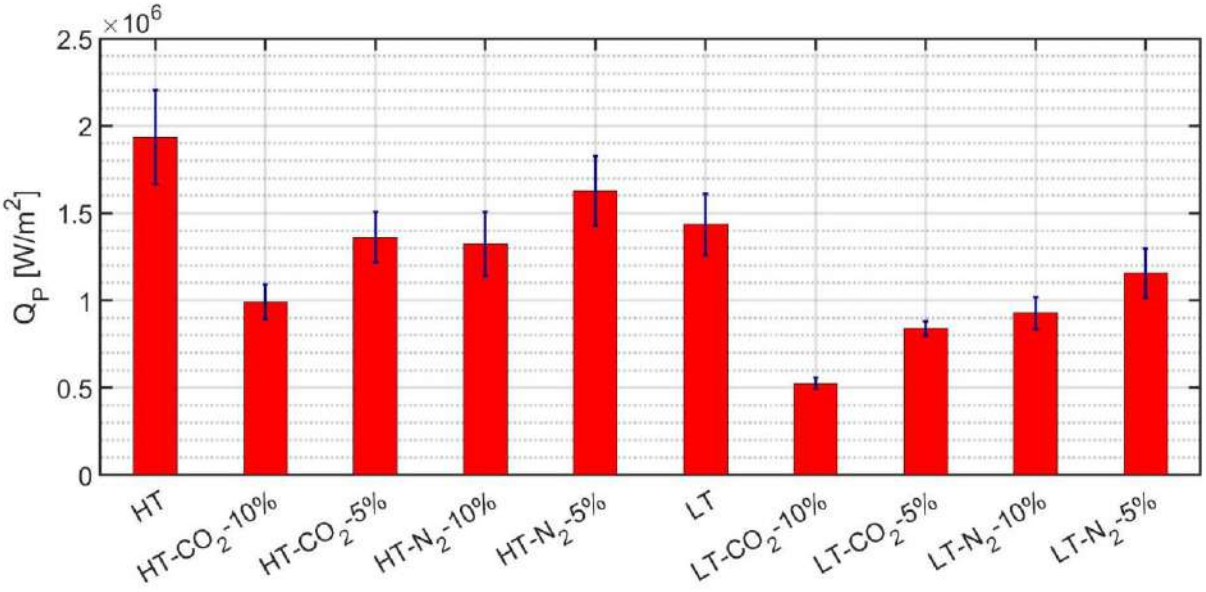

Figure 131: Q_P for all experiments in Table 11

To decipher the change in Q_P, flame power (Q_Σ), laminar flame speed (S_L), thermal flame thickness (δ), P_{int}, specific heat capacity (C_P), burnt gas temperature (T_{max}), and conductivity (k) at FWI timing is analyzed. Table 12 and Table 13 present these properties for laminar and turbulent regimes respectively.

Table 12: Flame properties at the instant of quenching for laminar regimes of dilution variation

Conditions	Q_P MW/m^2	Q_Σ MW/m^2	S_L m/s	δ µm	P_{int} bars	T_{max} K	C_P J/KgK	k W/mK	$\frac{Q_P}{Q_\Sigma}$
LT	1.44±0.18	8.47±0.13	0.22±0.06	41±0	29±1	2206±2	1147±1	0.047	0.17
LT-CO_2-5%	0.88±0.04	4.04±0.06	0.13±0.03	73±1	22±0	2058±2	1124±1	0.043	0.22
LT-CO_2-10%	0.53±0.02	1.97±0.04	0.08±0.02	127±3	19±1	1944±3	1107±1	0.041	0.27
LT-N_2-5%	1.19±0.12	5.80±0.15	0.18±0.07	54±1	26±1	2126±3	1136±2	0.045	0.21
LT-N_2-10%	0.95±0.07	4.07±0.15	0.14±0.07	70±2	24±1	2052±5	1129±2	0.044	0.23

Table 13: Flame properties at the instant of quenching for turbulent regimes of dilution variation

Conditions	Q_P MW/m^2	Q_Σ MW/m^2	S_L m/s	δ µm	P_{int} Bars	T_{max} K	C_P J/KgK	k W/mK	$\frac{Q_P}{Q_\Sigma}$
HT	1.94±0.27	10.72±2.32	0.23±0.01	28±7	46±4	2235±29	1174±5	0.052	0.18
HT-CO_2-5%	1.34±0.14	6.93±0.67	0.15±0.00	44±4	41±4	2137±12	1159±6	0.050	0.19
HT-CO_2-10%	0.99±0.11	3.52±0.78	0.09±0.00	78±22	38±4	2011±31	1146±8	0.048	0.28
HT-N_2-5%	1.58±0.19	8.51±1.38	0.19±0.01	37±7	42±4	2176±24	1165±6	0.051	0.19
HT-N_2-10%	1.30±0.21	6.02±1.18	0.15±0.01	50±11	41±3	2102±29	1158±7	0.050	0.22

Further, the chemical effect of N_2/CO_2 on Q_P during FWI can be studied by observing heat flux trace of 5% CO_2 dilution and 10% N_2 dilution in both the laminar regimes and turbulent regimes (see Figure 129 and Figure 130). In these two cases, the flame properties ($\boldsymbol{Q_\Sigma}$, $\boldsymbol{S_L}$, $\boldsymbol{\delta}$, $\boldsymbol{P_{int}}$, $\boldsymbol{C_P}$, $\boldsymbol{k}$) are approximately equal. $\boldsymbol{Q_P}$ is also approximately equal. This indicates that the chemical constituents of dilution gas have no impact on $\boldsymbol{Q_P}$. Dilution affects the heat flux in the thermal aspect by reducing the flame power, subsequently reducing $\boldsymbol{Q_P}$.

The maximum variation of $\boldsymbol{Q_P}$, $\boldsymbol{k}$, and $\boldsymbol{C_P}$, is for LT-CO_2-10% when compared to LT. For LT-CO_2-10%, the variation in $\boldsymbol{C_P}$ is ~5% and $\boldsymbol{k}$ is ~13% whereas the variation in $\boldsymbol{Q_P}$ is ~63% when compared to LT. The variation in $\boldsymbol{C_P}$ and $\boldsymbol{k}$ reduces to <5% for HT-CO_2-10% compared to HT. $\boldsymbol{Q_P \sim k}$, using 1D conduction of heat in the small layer of gas near the wall, indicating linear relationship. 5% change in $\boldsymbol{C_P}$ has leads to 5% change in $\boldsymbol{Q_\Sigma}$ independently. During quenching, heat from flame ~$\boldsymbol{Q_\Sigma}$ is transferred to the wall as $\boldsymbol{Q_P}$ across the quenching distance (thin layer of fresh gas). With change in $\boldsymbol{C_P}$(~5%) fraction of the heat from $\boldsymbol{Q_\Sigma}$ that is absorbed by the quenching layer changes by the same order (~5%). That means an increase in $\boldsymbol{Q_\Sigma}$ due to $\boldsymbol{C_P}$ is likely compensated by an increase in the temperature of fresh gas in the quenching layer, indicating the net effect of $\boldsymbol{C_P}$ on $\boldsymbol{Q_P}$ is negligible. This leads us to conclude that the variation in $\boldsymbol{C_P}$ and $\boldsymbol{k}$ is too small to play a role in the big variation of $\boldsymbol{Q_P}$.

For LT-CO_2-10% $\boldsymbol{P_{int}}$ is 34% less than that of $\boldsymbol{P_{int}}$ for LT. To take into account the dependency of $\boldsymbol{Q_P}$ in $\boldsymbol{P_{int}}$, we here assume that it follows the power-law relationship previously established in 3.1.3(Equation 36). This assumption would need to be validated since using CO_2 changes the gas composition. Nevertheless, since the dilution level is rather low (10%), the coefficient $\boldsymbol{b}$ is not expected to be much different. We can therefore estimate that $\boldsymbol{P_{int}}$ causes a reduction in $\boldsymbol{Q_P}$ for LT-CO_2-10% of <14% when compared to $\boldsymbol{Q_P}$ for LT. This reduction in $\boldsymbol{Q_P}$ due to reduction in $\boldsymbol{P_{int}}$ falls to <10% in HT conditions. This leads us to conclude that the differences in $\boldsymbol{P_{int}}$ are too small to explain the 63% difference in $\boldsymbol{Q_P}$.

From a thermal point of view, $\boldsymbol{Q_\Sigma}$ acts as a reservoir of energy in the flame, a part of which needs to be transported to the wall over the quenching distance during FWI, which is the wall heat flux. When the heat flux reaches a critical fraction of $\boldsymbol{Q_\Sigma}$ i.e. $\boldsymbol{Q_P}$, then the flame quenches [40]. $\boldsymbol{Q_\Sigma}$ for LT-CO_2-10% is reduced by 76% of $\boldsymbol{Q_\Sigma}$ for LT. This order of reduction in $\boldsymbol{Q_\Sigma}$ (76%) is comparable to the order of reduction in $\boldsymbol{Q_P}$ (63%) for LT-CO_2-10%, compared with LT. Hence, we conclude that the large variation in $\boldsymbol{Q_P}$, obtained in the dilution experiments is due to a change in overall $\boldsymbol{Q_\Sigma}$.

$\frac{\boldsymbol{Q_P}}{\boldsymbol{Q_\Sigma}}$ lies in the range of 0.17-0.27 for all LT cases and 0.18-0.28 for all HT cases indicating that there is the presence of small variation in $\frac{\boldsymbol{Q_P}}{\boldsymbol{Q_\Sigma}}$ for different dilution experiments. We will study the specific influence of $\boldsymbol{Q_\Sigma}$ on $\frac{\boldsymbol{Q_P}}{\boldsymbol{Q_\Sigma}}$ in the next section using experiments with large variation on $\boldsymbol{Q_\Sigma}$.

3.3.3. EFFECT OF VARIATION OF Q_Σ ON Q_P

Two effects are expected to influence the heat flux: chemistry effect or thermal effect. To decorrelate these two, a variation of flame power ($\boldsymbol{Q_\Sigma}$) is used to address the thermal effect. Hence experiments which produce a significant variation in flame power are analyzed. These experiments are conducted by varying the mole fraction of oxygen in the fuel-air mixture while keeping the fuel, fuel-oxygen ratio, and density constant. For these experiments, the mole fraction of O_2 is varied in the fuel-air mixture such that larger variations are obtained in $\boldsymbol{Q_\Sigma}$. The corresponding experiment matrix is given in Table 7.

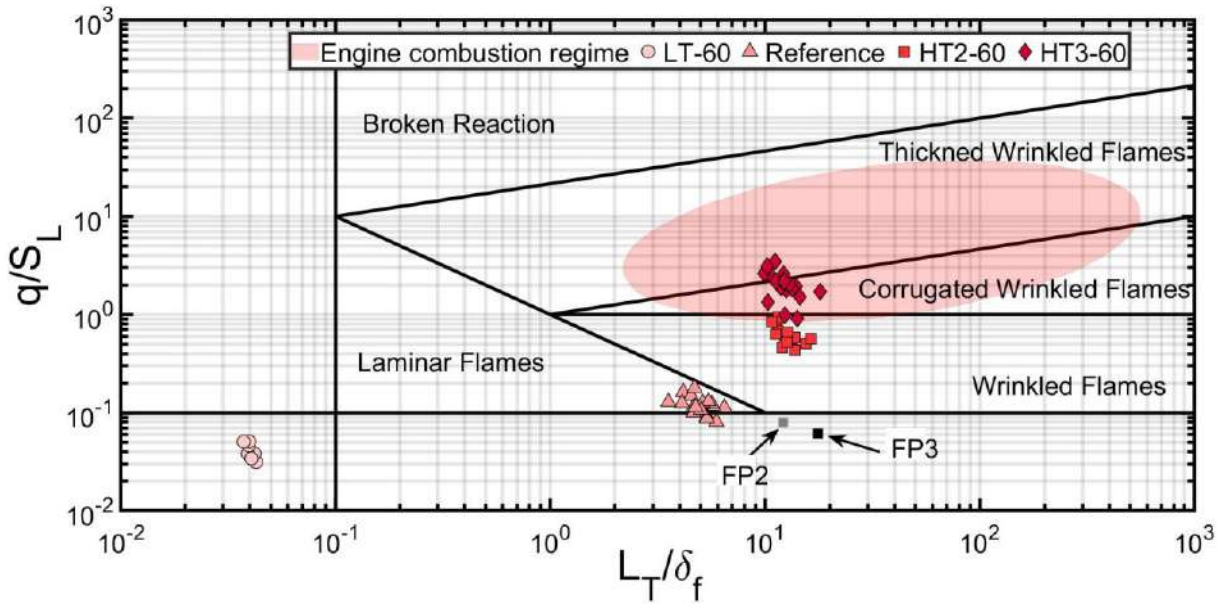

Figure 132: Experiments with flame power variation in the combustion regime diagram

For this specific set of experiments, PIV was not carried out, and type 1 wall-TC assembly was used. To estimate the position of these experiments in the combustion regimes diagram (Figure 26) we use our conclusion found in section 3.3 that the turbulence properties are a function of fan operation only. Therefore, we use the turbulence properties computed from the reference condition (Table 4) along with calculated laminar flame properties. Thus, we estimate that all experiments in Table 14 lie in the wrinkled flame regime.

Table 14: Experiment matrix for oxygen-enriched condition

Flame power variation at equivalence ratio = 0.8, X_D = 60mm, wall-TC type 1, Reference turbulence condition in Table 9			
Fuel: CH_4 bars	O_2 bars	N_2 bars	Code
1.10	2.76	N2: 10.38	Reference
1.39	3.45	N2: 9.42	FP2
1.81	4.52	N2:8.00	FP3

In this section we analyze the heat flux data recorded for experiments listed in Table 14, targeting parametric variation of Q_Σ. The average heat flux trace for the experiments listed in Figure 131 is given in Figure 133. As expected Q_P for the highest flame power case is the highest. Δt is not used for analysis (see

section 2.3.2 in chapter 2). The corresponding laminar flame properties at the instant of quenching for the variations in oxygen enrichment are given in Table 15. Like in dilution variation the effect of C_P, k, T_{max} is small compared to the variation in Q_P. Hence these properties are considered negligible to explain the differences measured in Q_P.

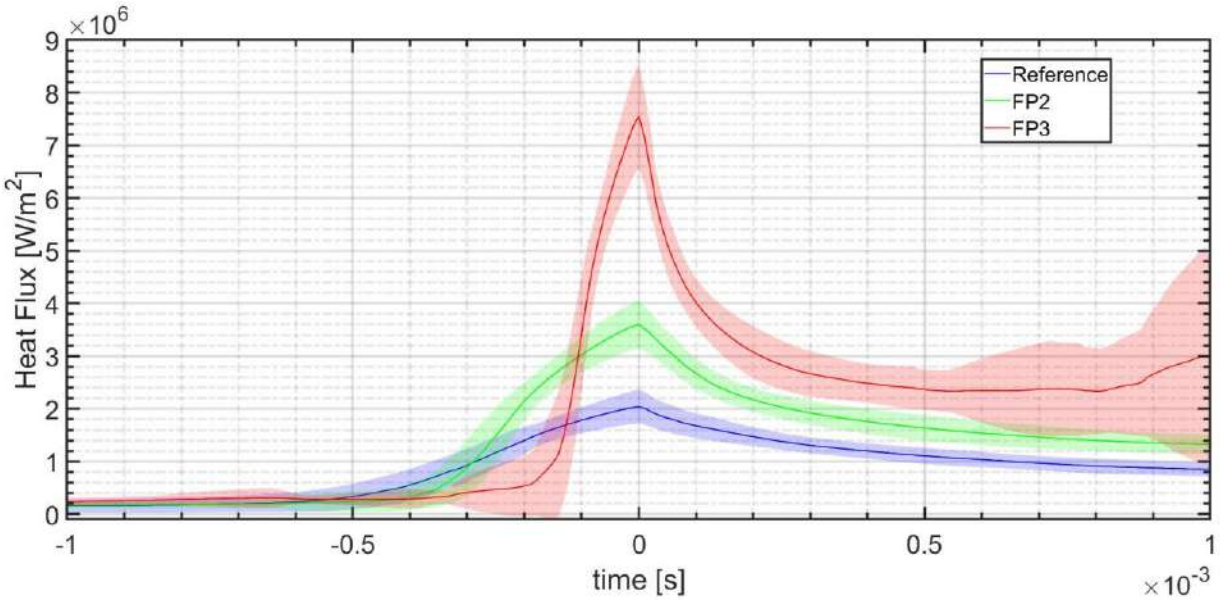

Figure 133: Average heat flux trace for experiments in Table 14

Table 15: Flame properties at the instant of quenching for oxygen enrichment variations

Conditions	Q_P MW/m^2	Q_Σ MW/m^2	S_L m/s	δ µm	P_{int} bars	$\frac{Q_P}{Q_\Sigma}$
Reference	2.04±0.32	9.50±1.49	0.22±0.01	37±5	33±6	0.21
FP1	3.60±0.46	39.39±4.0	0.54±0.01	13±1	52±6	0.09
FP2	7.55±0.99	108.89±5.1	0.92±0.01	6±3	78±4	0.07

On the other hand, change in P_{int} is significant. Using the hypothesis that the dependency of Q_P on P_{int} is similar to the one found in section 0, the maximum change in Q_P due to P_{int} can be estimated at 35%. In contrast, the maximum variation in Q_P is 270%. This indicates that P_{int} is not a major factor affecting Q_P. This observation is visually presented in Figure 134. In this figure, we can see that the trends on Q_P remain

the same even after considering the effect of P_{int}. Like in the case of experiments with dilution, we conclude that the difference in Q_P is due to a change in Q_Σ (1146%). Indeed, a minimum energy needs to remain in the flame front, after the heat losses, which is necessary to allow the temperature of fresh gas to be high enough to insure reactive front propagation. When the flame power is small, a small part of flame power as heat loss induces flame non-propagation and then extinction. This is the same physics that limits the existing flame propagation for lean premixtures (usually an equivalence ratio of around 0.5 for hydrocarbon/air mixture).

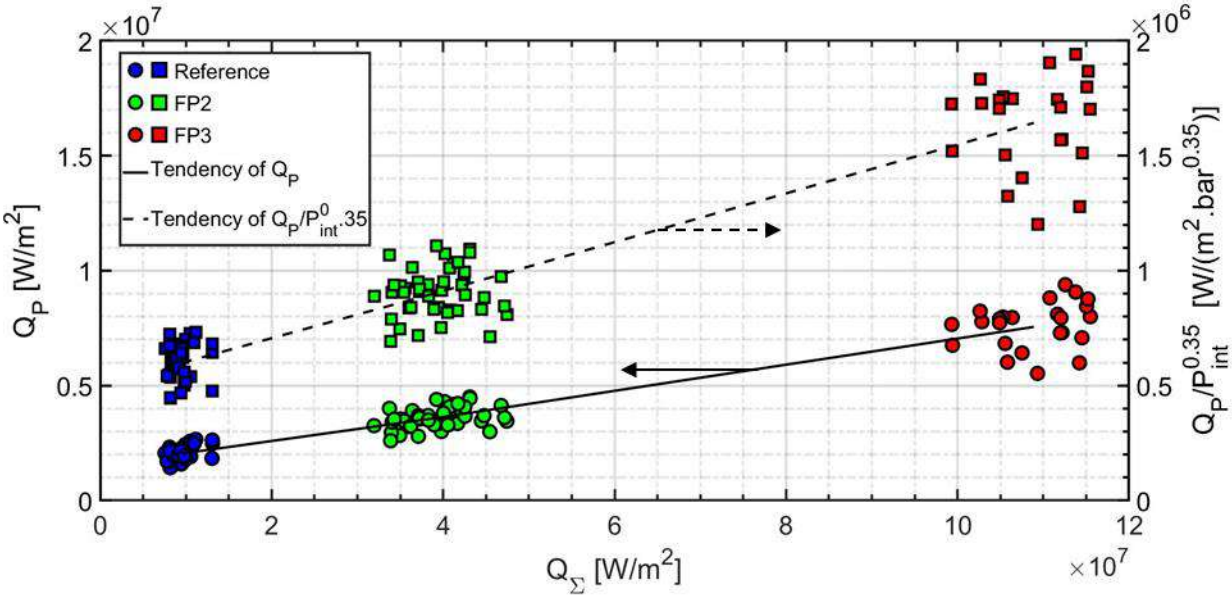

Figure 134: Variation of Q_P and adjusted Q_P for different conditions of oxygen enrichment

It is interesting to note that $\frac{Q_P}{Q_\Sigma}$ changes drastically with the variation of flame power (see column $\frac{Q_P}{Q_\Sigma}$ in Table 15

Table 15), unlike the small change in the variations in dilution presented in section 3.3.2. It means Q_P increases significantly with the increase in Q_Σ. However, this increase is not linear in $\frac{Q_P}{Q_\Sigma}$, even after correcting for effects of P_{int}. This is presented in Figure 135. In this figure, we can see that the trend of $\frac{Q_P}{Q_\Sigma}$ remain intact even after taking the effect of P_{int} into account.

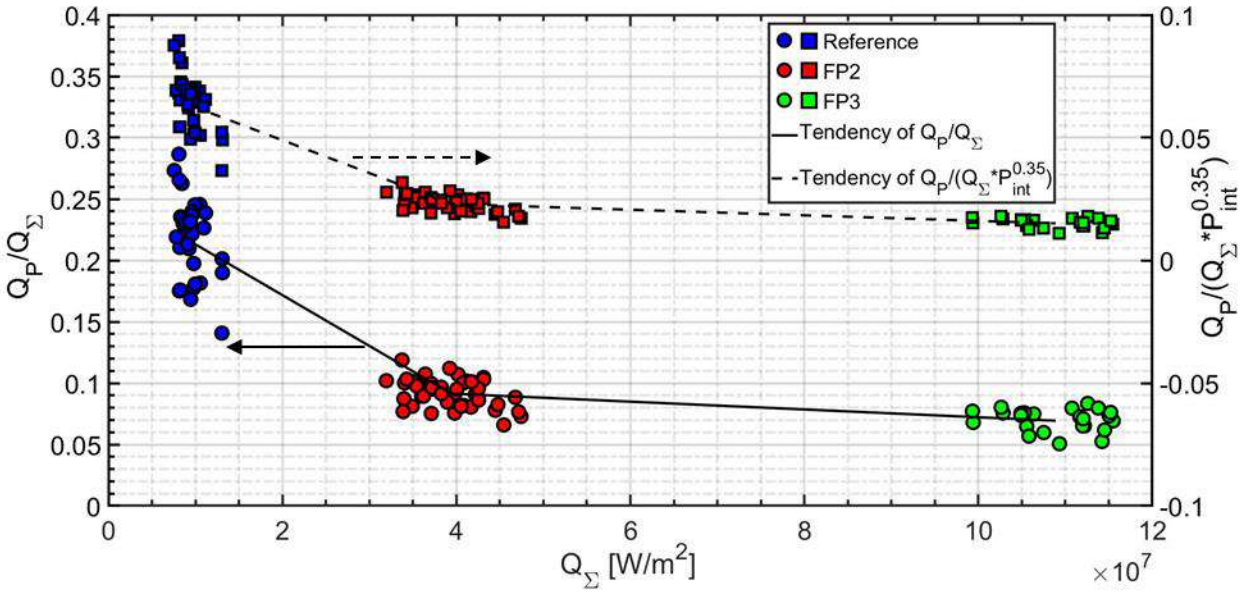

Figure 135: Variation of Q_P/Q_Σ and adjusted Q_P/Q_Σ for different conditions of oxygen enrichment

From the variations conducted in this thesis it is clear that $\frac{Q_P}{Q_\Sigma}$ decreases with an increase in Q_Σ. Although the effects of S_L and δ are accounted for in Q_Σ, their individual effects could not be separately studied. Since the fan operation is the same for all the operating points considered here, it can be assumed that q is constant. Therefore, we suppose $\frac{q}{S_L}$ to remain constant. Thus, these cases lie in the wrinkled flame area of the combustion regime diagram (Figure 128), hence the results obtained are relevant for engines applications. An empirical connection can be made by looking at the physical meaning of Q_P and Q_Σ. The first quantity is directly related to heat losses. An increase in Q_P will lead to an increase in heat losses. Regarding Q_Σ, the interpretation is more complex. By definition, Q_Σ is proportional to the LHV of the fuel and density of the fuel (see Equation 6). Therefore, in a closed adiabatic chamber, Q_Σ can be related to the total energy produced by the flame. Using this interpretation, we can then relate Q_P/Q_Σ to the fraction of total fuel energy wasted as heat losses in engines. An extrapolation of this idea indicates that increasing the Q_Σ of the fuel-air mixture would lead to a reduction in heat losses which could lead to an

increase in the efficiency of engines (as $\frac{Q_P}{Q_\Sigma}$ falls). This increase in efficiency in engines with the addition of oxygen (increases the Q_Σ) is reported in the literature [110, 112].

In the section 3.3 we studied the effect of the addition of diluents (N_2 and CO_2) on the Q_P during FWI. It is found that the diluents reduce the Q_Σ which leads to low Q_P. A variation of Q_Σ shows that $\frac{Q_P}{Q_\Sigma}$ decreases with an increase in Q_Σ.

3.4. EFFECT OF LOCATION OF TEMPERATURE MEASUREMENT

Type 2 wall-TC assembly is used to measure the surface temperature at two different locations simultaneously. This experimental specificity allows characterizing the heat flux during FWI at two locations simultaneously. HT2-60 operating point (cf. Table 8) is chosen to conduct this parametric variation. The schematic of TC locations and the ROI is presented in Figure 136. TC2 and TC3 represent the location of two TCs used for surface temperature measurement. In section 3.2.2, it has been found that the large-scale mean flow near the wall vanishes during FWI. Hence the mean flow is not expected to affect Q_P. Given that turbulence in our experiments is found to be homogenous in space, we can expect that Q_P will not be impacted by a difference in turbulence depending on the location of measurement. The average P_{int} at TC2 (46.47±3.50 bars) is very close to P_{int} at TC3 (46.41±3.8 bars). Figure 137 shows the average heat flux trace measured at two different locations simultaneously. It is seen that the two heat flux traces are identical with the same Q_P. Hence, we conclude that the heat flux during FWI observed in our experiments is independent of the tested location at which surface temperature is measured.

Typically variations in the local heat flux trace and Q_P is observed during measurements at a different location inside an engine [26, 32, 113]. In engines, the FWI at different locations of surface temperature measurement happens at different CAD where variation in P_{int} and q can be expected. We hypothesize that these variations are translated on both the heat flux trace and Q_P measured at different locations is

due to variations in P_{int}, q, or both. This hypothesis is backed by our measurements where similar P_{int} and q, lead to identical heat flux trace and Q_P at two different locations of surface temperature measurement.

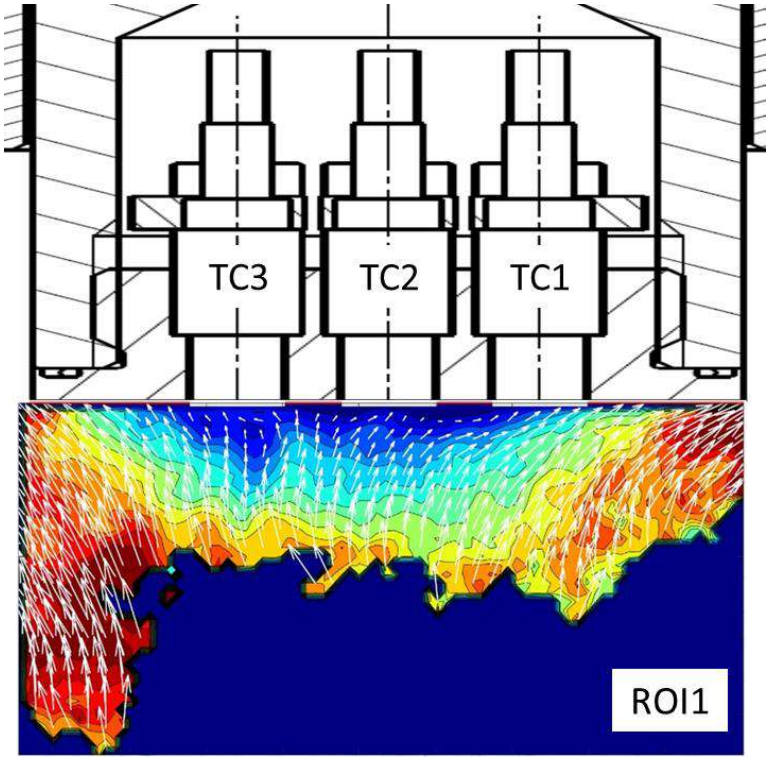

Figure 136: Schematic of the different locations where surface temperature measurement

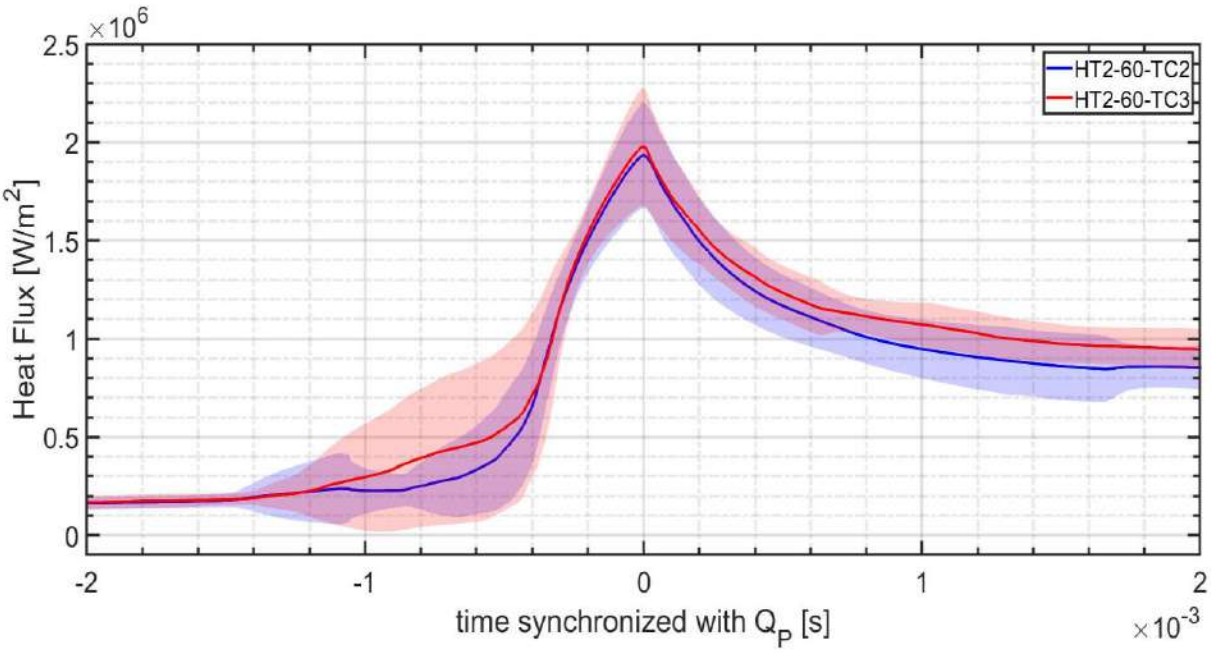

Figure 137: Average heat flux trace, simultaneously acquired at two different locations

3.5. FUEL VARIATION

In this section, we analyze the influence of the fuel composition on the heat flux during FWI. Three different fuels are used i.e., H_2, CH_4, and C_2H_2-H_2 mixtures targeting different Lewis numbers of the air-fuel mixture and chemistry near the wall.

3.5.1. EXPERIMENT MATRIX

To understand the effects of different fuels, the thermal effects are somewhat mitigated by choosing fuel-air mixture conditions such that Q_Σ is of the same order (~100 MW/m^2). For example, CH_4 uses an oxidizer (mixture of N_2 and O_2) with a high mole fraction of oxygen compared to air, so that Q_Σ is of the similar order as for H_2, C_2H_2-H_2 mixtures. Likewise, variations in density and P_{int} are kept to a minimum. The experiment matrix is given in Table 16.

Table 16: Fuel Variation matrix

The gas composition used to obtain FWI for different fuels, wall type 1 (Reference condition, Table 8)					
Fuel bars	O_2 bars	N_2 bars	Initial Pressure bars	Le	Notation
CH_4: 1.81	4.52	8.00	14	0.93	FP3
H_2: 4.52	2.83	10.62	18	0.42	Le2
C_2H_2: 0.85, H_2:0.13	2.73	10.26	14	1.14	Le3

PIV experiments were not carried out for these experiments. Nevertheless, ***q*** can be estimated from PIV measurements under similar conditions with type 2 wall-TC assembly. As done previously, we assume that ***q*** in fresh gas is dependent solely on the fan and the chamber geometry. The experiments conducted in this section can then be placed in the combustion diagram (Figure 138). We observe that the three operating points lie in the same combustion regime area.

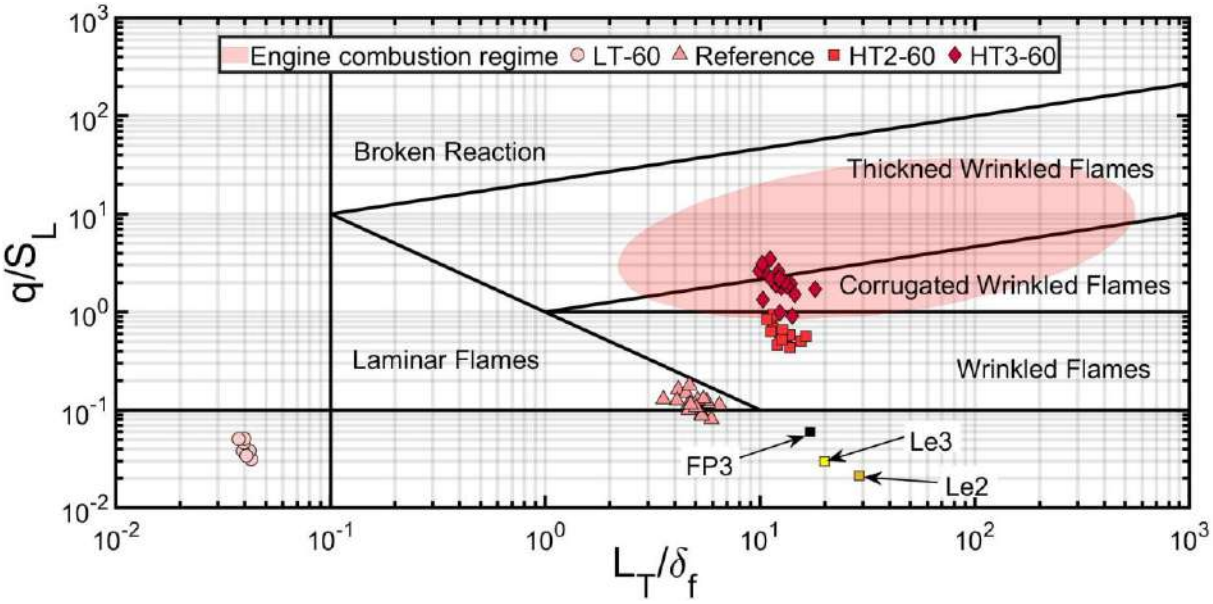

Figure 138: Position of experiments with fuel variation on the combustion regimes diagram

3.5.2. EFFECT OF FUEL VARIATION ON HEAT FLUX

The average heat flux trace for the fuel variations is presented in Figure 139. Q_P for FP3 and Le3 are close to each other. Whereas for Le2, Q_P is significantly different. At the rise of heat flux trace, all three different fuels show a similar slope. However, the heat flux trace for Le2 tapers off much earlier into a lower Q_P. The tapering is observed in all individual repetitions for Le2. The laminar flame properties for these experiments at the instant of quenching are given in Table 17. P_{int} for all variations is close to each other, shown in Table 17. With a hypothesis that the pressure dependency can be expressed by the power-law derived in 3.1.3we can estimate differences in Q_P due to P_{int}. Using b = 0.35, we expect Le2 to have ~1-4% high Q_P. Even if a different b is obtained for different compositions (FP3, Le2, Le3) we expect the change in Q_P due to P_{int} to remain in similar order as P_{int} are very close to each other within 10% of each other. This extrapolation does not explain the difference in Q_P. In section 3.3.3we have seen that for a given mixture and experiment setup $Q_P \sim Q_\Sigma$. Inspite of having the largest Q_Σ, Q_P is the lowest for Le2. This indicates that the tapering of heat flux trace to give a low Q_P in Le2 is purely due to different fuel properties.

In literature, at P_{int} ~ 1 bar, it is found that $\frac{Q_P}{Q_\Sigma}$ for HC fuels is ~ 0.3 whereas for H_2 it is ~ 0.15 [54]. The values of $\frac{Q_P}{Q_\Sigma}$ obtained in this thesis is significantly different from the literature. In the current experiments, we obtain $\frac{Q_P}{Q_\Sigma} \sim$0.06 for HC fuel (FP3 and Le3) whereas 0.03 for H_2(Le2). This discrepancy could be due to the high Q_Σ used in the experiments (relation of $\frac{Q_P}{Q_\Sigma}$ and Q_Σ is explored in section 3.3.3). From our analysis, we could not pinpoint which property of Le2 leads to a low Q_P compared to Le3 and FP3.

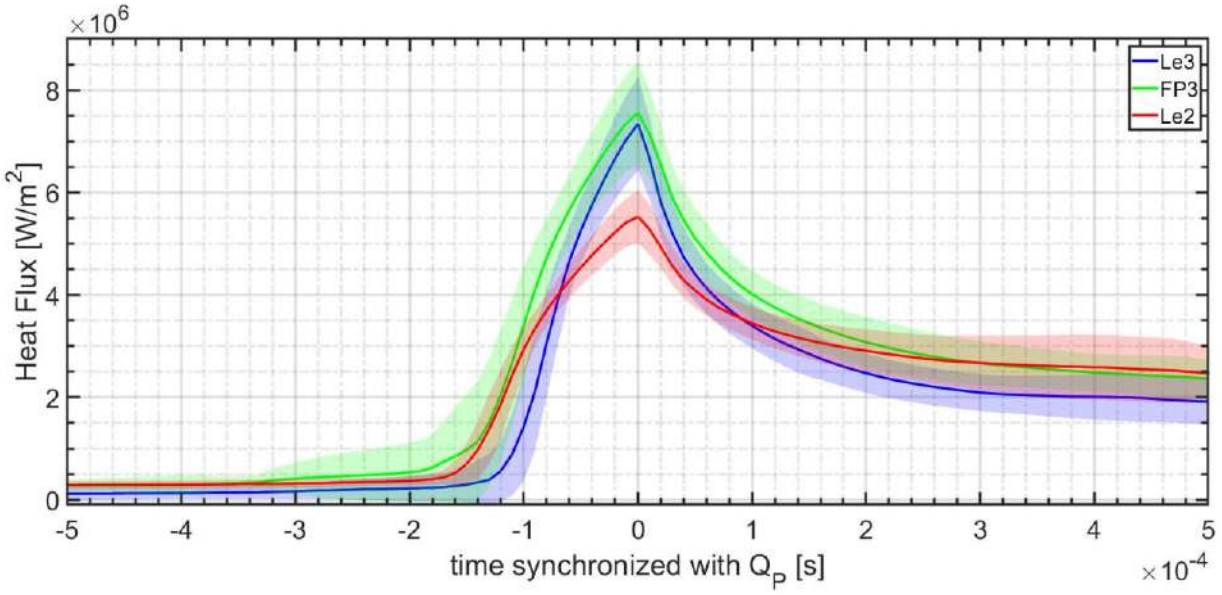

Figure 139: Average heat flux trace for different fuel variation

Table 17: Flame properties during FWI for different fuel variations

	Q_P MW/m^2	Q_Σ MW/m^2	S_L m/s	δ µm	P_{int} bars	T_{max} K	C_P J/KgK	k W/mK	$\frac{Q_P}{Q_\Sigma}$
FP3	7.55±0.99	108.89±5.07	0.92±0.01	6.4±0.3	79±4	2809±7	1255±4	0.059	0.07
Le2	5.53±0.50	176.53±1.74	2.10±0.00	4.0±0.0	83±1	2478±2	1396±0	0.097	0.03
Le3	7.34±0.92	134.03±4.32	1.40±0.01	5.3±0.2	74±3	2735±5	1168±2	0.056	0.05

In engines, measurements comparing heat loss for CH_4-air mixture and H_2-air mixture have been carried out in literature [30]. It is found that Q_P for H_2 is significantly higher than that of Q_P for CH_4 at the same indicated power [30]. The high Q_P for H_2 compared to CH_4 in the cited publication is due to a multifold increase in Q_Σ for the stoichiometric air-fuel ratio. In the cited article, the authors were able to reach high indicated thermal efficiency for H_2, inspite of high Q_P, compared to CH_4. They hypothesize the gain in efficiency is due to faster combustion in the case of H_2. Faster combustion will also lead to higher peak pressure and earlier FWI. This will lead to higher P_{int} which could offset some of the advantages of faster combustion as $Q_P \sim P_{int}^{\,b}$ (Equation 36). We propose that higher Q_Σ and lower $\frac{Q_P}{Q_\Sigma}$ for H_2 compared to CH_4 at stoichiometric ratio, is a major cause in achieving higher indicated thermal efficiency in the cited

work. In the context of engine application, with H_2 as fuel, we can expect $\frac{Q_P}{Q_\Sigma}$ to remain low leading to the possibility of high efficiency.

3.6. CONCLUSION

In this chapter, we present the results from experiments with premixed propagative FWI conducted in a CVC. An increase in P_{int} is found to increase Q_P in laminar combustion regimes. In laminar combustion regimes, Q_P dependency on P_{int} is determined using a power-law where $Q_P \sim P_{int}^{0.35}$. With different fan operations, we achieved q close to turbulent combustion regime in engines. In our setup, the FWI occurs in a HOQ configuration, during which the large-scale mean velocity during FWI approaches zero. The net effect of different fan operations is attributed to q. Using $Q_P \sim P_{int}^{0.35}$, we can separate the additional effect of q on Q_P. We find that Q_P increases with an increase in turbulence intensity.

The effect of dilution of the fuel-air mixture on Q_P is also studied in this thesis. It is found that Q_P is primarily affected by Q_Σ of the gas mixture with dilution. Using different dilution gases (CO_2 and N_2) it is found that the chemical composition of dilution does not affect Q_P at similar Q_Σ. Dilution decreases Q_Σ significantly resulting in lower Q_P.

Variation in Q_Σ achieved by increasing the mole fraction of O_2 in air composition yields significantly different Q_Σ during FWI leading to different Q_P. With an increase in Q_Σ, $\frac{Q_P}{Q_\Sigma}$ falls. Through measurement at different locations where P_{int} and q are identical, we find that the heat flux during the premixed propagative FWI in our experiments is homogenous. The effect of different fuels (and Lewis number of fuel-air mixture) is studied at a similar order of Q_Σ using H_2, CH_4 (modified air composition with high O_2 mole fraction), and C_2H_2-H_2 as fuels. Despite having the highest temperature gradient and conductivity, Q_P and $\frac{Q_P}{Q_\Sigma}$ for H_2-air FWI is significantly lower than other fuels.

Chapter 4: Results of non-premixed spray FWI in CVC

In this chapter, we present the results of the experiments on spray-wall interaction with a focus to understand the heat flux trace due to reactive spray-wall interaction. First, we investigate the respective influence of spray momentum and combustion reaction on wall heat transfer by comparing non-reactive spray-wall interaction with reactive spray-wall interaction under ECN spray A conditions. The influence of ignition timing relatively to spray impingement is then studied with a modified spray A boundary condition. Using simultaneous OH* imaging, Mie scattering, and surface temperature measurements the spray wall interaction is studied.

4.1. Effect of position of TC, ambient temperature, and spray momentum on the wall heat flux

In this section, the heat flux due to reactive spray-wall interaction is studied at two different radial locations on the wall. Moreover, the effect of variation in ambient temperature on the heat flux during reactive spray wall interaction is also presented. Finally, we will present the results of non-reactive spray-wall interaction carried out to understand the effect of spray momentum on the heat flux.

4.1.1. Boundary conditions and experiment setup

Various boundary conditions can affect the spray FWI. We choose to use spray A as the representative boundary condition to observe spray FWI [47]. Spray A has been well characterized in the CVC at IFPEN through experiments, within the ECN framework, providing us with the relevant information to conduct studies on spray FWI [78]. Type 2 wall-TC assembly (Chapter 2, section 2.2.1.1) is used to measure wall surface temperature. A schematic of the experiment setup is shown in Figure 140. The

distance of the injector tip to the wall is Y_D. For all the experiments presented in section 3the Y_D = 30 mm is used for surface temperature measurements.

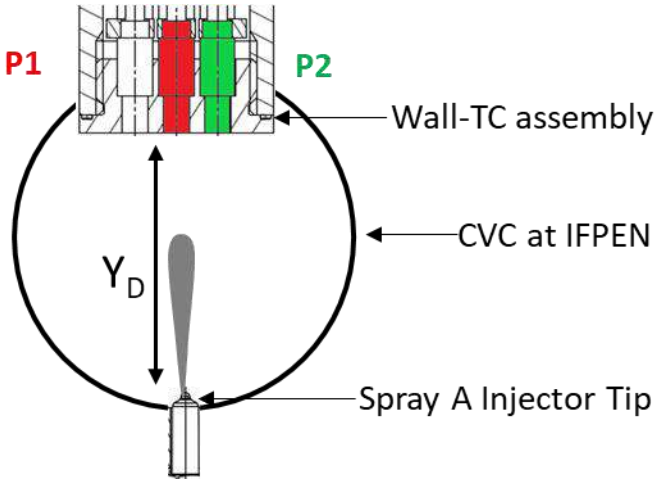

Figure 140: Schematic of spray-wall interaction

The main boundary conditions are listed in Table 18. More details can be found on the ECN website. The conditions used in the set of experiments presented here are verified by measuring the lift-of-length (***LoL***) of the free spray. ***LoL*** was measured using OH* imaging using a narrow pass filter at 305-310 nm. The average ***LoL*** was verified over 10 repetitions to be 15.33±0.45 mm, thus matching ***LoL*** measured within ECN experiments at IFPEN. ***LoL*** measured during reactive spray wall interaction is the same as ***LoL*** during free spray FWI suggesting that the presence of the wall does not affect ***LoL***, when the Y_D is larger than ***LoL***. This is illustrated in Figure 141, where a false-colored image shows the natural OH* luminosity during a free spray and spray-FWI. Wall temperature is maintained at T_W = 473±3.6 K at the start of experiments (t = 0).

Table 18: Spray A boundary conditions

Injection pressure (P_{inj})	1500 Bars
Ambient temperature (T_{amb})	900 K
Density	22.8 Kg/m^3
% Of oxygen	15 %
Duration of injection	1.5 ms
Fuel	n-Dodecane

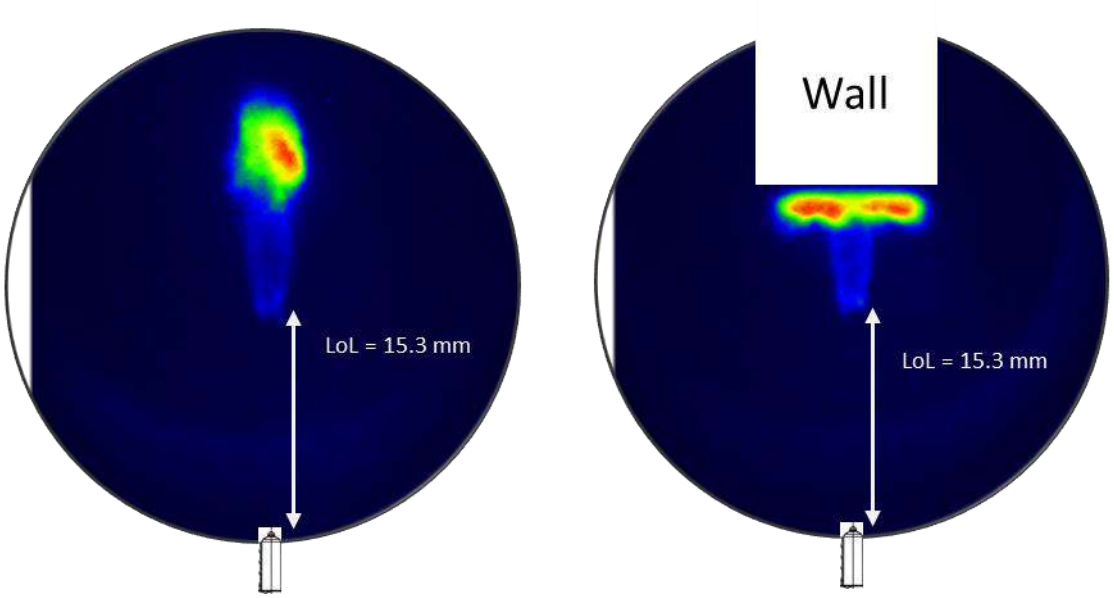

Figure 141: Lift-off length measured during Spray A free jet and Spray A wall interaction. The false-color image shows the signal intensity of OH*

To understand the effect of spray momentum during the interaction with the wall, experiments in non-reactive conditions are carried out. Further, the influence of the effect of ambient temperature on the heat flux due to spray wall interaction variation in ambient temperature is also carried out. Moreover, surface temperature measurements are carried out at two different radial locations i.e., P1, P2 shown in Figure 140. P1 corresponds to the stagnation point exactly opposite of the injector. P2 is radially located with the center-to-center distance between P1 and P2 being 10 mm. The experiments and the corresponding notations are given in Table 19. For calculating statistics, 10 repetitive tests are performed for each condition. Wall temperature ($\boldsymbol{T_W}$) evolves during the precombustion. So, $\boldsymbol{T_W}$ after the start of injection (ASOI) is listed in the corresponding experiment matrix.

Table 19: Non-premix Spray ignition experiment Matrix

P_{inj}: 1500 bars, Density: 22.8 Kg/m^3, Duration injection: 1.5 ms, Fuel: n-Dodecane, Y_D = 30 mm, Type 2 wall-TC assembly, $T_W(t = 0) = 473$ K					
Reactive/non-reactive	T_{amb} K	Ignition	Position	T_W at SOI K	Operating point notation
Reactive	900	natural	1	524	900-P1-R
Non-reactive	900	-	1	517	900-P1-NR
Reactive	900	natural	2	513	900-P2-R
Non-reactive	900	-	2	511	900-P2-NR
Reactive	1100	natural	1	517	1100-P1-R
Non-reactive	1100	-	1	531	1100-P1-NR
Reactive	1100	natural	2	545	1100-P2-R
Non-reactive	1100	-	2	516	1100-P2-NR

4.1.2. Effect of location of TC on the heat flux

Heat fluxes from surface temperature measurement at two locations (P1 and P2) for the two reactive conditions (900K and 1100K) are shown in Figure 142 and Figure 143. In these figures, we can see that Q_P at P1, i.e., at the stagnation point, is higher than that at P2, for both conditions. The exact values of Q_P are given in Table 20. This tendency is as per results obtained in literature [45, 114]. Although the absolute Q_P differs due to variation in the conditions of experiments.

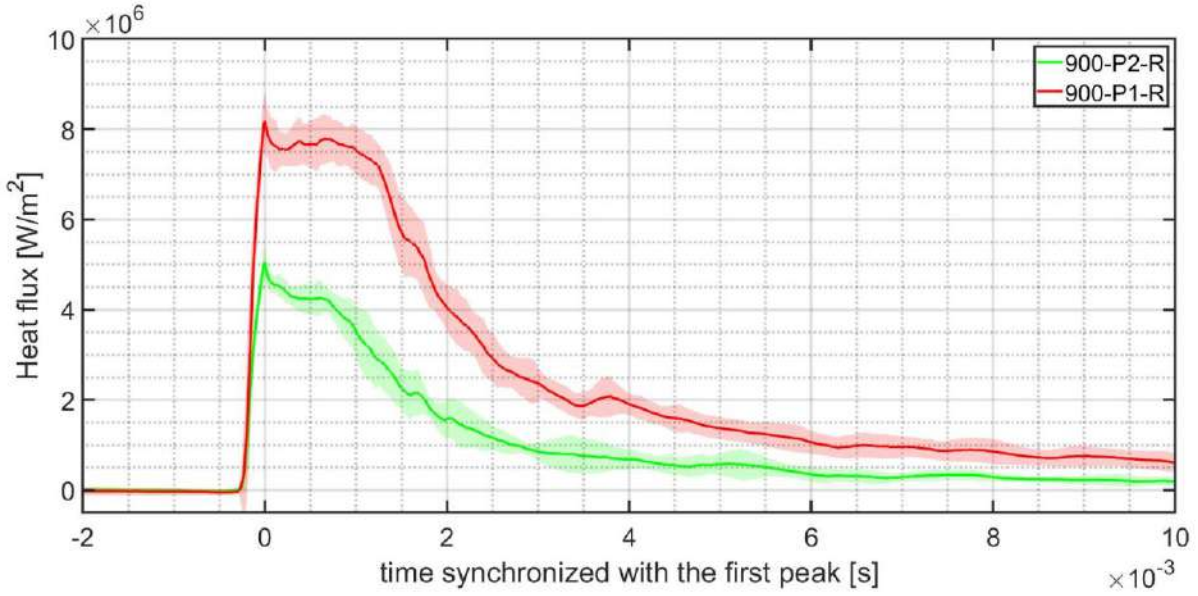

Figure 142: Comparison of heat flux from surface temperature measurements at two different locations, P1, P2 as per schematic shown in Figure 140 for T_{amb}= 900 K

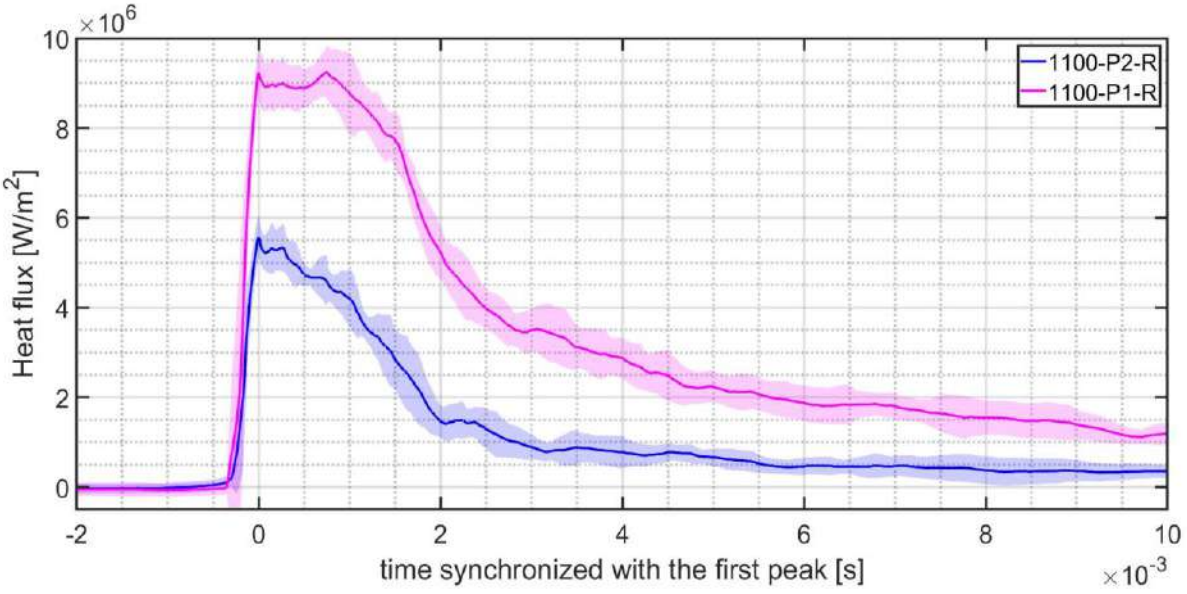

Figure 143: Comparison of heat flux from surface temperature measurements at two different locations, P1, P2 as per schematic shown in Figure 140 for T_{amb} = 1100 K

Table 20: Measured Q_P and computed h for reactive spray wall interaction

Operating point	Q_P MW/m^2	h kW/m^{2}K
900-P1-R	8.19±0.65	4.72
1100-P1-R	9.25±0.60	4.68
900-P2-R	5.05±0.38	2.91
1100-P2-R	5.58±0.46	2.81

Heat flux near the wall can be modelled by the convection equation. This is shown in Equation 37. h is the convection heat transfer coefficient, T_g is hot gas temperature and T_W is wall surface temperature. It is not possible to find T_g from the literature for the exact experiment setup and boundary conditions employed in this thesis i.e., spray A facing the wall. Hence, we will look to estimate T_g using data from the literature for a reactive free spray. For this purpose, we need to understand the spray combustion development before spray-wall interaction. The OH* visualization for experiment conditions 900-PX-R 1100-PX-R is shown in Figure 144 and Figure 145 respectively. In these figures, the spray combustion appears well developed prior to wall interaction. This observation is strengthened by the fact that ***LoL*** of free spray is similar to ***LoL*** of wall-bounded spray. Hence, we hypothesize that T_g for the fully developed

wall-bounded spray as observed in this thesis is similar to T_g in a fully developed free spray. Studies on spray structure and gas temperature in literature find that T_g is of the order of 2250 K for T_{amb} = 900 K and T_g is of the order of 2500 K for T_{amb} = 1100 K [115, 116]. Since the spray is well developed, we also hypothesize that the T_g at both P1 and P2 is the same.

Corresponding ***h*** values computed based on Q_P are given in Table 20. An uncertainty of 100 K in T_g leads to 6% uncertainty on ***h*** which we can consider to be negligible as it is less than the uncertainty on Q_P (8%). Hence, ***h*** values computed by using the values of T_g as per free spray are still relevant even though the uncertainty on T_g is ±100 K. The computed ***h*** values are close (almost the same order 2-4 kW/m^{2}K) to what has been found in the literature [35, 116, 117]. Comparing ***h*** for P1 and P2 we can see that ***h*** at P1 is larger than ***h*** at P2. Spray wall interaction can be imagined analogous to jet-wall impingement. A description of jet wall impingement is given in the literature [34]. During jet wall impingement the thinnest ***BL*** exists at the stagnation point. The high heat flux at the stagnation point (P1) compared to other radial locations (P2), could be related to the possible thin ***BL*** and subsequent high convection heat transfer coefficient at the stagnation point. In jet-wall flows, the velocity near P1 has a larger normal (to the wall) component while the velocity near P2 has a larger tangential (to the wall) component. The dynamic pressure linked to the normal component of the velocity compresses the ***BL***. Hence the ***BL*** is thinner at P1 compared to P2. This thin ***BL*** is the reason behind the high heat transfer coefficient at P1 compared to P2.

Equation 37: $$Q = h(T_g - T_W)$$

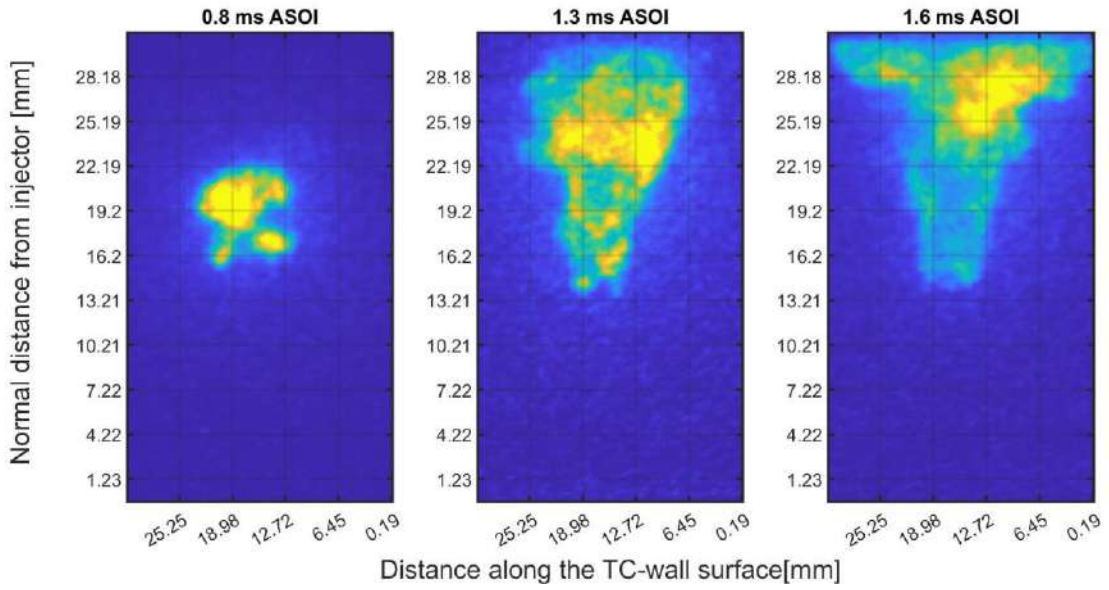

Figure 144: OH* intensity images showing spray flame development during spray wall interaction at different times after the start of injection (ASOI) for one repetition of 900-PX-R

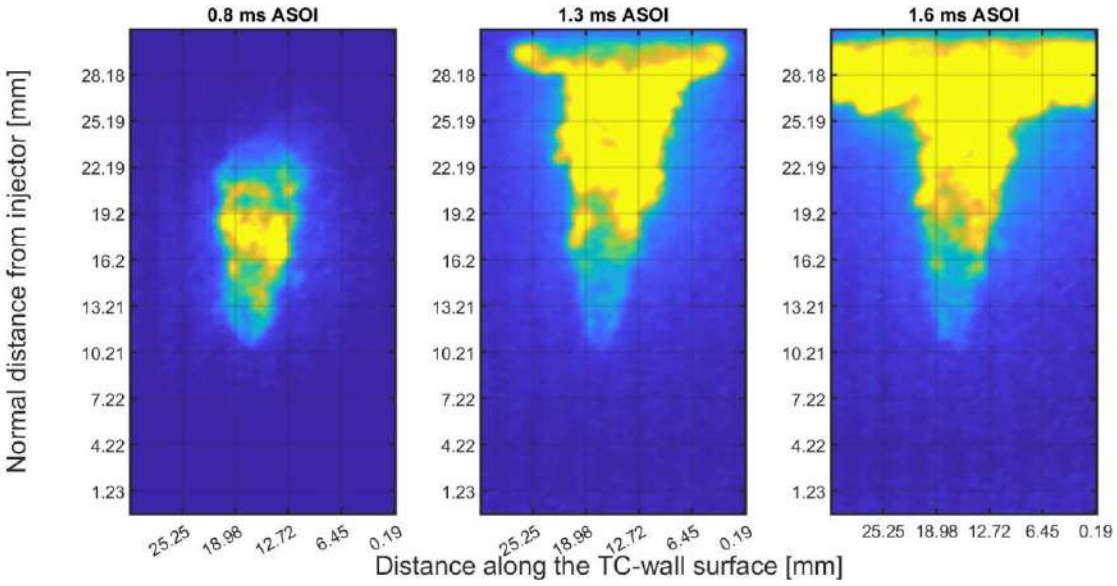

Figure 145: OH* intensity images showing spray flame development during spray wall interaction at different times after the start of injection (ASOI) for one repetition of 1100-PX-R

4.1.3. Effect of ambient temperature

The heat flux measured at two different ambient conditions is shown in Figure 146. Two sets of heat flux curves corresponding to two different locations of measurements are represented. With the increase

in ambient temperature (T_{amb}), Q_P increases. The corresponding Q_P values are given in Table 20. This is also shown by the double arrow in Figure 146. This increase is consistent at both the locations of measurement. Going in line with the hypothesis formed in the previous section 4.1.2, T_g~2250 K for T_{amb}=900 K and T_g~2500 K for T_{amb} = 1100 K. For explanations see the previous section 4.1.2. Corresponding h values computed based on Q_P is given in Table 20. Computed h values are close to what has been found in the literature (almost same order 2-4 kW/m^{2}K) for spray-wall interactions [35, 116, 117]. For two different T_{amb}, we can find that h values are independent of T_{amb}.

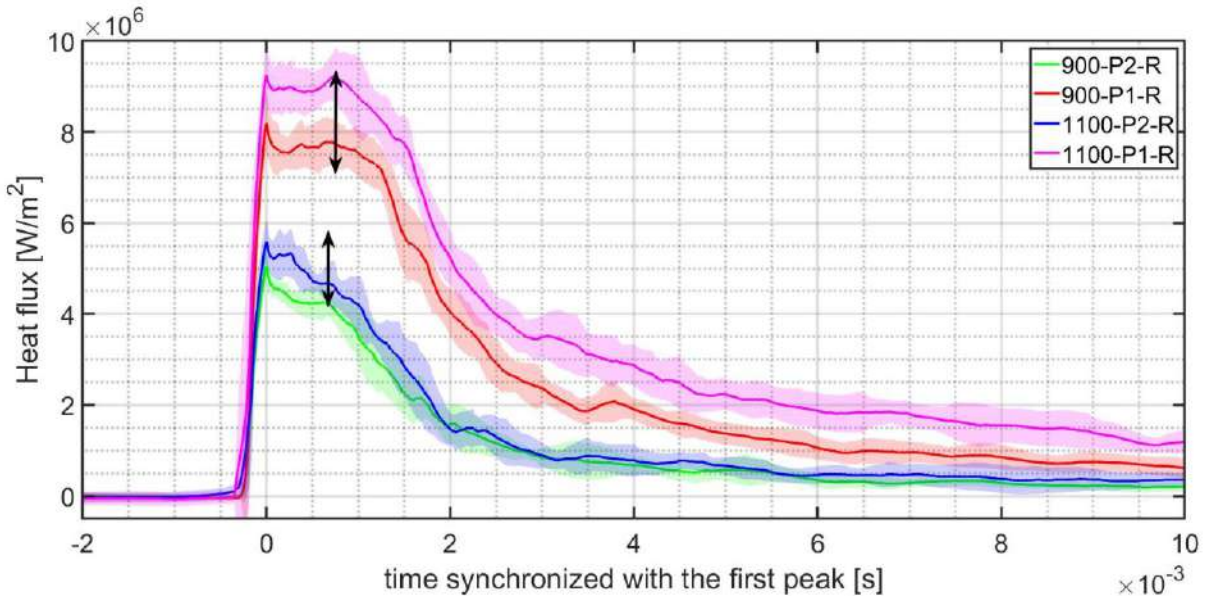

Figure 146: Effect of T_{amb} on the heat flux during spray wall interaction

4.1.4. EFFECT OF SPRAY MOMENTUM ON THE HEAT FLUX DURING SPRAY-WALL INTERACTION

The heat fluxes due to non-reactive and reactive spray interacting with the wall under spray A condition measured at two different locations are shown in Figure 147 and Figure 148, for T_{amb}= 900K and 1100K, respectively. In non-reactive cases, Q_P is of the order of 1-3 MW/m^2. This heat flux without the presence of flame is significant. Researchers have also recorded such high heat flux during non-reactive spray interacting with the wall under diesel engine conditions [45]. Calculation of the convection heat transfer coefficient (h) requires an estimation of T_g. It is expected that the temperature of the hot gas

near the wall will fall slightly with the evaporation of spray. However, there is no such accurate estimation of T_g available to us. The estimation of the change in T_g due to vaporization is <1K. Hence, we hypothesize that $T_g \sim T_{amb}$. Corresponding values of h are given in Table 21. We can see that the computed h values for non-reactive spray wall interaction are very close to the computed h for reactive spray-wall interaction at one given location (P1 or P2). Further h values are not dependent on T_{amb}, in line with section 4.1.3. The difference between h for experiments 900-P1-NR and 1100-P1-NR is 6% which is negligible as the uncertainty on Q_P~8%.

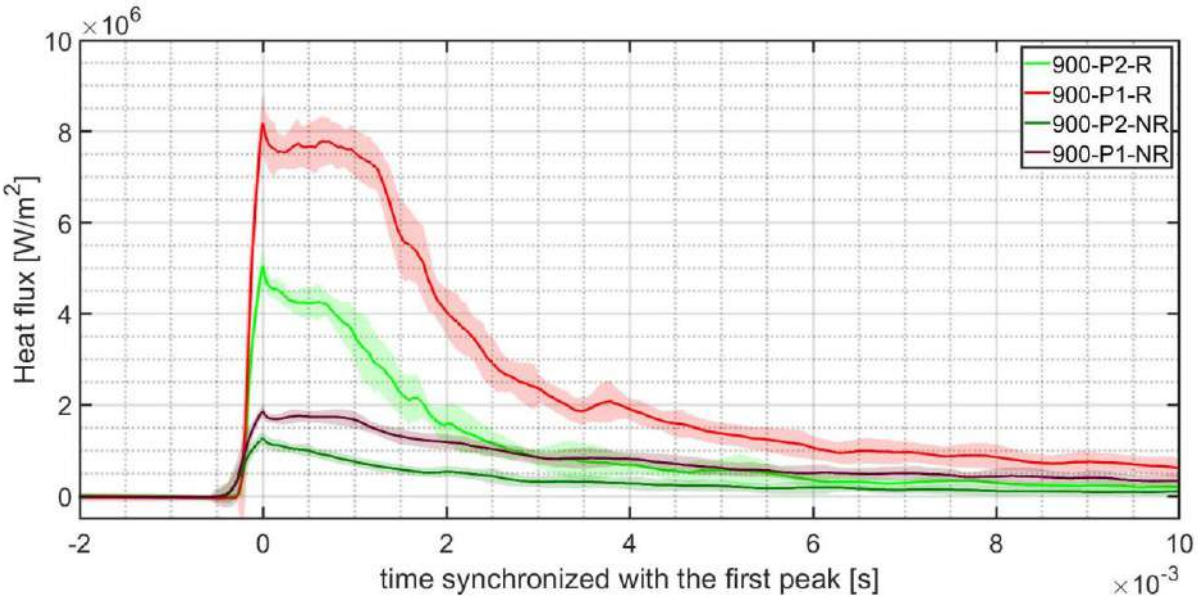

Figure 147: Heat flux trace during spray FWI in reactive and non-reactive conditions, at two locations of measurements (P1, P2) for T_{amb} = 900 K

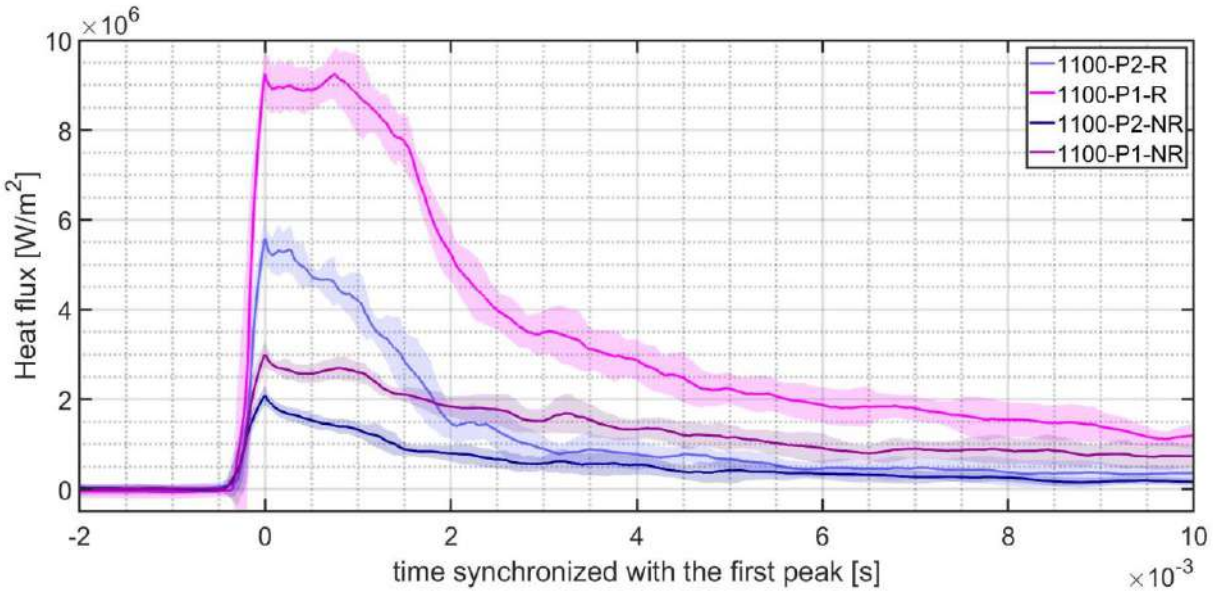

Figure 148: Heat flux trace during spray FWI in reactive and non-reactive conditions, at two locations of measurements (P1, P2) for T_{amb} = 900 K

Table 21: Measured Q_P and computed h for non-reactive spray wall interaction

Operating point	Q_P MW/m^2	h kW/m^{2}K
900-P1-NR	1.86±0.13	4.81
1100-P1-NR	3.00±0.28	5.11
900-P2-NR	1.27±0.15	3.28
1100-P2-NR	1.92±0.61	3.27

Further, we can compute a ratio of the heat flux trace for reactive spray-wall interaction over the heat flux trace for non-reactive spray-wall interaction ($\frac{Q_R}{Q_{NR}}$). The result of this calculation is presented in Figure 149. In this figure, the shaded grey region denotes the area in the plateau region of the heat flux trace when this ratio is constant. The statistics of this ratio in the plateau region (period of ~1.5 ms) are given in Table 22. The ratio of $\frac{Q_R}{Q_{NR}}$, is very similar to $\frac{T_g - T_W}{T_{amb} - T_W}$. which indicates that h for reactive and non-reactive spray wall interaction is not only close during Q_P but also during the whole plateau region of heat flux.

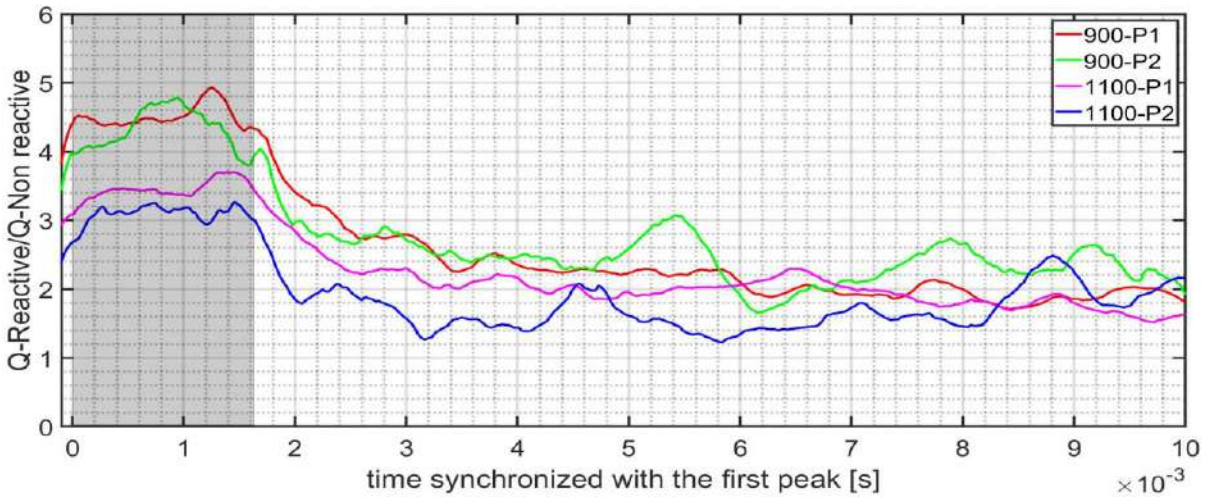

Figure 149: Ratio of reactive heat flux to non-reactive heat flux. The ratio of $\boldsymbol{Q}$ of 900-P1-R to $\boldsymbol{Q}$ of 900-P1-NR is given by curve 900-P1. This convention is applied to other cases

Table 22: Ratio of reactive heat flux over non-reactive heat flux

Operating point	$\frac{Q_R}{Q_{NR}}$	$\frac{T_g - T_W}{T_{amb} - T_W}$
900-P1	4.50±0.17	4.49
1100-P1	3.45±0.15	3.37
900-P2	4.30±0.30	4.49
1100-P2	3.08±0.14	3.37

4.2. Influence of ignition timing relative to spray impingement on spray-wall interaction

In the last section, we have observed significant heat fluxes for non-reactive spray wall interactions. Q_P for non-reactive spray wall interaction corresponds to 20-30% of Q_P under reactive conditions. Hence it is hypothesized that the two-step heat flux sometimes observed during spray wall interaction may be a result of two steps of spray wall interaction [45, 46]. According to this hypothesis, for conditions when autoignition happens after spray impingement, the first peak of heat flux is observed due to non-reactive spray wall interaction followed by a second step when the heat flux rises to a second peak due to reactive spray wall interaction. In this section, we will test this hypothesis. First, the experimental setup is presented, and then the results of the experiments.

4.2.1. EXPERIMENT SETUP

For the spray to auto-ignite after impingement, Y_D needs to be less than ***LoL*** of the spray. By decreasing the ambient density and T_{amb}, spray penetration and ***LoL*** increase. Hence, for this purpose, we employed a modified spray A condition. This modified condition was previously studied at IFPEN [79]. The boundary conditions are listed in Table 23. ***LoL*** of 49.1±0.1 mm (established from free spray characterization) is obtained. The wall-TC assembly is placed at Y_D = 42 mm. This configuration enables us to reach the condition of autoignition after spray impingement. Wall temperature is maintained at T_W = 473±3.6 K at the start of experiments (t = 0). To compute statistics, 10 repetitions of each operating point are carried out.

Table 23: Modified Spray A boundary conditions

Injection pressure	1500 Bars
Ambient temperature	800 K
Density	12 Kg/m^3
% Of oxygen	16 %
Duration of injection	3 ms

In order to force the ignition to happen before spray impingement we employed laser ignition. The setup for laser ignition is explained in Chapter 2. For the laser ignition to be successful, the ignition location and time of ignition need to be chosen such that the fuel-air mixture is present, well mixed, and in vapor form. In order to find this optimum location and timing, the vapor penetration of the modified spray A is studied. Figure 150 presents the vapor penetration of modified spray A obtained from the ECN database. The blue curve gives the mean vapor penetration while its standard deviation is given by the red curves. A choice of location is made at 31.5 mm from the injector tip, at the axis of the spray, that allows for the laser ignition to make ignition such that the flame to has enough time and distance for development, before impinging onto the wall (green dot in Figure 150). However, after using a variation of timing in

steps of 0.1ms, we were able to obtain consistent laser ignition for the timing of 0.7 ms ASOI at 31.5 mm from the injector on the axis of the spray. The spray jet reaches P1 at the wall at 0.9-1 ms and P2 at ~1.3 ms. The camera clock is offset from the laser clock by 1 µs.

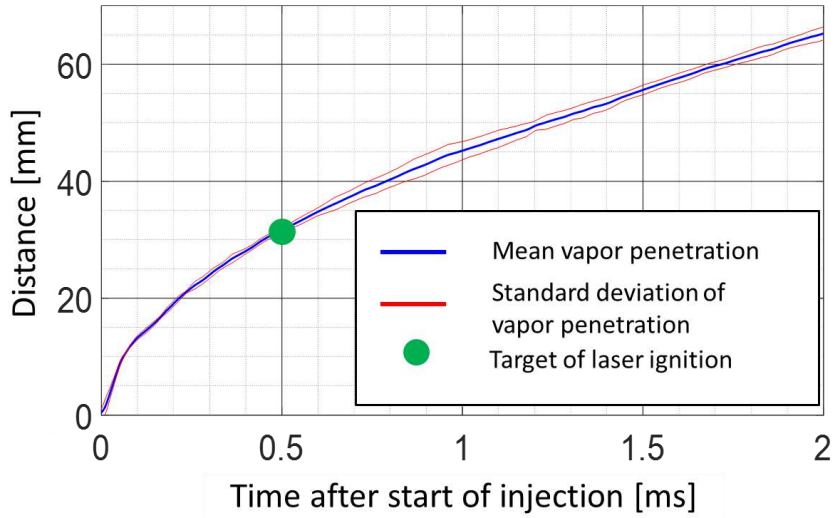

Figure 150: Vapor penetration of modified spray A from ECN database

We also studied non-reactive spray wall interaction for this modified spray A condition. For each experiment, non-simultaneous surface temperature measurements are carried out at two different locations corresponding to P1 and P2 in the previous section 4.1.2The corresponding experiment matrix with notations for different experiments is presented in Table 24. Apart from surface temperature measurements, OH* imaging and Mie-scatter imaging were carried out simultaneously. OH* images provided ignition and flame information while Mie-scattering images provided the location of the vapor jet.

Table 24: Non-premix Spray ignition experiment Matrix

P_{inj}: 1500 bars, Density: 12 Kg/m^3, Duration of injection: 3 ms, Fuel: n-Dodecane, Y_D = 42 mm, T_{amb} = 800K, Type 2 wall-TC assembly, T_W (t =0) = 473 K				
% of oxygen	Ignition	Position	T_W at SOI	code
16	natural	1	473 K	NLI-R-P1
16	laser	1	469 K	LI-R-P1
0	-	1	455 K	NLI-NR-P1
16	natural	2	463 K	NLI-R-P2
16	laser	2	459 K	LI-R-P2
0	-	2	453 K	NLI-NR-P2

One example of spray autoigniting after impingement is shown in Figure 151. For all the experiments with modified spray A condition, the spray impingement at the stagnation point (P1) occurs 0.9-1.1 ms ASOI. The tip of the spray jet reaches the sensor on the side (P2) within the next 0.3 ms (<1.4 ms). From Figure 151 we can see that autoignition (bright spots on OH*images) occur at a time after spray impingement (1.5 ms ASOI). For all the repetitions the autoignition appears after 1.5 ms ASOI. Hence, we can achieve the condition where the spray auto ignites after the spray jet has reached both P1 and P2 locations.

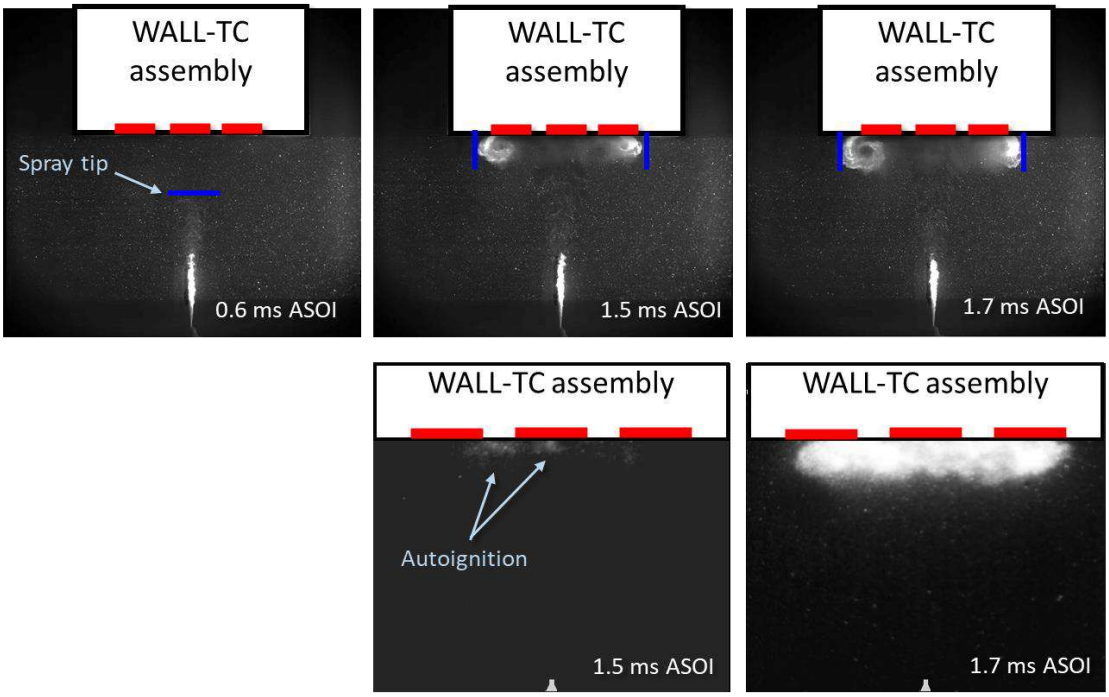

Figure 151: Simultaneous Mie scattering images (Top) showing the spray (liquid and gaseous) and OH* images (Bottom) showing the reaction regions for modified reactive Spray A without laser ignition. ***t*** = 0 corresponds to the start of injection (SOI)

On the same lines, one example of spray-wall interaction when spray ignites before spray impingement is shown in Figure 152. From the OH* images we can observe that laser ignition occurs at 0.7 ms (appearance of bright spots on the spray). This timing of laser ignition is consistent for all experiments with laser ignition. From the Mie-scattering image presented in Figure 152, we can record the time of spray impingement at P1 (1ms ASOI), when we can already see spots of autoignition. Spray arrives at P2 at a later time. This means that spray ignition is achieved before spray jet arrival at both P1 and P2. This observation is consistent with all the repetitions of the experiments. Hence, we can achieve conditions during which spray ignites prior to jet arrival at both P1 and P2 locations.

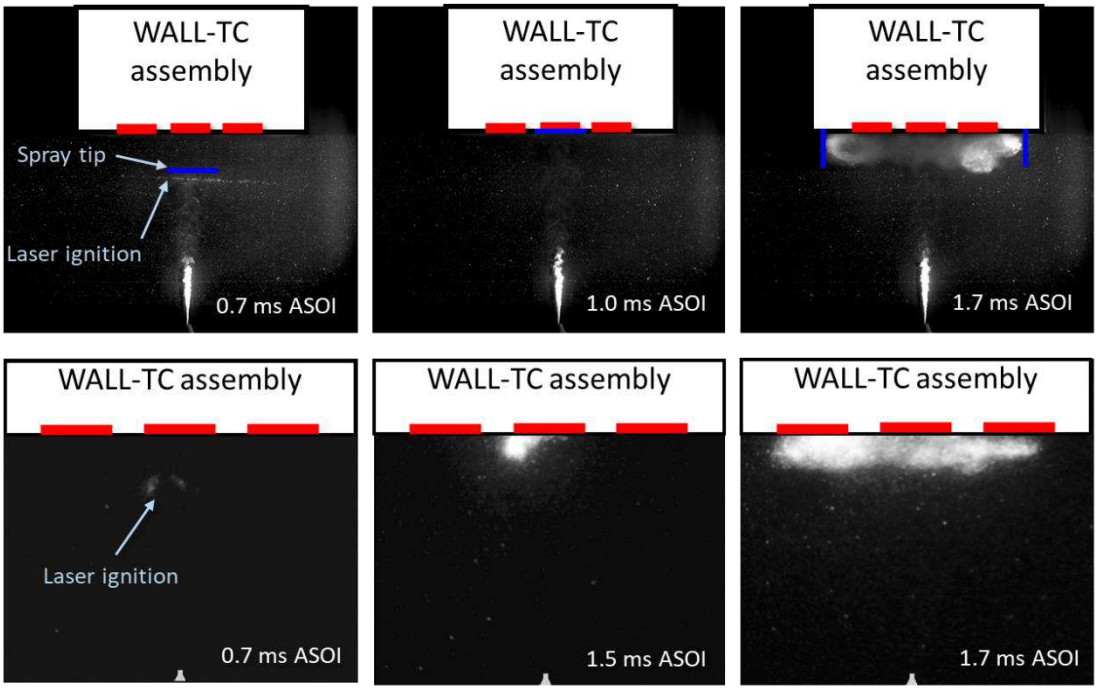

Figure 152: Simultaneous Mie-scattering images (Top) showing the spray (liquid and gaseous) and OH* images (Bottom) showing the reaction regions for modified reactive Spray A with laser ignition. ***t*** = 0 corresponds to the start of injection (SOI)

4.2.2. RESULTS

Q_P for these three variations is presented in Table 25. The corresponding time-resolved heat flux traces (***Q(t)***) are presented for P1 and P2 in Figure 153 and Figure 154, respectively. In these figures, we verify that the nature of the average heat flux trace remains like the heat flux trace in the previous section, i.e., we see a plateau of heat flux which falls later likely due to the end of combustion. We also observe noise from the laser on the heat flux trace before Q_P in the LI-R-PX. Q_P and ***Q(t)*** obtained for the modified Spray A reactive conditions are lower than for the conventional Spray A reactive experiments (cf. section3). This could be due to the low T_{amb} and low density employed in the modified Spray A conditions. We cannot estimate T_g for these modified spray A conditions as the spray structure is expected to change significantly when Y_D is less than LoL.

Table 25: Measured Q_P for non-reactive spray wall interaction

Notation	Q_P MW/m^2
NLI-R-P1	1.49±0.25
LI-R-P1	1.57±0.23
NLI-NR-P1	1.43±0.26
NLI-R-P2	1.69±0.36
LI-R-P2	2.08±0.35
NLI-NR-P2	0.87±0.07

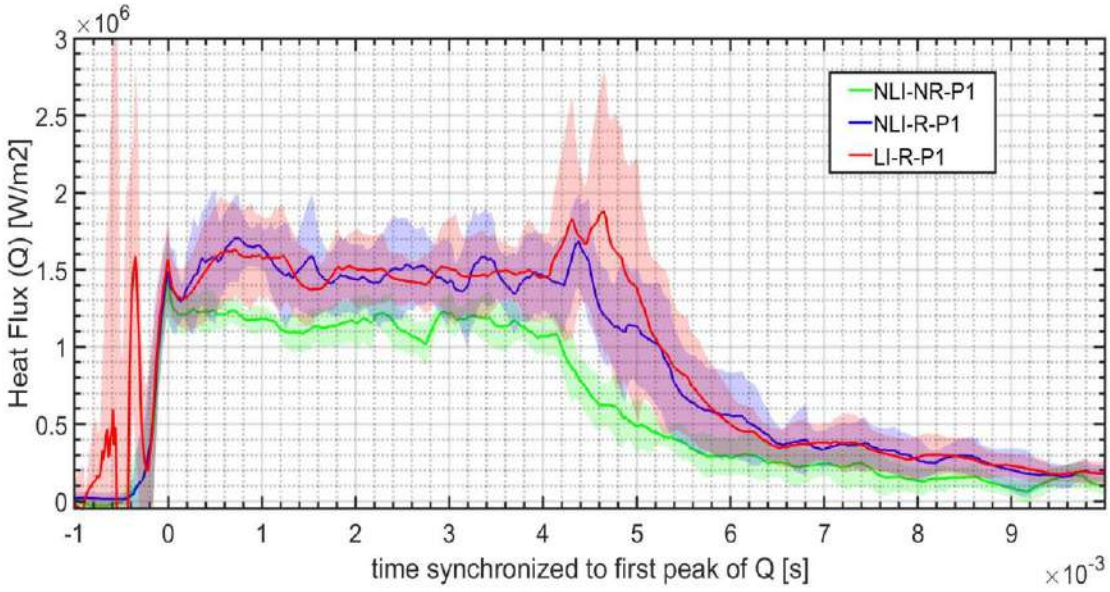

Figure 153: Heat flux trace during spray FWI measured at the center sensor

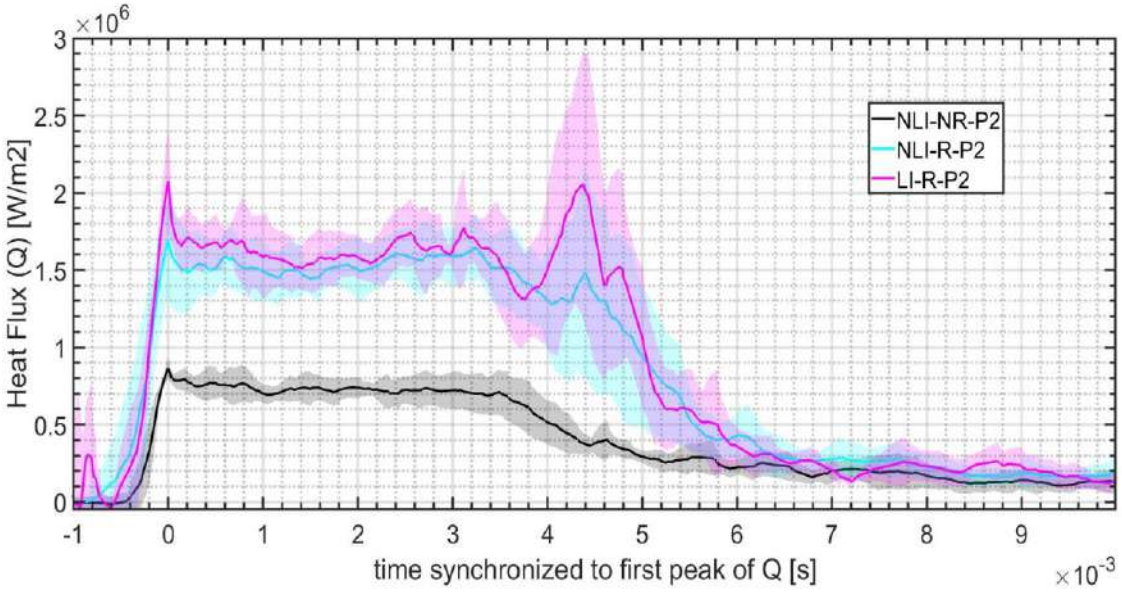

Figure 154: Heat flux trace during spray FWI measured at the side sensor

Q_P and $Q(t)$ for NLI-NR-P1 are larger than for NLI-NR-P2. This variation is consistent with the observation in previous section 1.1. where we have found that the convective heat transfer coefficient is larger at P1 than at P2.

At P1, Q_P and $Q(t)$ for all three variations (both reactive and non-reactive) are close to each other. Q_P for LI-R-P2 is only slightly larger than Q_P for NLI-R-P2 however $Q(t)$ is close to each other later in the plateau region. $Q(t)$ in the plateau region and Q_P for NLI-NR-P2(non-reactive) is almost half of $Q(t)$ and Q_P for NLI-R-P2 and LI-R-P2 (reactive).

However, Q_P for NLI-R-P2 and LI-R-P2 is larger than that for NLI-R-P1 and LI-R-P1 respectively. $Q(t)$ in the plateau is very close for all reactive heat flux traces at P1 and P2. Both these trends in Q_P and $Q(t)$ are opposite to what we have observed in the previous section 3, where we have seen that Q_P and $Q(t)$ are higher at P1 location than at the P2 location. Comparing $Q(t)$ for NLI-R-P2 or LI-R-P2 with NLI-NR-P2 we see a difference of ~1 MW/m^2. Comparing $Q(t)$ for NLI-R-P1 or LI-R-P1 with NLI-NR-P1, we see a difference of ~0.2 MW/m^2. Q_P for the non-reactive case ~0.91-0.95 times of Q_P for the reactive case at P1. Q_P for the non-reactive case ~0.42-0.52 times of Q_P for the reactive case at P2. We can conclude that there exists a smaller difference in Q_P and $Q(t)$ between reactive and non-reactive heat flux traces at P1 than at P2. From results in section 3, we know that Q_P and $Q(t)$ for the non-reactive spray are 0.2 to 0.3 times that of the reactive spray. Because of the difference in experiment boundary conditions, we can expect slight variation in this ratio. However, we do not expect this ratio to vary significantly as is seen at P1 in this case. The non-reactive $Q(t)$ is close to reactive $Q(t)$ in the plateau region for P1. This could indicate the center of the reactive spray has gasses with very low temperature during spray-wall interaction (due to no chemical reaction), despite reactive gas composition and laser ignition. Although, we do not have evidence to support this hypothesis.

We could not observe any two-step heat flux in the average heat flux trace obtained from our experiments with no significant difference in the NLI-R-PX and LI-R-PX cases (see Figure 153 and Figure 154). Hence, we will analyze the heat flux trace of each repetition to ensure that the phenomenon is not masked by averaging. As the heat flux trace at P1 shows a minor difference between both reactive cases and non-reactive cases, even if we obtain 2 step heat flux trace in individual repetitions, we will not be able to distinguish the two steps. Hence, we will study the heat flux trace of individual repetitions at P2.

No 2-step heat flux is observed for different repetitions of LI-R-P2. However, some repetitions for NLI-R-P2 showed 2 step heat flux trace. Heat flux traces of different repetitions for NLI-R-P2 are shown in Figure 155. Some individual heat flux traces are highlighted for better readability.

All individual heat flux traces (of different repetitions) for NLI-R-P2 are shown in Figure 155, shown in colored curves. We can see that there exist many heat flux traces that have no 2-step heat flux till its first peek at ~1.5-2 MW/m^2. However, some heat flux traces show evidence of 2 step heat flux, first peak at 0.8-1 MW/m^2 which corresponds to the average $\boldsymbol{Q_P}$ of non-reactive heat flux at similar conditions (shown in black in Figure 155). The differentiation in the 2 steps is not so evident in some other repetitions, while it's non-existent in the remaining repetitions. Further majority of the heat flux trace of various repetitions, show a multistep rise to the first peak indicating that 2 step heat flux could be an exaggerated multistep interaction. A few examples are shown in Figure 156 which is a zoomed version of Figure 155 here multistep in the heat flux trace is highlighted by circles.

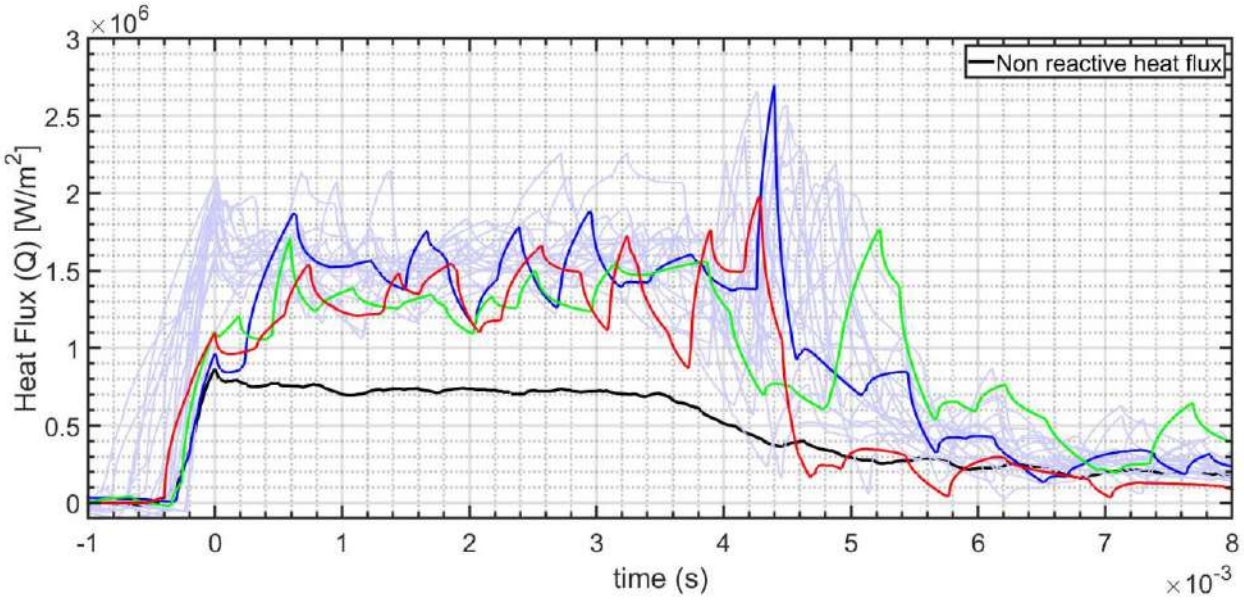

Figure 155: Some individual heat flux traces are highlighted which are measured in reactive conditions without laser ignition on the side sensor during spray FWI where distinct 2 steps are observed. The non-reactive heat flux trace is shown in black, rest traces are for individual repetition of an experiment

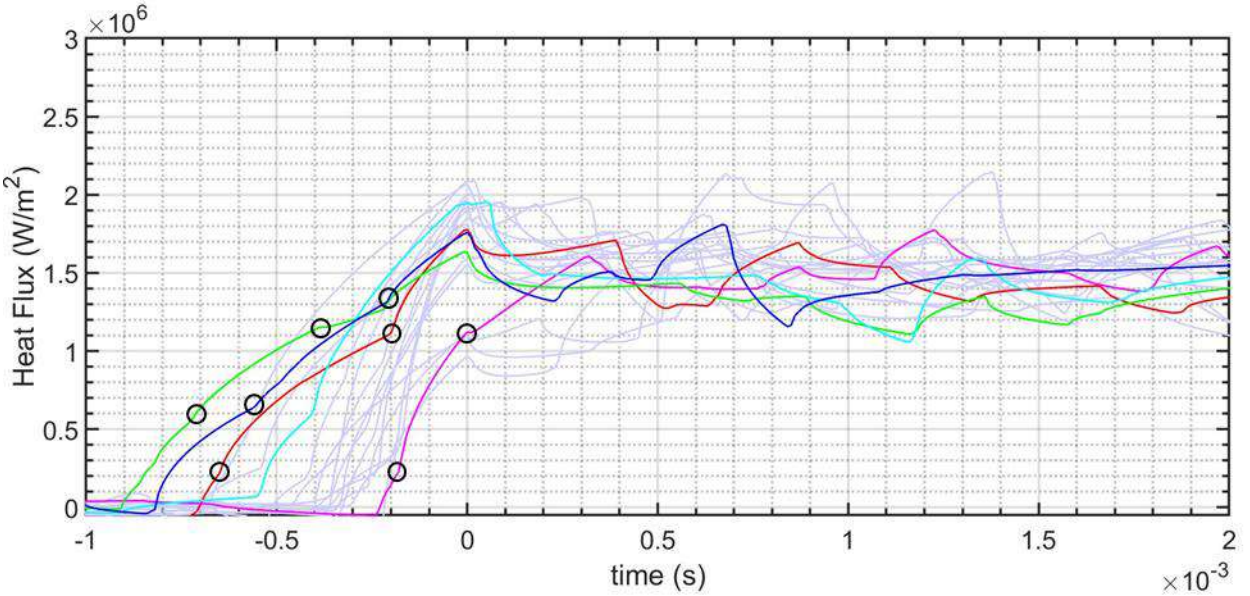

Figure 156: Zoomed version of Figure 155

Individual heat flux trace shows fluctuations during the plateau of spray FWI (Figure 155). These fluctuations can be due to turbulent structures that are present during spray-wall interactions. These turbulent vortices are visible in the Mie-scattering images (see Figure 157) These structures start from a

very small size at the start of spray wall interaction (~ 2mm), moving along the wall at speeds of ~ 32 m/s. They grow to large sizes (~9 mm), moving at speed of ~ 19 m/s. Because of the blurring of the PIV image near the wall, we could not determine the characteristic time of rotation of these structures.

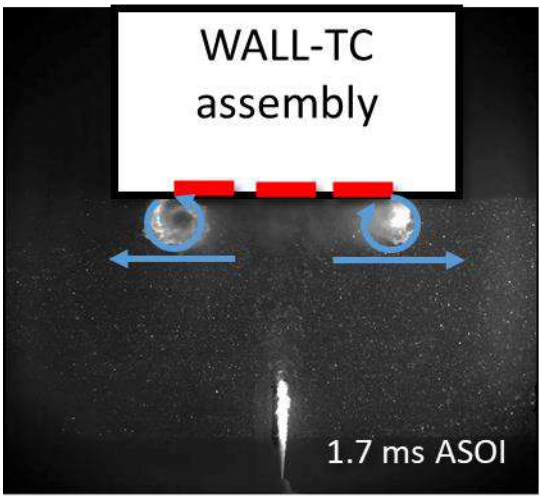

Figure 157: Turbulent structures during spray FWI

4.3. CONCLUSION

In this chapter, we present the surface temperature measurements carried out during spray FWI in the constant volume chamber. We used the boundary conditions of Spray A where the wall-TC assembly is placed at 30 mm from the injector. We verified that the ***LoL*** doesn't change when we introduce the wall. In this configuration, we computed the heat flux for both reactive and non-reactive spray for different locations of TC measurements and different ambient temperatures. Side location(P2) is found to have lower heat flux than at the center(P1) for both reactive and non-reactive spray-wall interactions. Such behaviours could be related to the convection heat transfer coefficient which is estimated to be higher at the center(P1) than at the side(P2) due to high dynamic pressure at P1 leading to thin BL near the stagnation zone. It is also found that the non-reactive spray wall interaction led to a Q_P that is 0.2-0.33 of Q_P observed in reactive spray wall interactions. The convective heat transfer coefficient(***h***) during spray wall interaction is found to be independent of reactive and unreactive conditions for each location of TC

measurements. Further, ***h*** is found to remain the same at 900 K and 1100 K indicating, ***h*** is independent of ambient temperature. It is also found that ***h*** at P1 location is higher than ***h*** at P2 location.

Another set of experiments is also carried out where a modified spray A condition is used to obtain an LoL = 49 mm. In this configuration, the wall is placed at 42 mm from the injector tip. This configuration yields 3 experiment conditions. They are non-reactive, reactive spray wall interactions where autoignition happens after impingement and vice versa (using laser ignition). In all these conditions heat flux is computed at two different locations (P1 and P2). Non-reactive average $\boldsymbol{Q_P}$ and ***Q*** are in a similar order as that of reactive $\boldsymbol{Q_P}$ and ***Q*** at the center locations. While reactive $\boldsymbol{Q_P}$ is higher (by ~ 2 times) than the non-reactive $\boldsymbol{Q_P}$ at the side location. Large vortex structures are seen during spray–wall interaction which could be linked to large fluctuations during the plateau of the heat flux trace. By checking the heat flux profiles of individual repetitions, we could obtain at least 3 repetitions with a distinct 2 step heat flux for the experiments where autoignition occurs after spray jet arrival at the sensor.

Chapter 5: Results of propagative flame in the engine

In this section, we will present the study of propagative FWI in a spark-ignition optical engine using the heat flux data derived from the fast surface temperature measurements exactly as used for experiments in the CVC. For the experiments presented in this chapter, we don't have complimentary diagnostics as in Chapter 3 and Chapter 4. Hence, we will use the heat flux and pressure data along with qualitative information from the literature for our analysis. Variations of pressure during interaction (P_{int}) and measurement location are carried out in this campaign, to enable comparison with results from the CVC campaign. Further, a tumble variation is performed, under the hypothesis that a higher tumble leads to higher turbulence intensity. In addition to the conventional spark-ignition strategy, a passive pre-chamber mode of ignition is also used for all the above parametric variations. Ignition timing and IMEP variations are other parametric variations conducted in this study. In this chapter, the experiment matrix is first discussed. Then the results of heat flux measurements are presented for all parametric variations, i.e., P_{int}, tumble, ignition system, ignition timing, location, and IMEP.

5.1. EXPERIMENT MATRIX

The test bench used to study the heat flux during a propagative FWI in an engine is presented in chapter 2. This section aims at presenting the experiment matrix. The flow field in the engine is inherently turbulent, leading to natural variation in the timing of FWI from one cycle to another, hence a different P_{int} for each cycle. This cycle-to-cycle variation of P_{int} will give us the effect of P_{int} on the peak of heat flux (Q_P).

The tumble is represented as the ratio of the angular speed of the flow to the angular speed of the crankshaft of the engine. The tumble variation is expected to affect the turbulence intensity inside the engine. Two types of the ignition system (PC and SI) are used to determine the effect of the ignition system

on Q_P. The location variation is designed targeting locations where we expect the maximum effect of the flame jet (P1, located opposite to the PC hole) and the minimum effect of the flame jet (P2, located in between two PC holes). A schematic representation of the two locations is shown in Figure 158. Varying ignition timing can lead to a delayed or advanced FWI. Both pressure and turbulence intensity evolve during the engine cycle [118]. The variation in time of FWI due to variation in ignition timing can lead to a study of the effect of change in pressure during FWI and turbulence intensity on the Q_P. Two values of IMEP are used, 4 and 6 bars. This variation is achieved by changing the gas pressure at the intake manifold keeping the equivalence ratio constant, i.e., 0.9. This variation in intake pressure induces a change in the density of the intake gas mixture. The ignition timing, tumble, location, and ignition type variations are conducted for each IMEP. The complete matrix is given in Table 26. In this thesis, absolute CAD is used to denote the ignition timing, where 360 CAD corresponds to the compression TDC. A specific notation is designed to identify each operating point. It consists of a combination of the parameter's values. For instance, an experiment using conventional SI, at an ignition timing of 345 CAD (15 CAD BTDC), using a tumble of 1.1 at IMEP of 4 bars is named after the following notation: SI-345-1.1-4. Whenever the location is required, the notation will include P1 or P2 (the notation for the P1 location of the previous experiment would then be SI-345-1.1-4-P1).

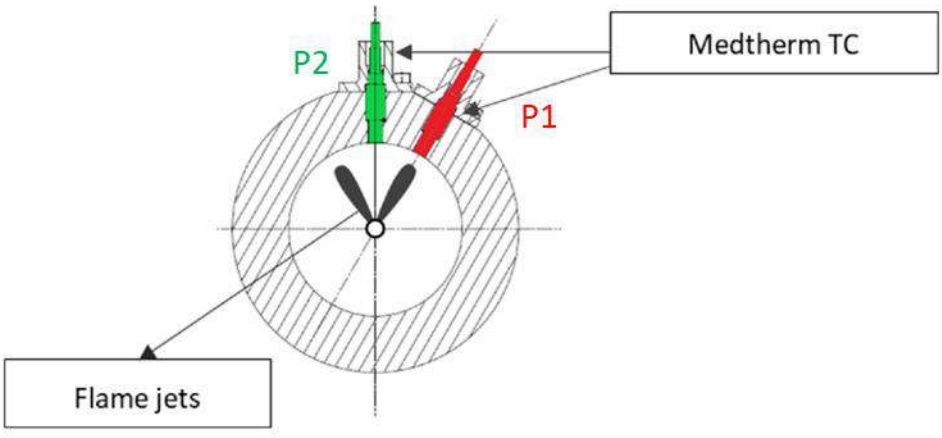

Figure 158: Two different locations of surface temperature measurement

Table 26: Experiment matrix for surface temperature measurements in the optical engine

Ignition system	IMEP bars	Ignition timing CAD	Tumble	Location
PC	4	345/355	1.1/1.5	1/2
SI	4	343/353	1.1/1.5	1/2
PC	6	356/361	1.1/1.5	1/2
SI	6	350/355	1.5	2

The average pressure traces corresponding to the experiments in Table 26 are shown in Figure 159 and Figure 160 for the conventional spark-ignition engine and pre-chamber ignition system, respectively. In Figure 159 and Figure 160, we can see that, with a change in ignition timing the peak pressures and pressure trace change while IMEP is fairly constant. The standard deviation of mean IMEP for each experiment (consisting of many repetitions) is <2.5% of the mean. There is a small variation within repetitions of each experiment, <5% standard deviation of the mean of various repetitions. A change in tumble affects the peak pressure slightly. A change in the IMEP affects the peak pressure and pressure trace significantly. Now we will present the results of these variations.

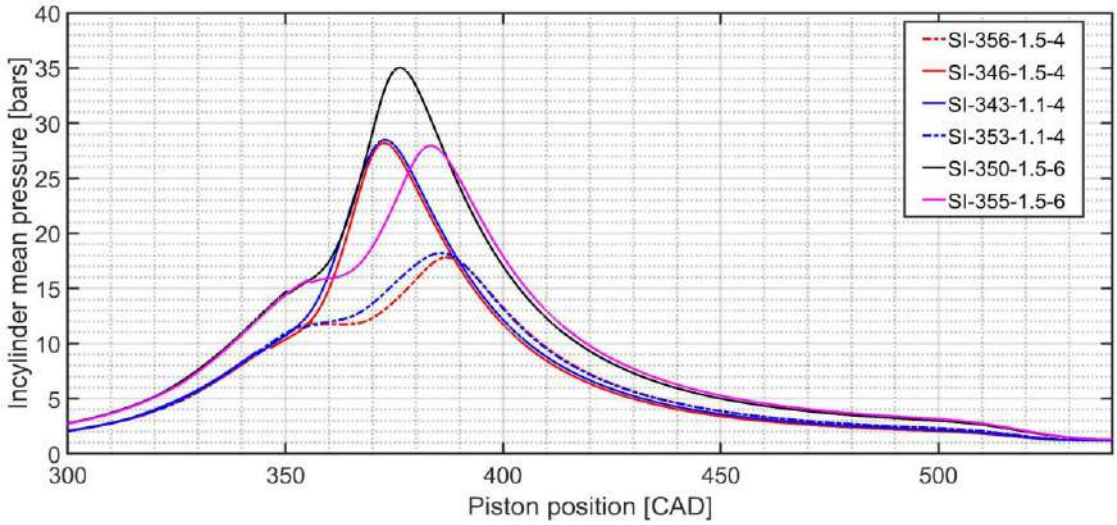

Figure 159: Mean in-cylinder pressure trace of different variations (ignition timing, tumble, and IMEP) with the conventional spark ignition system

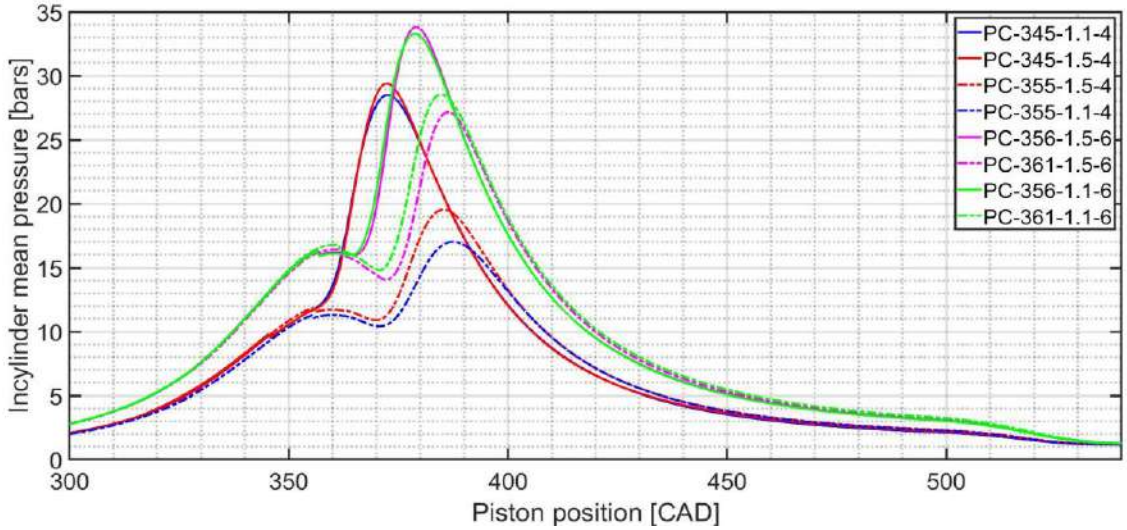

Figure 160: Mean in-cylinder pressure trace of different variations (ignition timing, tumble, and IMEP) with the passive pre-chamber ignition system

5.2. Effect of P_{INT} on Q_P

The cycle-to-cycle variation allows us to derive the tendency of Q_P vs P_{int} using the individual cycle measurements done for each operating point in Table 26 . There are a large number of plots (32) which show this Q_P vs P_{int} for individual experiments in Table 26. We have selected two plots to show the tendency we want to highlight. Figure 161 shows Q_P vs P_{int} for PC-355-1.5-4-P1 and Figure 162 shows Q_P vs P_{int} for PC-345-1.5-4-P1. In these figures, we can see that Q_P increases with P_{int}, in line with observations from Chapter 3. In line with Chapter 3 we will use a power-law fit ($Q_P = aP_{int}^{b}$) to explain the tendency of Q_P vs P_{int}, shown in both Figure 161 and Figure 162. The data has a large scatter with a small range of P_{int}. The scattering on the data and the small range of P_{int} makes the power-law fit and coefficient less accurate. For our comparison, we will still use these coefficients. Care must be taken when using these coefficients for comparison across different setups. This power-law fit is qualitatively like the power-law fit obtained in Chapter 3 for turbulent FWI with a power-law coefficient, b>1 (for laminar FWI b <1 for our experiments in Chapter 3 and in the literature). In all the experiments carried out in the engine, we can detect a similar tendency of Q_P vs P_{int} with a power-law coefficient, b>1. Plots of Q_P vs P_{int} is the basic relationship that is used for comparison of the effect of different parameters throughout this chapter. In the upcoming

sections, we will present Q_P vs P_{int} for different experiments in Table 26 to find out the effect of different parameters.

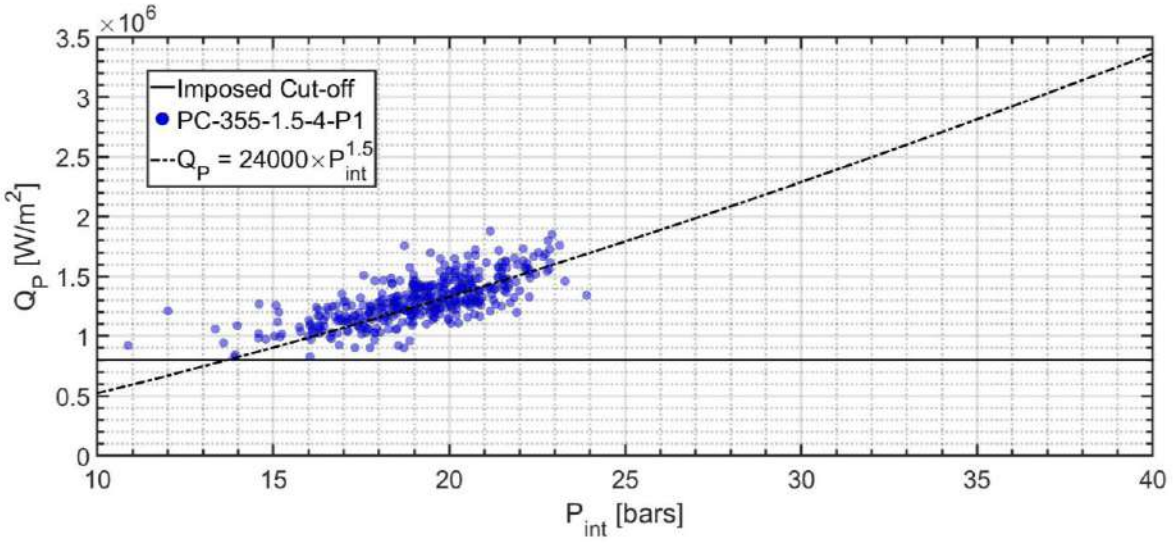

Figure 161: Sample 1 Q_P vs P_{int}, black line denotes a possible detectable tendency

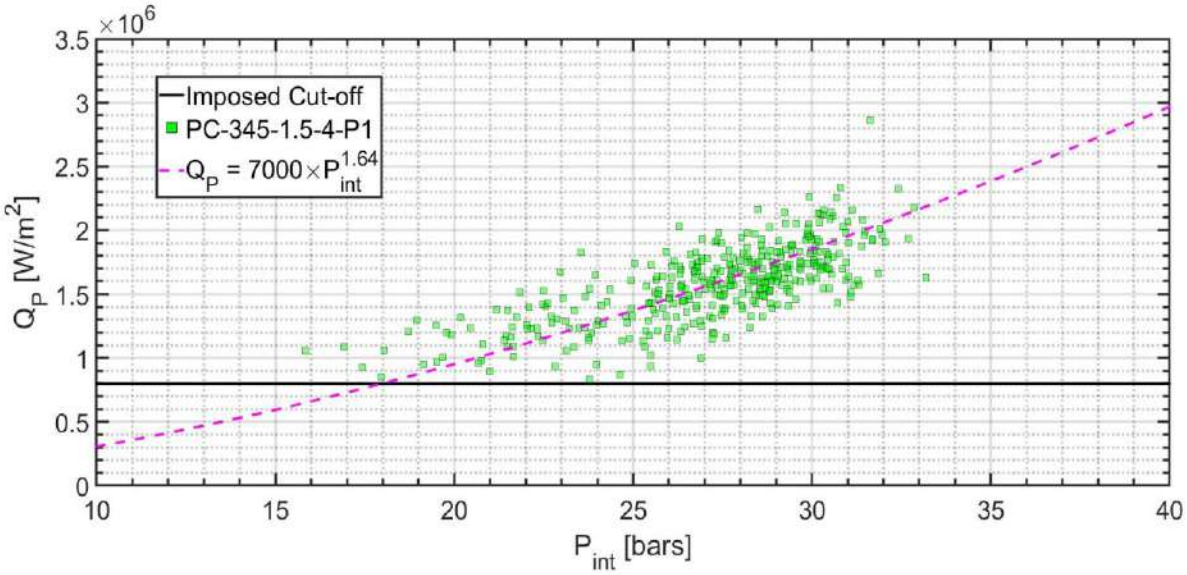

Figure 162: Sample 2 Q_P vs P_{int}, pink line denotes a possible detectable tendency

5.3. Effect of tumble variation on Q_P

Two tumble values are used in the engine i.e., 1.1 and 1.5. In literature, higher tumble is associated with higher turbulence intensity [118]. We will use this information qualitatively to analyze the heat flux

measurements. Two operating points are comparatively plotted as Q_P vs P_{int} in Figure 163, showing the effect of tumble variation. In order to compare the two plots, we have binned Q_P vs P_{int} data, with bins of 3 bar with a constraint of at least 20 points in each bin. Figure 164 shows the average of Q_P vs average of P_{int} over a bin of 2 bars. Q_P when binned and averaged shows that at a given P_{int}, the average Q_P for tumble 1.5 is slightly higher (by 8-14 %) than tumble 1.1. This result is in line with the results in Chapter 3 and the literature where higher turbulence intensity and mean velocity are found to increase the Q_P during FWI.

We observe scattering on X-axis (P_{int}) and Y-axis (Q_P). P_{int} scattering (X-axis) is a cycle-to-cycle variation which is due to turbulence in the engine. The overall range of P_{int} occupied in case of tumble = 1.5 is larger than in the case of tumble = 1.1 (see Figure 164). This is consistent with the expectations that high turbulence (high tumble) would lead to high cycle-to-cycle variation leading to high scattering in P_{int}. In chapter 3, we have seen that high turbulence intensity in the bulk flow can lead to faster flame propagation with a higher flame speed. In engines, we expect there will be stronger air flow prior to combustion. In such a scenario, there will likely be a competition between the flow field and flame leading up to FWI. Stronger flames with higher flame speed will likely lead to more HOQ while weaker flames with lower flame speed will have more chance of SWQ (as the flow field prior to combustion dominates). Typically HOQ has a high Q_P compared to SWQ [40]. Hence, we hypothesize that lower tumble (low turbulence) leads to a mix of SWQ and HOQ leading to a large scatter in Y-axis or Q_P. On the same line, higher tumble leads to more HOQ leading to lower scatter in Y-axis or Q_P.

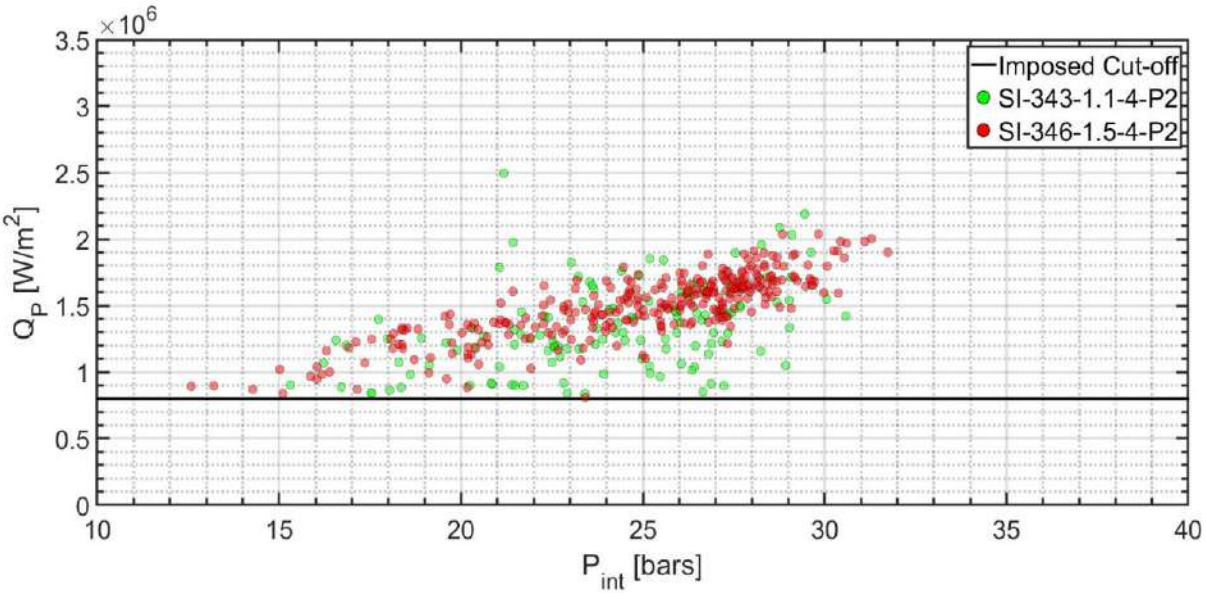

Figure 163: Q_P vs P_{int} for Tumble variation for SI at ~345 CAD measured at P2 for IMEP = 4 bars

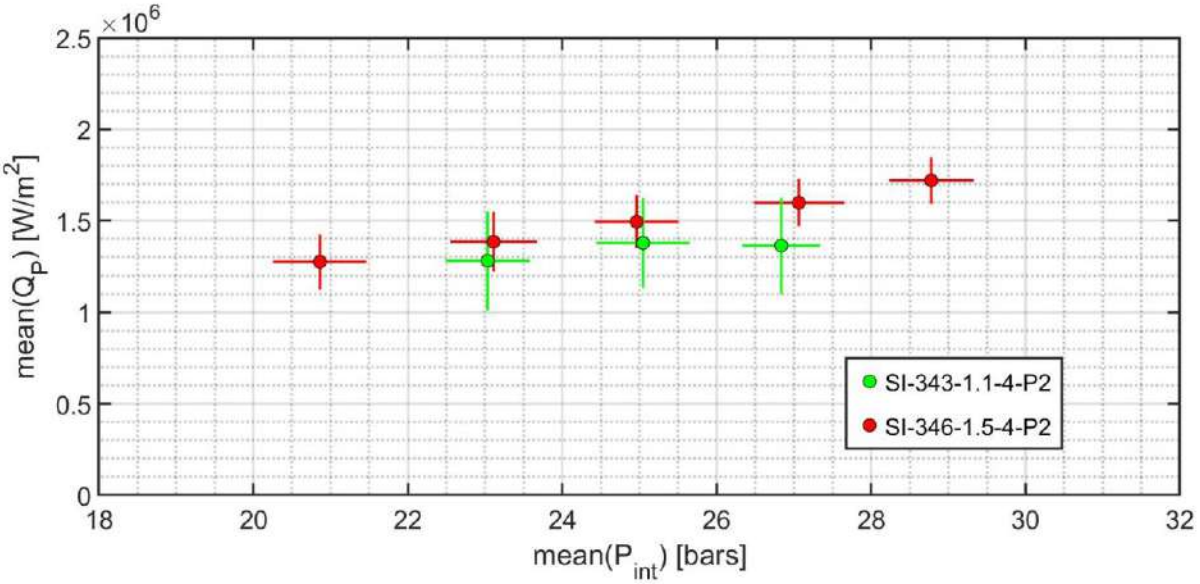

Figure 164: Binned average Q_P vs binned average P_{int} for scatter plot shown in Figure 163

Another example of tumble variation for higher IMEP is shown in Figure 165 and Figure 166. The observations listed for comparison shown in this section are true for all tumble variations presented in this chapter. Owing to the large scattering and similarity in the tendency of Q_P vs P_{int}, we will not analyze low tumble cases from this point.

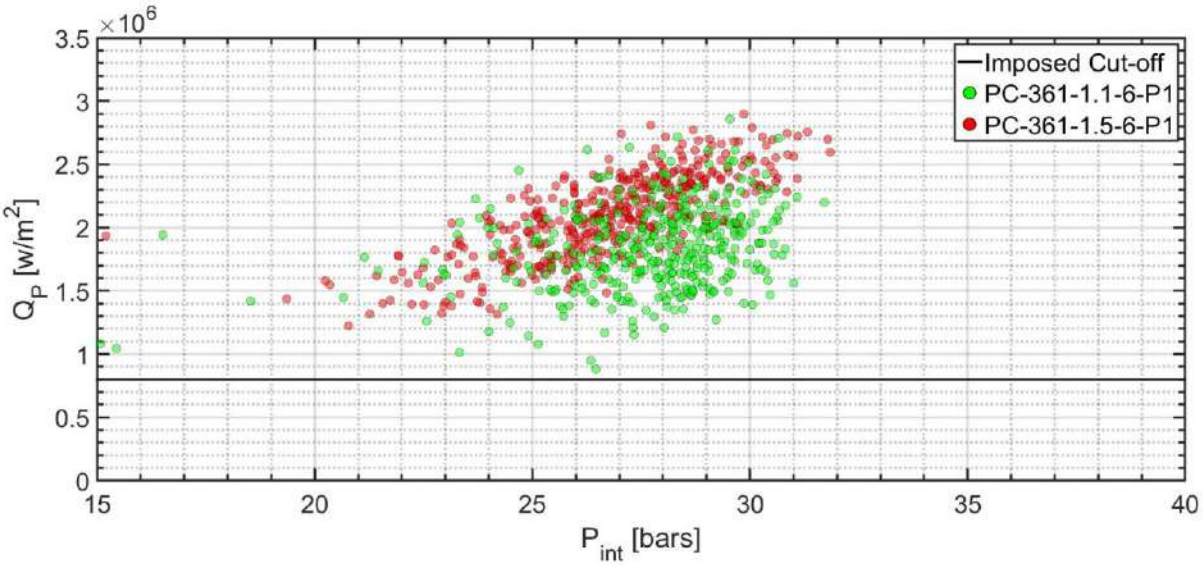

Figure 165: Q_P vs P_{int} for Tumble variation for PC at ~361 CAD measured at P1 for IMEP = 6 bars

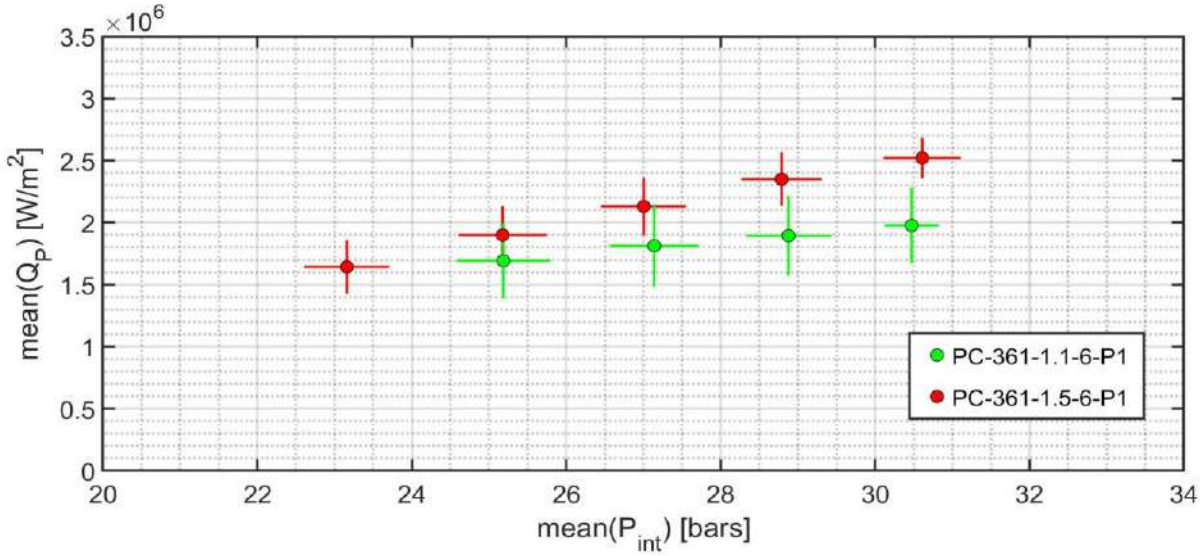

Figure 166: Binned average Q_P vs binned average P_{int} for scatter plot shown in Figure 165

5.4. Effect of Ignition System Variation on Q_P

One of the interesting comparisons targeted in this thesis is the heat flux comparison during FWI for a PC and conventional spark ignition system. The motivation for such a comparison comes from the advantages that the PC ignition system provides, i.e. faster combustion [18]. We need to evaluate whether PC leads to a higher heat loss or not. A comparison of heat loss for both PC and SI at IMEP = 4 bars for P2 is shown in Figure 167 and Figure 169. In Figure 167, and Figure 169 we don't see any difference between

SI and PC cases as the scatter data cloud for PC and SI overlap each other. This observation is also consistent with binned average plots shown in Figure 168 and Figure 170 where the difference between PC ignition and SI ignition is <1%.

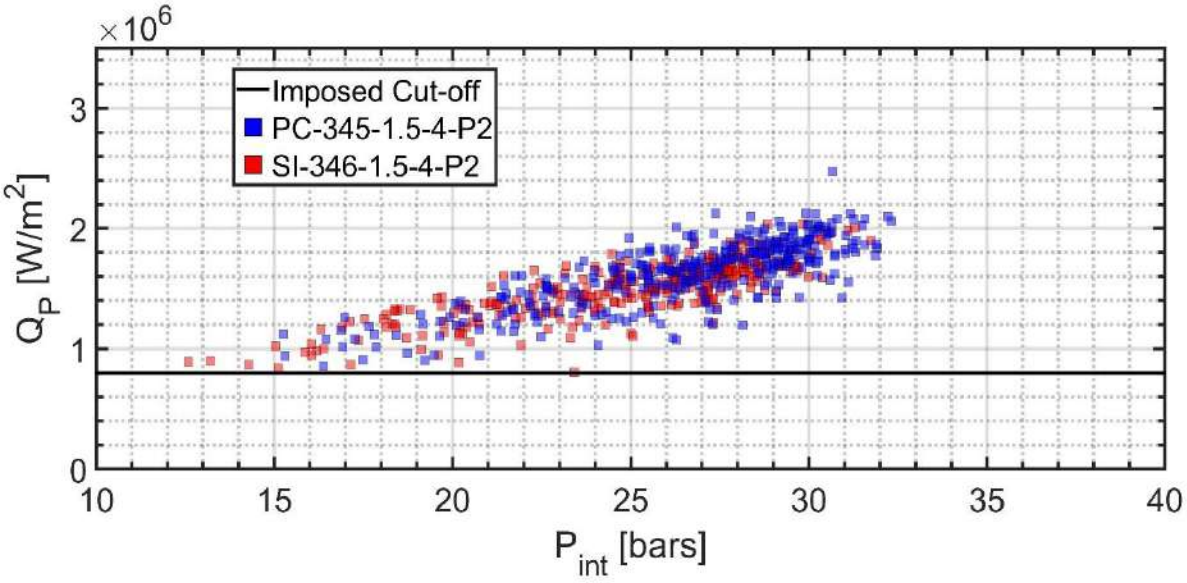

Figure 167: Q_P vs P_{int} for location P1 for PC/SI with ignition at ~345 CAD measured for IMEP = 4 bars and tumble 1.5

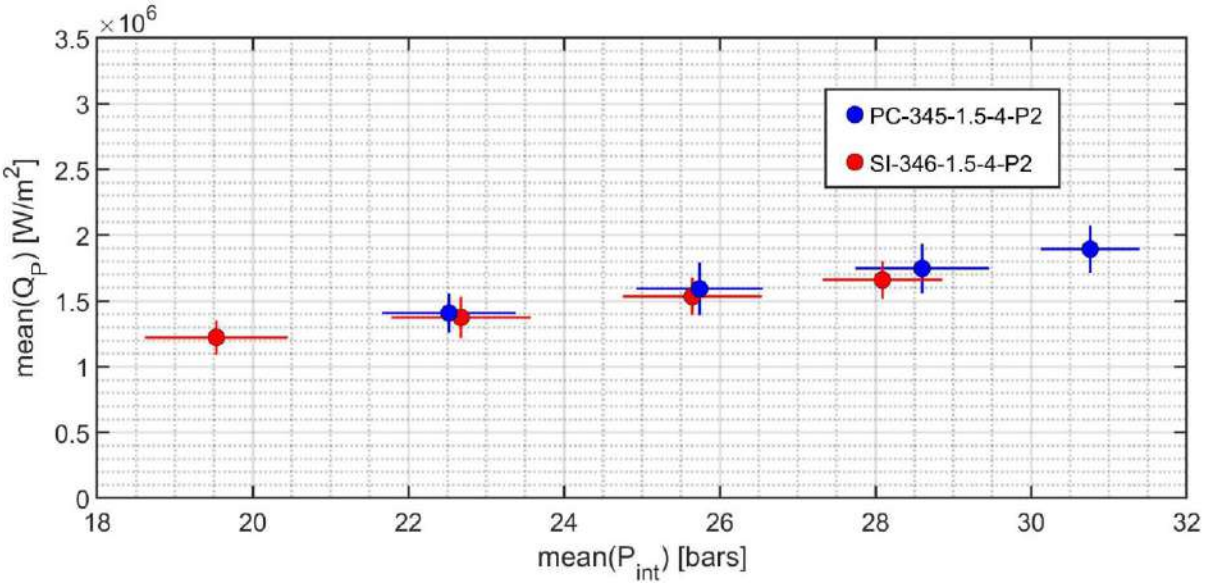

Figure 168: Binned average Q_P vs binned average P_{int} for scatter plot shown in Figure 167

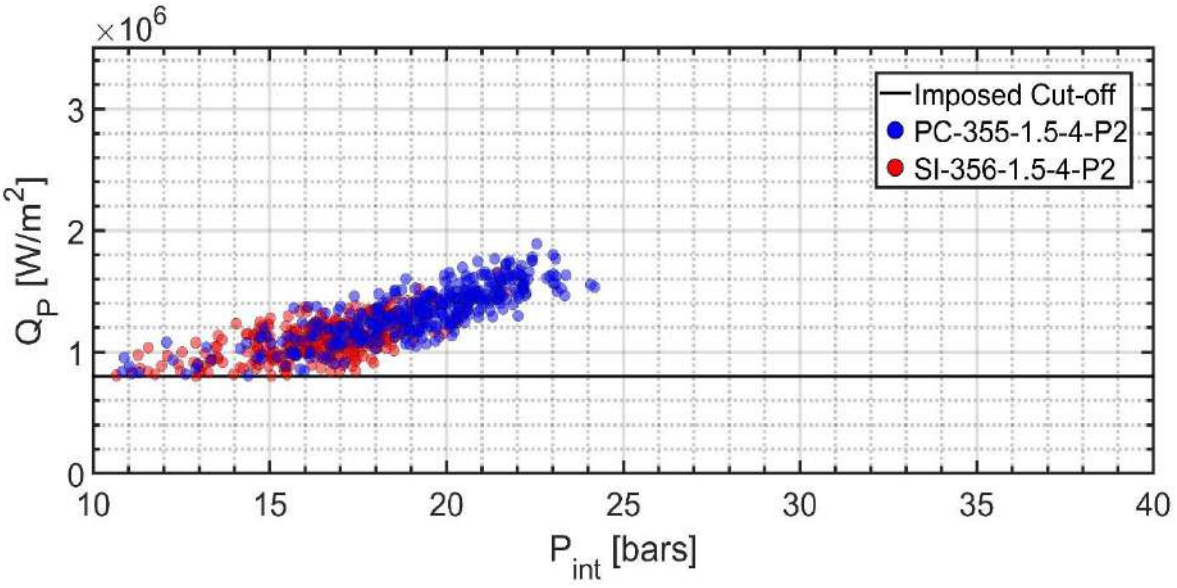

Figure 169: Q_P vs P_{int} for location P2 for PC/SI with ignition at ~355 CAD measured for IMEP = 4 bars and tumble 1.5

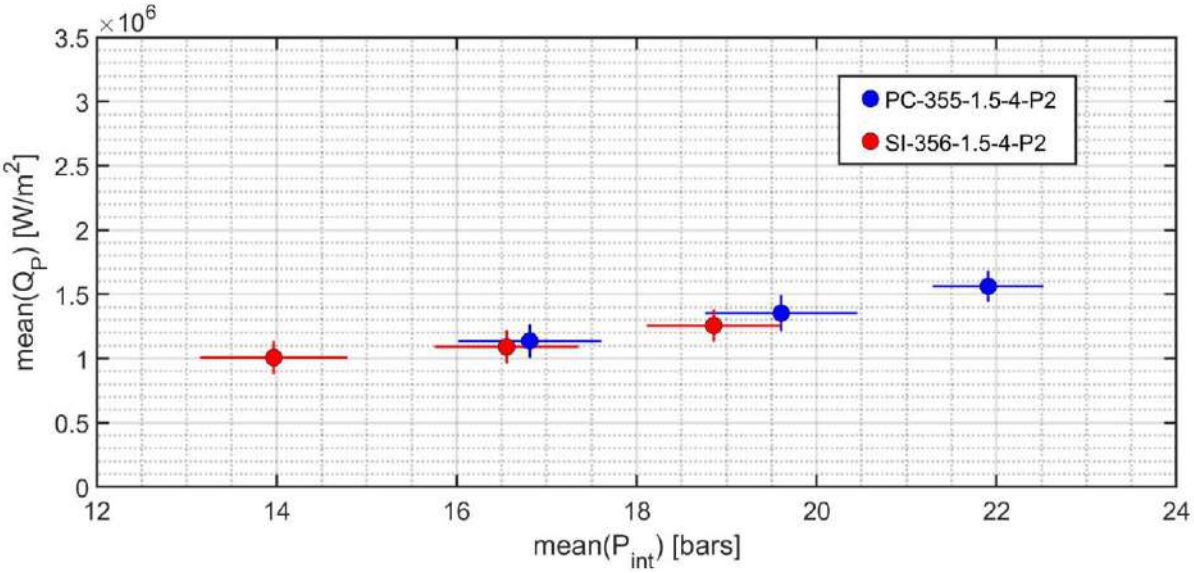

Figure 170: Binned average Q_P vs binned average P_{int} for scatter plot shown in Figure 169

Similarly, Q_P vs P_{int} scatter plot for two types of ignition system for IMEP = 4 bars at P1 location, ignition at 345 CAD and 355 CAD is given in Figure 171 and Figure 173 respectively. Corresponding binned mean Q_P vs mean P_{int} is given in Figure 172 and Figure 174. The Q_P for SI-346-1.5-4-P1 is slightly higher (by

up to 8%) compared to PC-345-1.5-4-P1, for which we don't have an explanation. However, the difference in Q_P for SI-356-1.5-4-P1 and Q_P for PC-355-1.5-4-P1 is very small (<1%). Hence, we conclude that the tendency of Q_P vs P_{int} is unchanged for both types of ignition system at IMEP = 4 bars.

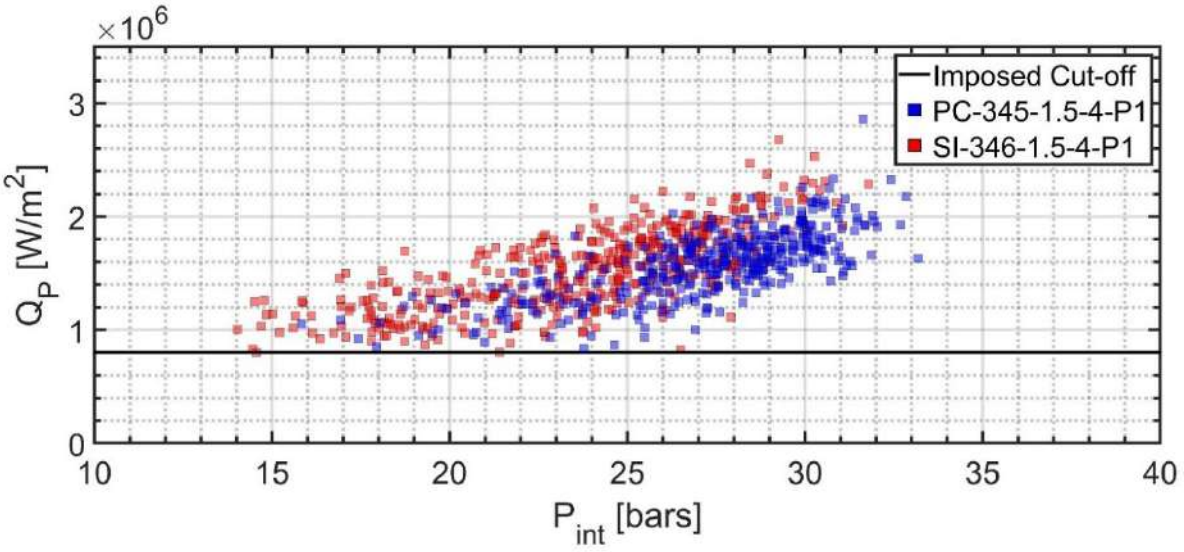

Figure 171: Q_P vs P_{int} for location P1 for PC/SI with ignition at ~345 CAD measured for IMEP = 4 bars and tumble 1.5

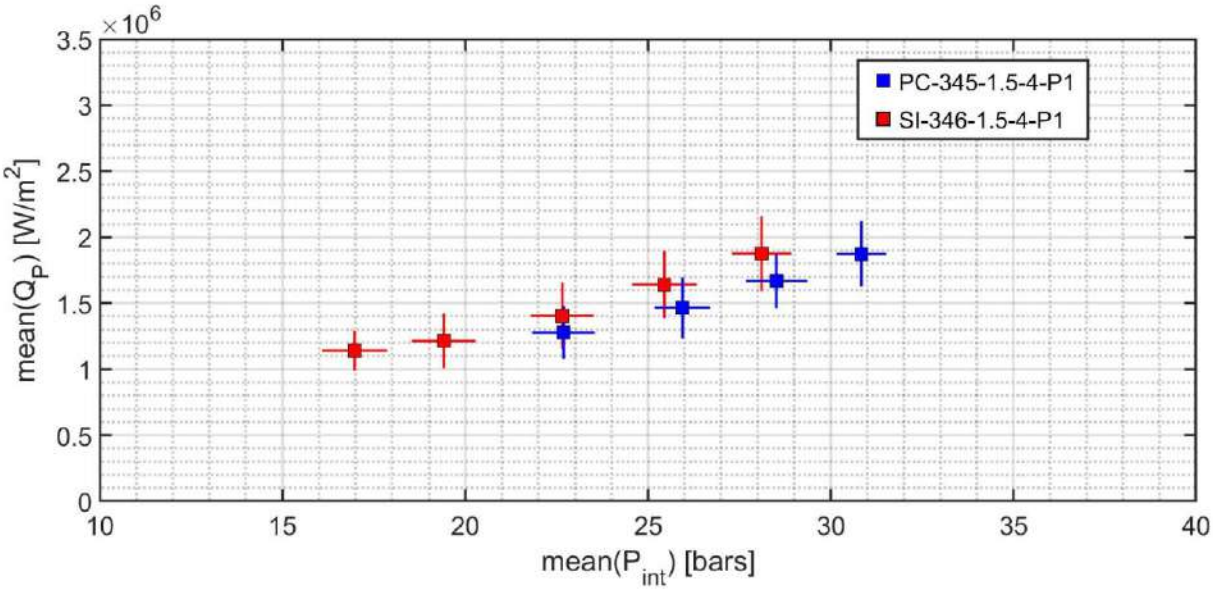

Figure 172: Binned average Q_P vs binned average P_{int} for scatter plot shown in Figure 171

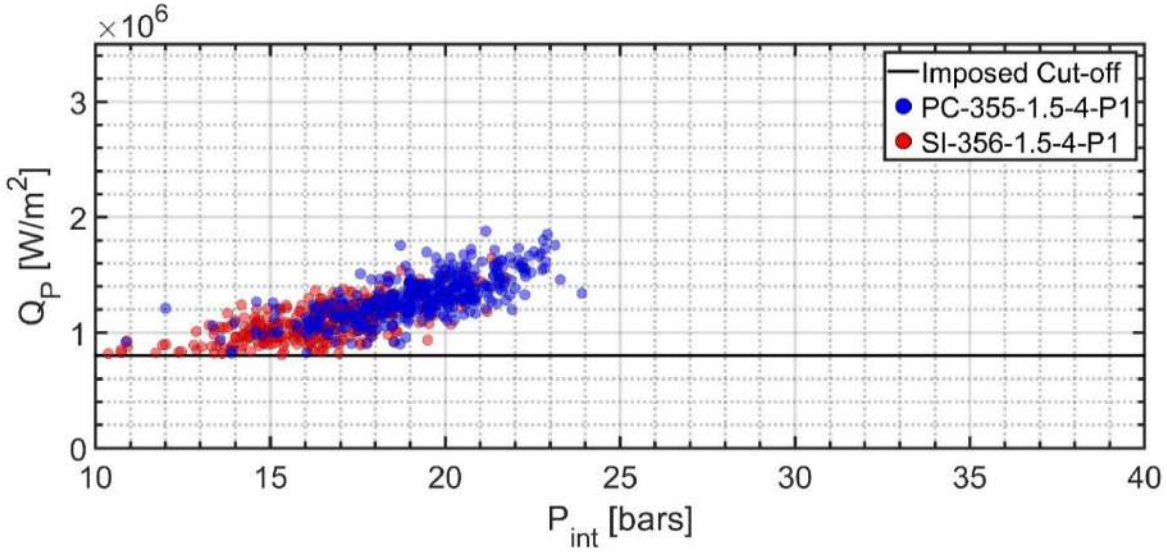

Figure 173: Q_P vs P_{int} for location P1 for PC/SI with ignition at ~355 CAD measured for IMEP = 4 bars and tumble 1.5

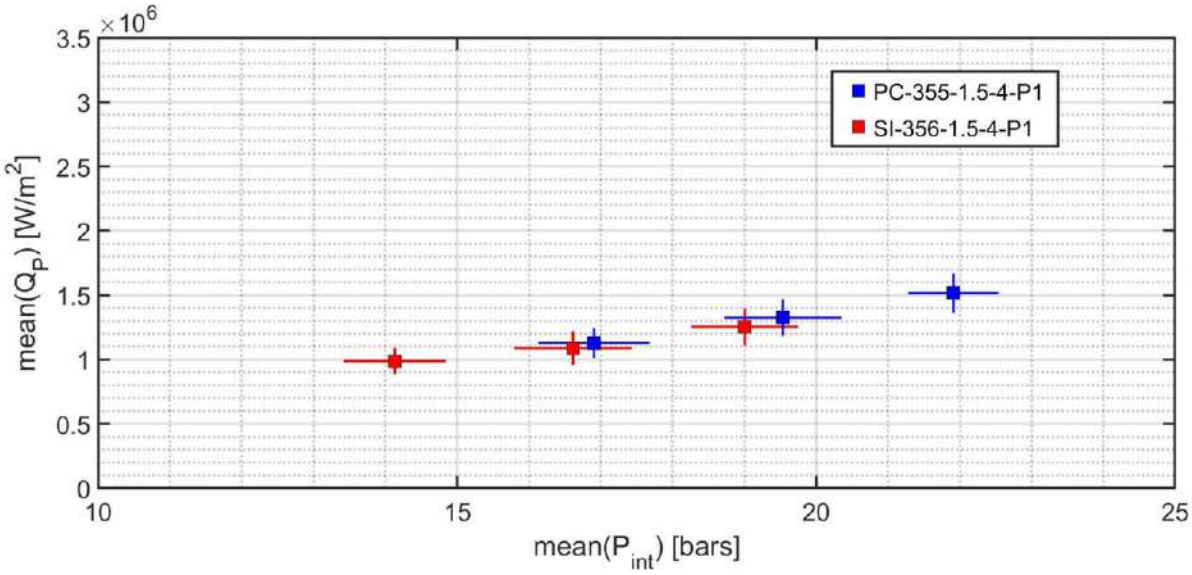

Figure 174: Binned average Q_P vs binned average P_{int} for scatter plot shown in Figure 173

At IMEP = 6 bars, a similar observation is also found. Due to the overlapping scatter for both PC and SI, we hypothesize that FWI in both cases is due to propagative FWI (no effect of flame jets due to PC ignition system). In the case of PC, the flame jet exiting out of the prechamber might lead to a propagative flame that interacts with the wall.

5.5. EFFECT OF LOCATION VARIATION

In the series of measurements carried out in the engine, two different locations were instrumented (cf. Figure 158). The results of location variation (P1 and P2) for conventional SI for IMEP = 4 bars at ignition timing of~346 CAD is shown as Q_P vs P_{int} in Figure 175. The overlapping scatter cloud data in Figure 175 suggest that Q_P is independent of the location of measurement for the SI case. The binned mean Q_P vs mean P_{int} plot is shown in Figure 176. A similar observation is found. This observation is constant for all other variations in the SI case.

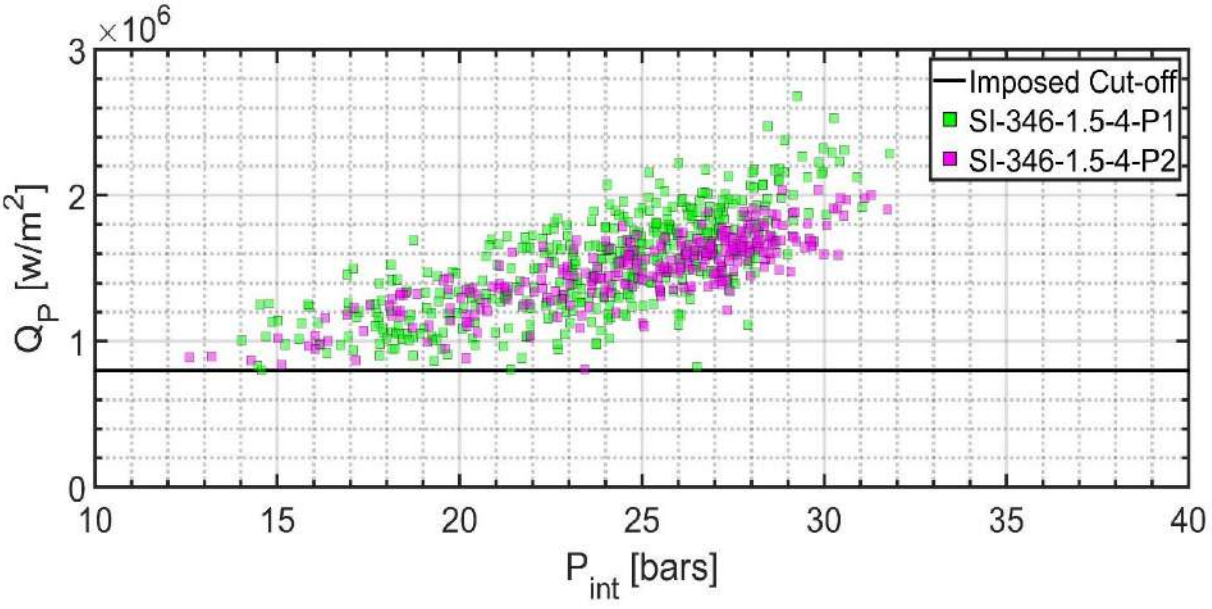

Figure 175: Q_P vs P_{int} for location variation (P1 and P2) for SI with ignition at ~346 CAD measured for IMEP = 4 bars and tumble 1.5

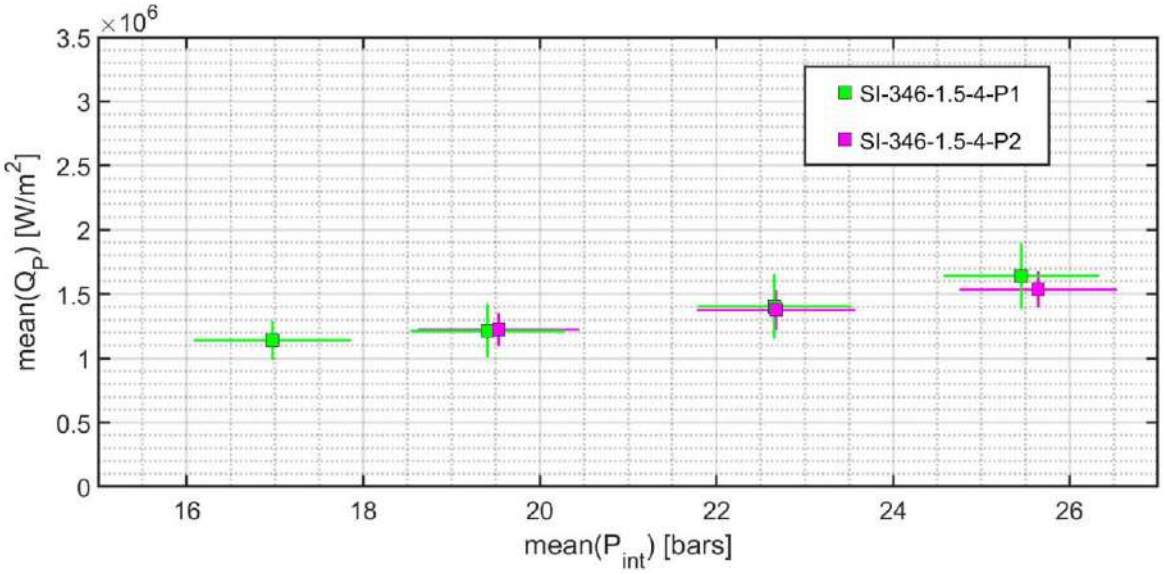

Figure 176: Binned average Q_P vs binned average P_{int} for scatter plot shown in Figure 175

The results of location variation (P1 and P2) for PC ignition for IMEP = 4 bars at ignition timing of ~345 CAD is shown in Figure 177. The binned mean Q_P vs mean P_{int} is shown in Figure 178. For PC, at IMEP = 4 bars, the overlapping scatter cloud also shows that there is no difference in the Q_P measured at two different locations. Similar observation is also found in binned plot. This results in the PC case indicate that there is no preferential effect of the flame jet developed during passive PC ignition, at two different locations during FWI. This is true for other variations, at IMEP = 6 bar.

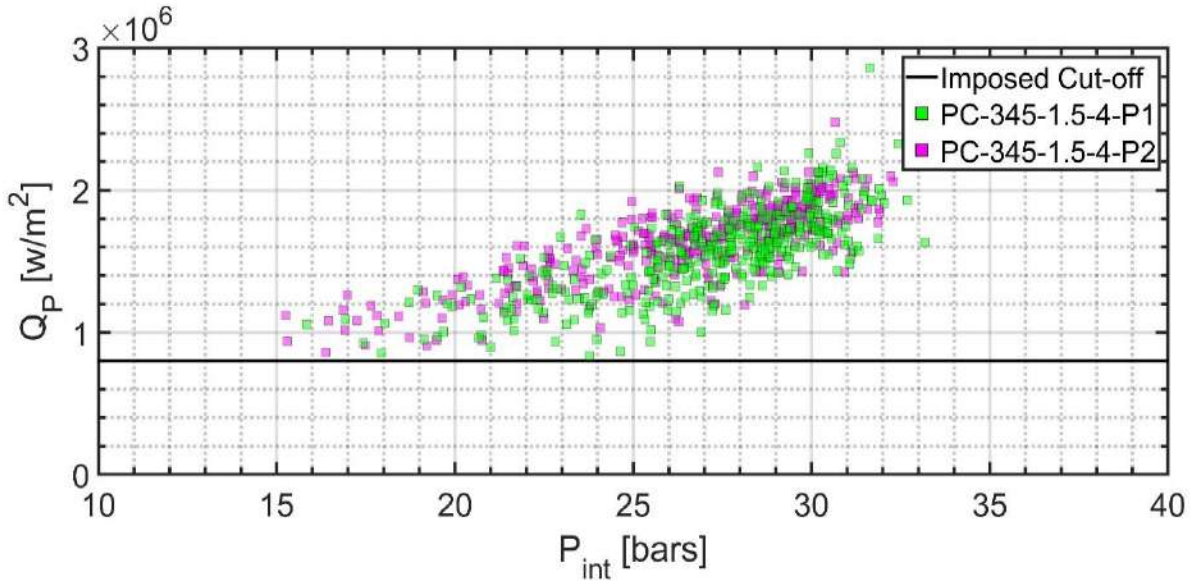

Figure 177: Q_P vs P_{int} for location variation (P1 and P2) for PC with ignition at ~345 CAD measured for IMEP = 4 bars and tumble 1.5

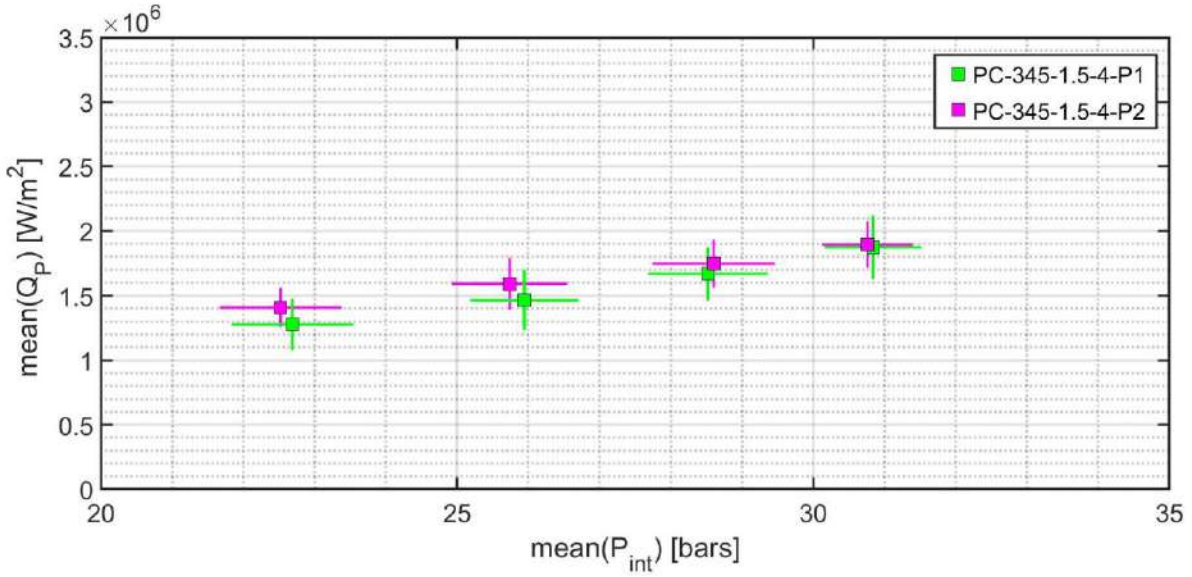

Figure 178: Binned average Q_P vs binned average P_{int} for scatter plot shown in Figure 177

5.6. Effect of Ignition Timing Variation on Q_P

The variation of turbulence intensity in an engine during an engine cycle is well documented in the literature [119]. Variation of ignition timing can provide us with the variation of the time of FWI (in CAD) at the TC. Hence, by varying ignition timing we can qualitatively study the influence of change in turbulence intensity and P_{int} (over larger variation than what is seen at one ignition timing) on Q_P.

Figure 179 shows the effect of ignition timing variation for SI cases i.e., SI-346-1.5-4-P1 and SI-356-1.5-4-P1. Figure 180 shows the binned mean Q_P vs mean P_{int} for the same conditions. In Figure 179 we can see that the data cloud of Q_P vs P_{int} for two different ignition timing follow one power-law. A similar observation is also seen in Figure 180. This is verified by the overlap region, shown in the black box in Figure 179 where we can see at a given average P_{int} (17-20 bars) the average Q_P is equal for both the ignition timings. Changing ignition timing changes the in-cylinder pressure at which ignition takes place i.e.,~1-2 bar difference in pressure during ignition (see Figure 159). Such change in pressure during ignition will affect P_{int} during FWI in the SI case. However, the fact that one power-law is able to fit both ignition timing indicates that there is no other significant change in FWI between the two-ignition timing for SI cases. This implies that the change in turbulence intensity inside the engine over 10 CAD difference in the ignition timing is negligible, during FWI for the SI case. This conclusion can be extended to use variation in ignition timing to study the dependency of Q_P on P_{int} across a large range for SI. Such Q_P vs P_{int} over a large range can be used to study the effect of turbulence intensity and optimize heat loss in engines. The same variation is seen in other all other experiments with ignition timing variation in the SI case.

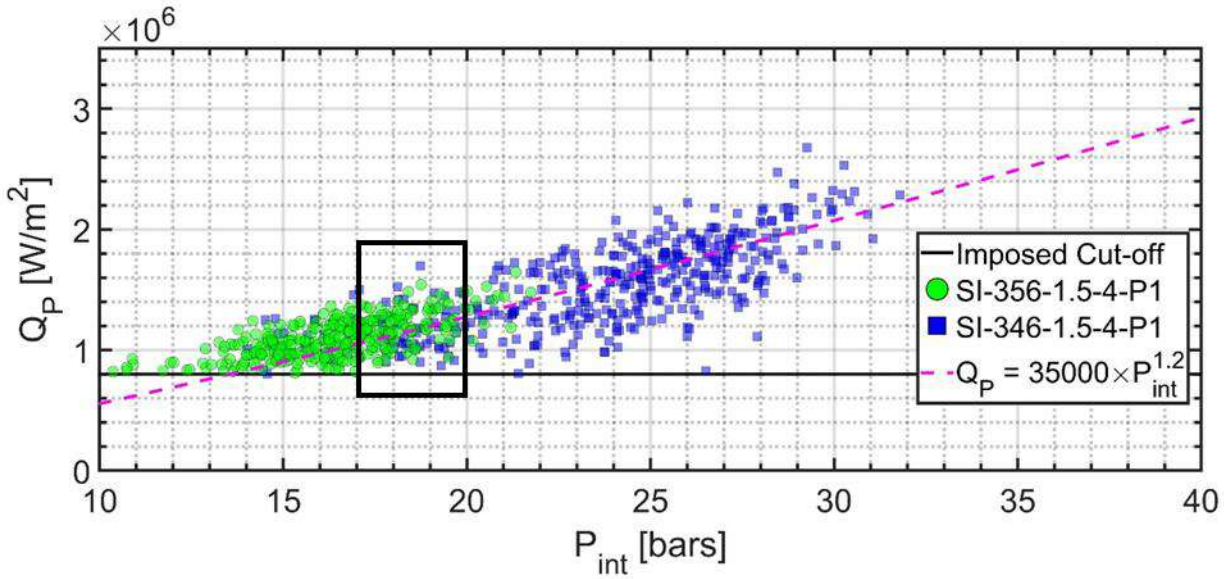

Figure 179: Q_P vs P_{int} for two ignition timing, tumble = 1.5 for SI ignition at P2 for IMEP = 4 bars

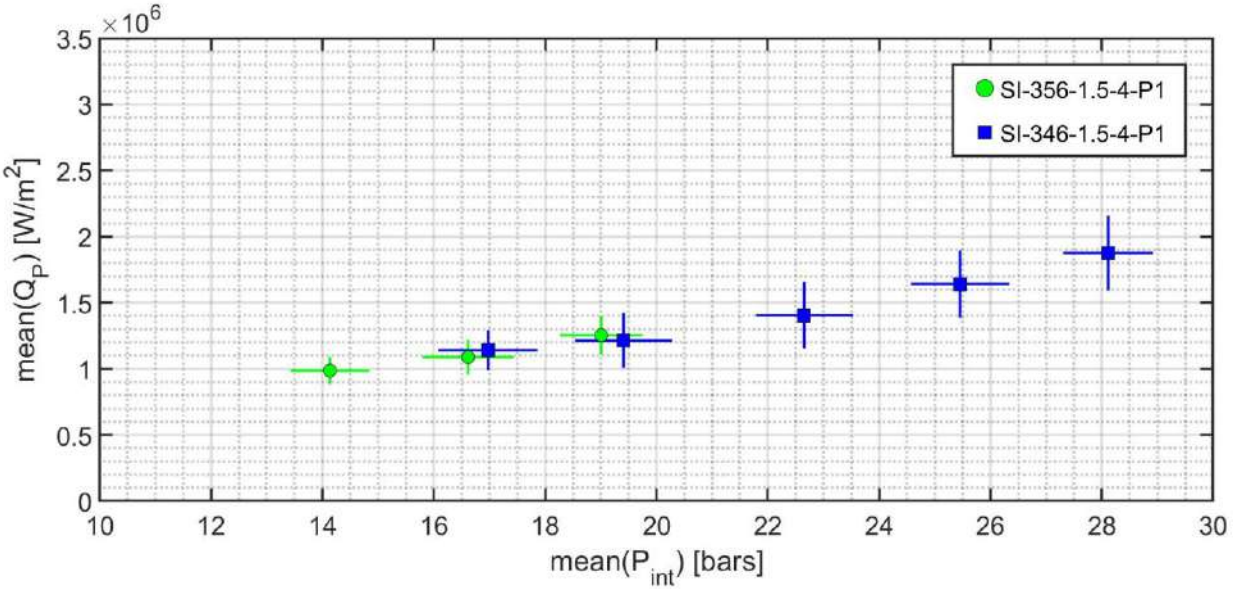

Figure 180: Binned average Q_P vs binned average P_{int} for scatter plot shown in Figure 179

For the PC case shown in Figure 181, we can see that the two scatter clouds of Q_P vs P_{int} for two different ignition timing are well separated, given by two separate power-law. This trend is confirmed by the binned plot of mean Q_P vs mean P_{int} shown in Figure 182. Two separate power-law indicate the dependency of Q_P on another factor other than P_{int}. We already know that the change in turbulence intensity between the two different ignition timings of 10 CAD is negligible. Moreover, from section 5.4, and section 5.5 we know that the flame jet is not affecting the FWI. Hence, we cannot conclude why we observe two separate power-law. This observation is similar to all other ignition timing variations presented in Table 26.

In section 5.4 we have already found that there is no effect of the ignition system on Q_P vs P_{int} distribution. However, in this section with a variation of ignition timing, we find that for SI there is no effect of ignition timing on the distribution of Q_P vs P_{int} whereas for PC we can clearly identify that there is a big difference in the distribution of Q_P vs P_{int}. Both these observations indicate two possible hypotheses. First, the scattering on the SI case is high enough to hide the difference in the distribution of

Q_P vs P_{int} for two ignition timings. The second hypothesis is that with each different ignition timing we obtain one of the predominant FWI (SWQ or HOQ) for the PC case while in the case of SI there is a mix of SWQ and HOQ. In such a scenario, we would obtain a significant difference in PC case for different ignition timing whereas somewhat large scattering in the distribution of Q_P vs P_{int} data. At this point, we cannot ascertain why such a contrasting observation is obtained.

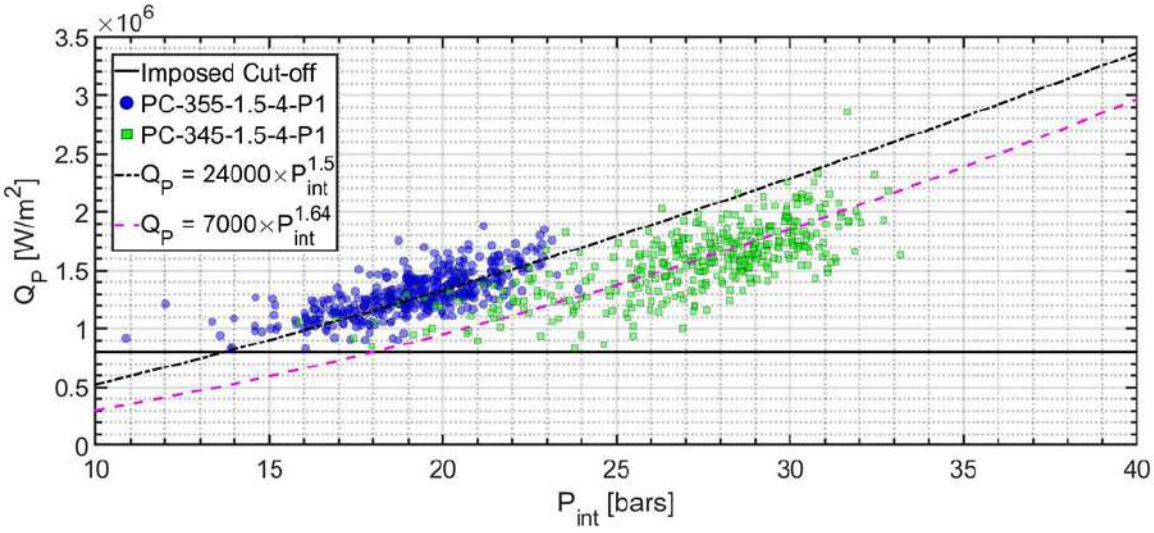

Figure 181: Q_P vs P_{int} for two ignition timing, tumble = 1.5 for PC ignition at P1 for IMEP = 4 bars

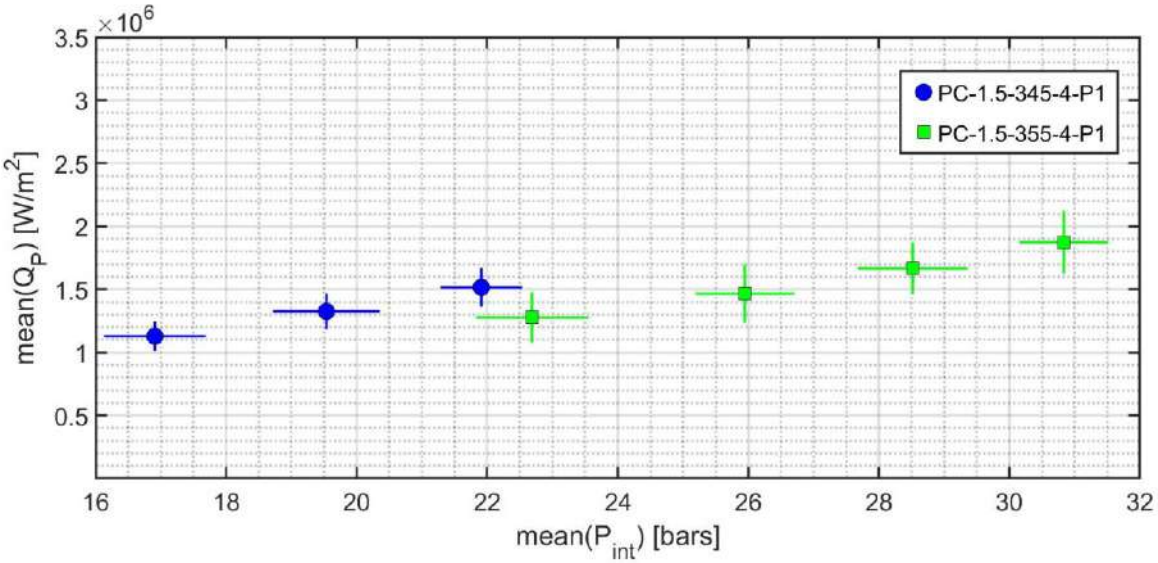

Figure 182: Binned average Q_P vs binned average P_{int} for scatter plot shown in Figure 181

5.7. EFFECT OF IMEP VARIATION

Heat flux is also studied with IMEP variation in engines. IMEP is varied by increasing the intake pressure at an equivalence ratio of 0.9, so that mass (or density) of the intake fuel-air mixture increases at the end of the intake stroke. During this variation, we increase the amount of fuel energy that goes into one cycle of the engine so that we can compare the ratio of Q_P to the total fuel energy going into one cycle among different IMEP variations.

Figure 17 shows Q_P vs P_{int} for SI-356-1.5-4-P2 and SI-355-1.5-6-P2. Figure 184, shows Q_P vs P_{int} for PC-356-1.5-4-P2 and PC-355-1.5-6-P2. In all these figures, we can see that Q_P vs P_{int} can be explained by one power-law fit. Further, we can see that Q_P and P_{int} are higher for IMEP = 6 bars compared to IMEP = 4 bars. Naturally, with larger intake pressure and density (in IMEP = 6 bars case compared to IMEP = 4 bar case) and the same geometrical compression, we expect that the average in-cylinder pressure is higher for cases with IMEP = 6 bar. The higher average pressure trace leads to higher P_{int} and subsequently higher Q_P for IMEP = 6 bar case than for IMEP = 4 bar case.

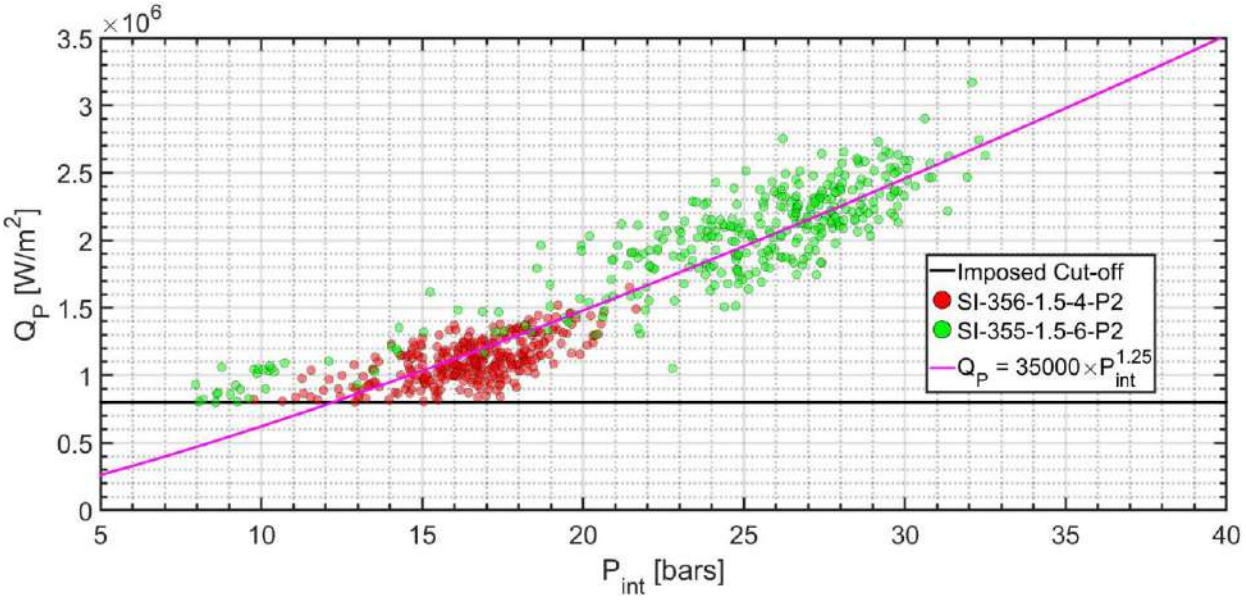

Figure 183: Q_P vs P_{int} for location P2 for SI with ignition at ~355 CAD measured at location P2 with tumble 1.5 for IMEP = 4 and 6 bars

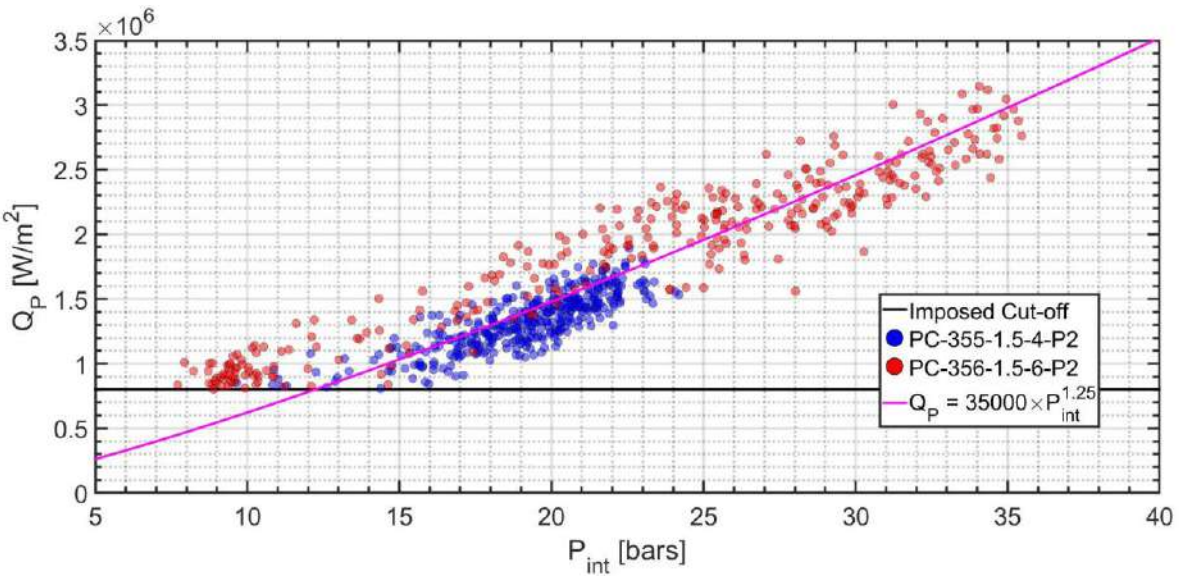

Figure 184: Q_P vs P_{int} for location P2 for PC with ignition at ~355 CAD measured at location P2 with tumble 1.5 for IMEP = 4 and 6 bars

IMEP can be converted to a non-dimensional heat flux equivalent (Q_π) by Equation 38 where $\dot{m}$ is the mass flow rate of the fuel, A is the total surface area of the engine cylinder and LHV is the lower heating value of the fuel i.e., Q_π is the ratio of Q_P to the total fuel energy per unit area of the engine cylinder going into one cycle. For the calculation of A, we have used a simple solid cylinder model. This assumption does not affect the comparison of Q_π as the value of A (0.032 m^2) used is the same for all cases. By definition, Q_π is an equivalent to the $\frac{Q_P}{Q_\Sigma}$ made in chapter 3 where Q_Σ is the flame power during FWI. Figure 185 shows the $Q_\pi$vs P_{int} scatter cloud corresponding to Figure 184.

Equation 38: $$Q_\pi = \frac{Q_P \times A}{\dot{m} \times LHV}$$

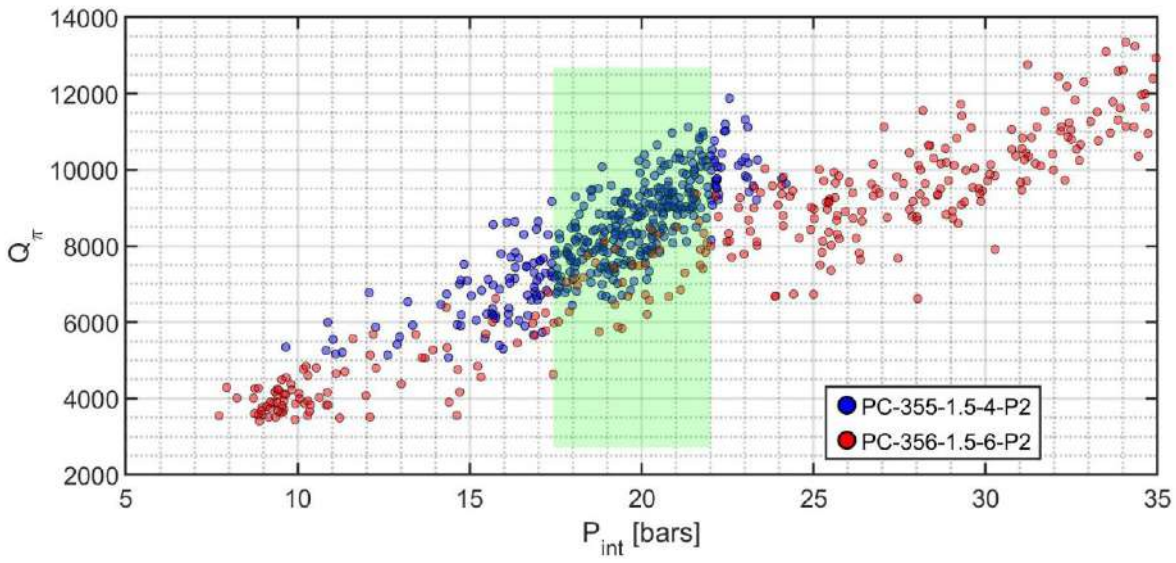

Figure 185: $Q_\pi$vs P_{int} and mean of Q_P vs mean of P_{int} for PC-355-1.5-X-P2

In Figure 185, we can see that the blue scatter (IMEP = 4 bars) is higher in Q_π even at low P_{int} (shaded region in Figure 185) when compared to red scatter (IMEP = 6 bars). This indicates that with an increase in IMEP we get higher absolute Q_P but Q_π falls. As Q_π is an equivalent to the $\frac{Q_P}{Q_\Sigma}$, this result is similar to the result of flame power variation in chapter 3 which indicates that the heat losses as a fraction of total fuel energy fall, as fuel energy in one engine cycle is increased. This result can be improved by conducting experiments with a large amount of data so that we can have multiple cycles at a given P_{int} possibly with lesser scattering, large variation of P_{int}, and exact calculations of the Q_Σ during FWI. As pressure during FWI is higher than the pressure at the end of the intake stroke, we expect a high Q_Σ leading to a larger difference in $\frac{Q_P}{Q_\Sigma}$ vs P_{int} trace than what we observe for $Q_\pi$vs P_{int} trace.

5.8. Conclusion

In this chapter, we have presented the surface temperature measurement carried out in an engine. The corresponding instantaneous heat flux is analyzed for different parametric variations (effect of P_{int}, tumble, location of measurement, type of ignition system and IMEP). Q_P is found to increase with P_{int}

similar to our experiments in CVC, as presented in Chapter 3. A higher tumble (1.5) gives high Q_P compared to a lower tumble (1.1). Further, the higher tumble (1.5) yields low scattering on the Q_P. Hence the parametric comparisons are carried out with a higher tumble (1.5) only. A comparison of Q_P vs P_{int} curves for two different ignition systems leads us to conclude that the tendency of Q_P vs P_{int} measured during FWI with PC and SI systems are similar, at the specific operating points measured in this thesis with IMEP = 4 bars and IMEP = 6 bars. At two locations of temperature measurement (P1 and P2), we record more or less similar Q_P, $P_{int,}$ and tendency of Q_P vs P_{int} for both PC and conventional SI systems at IMEP = 4 bars and 6 bars. The tendency of Q_P vs P_{int} is different for different ignition timings for PC ignition. For SI the tendency of Q_P vs P_{int} remains the same for two different ignition timings. With the increase of IMEP, we find that P_{int} increases which leads to an increase in Q_P.

Conclusions and Perspectives

The objective of this thesis is to identify important parameters and their effect on the heat flux to the combustion engine walls with the target of finding avenues to reduce heat losses and improving the prediction of heat losses in IC engines. Two different modes of combustion, i.e., premixed propagative flame and non-premixed diffusive combustion, commonly employed in IC engines were studied.

The objective of Chapter 1 was to provide the current state of the knowledge of heat losses in engines (in two modes of combustion) and identify the important open questions to understand heat losses. The general working of an engine and the different modes of loss in engines were discussed to identify that heat loss as one of the major losses in the engine. The two different modes of combustion i.e., premixed propagative and non-premixed diffusive or spray combustion were discussed to highlight the different phenomena for each mode of combustion. Heat loss measurements in engines and other combustion chambers carried out in literature were analyzed leading us to choose the method of using fast surface temperature measurements and Duhamel integral to calculate the instantaneous heat flux at the surface. High heat flux is generally found during flame wall interaction (FWI) where heat flux is of the order of MW/m^2. The topic of premixed propagative FWI was analyzed from the knowledge in literature. Researchers find that the premixed propagative FWI is a coupled phenomenon between flame, flow, and the wall. Hence to understand the heat losses during FWI we required complimentary data characterizing the laminar flame, flowfield, turbulence, and temperature field. Lacking similar in-depth details for spray FWI from literature we used the literature on jet-wall interaction and premixed FWI to break down the spray FWI into two phenomena, i.e., non-reactive spray-wall interaction and turbulent spray FWI. Finally, we drew a set of open questions that would aid us to understand the heat flux during FWI. We planned to study premixed FWI and spray FWI in a CVC. For premixed FWI in CVC, these questions led us to find the effect of pressure during interaction ($\boldsymbol{P_{int}}$), turbulence intensity ($\boldsymbol{q}$), dilution of the fuel-air mixture,

flame power (Q_{Σ}), surface temperature measurement location, and fuel type on the heat flux during FWI. For spray FWI we were set to find the effect of ambient temperature (T_{amb}) and surface temperature measurement location on the heat flux. In this set of experiments, we also targeted to separate the contribution of spray dynamics and reaction on the heat flux during spray FWI. Further, we were set to obtain both two-step heat flux and single-step heat flux in the same thermodynamic conditions in order to be able to compare the two types of heat flux. Premixed FWI was also planned to be studied in an engine. In these experiments, we targeted to find the effect of tumble, location of temperature measurement, ignition type, ignition timing, and IMEP on the heat flux during FWI.

The objective of chapter 2 was to present the experiment setup and post-processing of the raw experimental data to analyze the heat flux during FWI. The CVC used to conduct experiments was discussed in detail. This CVC had provisions to control the gas composition, density, and temperature of the walls before the start of the experiment. The engine, which was used to conduct experiments, was discussed along with two types of the ignition system (conventional spark ignition and prechamber ignition). Two types of wall-TC assembly were designed with Medtherm thermocouples (TC), which were used to measure surface temperature. The surface temperature was converted to heat flux using Duhamel integral and Tikhonov regularization. Other complimentary diagnostics were employed to understand FWI. Simultaneous particle image velocimetry (PIV), planar laser-induced fluorescence (PLIF), and chemiluminescence (OH*) visualization were used to determine the flow field in the CVC. Further numerical calculations using Canterra were employed to determine laminar flame properties for our analysis. The first peak of the heat flux trace (Q_P) was the important property of the heat flux trace which was used for comparative analysis. The flowfield obtained from PIV was decomposed using a frequency filter, into an in-cycle mean and turbulent fluctuations (>100 Hz) which were used to characterize turbulence.

Chapter 3 presented the results of experiments of premixed propagative FWI in CVC. The CVC at IFPEN (HPHT) includes provision for multiple fans which were used to induce flowfields with different turbulent intensities (laminar and turbulent). P_{int} was varied by changing the distance between the wall to spark plug. For laminar FWI, Q_P increases with P_{int}, resembling power-law ($Q_P \sim P_{int}^{b}$, b = 0.35). Such a relationship is already reported in the literature. Establishing the power-law dependency of Q_P in the setup used for this thesis was important to understand different parametric variations carried out. Q_P dependency on P_{int} for turbulent combustion shows that Q_P is higher, beyond the dependency of Q_P on P_{int} for laminar regimes. This effect of turbulence increases with P_{int}, following a power-law dependency, with b >1. Further experiments were carried out with a diluted air-fuel mixture with extra CO_2 and N_2 added to the air-fuel mixture, to gain insights into the heat loss. With dilution, we found that Q_P decreases due to a decrease in the flame power during FWI. To understand the effect of Q_Σ on Q_P, experiments were designed to have different Q_Σ while having the same chemical composition of fuel and air. Q_P increases with an increase in Q_Σ. However, the non-dimensional heat flux ($\frac{Q_P}{Q_\Sigma}$) decreases with an increase in Q_Σ. Measuring Q_P at two different locations simultaneously yielded no difference in Q_P, meaning the heat flux is homogenous in space (in line with the literature). Q_P for three different fuels (CH_4, C_2H_2 +H_2, H_2) was measured at a similar order of Q_Σ. It is found that Q_P is lower for H_2 while Q_Σ for H_2 is almost half that of other fuels. We could not ascertain the cause of such discrepancy in both Q_P and Q_Σ, and this topic would need more investigation.

Chapter 4 presented the results of experiments on spray FWI in the CVC at IFPEN. Spray FWI has been studied for both reactive and non-reactive spray in ECN spray A conditions. The wall is placed at a distance of 30 mm from the injector tip, which is larger than the lift-off length (***LoL***) of 15.4 mm. The heat flux trace was analyzed in reactive and non-reactive spray wall interaction. Simultaneous surface temperature measurements at two different locations (P1, stagnation location, and P2, located at 10 mm radial distance from P1) yield that Q_P is different for two different locations of TC for one ambient

temperature. This means that the heat flux during spray FWI is non-homogenous in space, in line with impinging jet studies in the literature. The calculated convective heat transfer coefficient (***h***) yields a high convection coefficient at P1 compared to P2, which is attributed to the thin boundary layer due to high dynamic pressure at P1 compared to P2. For high ambient temperature, both the reactive and non-reactive $\boldsymbol{Q_P}$ is higher, at a given location. However, ***h*** at one location does not change with different ambient temperatures. Non-reactive gas composition is used with spray A boundary condition to separate the contribution of spray momentum and reaction to $\boldsymbol{Q_P}$. Non-reactive conditions also yield high heat flux with $\boldsymbol{Q_P}$~0.2-0.3 times of $\boldsymbol{Q_P}$ obtained for reactive conditions. This indicates a significant contribution of spray momentum to total $\boldsymbol{Q_P}$. It is found that ***h*** for the non-reactive case is equal to the reactive case at one location of TC. The ratio of heat flux for reactive to non-reactive spray is constant during the duration of the plateau in the heat flux trace. In another set of experiments spray FWI was studied using a modified spray A condition where the wall-TC was inserted at a distance less than ***LoL*** of 49 mm. Consequently, natural autoignition was observed after the spray wall interaction. TC at two locations (P1, P2) was used to obtain the heat flux at two locations. Using laser ignition, we could achieve forced ignition before spray wall interaction. Moreover, the non-reactive gas composition was utilized to determine the contribution of spray momentum to the heat flux. These configurations yielded 3 experiment conditions i.e., non-reactive, reactive spray wall interactions where autoignition happens after impingement and vice versa (using laser ignition). Non-reactive $\boldsymbol{Q_P}$ is similar to that of reactive $\boldsymbol{Q_P}$ at P1. While reactive $\boldsymbol{Q_P}$ is higher (by ~2 times) than non-reactive $\boldsymbol{Q_P}$ at P2. By checking the heat flux profiles of individual repetitions, we can obtain at least 3 repetitions with a distinct 2-step heat flux for the experiments where natural autoignition occurs after spray jet arrival at the sensor. The first step is due to non-reactive spray-wall interaction and the second step is due to the reaction of spray.

Chapter 5 presented the results of experiments on premixed propagative FWI in an engine. Propagative FWI was also studied in an engine for two modes of ignition, conventional spark ignition (SI)

and passive pre-chamber (PC) ignition. Heat flux traces for cycles where $Q_P > 0.8$ MW/m^2 were used for our analysis. Q_P is found to increase with P_{int} resembling a power-law in line with findings in Chapter 3 for turbulent FWI. Results of tumble variation indicate that at a given P_{int}, Q_P for lower tumble case is lower than Q_P for higher tumble case. We also observe higher scattering on Q_P vs P_{int} for low tumble cases. Hence, the data at low tumble was not analyzed any further. A comparison of Q_P vs P_{int} curves for two different ignition systems leads us to conclude that the tendency of Q_P vs P_{int} measured during PC and SI systems are similar. At two locations of temperature measurement (P1 and P2), we record similar Q_P, P_{int}, and tendency of Q_P vs P_{int}. We find two different tendencies of the scatter cloud of Q_P vs P_{int} for two different ignition timings in PC ignition. The two different ignition timings, for SI, did not produce any change in the tendency of Q_P vs P_{int}. With the increase of ***IMEP*** from 4 bars to 6 bars while keeping other parameters constant we find that the P_{int} increases which leads to an increase in Q_P.

Now, we will present the perspectives coming out of this thesis. Only a few studies have found the power-law relationship of Q_P vs P_{int}. It will be interesting to track the change in the exponent of the power-law over different experiment setups, initial conditions, and fuel types. In this thesis, we find that turbulent intensity (q) affects the heat loss during FWI in closed chamber combustion. More studies in the future can be planned to obtain both laminar and turbulent FWI in the same setup and a much larger range of P_{int} (than what is obtained in this thesis) to compare their heat flux. Such studies will help solidify the finding. From a fundamental point of view, considering the extremely small scales of FWI, these results increase the curiosity about the mechanism of augmentation of heat flux to the wall. In the future, these mechanisms can be studied for extending this finding. Quantification of the effect of q in engine-like turbulence conditions will help us to find out the magnitude of augmentation of the heat loss due to q. We know that q helps to increase the flame speed which can reduce the combustion duration. Comparing the augmentation of the heat loss with the improvement due to reduction in combustion duration can lead to better engine operation and engine designs. Dilution is found to decrease the flame power (Q_Σ)

which decreases $\boldsymbol{Q_P}$ and vice-versa. While the increase in flame power for one fuel leads to a decrease in $\frac{\boldsymbol{Q_P}}{\boldsymbol{Q_\Sigma}}$ and vice-versa. There is some sense to use the equivalency of $\frac{\boldsymbol{Q_P}}{\boldsymbol{Q_\Sigma}}$ to that of the fraction of heat loss in engines which would indicate that increasing flame power can lead to a decrease in $\frac{\boldsymbol{Q_P}}{\boldsymbol{Q_\Sigma}}$ which could lead to an increase in efficiency. This result needs to be studied carefully to identify if the increase in $\boldsymbol{Q_\Sigma}$ leads to an actual increase in work relative to the losses. These questions can help us in designing new engine operating modes and possibly better fuels for the future.

The heat transfer coefficient during spray FWI is found to be independent of reactive case/non-reactive case and ambient temperature. However convective heat transfer coefficient is dependent on the location of TC relative to the injector i.e., heat transfer coefficient during spray FWI is a function of location. More experiments should be planned to test this result in different boundary conditions to validate this finding in a wider range of conditions. The conclusion also indicates that complex near-wall experimental diagnostics (such as PIV, LIF, etc. which are typically affected by noise from combustion when employed in reacting spray conditions) can be employed in non-reacting spray wall interaction to characterize the heat transfer coefficient which will remain valid for both reacting spray FWI and non-reacting spray wall interaction. Some individual repetitions exhibited two-step heat flux as identified in literature where autoignition occurs after impingement. However, we did not obtain them repeatedly. There is more work to do in the future to find out the conditions to obtain repeatably two-step heat flux and compare it with single-step heat flux.

The method of using $\boldsymbol{Q_P}$ vs $\boldsymbol{P_{int}}$ to analyze the heat flux data from engine experiments can be used to analyze the heat flux data in engines, to compare different parametric variations. The exact quantification of power-law will need a larger range of $\boldsymbol{P_{int}}$. It will be interesting to find the power-law coefficients for different engines and operating points. Using this method, there exists a potential to optimize engine operation by targeting the reduction of heat loss. The distribution of $\boldsymbol{Q_P}$ vs $\boldsymbol{P_{int}}$ measured during PC and SI

systems are overlapping for the specific operating points measured in this thesis. More experiments, in the same setup or different setups and operating points, are required to solidify this finding. The two different ignition timings, for SI at both P1 and P2, did not produce any change in the tendency of $\boldsymbol{Q_P}$ vs $\boldsymbol{P_{int}}$. We find two different tendencies of the scatter cloud of $\boldsymbol{Q_P}$ vs $\boldsymbol{P_{int}}$ for two different ignition timings for PC. More experiments can be designed to understand the cause of different tendencies with ignition timing variation in PC ignition. Further, we had difficulties analyzing the result because of the lack of simultaneous complementary measurements like flow field as well as flame dynamic visualization. Such complementary diagnostics would improve the understanding of premixed FWI in PC and SI systems in an engine.

Annex

ANNEX 1: ENGINEERING DRAWINGS OF FANS USED IN THIS THESIS

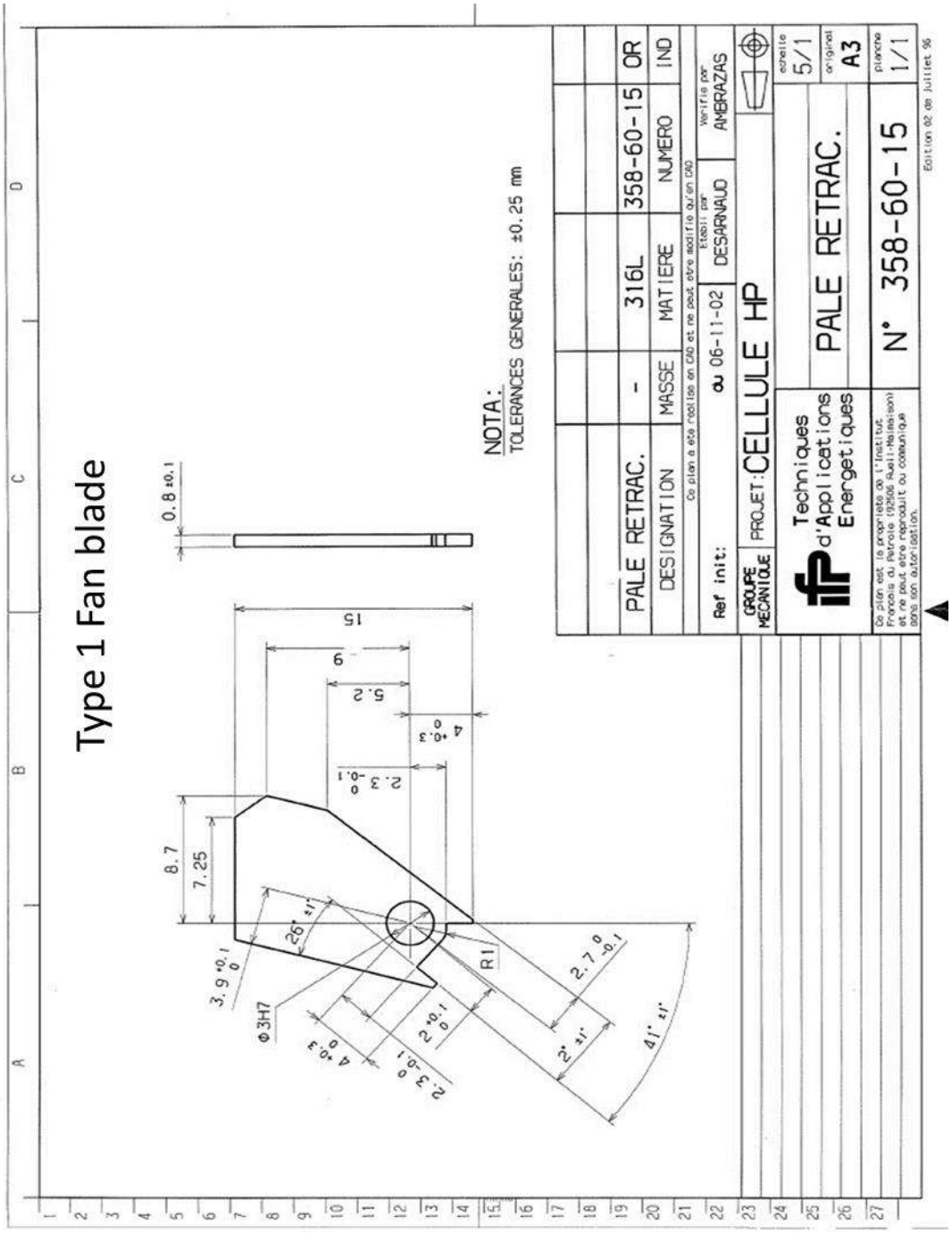

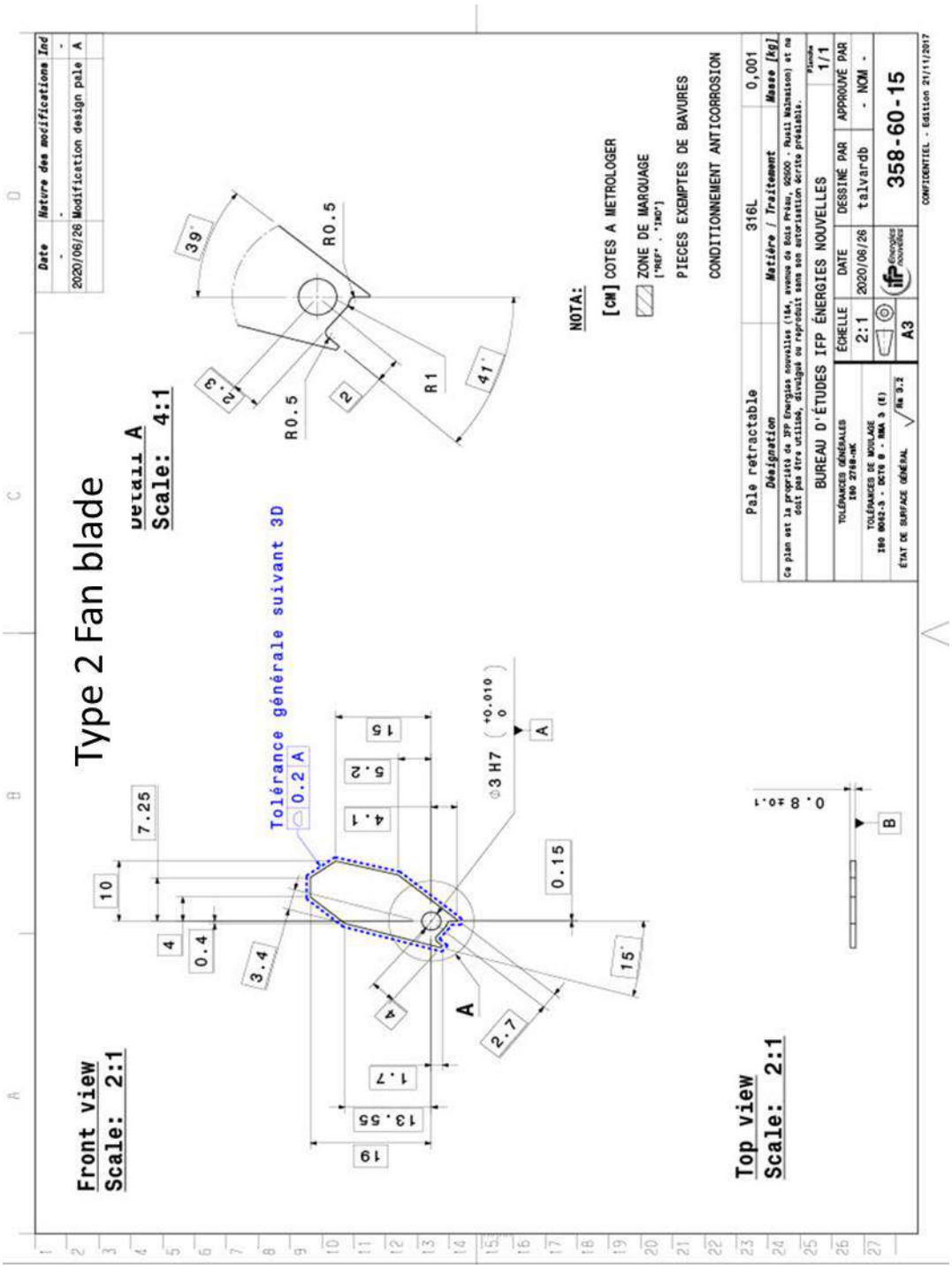
Type 2 Fan blade
Front view
Scale: 2:1
Detail A
Scale: 4:1
Top view
Scale: 2:1
Tolérance générale suivant 3D
0.2 A
NOTA:
[CM] COTES A METROLOGER
ZONE DE MARQUAGE
["REF" . "NO"]
PIECES EXEMPTES DE BAVURES
CONDITIONNEMENT ANTICORROSION
Pale retractable
316L
0,001
Désignation
Matière / Traitement
Masse [kg]
BUREAU D'ÉTUDES IFP ÉNERGIES NOUVELLES
ÉCHELLE
DATE
DESSINÉ PAR
APPROUVÉ PAR
2:1
2020/06/26
talvardb
- NOM -
358-60-15
A3
CONFIDENTIEL - Edition 21/11/2017

ANNEX 2: STEPS OF PIV CALCULATION

1. The whole set of images for one repetition is first arranged into sets of 2.
2. Intensity correction is applied
3. Particles are determined by subtraction of sliding background (50 Pixels) and then particle intensity is normalized over 9 pixels.
4. Multipass PIV + PTV calculation with hybrid cross-correlation starting from window size of 64×64 pixels to window size 16×16 Pixels with symmetric shift with 50% overlap and 3 passes.
5. Vectors are deleted if the correlation value is < 0.4 or vectors lie away from average by 3 times the standard deviation
6. Empty vectors are filled up with interpolation among the neighboring vectors
7. Then a time filter with a second-order polynomial fit over 9 points is applied.

References

[1] K. Senecal and F. Leach, *Racing Toward Zero: The Untold Story of Driving Green*.

[2] *IEA, Data and statistics, CO2 emissions by sector.* [Online]. Available: https://www.iea.org/data-and-statistics/data-browser?country=WORLD&fuel=CO2%20emissions&indicator=CO2BySector

[3] *IEA, Transport sector CO2 emissions by mode in the Sustainable Development Scenario, 2000-2030, IEA, Paris.* [Online]. Available: https://www.iea.org/data-and-statistics/charts/transport-sector-co2-emissions-by-mode-in-the-sustainable-development-scenario-2000-2030

[4] John B: Heywood, *Internal combustion engine fundamentals*. New York: McGraw-Hill, 1988.

[5] A. Trattner, F. Kupelwieser, P. Pertl, F. Winkler, S. Schmidt, and R. Kirchberger, "Thermodynamic Limits of Efficiency Enhancement of Small Displacement Single-Cylinder Engines," in *JSAE/SAE 2015 Small Engine Technologies Conference & Exhibition*, 2015.

[6] N. Lam, M. Tuner, P. Tunestal, A. Andersson, S. Lundgren, and B. Johansson, *Double Compression Expansion Engine Concepts: A Path to High Efficiency*, *(None).* [Online]. Available: https://doi.org/10.4271/2015-01-1260

[7] M. L. Baglione, "Development of system analysis methodologies and tools for modeling and optimizing vehicle system efficiency," University of Michigan, 2007.

[8] J. K. Ausserer, M. D. Polanka, J. A. Baranski, K. D. Grinstead, and P. J. Litke, *Measurement of Loss Pathways in Small, Two-Stroke Internal-Combustion Engines*, *(None).* [Online]. Available: https://doi.org/10.4271/2017-01-9276

[9] B. Johnson and C. Edwards, "Exploring the Pathway to High Efficiency IC Engines through Exergy Analysis of Heat Transfer Reduction," *SAE Int. J. Engines*, vol. 6, no. 1, pp. 150–166, 2013, doi: 10.4271/2013-01-0278.

[10] J. A. Caton, "Exergy destruction during the combustion process as functions of operating and design parameters for a spark-ignition engine," *International Journal of Energy Research*, vol. 36, no. 3, pp. 368–384, 2012, doi: 10.1002/er.1807.

[11] G. Bourhis and P. Leduc, "Energy and Exergy Balances for Modern Diesel and Gasoline Engines," *Oil Gas Sci. Technol. - Rev. IFP*, vol. 65, no. 1, pp. 39–46, 2010, doi: 10.2516/ogst/2009051.

[12] K. Mukai, H. Miyazaki, and S. Yashuara, "Measuring technique of the cooling loss and the influences of the operating variables on heat balance in a gasoline engine," *SAE Technical Paper Series*, 2003.

[13] K. Mukai, T. Iijima, H. Miyazaki, and S. Yasuhara, "The Effects of Design Factors of the Combustion Chamber on Heat Balance in a Gasoline Engine," *SAE Technical Paper*, 2005, doi: 10.4271/2005-01-2021.

[14] I. Taymaz, "An experimental study of energy balance in low heat rejection diesel engine," *Energy*, vol. 31, 2-3, pp. 364–371, 2006, doi: 10.1016/j.energy.2005.02.004.

[15] K. Holmberg, P. Andersson, and A. Erdemir, "Global energy consumption due to friction in passenger cars," *Tribology International*, vol. 47, pp. 221–234, 2012, doi: 10.1016/j.triboint.2011.11.022.

[16] B. Peterson, E. Baum, A. Dreizler, and B. Böhm, "An experimental study of the detailed flame transport in a SI engine using simultaneous dual-plane OH-LIF and stereoscopic PIV," *Combustion and Flame*, vol. 202, pp. 16–32, 2019, doi: 10.1016/j.combustflame.2018.12.024.

[17] T. Poinsot and D. Veynante, *Theoretical and Numerical Combustion*: Edwards, 2005. [Online]. Available: https://books.google.fr/books?id=cqFDkeVABYoC

[18] O. Laget, S. Chevillard, G. Pilla, X. Gautrot, and T. Colliou, "Investigations on Pre-chamber Ignition Device Using Experimental and Numerical Approaches," in *2019 JSAE/SAE Powertrains, Fuels and Lubricants*, 2019.

[19] J. E. Dec, “A Conceptual Model of DI Diesel Combustion Based on Laser-Sheet Imaging,” in *SAE International Congress & Exposition*, 1997.

[20] G. Bruneaux, “Combustion structure of free and wall-impinging diesel jets by simultaneous laser-induced fluorescence of formaldehyde, poly-aromatic hydrocarbons, and hydroxides,” *International Journal of Engine Research*, vol. 9, no. 3, pp. 249–265, 2008, doi: 10.1243/14680874JER00108.

[21] G. Bruneaux, “Mixing Process in High Pressure Diesel Jets by Normalized Laser Induced Exciplex Fluorescence Part I: Free Jet,” in *2005 SAE Brasil Fuels & Lubricants Meeting*, 2005. [Online]. Available: https://doi.org/10.4271/2005-01-2100

[22] G. Bruneaux, “Mixing Process in High Pressure Diesel Jets by Normalized Laser Induced Exciplex Fluorescence Part II: Wall Impinging Versus Free Jet,” in *2005 SAE Brasil Fuels & Lubricants Meeting*, 2005. [Online]. Available: https://doi.org/10.4271/2005-01-2097

[23] *Engine Combustion Network (ECN).* [Online]. Available: https://ecn.sandia.gov/

[24] G. Borman and K. Nishiwaki, “Internal-combustion engine heat transfer,” *Progress in Energy and Combustion Science*, vol. 13, no. 1, pp. 1–46, 1987, doi: 10.1016/0360-1285(87)90005-0.

[25] Eric Gingrich, Michael Tess, Vamshi Korivi, and Jaal Ghandhi, “High-output diesel engine heat transfer: Part 1 - comparison between piston heat flux and global energy balance,” *International Journal of Engine Research*, vol. 0, no. 0, 14680874211017032, 0, doi: 10.1177/14680874211017032.

[26] T. LeFeuvre, P. S. Myers, and O. A. Uyehara, “Experimental Instantaneous Heat Fluxes in a Diesel Engine and Their Correlation,” in *Mid-Year Meeting*, 1969. [Online]. Available: https://doi.org/10.4271/690464

[27] D. J. O. Nijeweme, J. B. W. Kok, C. R. Stone, and L. Wyszynski, “Unsteady in-cylinder heat transfer in a spark ignition engine: Experiments and modelling,” *Proceedings of the Institution of Mechanical Engineers, Part D: Journal of Automobile Engineering*, vol. 215, no. 6, pp. 747–760, 2001, doi: 10.1243/0954407011528329.

[28] J.-L. Saulnier, A. Dupont, and J.-P. Rivere, “Effects of Aerodynamics on Fuel Consumption of a Multivalve S-I Engine. Investigation of the Instantaneous Local Heat Transfer at Part Loads and Distinct Equivalence Ratios,” in *International Fuels & Lubricants Meeting & Exposition*, 1997.

[29] D. Lejsek and A. Kulzer, “Investigations on the Transient Wall Heat Transfer at Start-Up for SI Engines with Gasoline Direct Injection,” *SAE Int. J. Engines*, vol. 2, no. 1, pp. 381–397, 2009, doi: 10.4271/2009-01-0613.

[30] J. Demuynck, N. Raes, M. Zuliani, M. de Paepe, R. Sierens, and S. Verhelst, “Local heat flux measurements in a hydrogen and methane spark ignition engine with a thermopile sensor,” *International Journal of Hydrogen Energy*, vol. 34, no. 24, pp. 9857–9868, 2009, doi: 10.1016/j.ijhydene.2009.10.035.

[31] J. Demuynck, M. de Paepe, H. Huisseune, R. Sierens, J. Vancoillie, and S. Verhelst, “On the applicability of empirical heat transfer models for hydrogen combustion engines,” *International Journal of Hydrogen Energy*, vol. 36, no. 1, pp. 975–984, 2011, doi: 10.1016/j.ijhydene.2010.10.059.

[32] J. Chang *et al.,* “New Heat Transfer Correlation for an HCCI Engine Derived from Measurements of Instantaneous Surface Heat Flux,” *SAE Technical Paper Series*, 2004.

[33] G. Woschni, “A universally applicable equation for the instantaneous heat transfer coefficient in the internal combustion engine,” *SAE Technical Paper Series*, no. 670931, 1967.

[34] T. L. Bergman, F. P. Incropera, A. S. Lavine, and D. P. Dewitt, *Introduction to heat transfer,* 6th ed.: Wiley, 2011.

[35] Y. Enomoto, Y. Aoki, M. Emi, and S. Kimura, “Heat transfer coefficient on the combustion chamber wall surfaces in a naturally aspirated direct-injection diesel engine,” *International Journal of Engine Research*, vol. 15, no. 5, pp. 606–625, 2014, doi: 10.1177/1468087413500060.

[36] T. Hendricks and J. Ghandhi, “Estimation of Surface Heat Flux in IC Engines Using Temperature Measurements: Processing Code Effects,” *SAE Int. J. Engines*, vol. 5, no. 3, pp. 1268–1285, 2012, doi: 10.4271/2012-01-1208.

[37] T. L. Hendricks, *Instantaneous heat flux measurements in internal combustion engines*: 2011, 2011.

[38] C. J. Weingartz, C. L. Anderson, and S. A. Miers, “Determination of Heat Transfer Augmentation Due to Fuel Spray Impingement in a High-Speed Diesel Engine,” in *SAE World Congress & Exhibition*, 2009.

[39] E. Gingrich, J. B. Ghandhi, and R. D. Reitz, “Experimental Investigation of Piston Heat Transfer in a Light Duty Engine Under Conventional Diesel, Homogeneous Charge Compression Ignition, and Reactivity Controlled Compression Ignition Combustion Regimes,” *SAE Int. J. Engines*, vol. 7, no. 1, pp. 375–386, 2014, doi: 10.4271/2014-01-1182.

[40] B. Boust, J. Sotton, S. A. Labuda, and M. Bellenoue, “A thermal formulation for single-wall quenching of transient laminar flames,” *Combustion and Flame*, vol. 149, no. 3, pp. 286–294, 2007, doi: 10.1016/j.combustflame.2006.12.019.

[41] B. Boust, J. Sotton, and M. Bellenoue, “Unsteady heat transfer during the turbulent combustion of a lean premixed methane–air flame: Effect of pressure and gas dynamics,” *Proceedings of the Combustion Institute*, vol. 31, no. 1, pp. 1411–1418, 2007, doi: 10.1016/j.proci.2006.07.176.

[42] B. Boust, “Etude expérimentale et modélisation des pertes thermiques pariétales lors de l’interaction flamme-paroi instantannaire,” 2006. [Online]. Available: http://www.theses.fr/2006POIT2308

[43] S. Labuda, M. Karrer, J. Sotton, and M. Bellenoue, “Experimental Study of Single-Wall Flame Quenching at High Pressures,” *Combustion Science and Technology*, vol. 183, no. 5, pp. 409–426, 2011, doi: 10.1080/00102202.2010.528815.

[44] M. Karrer, “Diagnostic des plasmas de combustion par sonde d’ionisation: Application à l’étude de l’interaction flamme-paroi instationnaire,” Université de Poitiers, 2009.

[45] S.-W. Li, T. Kamimoto, S. Kobori, and Y. Enomoto, “Heat Transfer From Impinging Diesel Flames to the Combustion Chamber Wall,” in *International Congress & Exposition*, 1997. [Online]. Available: https://doi.org/10.4271/970896

[46] J. Moussou, “Caractérisation expérimentale du flux thermique transitoire pariétal pour différents modes de combustion,” 2019. [Online]. Available: http://www.theses.fr/2019ESMA0010

[47] L. M. Pickett *et al., Comparison of Diesel Spray Combustion in Different High-Temperature, High-Pressure Facilities.* [Online]. Available: https://doi.org/10.4271/2010-01-2106

[48] M. Leidenfrost and E. Werner, “Measuring Temperature at a Cylinder Head under Thermal Load,” *MTZ Worldw*, vol. 73, no. 7, pp. 70–74, 2012, doi: 10.1007/s38313-012-0205-7.

[49] D. N. Assanis and E. Badillo, “Evaluation of Alternative Thermocouple Designs for Transient Heat Transfer Measurements in Metal and Ceramic Engines,” in 1989.

[50] J. A. Gatowski, M. K. Smith, and A. C. Alkidas, “An experimental investigation of surface thermometry and heat flux,” *Experimental Thermal and Fluid Science*, vol. 2, no. 3, pp. 280–292, 1989, doi: 10.1016/0894-1777(89)90017-4.

[51] J. Sotton, “Interactions entre une combustion turbulente et la paroi dans une enceinte fermée,” Université de Poitiers, 2003.

[52] W. J. Cook, “Determination of heat-transfer rates from transient surface temperature measurements,” *AIAA Journal*, vol. 8, no. 7, pp. 1366–1368, 1970, doi: 10.2514/3.5909.

[53] S. Julien, B. Boust, S. A. Labuda, and M. Bellenoue, “Head-on quenching of transient laminar flame: Heat flux and quenching distance measurements,” *Combustion Science and Technology*, vol. 177, pp. 1305–1322, 2005, doi: 10.1080/00102200590950485.

[54] A. Dreizler and B. Böhm, “Advanced laser diagnostics for an improved understanding of premixed flame-wall interactions,” *Proceedings of the Combustion Institute*, vol. 35, no. 1, pp. 37–64, 2015, doi: 10.1016/j.proci.2014.08.014.

[55] D. Suckart, D. Linse, E. Schutting, and H. Eichlseder, “Experimental and simulative investigation of flame–wall interactions and quenching in spark-ignition engines,” *Automotive and Engine Technology*, vol. 2, no. 1, pp. 25–38, 2017, doi: 10.1007/s41104-016-0015-z.

[56] F. Foucher, “Etude expérimentale de l’interaction flamme-paroi: Application au moteur à allumage commandé,” 2002. [Online]. Available: http://www.theses.fr/2002ORLE2057

[57] H. Kosaka *et al.,* “Wall heat fluxes and CO formation/oxidation during laminar and turbulent side-wall quenching of methane and DME flames,” *International Journal of Heat and Fluid Flow*, vol. 70, pp. 181–192, 2018, doi: 10.1016/j.ijheatfluidflow.2018.01.009.

[58] P. -H. Renard, D. Thévenin, J. C. Rolon, and S. Candel, “Dynamics of flame/vortex interactions,” *Progress in Energy and Combustion Science*, vol. 26, no. 3, pp. 225–282, 2000, doi: 10.1016/S0360-1285(00)00002-2.

[59] A. Bianco, F. Millo, and A. Piano, “Modelling of combustion and knock onset risk in a high-performance turbulent jet ignition engine,” *Transportation Engineering*, vol. 2, p. 100037, 2020, doi: 10.1016/j.treng.2020.100037.

[60] R. Hartmann, “Experimental Study of the Ignition, Flammability and Flame Propagation of Jet Fuels under Laminar and Turbulent Conditions,” 2016.

[61] A. N. Lipatnikov and J. Chomiak, “Effects of premixed flames on turbulence and turbulent scalar transport,” *Progress in Energy and Combustion Science*, vol. 36, no. 1, pp. 1–102, 2010, doi: 10.1016/j.pecs.2009.07.001.

[62] A. J. Smits, B. J. McKeon, and I. Marusic, “High–Reynolds Number Wall Turbulence,” *Annual Review of Fluid Mechanics*, vol. 43, no. 1, pp. 353–375, 2011, doi: 10.1146/annurev-fluid-122109-160753.

[63] D. O. Hubble, P. P. Vlachos, and T. E. Diller, “The role of large-scale vortical structures in transient convective heat transfer augmentation,” *J. Fluid Mech.*, vol. 718, pp. 89–115, 2013, doi: 10.1017/jfm.2012.589.

[64] A. R. Gifford, T. E. Diller, and P. P. Vlachos, “The Physical Mechanism of Heat Transfer Augmentation in Stagnating Flows Subject to Freestream Turbulence,” *J. Heat Transfer*, vol. 133, no. 2, p. 21901, 2011, doi: 10.1115/1.4002595.

[65] G. Arévalo, R. H. Hernández, C. Nicot, and F. Plaza, “Vortex ring head-on collision with a heated vertical plate,” *Physics of Fluids*, vol. 19, no. 8, p. 83603, 2007, doi: 10.1063/1.2759880.

[66] C. Jainski, L. Lu, V. Sick, and A. Dreizler, “Laser imaging investigation of transient heat transfer processes in turbulent nitrogen jets impinging on a heated wall,” *International Journal of Heat and Mass Transfer*, vol. 74, pp. 101–112, 2014, doi: 10.1016/j.ijheatmasstransfer.2014.02.072.

[67] M. J. Hall and F. V. Bracco, “Cycle-Resolved Velocity and Turbulence Measurements Near the Cylinder Wall of a Firing S.I. Engine,” in *1986 SAE International Fall Fuels and Lubricants Meeting and Exhibition*, 1986. [Online]. Available: https://doi.org/10.4271/861530

[68] C. -P. Ding, B. Peterson, M. Schmidt, A. Dreizler, and B. Böhm, “Flame/flow dynamics at the piston surface of an IC engine measured by high-speed PLIF and PTV,” *Proceedings of the Combustion Institute*, vol. 37, no. 4, pp. 4973–4981, 2019, doi: 10.1016/j.proci.2018.06.215.

[69] C. Jainski, L. Lu, A. Dreizler, and V. Sick, “High-speed micro particle image velocimetry studies of boundary-layer flows in a direct-injection engine,” *International Journal of Engine Research*, vol. 14, no. 3, pp. 247–259, 2013, doi: 10.1177/1468087412455746.

[70] P. H. Pierce, J. B. Ghandhi, and J. K. Martin, “Near-Wall Velocity Characteristics in Valved and Ported Motored Engines,” in *International Congress & Exposition*, 1992. [Online]. Available: https://doi.org/10.4271/920152

[71] A. GRUBER, R. SANKARAN, E. R. HAWKES, and J. H. CHEN, “Turbulent flame–wall interaction: A direct numerical simulation study,” *J. Fluid Mech.*, vol. 658, pp. 5–32, 2010, doi: 10.1017/S0022112010001278.

[72] G. Bruneaux, K. Akselvoll, T. Poinsot, and J. H. Ferziger, “Flame-wall interaction simulation in a turbulent channel flow,” *Combustion and Flame*, vol. 107, no. 1, pp. 27–44, 1996, doi: 10.1016/0010-2180(95)00263-4.

[73] T. Zirwes *et al.,* “Numerical Study of Quenching Distances for Side-Wall Quenching Using Detailed Diffusion and Chemistry,” *Flow Turbulence Combust*, vol. 106, no. 2, pp. 649–679, 2021, doi: 10.1007/s10494-020-00215-0.

[74] J. M. García-Oliver, L.-M. Malbec, H. B. Toda, and G. Bruneaux, “A study on the interaction between local flow and flame structure for mixing-controlled Diesel sprays,” *Combustion and Flame*, vol. 179, pp. 157–171, 2017, doi: 10.1016/j.combustflame.2017.01.023.

[75] R. Payri, J. P. Viera, H. Wang, and L.-M. Malbec, “Velocity field analysis of the high density, high pressure diesel spray,” *International Journal of Multiphase Flow*, vol. 80, pp. 69–78, 2016, doi: 10.1016/j.ijmultiphaseflow.2015.10.012.

[76] D. Bradley, M. Lawes, and M. Morsy, “Measurement of Turbulence Characteristics in a Large Scale Fan-Stirred Spherical Vessel,” *Journal of Turbulence*, vol. 20, 2019.

[77] B. Galmiche, N. Mazellier, F. Halter, and F. Foucher, “Turbulence characterization of a high-pressure high-temperature fan-stirred combustion vessel using LDV, PIV and TR-PIV measurements,” *Experiments in Fluids*, vol. 55, no. 1, p. 1636, 2013, doi: 10.1007/s00348-013-1636-x.

[78] L.-M. Malbec, J. Egúsquiza, G. Bruneaux, and M. Meijer, *Characterization of a Set of ECN Spray A Injectors: Nozzle to Nozzle Variations and Effect on Spray Characteristics.* [Online]. Available: https://doi.org/10.4271/2013-24-0037

[79] F. Tagliante-Saracino, “Combined study by Direct Numerical Simulation and optical diagnostics of the flame stabilization in a diesel spray,” 2019. [Online]. Available: http://www.theses.fr/2019SACLC017

[80] G. Bourhis, Chargé de R&I R104, “Formulaire de calculs banc moteur, Internal Records: R100-QI950-rev4,” IFP Energy Nouvelles, Rueil Malmasion, Sep. 2015.

[81] Michele Bardi, Guillaume Pilla, and Xavier Gautrot, “Experimental assessment of the sources of regulated and unregulated nanoparticles in gasoline direct-injection engines,” *International Journal of Engine Research*, vol. 20, no. 1, pp. 128–140, 2019, doi: 10.1177/1468087418817448.

[82] J. Taler and P. Duda, *Solving Direct and Inverse Heat Conduction Problems*, 2006.

[83] W. J. J. Cook and E. J. Felderman, “Reduction of data from thin-film heat-transfer gages - A concise numerical technique,” in 1966.

[84] A. Y. Alharbi and V. Sick, “Investigation of boundary layers in internal combustion engines using a hybrid algorithm of high speed micro-PIV and PTV,” *Experiments in Fluids*, vol. 49, no. 4, pp. 949–959, 2010, doi: 10.1007/s00348-010-0870-8.

[85] J. Westerweel, “On velocity gradients in PIV interrogation,” *Experiments in Fluids*, vol. 44, no. 5, pp. 831–842, 2008, doi: 10.1007/s00348-007-0439-3.

[86] Frederic Moisy, *PIVMat*: MATLAB Central File Exchange, 2021. Accessed: Aug. 6 2021. [Online]. Available: https://www.mathworks.com/matlabcentral/fileexchange/10902-pivmat-4-20

[87] B. Peterson, E. Baum, B. Böhm, and A. Dreizler, “Early flame propagation in a spark-ignition engine measured with quasi 4D-diagnostics,” *Proceedings of the Combustion Institute*, vol. 35, no. 3, pp. 3829–3837, 2015, doi: 10.1016/j.proci.2014.05.131.

[88] R. Hanson, R. Spearrin, and C. Goldenstein, *Spectroscopy and Optical Diagnostics for Gases*, 2016.

[89] F. Foucher, S. Burnel, and C. Mounaïm-Rousselle, “Evaluation of burning rates in the vicinity of the piston in a spark-ignition engine,” *Proceedings of the Combustion Institute*, vol. 29, no. 1, pp. 751–757, 2002, doi: 10.1016/S1540-7489(02)80096-7.

[90] C. Schulz and V. Sick, “Tracer-LIF diagnostics: Quantitative measurement of fuel concentration, temperature and fuel/air ratio in practical combustion systems,” *Progress in Energy and Combustion Science*, vol. 31, no. 1, pp. 75–121, 2005, doi: 10.1016/j.pecs.2004.08.002.

[91] B. Higgins and D. L. Siebers, “Measurement of the Flame Lift-Off Location on DI Diesel Sprays Using OH Chemiluminescence,” *SAE Technical Paper Series*, 2001-01-0918, 2001, doi: 10.4271/2001-01-0918.

[92] L. M. Pickett and D. L. Siebers, “Soot Formation in Diesel Fuel Jets Near the Lift-Off Length,” *International Journal of Engine Research*, vol. 7, no. 2, pp. 103–130, 2006, doi: 10.1243/146808705X57793.

[93] L. M. Pickett, D. L. Siebers, and C. A. Idicheria, “Relationship Between Ignition Processes and the Lift-Off Length of Diesel Fuel Jets,” *SAE Technical Paper Series*, 2005, doi: 10.4271/2005-01-3843.

[94] D. L. Siebers, B. Higgins, and L. M. Pickett, “Flame Lift-Off on Direct-Injection Diesel Fuel Jets: Oxygen Concentration Effects,” *SAE Technical Paper Series*, 2002.

[95] G.P. Smith, Y. Tao, and H. Wang, *Foundational Fuel Chemistry Model Version 1.0 (FFCM-1)*, 2016. Accessed: 06/082021. [Online]. Available: http://nanoenergy.stanford.edu/ffcm1

[96] Denis Lapalme, Romain Lemaire, and Patrice Seers, “Assessment of the method for calculating the Lewis number of H2/CO/CH4 mixtures and comparison with experimental results,” *International Journal of Hydrogen Energy*, vol. 42, no. 12, pp. 8314–8328, 2017, doi: 10.1016/j.ijhydene.2017.01.099.

[97] E. Gingrich, D. Janecek, and J. Ghandhi, “Experimental Investigation of the Impact of In-Cylinder Pressure Oscillations on Piston Heat Transfer,” *SAE Int. J. Engines*, vol. 9, no. 3, pp. 1958–1969, 2016, doi: 10.4271/2016-01-9044.

[98] R D Keane and R J Adrian, “Optimization of particle image velocimeters. I. Double pulsed systems,” *Meas. Sci. Technol.*, vol. 1, no. 11, pp. 1202–1215, 1990, doi: 10.1088/0957-0233/1/11/013.

[99] M. Greene, “Momentum Near-wall Region Characterization in a Reciprocating Internal-combustion Engine,” Ph.D.Thesis, Rackcham School of Graduate Studies, University of Michigan, 2017. Accessed: Jan. 9 2021.

[100] K. T. Christensen, “The influence of peak-locking errors on turbulence statistics computed from PIV ensembles,” *Experiments in Fluids*, vol. 36, no. 3, pp. 484–497, 2004, doi: 10.1007/s00348-003-0754-2.

[101] E.F.J. Overmars, N.G.W. Warncke,C. Poelma, J. Westerweel, *Bias errors in PIV: the pixel locking effect revisited.* Lisbon, Portugal, 2010.

[102] E. Baum, B. Peterson, B. Böhm, and A. Dreizler, “On The Validation of LES Applied to Internal Combustion Engine Flows: Part 1: Comprehensive Experimental Database,” *Flow Turbulence Combust*, vol. 92, no. 1, pp. 269–297, 2014, doi: 10.1007/s10494-013-9468-6.

[103] P. G. Aleiferis, M. K. Behringer, and J. S. Malcolm, “Integral Length Scales and Time Scales of Turbulence in an Optical Spark-Ignition Engine,” *Flow Turbulence Combust*, vol. 98, no. 2, pp. 523–577, 2017, doi: 10.1007/s10494-016-9775-9.

[104] A Sciacchitano, “Uncertainty quantification in particle image velocimetry,” *Meas. Sci. Technol.*, vol. 30, no. 9, p. 92001, 2019.

[105] Pijush K. Kundu, Ira M. Cohen, and David R. Dowling, Eds., *Fluid Mechanics (Sixth Edition)*. Boston: Academic Press, 2016.

[106] Ossama A. Mannaa, Morkous S. Mansour, Suk Ho Chung, and William L. Roberts, “Characterization of Turbulence in an Optically Accessible Fan-Stirred Spherical Combustion Chamber,” *Combustion Science and Technology*, vol. 193, no. 7, pp. 1231–1257, 2021, doi: 10.1080/00102202.2019.1686629.

[107] H.-Y. Kim, “Statistical notes for clinical researchers: assessing normal distribution (2) using skewness and kurtosis,” *Restorative dentistry & endodontics*, vol. 38, no. 1, pp. 52–54, 2013, doi: 10.5395/rde.2013.38.1.52.

[108] D. Bradley, M. Lawes, and M. Morsy, “Combustion-induced turbulent flow fields in premixed flames,” *Fuel*, vol. 290, p. 119972, 2021, doi: 10.1016/j.fuel.2020.119972.

[109] Wankang Zhang, “Measurements of flow and combustion in a strongly charged spark ignition engine,” University of Leeds, 2018. [Online]. Available: https://etheses.whiterose.ac.uk/24176/

[110] J. X. Zhou, B. Moreau, C. Mounaïm-Rousselle, and F. Foucher, “Combustion, Performance and Emission Analysis of an Oxygen-Controlling Downsized SI Engine,” *Oil Gas Sci. Technol. - Rev. IFP Energies nouvelles*, vol. 71, no. 4, p. 49, 2016, doi: 10.2516/ogst/2015035.

[111] C. Mounaïm-Rousselle, L. Landry, F. Halter, and F. Foucher, “Experimental characteristics of turbulent premixed flame in a boosted Spark-Ignition engine,” *Proceedings of the Combustion Institute*, vol. 34, no. 2, pp. 2941–2949, 2013, doi: 10.1016/j.proci.2012.09.008.

[112] Nidhi and K.A. Subramanian, “Experimental investigation on effects of oxygen enriched air on performance, combustion and emission characteristics of a methanol fuelled spark ignition engine,” *Applied Thermal Engineering*, vol. 147, pp. 501–508, 2019, doi: 10.1016/j.applthermaleng.2018.10.066.

[113] A. C. Alkidas, P. V. Puzinauskas, and R. C. Peterson, “Combustion and Heat Transfer Studies in a Spark-Ignited Multivalve Optical Engine,” in *International Congress & Exposition*, 1990.

[114] R. S. Wolf and W. K. Cheng, “Heat Transfer Characteristics of Impinging Diesel Sprays,” in *SAE Technical Paper*, 1989. [Online]. Available: https://doi.org/10.4271/890439

[115] Yuanjiang Pei *et al.,* “An analysis of the structure of an n-dodecane spray flame using TPDF modelling,” *Combustion and Flame*, vol. 168, pp. 420–435, 2016, doi: 10.1016/j.combustflame.2015.11.034.

[116] R. Mahmud *et al.,* “Characteristics of Flat-Wall Impinging Spray Flame and Its Heat Transfer under Small Diesel Engine-Like Condition,” in *JSAE/SAE Small Engine Technologies Conference & Exhibition*, 2017.

[117] T. Kamimoto, S. Kobori, S. H. Noh, and Y. Enomoto, “Effects of Flame Motion and Temperature on Local Wall Heat Transfer in a Rapid Compression-Expansion Machine Simulating Diesel Combustion,” in *International Fuels & Lubricants Meeting & Exposition*, 1992. [Online]. Available: https://doi.org/10.4271/922208

[118] K. Lee and C. Lee, “Effects of tumble and swirl flows on turbulence scale near top dead centre in a four-valve spark ignition engine,” *Proceedings of The Institution of Mechanical Engineers Part D-journal of Automobile Engineering - PROC INST MECH ENG D-J AUTO*, vol. 217, pp. 607–615, 2005, doi: 10.1243/095440703322114988.

[119] K. Y. Kang and J. H. Baek, “Tumble Flow and Turbulence Characteristics in a Small Four-Valve Engine,” in *International Congress & Exposition*, 1996.

A

Analysis of heat loss during flame wall interaction of premixed propagative flames and diffusive spray flames

Author: Abhijit Padhiary
Thesis Directors: Julien Sotton, Marc Bellenoue and Guillaume Pilla

A large part of the energy is lost by heat transfer to the wall during the combustion process in internal combustion engines, especially during flame wall interaction (FWI). The open issues in FWI require experimental insight into both premixed and spray combustion. In this work, the premixed FWI is studied in a constant volume chamber (CVC) and an engine while spray combustion is studied in a CVC using thin junction thermocouples (TCs) to characterize the wall heat flux. Simultaneous particle image velocimetry (PIV) is used to characterize the flow field in the CVC. For laminar FWI, the heat flux peak (Q_P) depends on the pressure during FWI (P_{int}) with a power-law ($Q_P \sim P_{int}^b$, $b = 0.35$). The average Q_P for turbulent FWI is larger than the laminar case by 24% to 55%, with b>1. Dilution of the mixture (with CO_2 and N_2) led to a reduction of Q_P, due to the decrease in the flame power (Q_Σ) during FWI. Experiments on the variation of Q_Σ led to lower non-dimensional heat flux peak for high Q_Σ. Non-premixed FWI experiments were carried out in ECN spray A conditions in CVC. The convective heat transfer coefficient (h) is found to be maximum near the tip of the spray i.e., stagnation zone. h is also found to remain unchanged for different ambient temperatures both in a reactive and non-reactive spray-wall interaction. Modifying the conditions, experiments were carried out where the autoignition occurs after spray-wall interaction leading us to obtain two-step heat flux where the first step is due to spray wall interaction and the second step is due to the reaction of spray and FWI. Propagative FWI is also studied in an engine for two modes of ignition, conventional spark ignition (SI) and passive pre-chamber ignition (PC). Q_P vs P_{int} for different locations of TCs and different ignition systems remained the same. Q_P vs P_{int} is different for different ignition timings for PC ignition, while it remains the same for SI. With the increase of IMEP, we find an increase in Q_P corresponding to increase in P_{int}.

Keywords: Heat—Convection; Combustion chambers; Combustion, Spontaneous; Flame; Internal combustion engines—Combustion; Heat—Transmission; Particle image velocimetry;

Résumé

Lors du processus de combustion dans les moteurs à combustion interne, une grande partie de l'énergie est perdue par transfert de chaleur à la paroi, notamment pendant l'interaction flamme-paroi. Afin d'améliorer la compréhension de ces phénomènes, un travail expérimental sur les modes de combustion prémélangé et diffusif a été effectué. Au cours de ces travaux de thèse, l'interaction flamme-paroi en mode prémélangé est étudiée dans une chambre à volume constant (CVC) ainsi qu'un moteur optique, tandis que l'interaction flamme-paroi en mode diffusif est étudié dans une CVC. Afin de caractériser les échanges thermiques, des thermocouples à jonction mince ont été mis en œuvre. Simultanément, la vélocimétrie par image de particules (PIV) a été utilisée pour caractériser les champs de vitesses dans la CVC, et plus particulièrement les niveaux de turbulence. En conditions d'écoulement laminaire, nous avons montré que le pic de flux thermique (Q_P) dépend de la pression au moment de l'interaction flamme-paroi (P_{int}) suivant une loi de puissance ($Q_P \sim P_{int}^b$, $b = 0.35$). En conditions turbulentes, nous avons montré que Q_P est supérieur au cas laminaire de 24% à 55%, avec un coefficient b>1. L'influence de la dilution du mélange combustible avec CO_2 et N_2 a été étudiée. Nous avons montré que la dilution conduit à une réduction de Q_P, qui s'explique par la diminution de la puissance de la flamme (Q_Σ) pendant l'interaction flamme-paroi. Des expériences de variations de Q_Σ ont permis de montrer que le pic de flux thermique adimensionné est plus faible pour Q_Σ élevé. Dans un deuxième temps le mode de combustion diffusif a été étudié dans la CVC, dans les conditions ECN spray A. Nous avons montré que le coefficient de transfert de chaleur par convection (h) est maximal près de l'extrémité du spray, c'est-à-dire dans la zone de stagnation. D'autre part, h reste également inchangé pour différentes températures ambiantes, et ce en conditions réactives et non-réactives de fonctionnement de la CVC. Des expériences ont été réalisées où l'auto-inflammation se produit après l'interaction entre le spray et la paroi, ce qui nous a permis de reproduire un pic de flux thermique en deux temps. Nous avons identifié que la première marche de flux est due l'interaction aérodynamique entre le spray et la paroi, et la seconde à l'interaction flamme-paroi. Pour finir, une étude des échanges thermiques instantanés en moteur optique a été réalisée. Deux systèmes d'allumage ont été testés, une bougie conventionnelle et une préchambre passive. Nous avons montré que l'influence principale du système d'allumage était liée aux écarts de P_{int} au moment de l'interaction flamme-paroi, et que l'influence de l'aérodynamique des jets issus de la préchambre est d'ordre deux.

Mots-clés: Chaleur--Convection**;** Chambres de combustion**;** Combustion spontanée**;** Flamme; Moteurs à combustion interne--Combustion; Transfert de chaleur; Vélocimétrie par images de particules